Title

Radial Echo Planar Spectroscopic Imaging: Acceleration and Applications for Diffusion-Weighted Acquisitions

Author

Saucedo, Andres

Publication Date

2023

Peer reviewed|Thesis/dissertation

UNIVERSITY OF CALIFORNIA

Los Angeles

Radial Echo Planar Spectroscopic Imaging: Acceleration and Applications for Diffusion-Weighted Acquisitions

A dissertation submitted in partial satisfaction of the

requirements for the degree Doctor of Philosophy

in Biomedical Physics

by

Andres Saucedo

2023

ABSTRACT OF THE DISSERTATION

Radial Echo Planar Spectroscopic Imaging: Acceleration and Applications for Diffusion-Weighted Acquisitions

by

Andres Saucedo

Doctor of Philosophy in Biomedical Physics

University of California, Los Angeles, 2023

Professor Michael Albert Thomas, Chair

Magnetic resonance spectroscopy (MRS) and spectroscopic imaging (MRSI) are powerful, non-invasive tools that are capable of assessing the concentrations and distributions of various metabolic compounds in vivo. Single-voxel MRS methods such as STEAM and PRESS measure the temporal signal from a specific, localized volume of interest. As such, single-voxel MRS does not require any type of spatial encoding, such as frequency and phase encoding which are used routinely in magnetic resonance imaging (MRI). Although simpler to implement for clinical applications, MRS methods are nonetheless limited in their ability to efficiently acquire spectra across large anatomical regions, since only a relatively small volume can be probed per measurement. On the other hand, multi-voxel acquisitions can be done with MRSI, which incorporates additional two-dimensional (2D) or three-dimensional (3D) spatial encoding dimensions (i.e., k-space) to resolve multiple spectra from a large volume or slice within a single scan session.

However, conventional MRSI techniques currently in clinical use depend on sequential phase encoding of each spatial dimension, which often results in long scan durations. Therefore, the focus of much research in MRSI has been to accelerate the acquisition through various means such as by undersampling or by using, often also in combination with undersampling, advanced sampling methods such as simultaneous spatiotemporal sampling of one spatial dimension and the spectral (time) dimension. The latter approach is accomplished by implementing so-called echo-planar k-t trajectories, which interleave the acquisition of one frequency-encoded spatial dimension (k) with the temporal samples (t) necessary for resolving the spectrum. The other spatial dimensions are often resolved with conventional phase encoding. Thus, echo-planar spectroscopic imaging (EPSI) is able to accelerate an MRSI scan session by at least an order of magnitude. When first proposed in the mid 1980's, EPSI was done with Cartesian trajectories and, since the late 1990's, non-Cartesian trajectories such as spirals, concentric circular, rosette, and radial trajectories have been implemented for fast MRSI. These non-Cartesian trajectories provide advantageous trade-offs in imaging speed, signal-to-noise ratio, and motion robustness compared with Cartesian EPSI.

More recently, as late as 2019, radial echo planar spectroscopic imaging (REPSI) has been described as a nascent subfield in proton (^{1}H) MRSI. Although radial projections were the first to be demonstrated for MRI, the adoption of radial sampling for MRSI had only found limited applications for non-proton MRSI, such as for phosphorus (^{31}P) and carbon (^{13}C), and had not yet been demonstrated for *in vivo* ^{1}H MRSI. This work presents a study of ^{1}H MRSI in the human brain *in vivo* using radial echo-planar trajectories, as well as applications for diffusion-weighted MRSI. The capability of REPSI for further acceleration compared to Cartesian EPSI are shown within a compressed sensing framework, in which the undersampled REPSI data can be

reconstructed with good fidelity by exploiting the sparsity of the data within a transform domain. In addition to its higher tolerance for accelerations, the motion robustness of REPSI is shown in free-breathing healthy liver and prostate acquisitions.

Both MRS and MRSI methods are compatible with diffusion-weighted (DW) techniques. DW-MRS and DW-MRSI are able to explore the microstructural characteristics of tissues *in vivo* due to the predominantly intracellular compartmentalization of metabolites. Unlike water, which permeates both the intra- and extra-cellular spaces, most metabolites are confined within the intracellular space, so that their diffusion reflects the structure and function of tissues at the microscopic scale. This compartment-specific assessment of tissue structure enables a clearer understanding of the cellular-level conditions and alterations that underlie various pathologies. This work also presents the first demonstration of a diffusion-weighted technique, first proposed in the mid 1990's and early 2000's, for *in vivo* single voxel DW-MRS and DW-MRSI in the human brain. This so-called "single-shot diffusion trace-weighted" scheme had been untestable in humans, until recently, due to earlier hardware limitations of clinical scanners. The acquisition and processing of the single voxel DW-MRS data was optimized as a precursor for the spectroscopic imaging version of the sequence. It is shown that radial echo planar trajectories are particularly advantageous for DW-MRSI, due to their self-navigation capability that enables post-processing-based corrections of the diffusion-weighted data, which is susceptible to shot-to-shot phase and frequency inconsistencies.

In the Appendix, further work in acceleration in the context of parallel imaging using low-rank approximations is also demonstrated for MRI acquisitions.

The dissertation of Andres Saucedo is approved.

Michael McNitt-Gray

Holden H. Wu

Paul M. Macey

Michael Albert Thomas, Committee Chair

University of California, Los Angeles

2023

Dedicated to my loving parents

TABLE OF CONTENTS

LIST OF ACRONYMS

GENERAL

T	-	Tesla
mm	-	millimeter
s	-	second
ms	-	millisecond

GENERAL MAGNETIC RESONANCE IMAGING AND SPECTROSCOPY

MRI	-	magnetic resonance imaging
MRS	-	magnetic resonance spectroscopy
MRSI	-	magnetic resonance spectroscopic imaging
EPSI	-	echo planar spectroscopic imaging
REPSI	-	radial echo planar spectroscopic imaging
2D/3D	-	two/three dimensional
FOV	-	field of view
VOI	-	volume of interest
TE	-	echo time
TR	-	repetition time
SNR	-	signal to noise ratio
RF	-	radiofrequency
PI	-	parallel imaging
CS	-	compressed sensing
ADC	-	apparent diffusion coefficient
PRESS	-	point resolved spectroscopy
STEAM	-	stimulated echo acquisition mode
CRLB	-	Cramer-Rao lower bound
DW	-	diffusion-weighting

SPECIAL TECHNICAL TERMS

CV	-	coefficient of variation
ROI	-	regions of interest
TV	-	total variation
ECG	-	Electrocardiogram
Semi-LASER	-	semi-localization by adiabatic selective refocusing
WET	-	water suppression enhanced through T1 effects

LIST OF FIGURES

LIST OF TABLES

ACKNOWLEDGEMENTS

I would like to sincerely express my gratitude to my advisor, Dr. M. Albert Thomas, for his support throughout my PhD journey. I appreciate his allowing me the freedom to explore the various topics that have been worked on in his lab and to pursue the projects that have culminated in my thesis work. I also want to especially thank Dr. Michael McNitt-Gray and the Physics and Biology in Medicine program for their support, both financial and academic, during my time as a graduate student researcher. I thank Dr. Paul M. Macey for his contributions to my studies and for providing resources and insightful advice which have helped with my studies. I thank Dr. Holden Wu for the scientific discussions that we have had and for his advice on my studies as well.

I also want to thank Dr. Mark Bydder for providing insightful pieces of advice on my research and sharing his wisdom on life and work. I also want to thank Fadil Ali for his support and friendship and for his help and collaboration, as well as for stimulating discussions on various MR physics topics, which have helped with my learning.

I am pleased to have known and have learned from past members and staff of the Magnetic Resonance Research Lab (MRRL): Tess Armstrong, Vahid Ghodrati, Zhaohuan Zhang, Zohaib Iqbal, Da Wang, Stanislas Rappachi, Isabel Dregely, Novena Rangwala, Ziwu Zhou, Fei Han, Daniel Ennis, Kyung Sung, Heather Wilbur, Ajin Joy, and more. I want to thank them for willing to be my volunteers for the research MRS/MRSI scans. I am proud of being a member of the Physics and Biology in Medicine program family. In particular, I would like to thank Dr. Michael McNitt-Gray, Reth Im, and Alondra Correa Bautista for their support and assistance throughout my Ph.D. journey. Lastly, I would like to thank my parents, Irma Porras and Hector Saucedo, and my brother Miguel for all their support and for giving me the freedom to pursue my goal.

VITA

Education:

- Ph.D. student, Physics and Biology in Medicine Interdepartmental Graduate Program, University of California at Los Angeles, Los Angeles, California, United States, 2012–2023
- M.Sc., Biomedical Physics, University of California at Los Angeles, Los Angeles, California, United States, 2012-2015
- B.S., Physics; B.S., Mathematics, University of California at Los Angeles, Los Angeles, California, United States, 2004-2009

First/Co-First Author Peer-Reviewed Publications:

1. **A Saucedo**, MA Thomas. Single-Shot Diffusion Trace Spectroscopic Imaging using Radial Echo Planar Trajectories. Magnetic Resonance in Medicine 2023 (under review).
2. **A Saucedo**, J Sayre, MA Thomas. Single-Shot Diffusion Trace-Weighted MR Spectroscopy: Comparison with Unipolar and Bipolar DW-PRESS. NMR in Biomedicine 2023 (revision under preparation).
3. **A Saucedo**, PM Macey, MA Thomas. Accelerated Radial Echo-Planar Spectroscopic Imaging Using Compressed Sensing with Total Variation Regularization. Magnetic Resonance in Medicine, 2021; 86: 46-61.
4. **A Saucedo**, S Lefkimmiatis, N Rangwala, K Sung. Improved Computational Efficiency of Locally Low-Rank MRI reconstruction using iterative random patch adjustments. IEEE Transactions on Medical Imaging, 2017; 36(6): 1209-1220.
5. A Joy, **ASaucedo***, M Joines, S Lee-Felker, S Kumar, MK Sarma, J Sayre, M DiNome, MA Thomas. Correlated MR Spectroscopic Imaging of Breast Cancer to Investigate Metabolites and Lipids: Acceleration and Compressed Sensing Reconstruction. BJR Open 2022; 4: 20220009. *1st co-author

Co-Author Peer-Reviewed Publications

1. MK Sarma, **A Saucedo**, CH Darwin, ER Felker, K Umachandra, D Kohanghadosh, E Xu, S Raman, MA Thomas. Noninvasive assessment of abdominal adipose tissues and quantification of hepatic and pancreatic fat fractions in type 2 diabetes mellitus. Magnetic Resonance Imaging, 2020; 72: 95-102.
2. M Bydder, F Ali, **A Saucedo**, A Hagiwara, C Wang, AD Pham, J Yao, B Ellingson. A Study of 3D radial density adapted trajectories for sodium imaging. Magnetic Resonance Imaging, 83 (2021): 89-95.
3. M Bydder, F Ali, **A Saucedo**, V Ghodrati, A Samsonov. Low rank off-resonance correction for double half-echo k-space acquisitions. Magnetic Resonance Imaging (2022); 94: 43-47.
4. A Joy, R Nagarajan, **A Saucedo**, Z Iqbal, M Sarma, NE Wilson, E Felker, RE Reiter, SS Raman, MA Thomas. Dictionary Learning Compressed Sensing Reconstruction: Pilot Validation of Accelerated Echo Planar J-resolved Spectroscopic Imaging in Prostate Cancer. Magnetic Resonance Materials in Physics, Biology and Medicine (2022); 35(4):667-682.
5. A Joy, R Nagarajan, ES Daar, J Paul, **A Saucedo**, SK Yadav, M Guerrero, E Haroon, P Macey, MA Thomas. Alterations of gray and white matter volumes and cortical thickness in treated HIV-positive patients. Magnetic Resonance Imaging (2023); 95: 27-38.
6. A Joy, M Lin, M Joines, **A Saucedo**, S Lee-Felker, J Baker, A Chien, U Emir, PM Macey, MA Thomas. Ensemble Learning for Breast Cancer Lesion Classification: A Pilot Validation Using Correlated Spectroscopic Imaging and Diffusion-Weighted Imaging. Metabolites (2023); 13(7): 835.

Chapter 1 Introduction

1.1 Outline

Magnetic resonance spectroscopy (MRS) and spectroscopic imaging (MRSI) are powerful tools capable of non-invasively measuring metabolic information in vivo, enabling the biochemical characterization of various pathologies. MRS and MRSI has been applied for diagnosing, monitoring, and understanding the causes of diseases in human brain, liver, kidney, and skeletal and cardiac muscle. In contrast to single voxel MRS, MRSI is able to measure spectra from multiple voxel locations within a single measurement period. However, the main limitation of MRSI is the long acquisition times necessary to encode the necessary spectral and spatial information. Consequently, one of the main challenges for MRSI is to shorten the scan time without compromising the spectroscopic imaging quality. An effective approach toward this end is to apply echo planar k-t trajectories that speed up the sampling time by an order of magnitude compared to conventional MRSI that relies solely on phase encoding each spatial dimension before spectral encoding. In contrast, echo planar spectroscopic imaging (EPSI) is a much faster alternative for MRSI because it interleaves the collection of spatial-spectral data. The combination of undersampling with echo planar trajectories is one of the most effective strategies for reducing the total scan time to within practical clinical durations.

Radial k-space sampling, already widespread in MRI research, has a number of advantages compared to Cartesian sampling, such as increased robustness to motion-induced artifacts, greater inherent SNR due to its dense sampling of the central k-space, and greater potential for acceleration. Radial sampling is particularly suitable for MRSI since the highest sampling density in radial k-space corresponds to the lowest spatial frequencies, which become more important in the case of

low spatial resolutions typically acquired in MRSI. Therefore, compared to Cartesian EPSI, non-Cartesian trajectories such as radial trajectories could offer a better alternative for acceleration and a better trade-off between sampling efficiency (greater for Cartesian sampling) and higher SNR or decreased sensitivity to motion-induced artifacts. However, as late as 2019, radial echo planar spectroscopic imaging (REPSI) was considered a nascent subfield of MRSI[1], and had yet to be demonstrated for ^{1}H spectroscopic imaging. This thesis includes a study of REPSI for accelerated acquisitions in human brain, and presents pilot data from free-breathing liver and prostate acquisitions.

Diffusion-weighting MRS and MRSI (DW-MRS/MRSI) offer a more specific tool for probing the intracellular conditions underlying pathology. Since most metabolites are confined within the intracellular space, measurements of the metabolite apparent diffusion coefficients (ADC) with DW-MRS/MRSI more specifically reflect the extent to which tissue structure and cellular function are affected by disease. Hence, diffusion-weighted spectroscopy, in general, contributes valuable information which cannot be ascertained with DW-MRI, which can only probe water diffusion that occurs indiscriminately between intra- and extracellular compartments. Several DW-MRS techniques have been reported, although an important subset is dedicated to measuring a particular quantity called the trace ADC, or mean diffusivity. The trace ADC is a more reliable quantity to estimate diffusion because, in principle, its value is independent of the relative orientation of the cell frame of reference with respect to the gradient frame of reference, thus avoiding this potential source of bias. Conventional DW-MRSI techniques require at least three separate measurements along orthogonal diffusion-sensitizing gradient directions to estimate the trace ADC, which prolongs the total measurement time. However, a DW-MRS method based on PRESS localization, first proposed in the early 2000's and based on work originally proposed in the mid 1990's, is able

to measure the trace ADC in one measurement. This "single-shot" diffusion trace-weighted spectroscopic technique had only been reported in small animal scanners up to as late as 2012[2], but was prevented from use in clinical scanners due to gradient amplitude and slew rate limitations, until recently. A variant of the original scheme studied in this work was shown in human brain most recently in 2020[3]. This thesis presents a study on single-shot trace-weighted MRS (Trace DW-MRS) in human brain using the originally proposed sequence. Acquisitions parameters and post-processing steps were explored and optimized in preparation for another study on extending Trace DW-MRS to Trace DW-REPSI.

Several studies have reported on DW-MRSI in human brain, mostly using Cartesian trajectories, either in the conventional phase-encoding mode or with echo planar trajectories. In general, DW-MRS/MRSI requires careful post-processing due to pulsatile motion which causes the diffusion-weighted signal to have large amplitude and phase fluctuations from shot-to-shot. Additionally, since DW-MRS/MRSI require multiple signal averages, thereby prolonging the scan time, frequency drifts during the long measurement period must also be corrected. Past techniques based on Cartesian trajectories have necessitated a separate navigator echo within the pulse sequence to track the relative phase and frequency inconsistencies of the data. However, as is now common practice in MRI, the self-navigation properties of radial sampling can be exploited to correct for these errors in DW-MRSI. The resulting single-shot diffusion trace-weighted REPSI (DW-REPSI) pulse sequence thus has a further advantage over conventional Cartesian approaches, not only because of its self-navigation, but also due to its better prospects for accelerated DW-MRSI. Therefore, this thesis also presents a study on the spectroscopic imaging version of the single-shot diffusion trace-weighted sequence.

1.2 Organization of the thesis

Chapter 2 Background: This chapter begins with a brief introduction of the concepts behind nuclear magnetic resonance and classical signal excitation and detection approaches for imaging and spectroscopy. A brief summary of echo planar spectroscopic imaging and the various radial k-space sampling approaches for MRSI are also presented. Lastly, a brief overview of diffusion-weighting and diffusion-weighted spectroscopy is discussed.

Chapter 3 Accelerated Radial Echo Planar Spectroscopic Imaging Using Golden Angle View Ordering and Compressed Sensing Reconstruction with Total Variation Regularization: This chapter presents an accelerated two-dimensional radial echo-planar spectroscopic imaging (REPSI) sequence using undersampled radial k-space trajectories and compressed sensing (CS) reconstruction and compares quantitation and imaging results with those from an undersampled Cartesian spectroscopic sequence. The results of this chapter have been published as a journal article[4].

Chapter 4 Single-Shot Diffusion Trace-weighted MR Spectroscopy: Comparison with Unipolar and Bipolar DW-PRESS: This chapter presents a single voxel study to demonstrate the feasibility and performance of the PRESS-based, single-shot diffusion trace-weighted sequence in quantifying the trace apparent diffusion coefficient (ADC) in phantom and in vivo using a 3T MRI/MRS scanner, and to compare results to trace ADC's derived from conventional diffusion-weighted PRESS sequences acquired with unipolar and bipolar diffusion gradient configurations. The results of this chapter have been submitted to a journal as a full research article and as of July 2023 is undergoing its first revision.

Chapter 5 Single-shot Diffusion Trace Spectroscopic Imaging using Radial Echo Planar Trajectories: This chapter presents the spectroscopic imaging version of the single voxel singe-

shot diffusion-trace weighted sequence described in the previous chapter. The goal of the study presented in this chapter is to demonstrate the feasibility and evaluate the performance of single-shot diffusion trace-weighted radial echo planar spectroscopic imaging (Trace DW-REPSI) for quantifying the trace apparent diffusion coefficient (ADC) in phantom and *in vivo* using a 3T clinical scanner. The results of this chapter have been submitted to a journal as a full research article and as of July 2023 is under review.

Chapter 6 Conclusion: This chapter includes a summary of the work in this thesis and discusses the significance and future directions of the methods implemented in this work.

Appendix: This portion of the thesis includes a study on parallel imaging-based reconstruction using low-rank sparsity along the coil dimension in the image domain within local neighborhoods. The main contribution of this work is to provide an alternative reconstruction approach that significantly increases the computational efficiency of the reconstruction algorithm, and a proof is provided to establish the convergence of the proposed algorithm.

Chapter 2 Background

This chapter introduces some basic background on MRI physics, single voxel MR spectroscopy and spectroscopic imaging in two and three spatial dimensions, including Cartesian and radial echo planar spectroscopic imaging, and diffusion-weighted MRS/MRSI. Acceleration and reconstruction techniques are covered in subsequent chapters. This chapter is not meant to be a comprehensive summary of these subjects but to briefly familiarize the readers with the material discussed in the rest of this thesis.

2.1 Basics of Magnetic Resonance Imaging

2.1.1 Magnetic Moment and Magnetization

The ^{1}H hydrogen atom contains a nucleus with odd mass number (one proton), a property which allows the ^{1}H nucleus to possess an intrinsic angular momentum, or spin, $\hat{\boldsymbol{I}}$. The associated magnetic moment $\hat{\boldsymbol{u}}$ of the proton (the charged portion of the nucleus) is represented as

$$\boldsymbol{\mu} = \gamma \boldsymbol{I} \tag{2-1}$$

where γ is the gyromagnetic ratio for ^{1}H and equals $267.522 \times 10^6\, rad \cdot T^{-1} \cdot s^{-1}$. In the absence of any external magnetic field, each proton within a given sample at thermal equilibrium exhibits a random orientation of its spin, and therefore the net magnetization $\boldsymbol{M}$ of the sample averages to zero. However, when an external magnetic field $\boldsymbol{B}_0 = B_0\hat{\boldsymbol{z}}$ is applied, the spins precess around an axis of rotation defined by the direction of the $\boldsymbol{B}_0$. The (angular) frequency of the precession (also called the Larmor frequency) is:

$$\omega_0 = -\gamma B_0 \tag{2-2}$$

The negative sign indicates that the rotation is clockwise when viewed down from the positive $\hat{\boldsymbol{z}}$ axis. Since the proton is a spin-1/2 system, the longitudinal component of $\boldsymbol{\mu}$, denoted by μ_z, becomes oriented either parallel or antiparallel to $\boldsymbol{B}_0$, with the parallel direction being more energetically favorable. Hence, there is a greater population of spins with μ_z parallel to the applied field, leading to a net magnetization vector $\boldsymbol{M} = M_z^0\hat{\boldsymbol{k}}$. In the transverse plane, the components of $\boldsymbol{\mu}$ for each spin are orientated randomly with respect to all other spins. Thus, at this equilibrium state with only the $\boldsymbol{B}_0$ field applied, the net transverse magnetization remains zero.

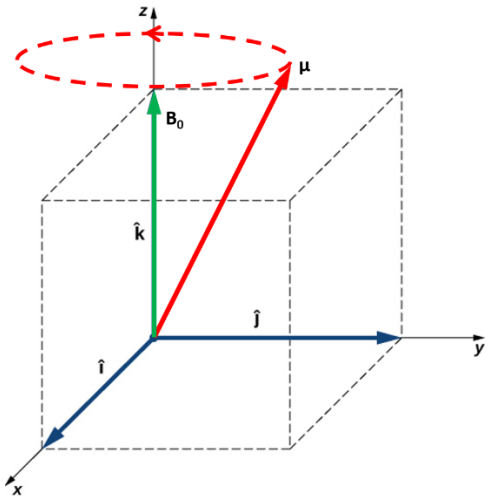

Figure 2-1: The main static magnetic field B_0 induces a precession of the magnetic moment whose axis of rotation is the direction B_0.

In the context MRI, $\boldsymbol{B}_0$ is the static field parallel to the bore axis of the scanner and it is the strongest magnetic field of the entire MRI system. Typical field strengths for clinical scanners are 1.5T and 3T, corresponding to Larmor frequencies of 63.9 MHz/T and 127.7 MHz/T, respectively.

2.1.2 Bloch Equations and Excitation

The main function of a pulse sequence is to manipulate the magnetization through radio-frequency (RF) excitation and by applying time-dependent gradients $\boldsymbol{G}(t)$. The magnetic field gradient $\boldsymbol{G}(t)$, in units of mT/m, varies linearly as a function of spatial direction but points in the $\hat{\boldsymbol{k}}$ direction. The RF field, denoted by $\boldsymbol{B}_1(t)$, acts on the net magnetization to induce a detectable

transverse component M_{xy}, and $\boldsymbol{B}_1(t)$ is usually circularly polarized in the same direction as the precessing spins, with a carrier frequency at or near the Larmor frequency. The magnetic field gradient $\boldsymbol{G}(t)$ may act simultaneously with the $\boldsymbol{B}_1$ field for the purposes of spatial localization and it can be applied during the readout period to spatially encode the signal. The $\boldsymbol{G}(t)$ gradient may also be used to sensitize the signal to diffusion and flow. Generally, the gradient $\boldsymbol{G}(t)$ is written as $\boldsymbol{G}(t) = G_x(t)\hat{\boldsymbol{\imath}} + G_y(t)\hat{\boldsymbol{\jmath}} + G_z(t)\hat{\boldsymbol{k}}$, such that its contribution to the magnetic field at position $\boldsymbol{r} = x\hat{\boldsymbol{\imath}} + y\hat{\boldsymbol{\jmath}} + z)\hat{\boldsymbol{k}}$ is $\boldsymbol{G}(t)\cdot\boldsymbol{r} = G_x(t)x + G_y(t)y + G_z(t)z$.

The temporal behavior of the magnetization vector $\boldsymbol{M}(t)$ is governed by the Bloch equation:

$$\frac{d\boldsymbol{M}}{dt} = \gamma(\boldsymbol{M}\times\boldsymbol{B}) - \frac{(M_x\boldsymbol{i} + M_y\boldsymbol{j})}{T_2} - \frac{(M_z - M_z^0)\boldsymbol{k}}{T_1} \tag{2-3}$$

where $\boldsymbol{B}$ is the total magnetic field (including $\boldsymbol{B}_0$, $\boldsymbol{B}_1(t)$, and $\boldsymbol{G}(t)\cdot\boldsymbol{r}$), M_z^0 is initial magnetization in the presence of $\boldsymbol{B}_0$ only, and T_1 and T_2 are the spin-lattice and spin-spin relaxation times, respectively. The relaxation time T_1 determines the rate of recovery of the longitudinal component $M_z(t)$ and T_2 the decaying time of the transverse component $\boldsymbol{M}_{xy} = M_x\hat{\boldsymbol{\imath}} + M_y\hat{\boldsymbol{\jmath}}$. Since the relaxation times are sample-specific and related to the tissue characteristics, the times at which the signal is sampled can be chosen in order to obtain a particular image contrast among the different tissues.

The applied RF field, $\boldsymbol{B}_1(t)$, can be modeled as [5]

$$\boldsymbol{B}_1(t) = B_1(t)\,(\cos\omega t\;\hat{\boldsymbol{\imath}} - \sin\omega t\,\hat{\boldsymbol{\jmath}}) \sim B_1(t)\,e^{-i\omega t} \tag{2-4}$$

where $B_1(t)$ is the envelope function that defines the magnitude of the RF pulse. To make the Bloch equations easier to solve, the problem is cast within an alternative coordinate system called

the rotating frame. Also, for simplicity, the effects of $T_1$and T_2 relaxation are ignored during the application of the excitation pulse $\boldsymbol{B}_1(t)$.

The change of basis transformation between the laboratory frame and the rotating frame is a matrix that represents a clockwise rotation about the $+\hat{z}$ axis by an angle ωt:

$$\boldsymbol{R_z}(\omega t) = \begin{pmatrix} \cos\omega t & -\sin\omega t & 0 \\ \sin\omega t & \cos\omega t & 0 \\ 0 & 0 & 1 \end{pmatrix} \tag{2-5}$$

For notational purposes, the coordinate axes $\{\hat{\imath}, \hat{\jmath}, \hat{k}\}$ (or $\{\hat{x}, \hat{y}, \hat{z}\}$) in the laboratory frame are written as $\{\hat{\imath}', \hat{\jmath}', \hat{k}'\}$ (or $\{\hat{x}', \hat{y}', \hat{z}'\}$) in the rotating frame, i.e., $\boldsymbol{M}_{rot}(t) = M_{x'}\hat{\imath}' + M_{y'}\hat{\jmath}' + M_{z'}\hat{k}'$.

The magnetization $\boldsymbol{M}(t)$ in the laboratory frame is related to the magnetization $\boldsymbol{M}_{rot}(t)$ in the rotating frame by:

$$\boldsymbol{M}(t) = \boldsymbol{R_z}(\omega t)\boldsymbol{M}_{rot}(t) \tag{2-6}$$

In the rotation frame, the $\boldsymbol{B}_1(t)$ field becomes

$$\boldsymbol{B}_{1,rot}(t) = \boldsymbol{R_z}(\omega t)\boldsymbol{B}_1(t) = B_1(t)\,\hat{\boldsymbol{\imath}}' \tag{2-7}$$

and the Block equation becomes (again, ignoring relaxation effects)

$$\frac{d\boldsymbol{M}_{rot}}{dt} = \gamma\boldsymbol{M}_{rot} \times \boldsymbol{B}_{eff} = \gamma\boldsymbol{M}_{rot} \times \left(B_1(t)\,\hat{\boldsymbol{\imath}}' + \left(B_0 - \frac{\omega}{\gamma}\right)\hat{\boldsymbol{k}}'\right) \tag{2-8}$$

Therefore, the magnetization $\boldsymbol{M}_{rot}(t)$ precesses about and effective magnetic field in the rotating frame defined by

$$\boldsymbol{B}_{eff}(t) = B_1(t)\,\hat{\boldsymbol{\imath}}' + \left(B_0 - \frac{\omega}{\gamma}\right)\hat{\boldsymbol{k}}' \tag{2-9}$$

Now, writing Equation (2-8) in matrix form

$$\frac{d\boldsymbol{M}_{rot}}{dt} = \begin{pmatrix} 0 & \omega_0 - \omega & 0 \\ -(\omega_0 - \omega) & 0 & \gamma B_1(t) \\ 0 & -\gamma B_1(t) & 0 \end{pmatrix} \boldsymbol{M}_{rot} \tag{2-10}$$

If the frequency of $\boldsymbol{B}_1(t)$ is on resonance, i.e., the carrier frequency ω matches that of the Larmor frequency ($\omega_0 = \omega$), the Equation (2-10) becomes

$$\frac{d\boldsymbol{M}_{rot}}{dt} = \begin{pmatrix} 0 & 0 & 0 \\ 0 & 0 & \gamma B_1(t) \\ 0 & -\gamma B_1(t) & 0 \end{pmatrix} \boldsymbol{M}_{rot} \tag{2-11}$$

This corresponds to a rotation about the $\hat{x}'$ axis with a flip angle $\theta(t)$ given by

$$\theta(t) = \gamma \int_0^t B_1(t')\, dt' \tag{2-12}$$

If the initial magnetization is $\boldsymbol{M}_{rot}(0) = (0, 0, M_z^0)$, then the solution to Equation (2-11) is

$$\boldsymbol{M}_{rot}(t) = \boldsymbol{R}_{x'}\big(\theta(t)\big)\boldsymbol{M}_{rot}(0) = \begin{pmatrix} 0 \\ M_z^0 \sin\theta(t) \\ M_z^0 \cos\theta(t) \end{pmatrix} \tag{2-13}$$

For example, if $B_1(t) = B_1$, a constant, and the pulse is on for a time τ, the magnetization rotates about the $+\hat{x}'$ axis with a total flip angle of $\theta(\tau) = \gamma B_1 \tau$. Such RF pulse is referred to as a $\theta(\tau)_{x'}$ pulse. If a $90^\circ_{x'}$ pulse is played, then at the end of the pulse, the magnetization points along the $+\hat{y}'$ axis.

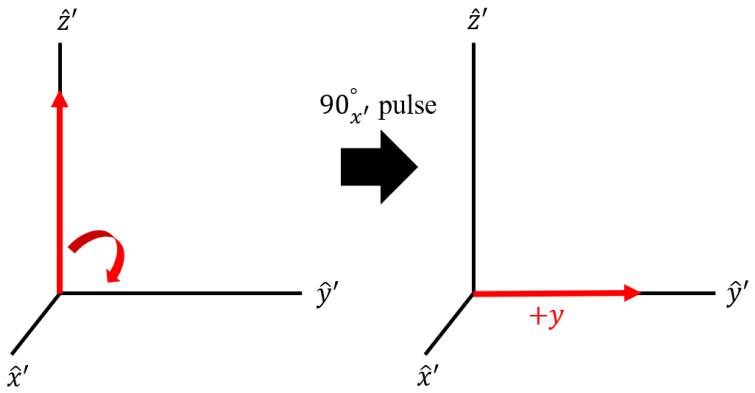

Figure 2-2: Action of a 90° excitation pulse which induces a rotation about the x' axis.

2.1.3 **Slice Selection**

An RF pulse $\boldsymbol{B}_1(t)$ with an on-resonant carrier frequency $\omega = \omega_0$ will excite all magnetization within the volume of interest that is precessing at the Larmor frequency and that is sufficiently sensitive to the RF excitation coil. In the presence of a gradient G_z, spins at different locations along z will have resonant frequencies given by $\omega(z) = \gamma B_z = \gamma G_z z$. Hence, the RF pulse can be designed to select a single plane within the volume which is perpendicular to z, provided that the temporal frequencies of $\boldsymbol{B}_1(t)$ match the resonant frequencies of the spins within that slice. Spins with resonant frequencies that are outside of the bandwidth of $\boldsymbol{B}_1(t)$ will not be affected by the excitation pulse. In this manner, the RF pulse acts in conjunction with the spatial gradient G_z to produce signal located from a specific $x - y$ plane within the volume.

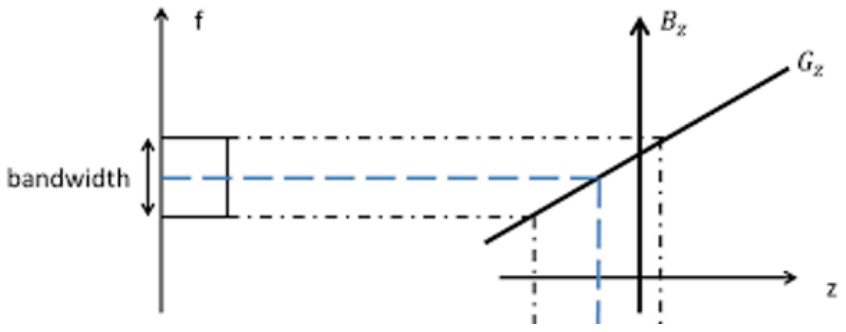

Figure 2-3: The linear relationship between the bandwidth of the excitation pulse and the corresponding extent of spatial selection, which is controlled by the slice select gradient G_z.

In general, with the gradient G_z turned on, the effective magnetic field in the rotating frame is

$$\boldsymbol{B}_{eff}(t) = B_1(t)\,\hat{\boldsymbol{\imath}}' + \left(B_0 + G_z z - \frac{\omega}{\gamma}\right)\hat{\boldsymbol{k}}' \tag{2-14}$$

Now, if the carrier frequency of the excitation pulse is tuned to the Larmor frequency ($\omega = \omega_0$) the Bloch equations become

$$\frac{d\boldsymbol{M}_{rot}}{dt} = \begin{pmatrix} 0 & \omega(z) & 0 \\ -\omega(z) & 0 & \gamma B_1(t) \\ 0 & -\gamma B_1(t) & 0 \end{pmatrix} \boldsymbol{M}_{rot} \tag{2-15}$$

The term $\omega(z) = \gamma G_z z$ indicates the degree of off-resonance of the spins at location z (again, assuming that $\omega = \omega_0$). The more off-resonant the spins are, the more the effective field, $\boldsymbol{B}_{eff}$, at that location along z, is tilted toward the $\hat{\boldsymbol{z}}'$ axis. When $\boldsymbol{B}_{eff}$ is predominantly pointing along $\hat{\boldsymbol{z}}'$, RF pulse is ineffective in generating transverse magnetization.

The Bloch equations for selective excitation in Equation (2-15) generally require numerical methods to solve. However, a closed-form solution exists for the special case when the flip angle of the excitation pulse is small, i.e. $\theta < 30°$, such that $M_{z'} \cong M_z^0$. Therefore, $\frac{dM_{z'}}{dt} = 0$, and Equation (2-15) becomes

$$\frac{d}{dt}\begin{pmatrix} M_{x'} \\ M_{y'} \\ M_{z'} \end{pmatrix} = \begin{pmatrix} 0 & \omega(z) & 0 \\ -\omega(z) & 0 & \omega_1(t) \\ 0 & 0 & 0 \end{pmatrix}\begin{pmatrix} M_{x'} \\ M_{y'} \\ M_{z'} \end{pmatrix} \tag{2-16}$$

where $\omega_1(t) = \gamma B_1(t)$. Denoting the transverse magnetization as $M_{x'y'} = M_{x'} + iM_{y'}$ (such that $\boldsymbol{M}_{x'y'} \cdot \hat{\imath}' = M_{x'}$ and $\boldsymbol{M}_{x'y'} \cdot \hat{\jmath}' = M_{y'}$), the solution to Equation (16) is

$$M_{x'y'}(t,z) = iM_z^0 e^{-i\omega(z)t}\int_0^t \omega_1(t')e^{i\omega(z)\cdot t'}dt' \tag{2-17}$$

If the duration of the RF pulse is τ, then at time $t = \tau$, the transverse magnetization is

$$M_{x'y'}(\tau, z) = iM_z^0 e^{-i\omega(z)\tau} \int_0^{\tau} \omega_1(s) e^{i2\pi f(z)\cdot s} ds \tag{2-18}$$

where $f(z) = \frac{\omega(z)}{2\pi} = \frac{\gamma}{2\pi} G_z z$. Since most RF pulses are designed to be symmetric about $\frac{\tau}{2}$, Equation (18) can be written with a change of variable $t' = s - \frac{\tau}{2}$ as follows:

$$M_{x'y'}(\tau, z) = iM_z^0 e^{-i\omega(z)\frac{\tau}{2}} \int_{-\frac{\tau}{2}}^{\frac{\tau}{2}} \omega_1\left(t' + \frac{\tau}{2}\right) e^{i2\pi f(z)\cdot t'} dt' \tag{2-19}$$

Hence, the transverse magnetization $M_{x'y'}$ at position z is proportional to the Fourier transform of $\omega_1(t + \frac{\tau}{2})$, evaluated at the frequency $-f(z)$. This result means that the slice profile along z is determined by the temporal frequency content of the RF pulse envelope $B_1(t)$. For example, if $B_1(t)$ is an ideal $sinc$ function, the Fourier transform would yield a $rect$ function, describing a constant profile amplitude for $M_{x'y'}$ across the selection bandwidth in the z direction.

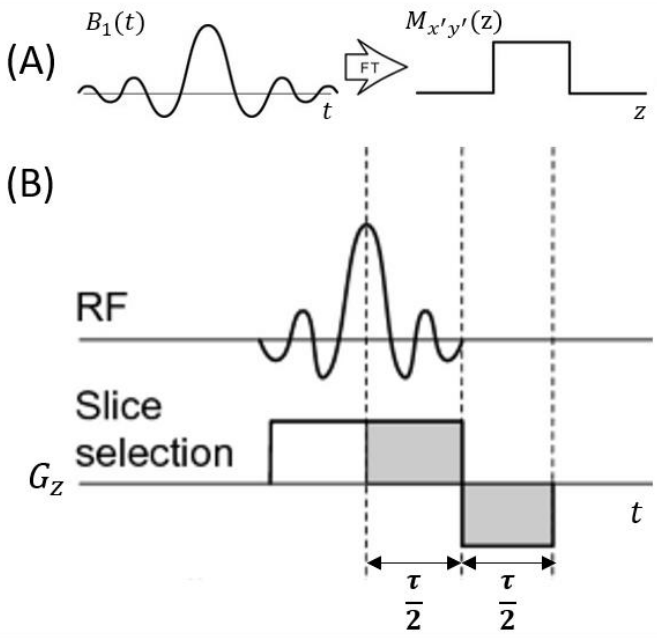

Figure 2-4: (A) Example of an ideal sinc pulse envelope whose Fourier Transform is the desired (rectangular) slice profile. (B) After slice excitation, a rephrasing lobe is required to avoid the phase dispersion accumulated during the RF pulse.

As seen in Equation (2-19), the RF pulse induces a spatially-dependent phase $\phi(z) = \frac{\tau}{2}\gamma G_z z$ across the slice thickness. If not corrected, the total effect of this phase distribution is signal loss, as the spins across the slice volume add incoherently. To undo this phase accrual, a negative gradient lobe $-G_z$ of duration $\frac{\tau}{2}$ is played immediately after the slice selection gradient. After the end of this slice refocusing lobe, the phases along z are coherent.

2.1.4 **Spatial Encoding**

After the applied $\boldsymbol{B}_1(t)$ is turned off, the longitudinal component of the bulk magnetization will start to relax toward its equilibrium state, and the signal from the detectable transverse component $\boldsymbol{M}_{xy}$ can be recorded. In both the non-selective or slice-selective excitation case, the detected signal originates from the entire excited slice or volume. Therefore, this signal must be localized across all relevant spatial dimensions in order to build an image. This localization is done by applying an additional longitudinal magnetic field known as the gradient field, written generally in vector form as $\mathbf{G}(t) = (G_x(t)\,, G_y(t)\,, G_z(t))$, since this gradient may also be a function of time. The role of this gradient is to make the precessional frequencies of the spins a linear function of the spatial coordinates. In this way, the received signal becomes spatially-encoded. The frequency of the spins at position $\boldsymbol{r}$ is given by

$$\omega(\boldsymbol{r}, t) = \gamma(B_0 + \mathbf{G}(t) \cdot \boldsymbol{r}) = \gamma\big(B_0 + G_x(t)x + G_y(t)y + G_z(t)z\big) \qquad (2\text{-}20)$$

Assuming that transverse magnetization has been produced after an excitation, and that the received signal has been demodulated with a demodulation frequency equal to $\omega_0 = \gamma B_0$, the MR signal $S(t)$ from the excited volume m in the presence of $\mathbf{G}(t)$ is

$$S(t) = \int m(\boldsymbol{r}) e^{-i2\pi\left(\frac{\gamma}{2\pi}\int_0^t \omega(\boldsymbol{r},\tau)d\tau\right)} d\boldsymbol{r} = \int m(\boldsymbol{r}) e^{-i2\pi\left(\frac{\gamma}{2\pi}\int_0^t \mathbf{G}(\tau)\cdot\boldsymbol{r}\, d\tau\right)} d\boldsymbol{r} \tag{2-21}$$

Defining the k-space vector $\boldsymbol{k}(t)$ as

$$\boldsymbol{k}(t) = \frac{\gamma}{2\pi}\int_0^t \mathbf{G}(\tau)d\tau \tag{2-22}$$

the Fourier relationship between the object and the detected signal, due to the application of this spatially dependent gradient $\mathbf{G}(t)$, can be observed:

$$S(t) = \int m(\boldsymbol{r}) e^{-i2\pi\boldsymbol{k}(t)\cdot\boldsymbol{r}} d\boldsymbol{r} = \widehat{M}(\boldsymbol{k}(t)) \tag{2-23}$$

In Equation (2-23), the detected signal $S(t)$ is essentially the spatial Fourier transform $\widehat{M}(\boldsymbol{k})$ of the underlying object $m(\boldsymbol{r})$. Thus, the MR acquisition process can be seen as sampling the spatial-frequency space with the trajectory described by $\boldsymbol{k}(t) = \left(k_x(t),\ k_y(t),\ k_z(t)\right)$. The k-space may follow different patterns such as rectilinear, radial, concentric circular, spiral, or rosette trajectories.

2.1.5 **Cartesian Sampling**

Cartesian sampling is one of the most common ways to sample the k-space. The sampling can be done for either 2D or 3D acquisitions, in which either one or two spatial dimensions are phase-encoded, respectively, while the remaining dimension is frequency-encoded. The frequency-encoded dimension is also called the readout direction and the corresponding gradient is called the readout gradient.

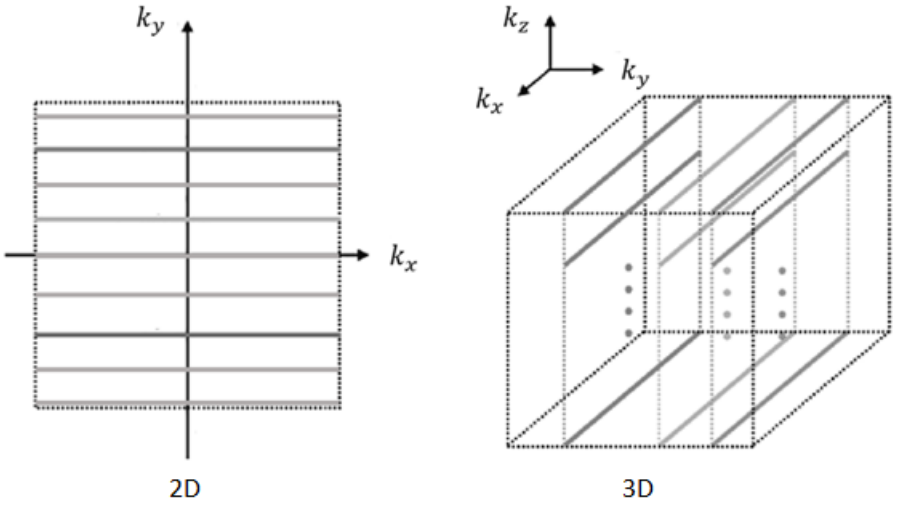

Figure 2-5. Examples of 2D and 3D Cartesian sampling trajectories.

In general, according to the Nyquist criterion, the k-space sampling increment Δk that is needed to encode a field of view L must satisfy

$$\Delta k \leq \frac{1}{L} \tag{2-24}$$

In practice, Δk is usually set to $\frac{1}{L}$, as this is the maximum Δk needed. The range of spatial frequencies that are sampled in k-space is denoted as $2k_{max}$ where k_{max} is related to the FOV and number of sampled points N as

$$k_{max} = \frac{N}{2L} \tag{2-25}$$

For the 2D Cartesian sampling case, if the readout direction is x, the amplitude of the gradient G_y along the phase-encoded direction, y, must be incrementally increased or decreased in order to spatially encode the signal along y. If the field-of-view along the phase-encoded direction is L_y,

and the duration of the gradient lobe G_y is ΔT, then the gradient increment ΔG_y for sampling the k_y dimension is

$$\Delta G_y = \frac{2\pi \Delta k_y}{\gamma \Delta T} = \frac{2\pi}{\gamma L_y \cdot \Delta T} \tag{2-26}$$

After a phase-encoding step, the constant readout gradient $G_x(t) = G_x$ is turned on for subsequent frequency-encoding, and the analog-to-digital converter (ADC) samples the signal. If the receiver or ADC bandwidth is $\Delta\nu$, then the ADC dwell time is $\Delta t = \frac{1}{\Delta\nu}$. While $G_x(t)$ is turned on, the spatial bandwidth of the object along x is $\frac{\gamma}{2\pi} G_x \cdot L_x$, where the prescribed field of view is L_x. To satisfy the Nyquist condition for sampling this spatial bandwidth, it follows that the constant gradient amplitude G_x must be

$$G_x = \frac{2\pi}{\gamma L_x \cdot \Delta t} \tag{2-27}$$

The signal corresponding to the phase-encoding line at the n_y^{th} step is

$$S(t) = \widehat{M}\left(n_y \Delta k_y, k_x(t)\right) = \int m(x,y) e^{-i2\pi(n_y \Delta k_y \cdot y)} e^{-i\frac{\gamma}{2\pi}(G_x \cdot x \cdot t)} dxdy = \tag{2-28}$$

Where $n_y = -\frac{N_y}{2}, -\frac{N_y}{2}+1, \dots, 0, 1, \dots, \frac{N_y}{2}-2, \frac{N_y}{2}-1$, and N_y is the total number of phase-encoding steps. If there are N_x points to be sampled along k_x, such that the resolution along x is $\frac{L_x}{N_x}$, then the total readout duration is $N_x \Delta t$.

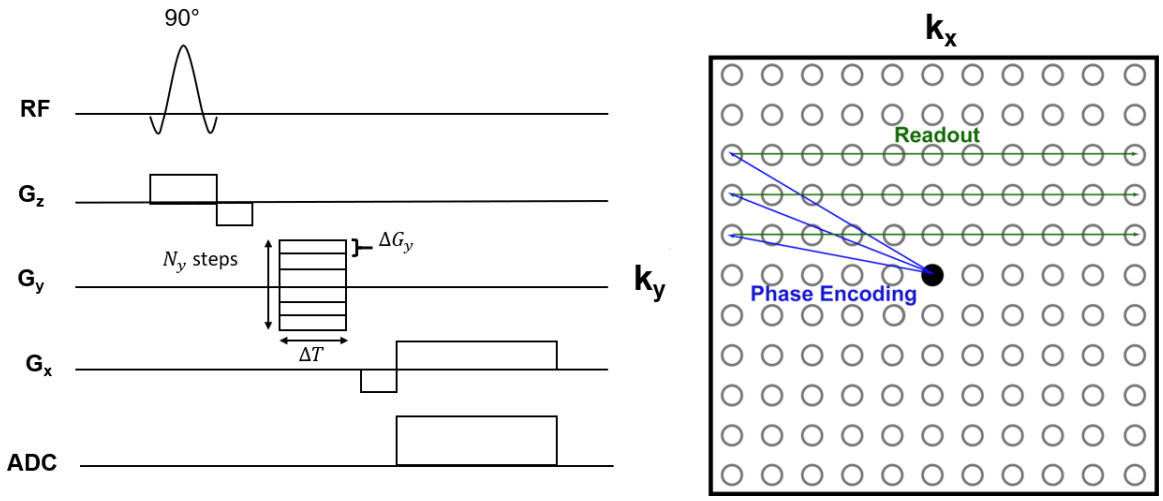

Figure 2-6: Basic pulse sequence using a gradient echo for frequency encoding along the x dimension and phase encoding along the y dimension. For each phase encoding step, the gradient echo is frequency-encoded during the readout period, generating a Cartesian sampling pattern.

For Cartesian MRI, the Fast Fourier Transform (FFT) algorithm is the most efficient digital implementation for transformation between k-space and image space. The k-space consists of equally-spaced points or lines on a rectilinear grid. Cartesian sampling is the most robust sampling strategy for dealing with several sources of system imperfections, such as off-resonance and eddy currents. However, it is highly sensitive to motion during the acquisition process.

2.1.6 **Non-Cartesian Sampling**

More recent MRI and MRSI techniques have made use of k-space trajectories that do not follow sampling patterns constrained on a rectilinear grid. In these cases, the imaging gradients are modified to traverse a curvilinear path that has several advantages over the more standard Cartesian trajectory. One of the main benefits of non-Cartesian trajectories is that the k-space can be sampled much faster, such as spiral MRI/MRSI which is able to sample the entire k-space in one shot without blipped gradients. Another benefit is the reduced gradient slew rates for curved paths with allows the use of larger gradient amplitudes for high resolution imaging, for example.

The faster k-space speed and lower slew rate demands of non-Cartesian trajectories are particularly important for MRSI because they allow a larger spectral width to be acquired for the same imaging parameters of a Cartesian acquisitions. Another advantage is that certain trajectories can more densely sample the central, low spatial frequency k-space points which are the most important for the low resolution imaging of MRSI and for retention of high SNR signal. Lastly, the repeated traversal of the central k-space for some trajectories such as spiral, radial, and rosette allows for averaging out the effect of motion-induced phase inconsistencies, making the acquisition more motion robust compared with the Cartesian case. Figure 2-8 shows the basic 2D k-space Cartesian and non-Cartesian trajectories that are common in MRSI applications. Further information on accelerated MRSI using various non-Cartesian trajectories can be found in the review article in Reference 1.

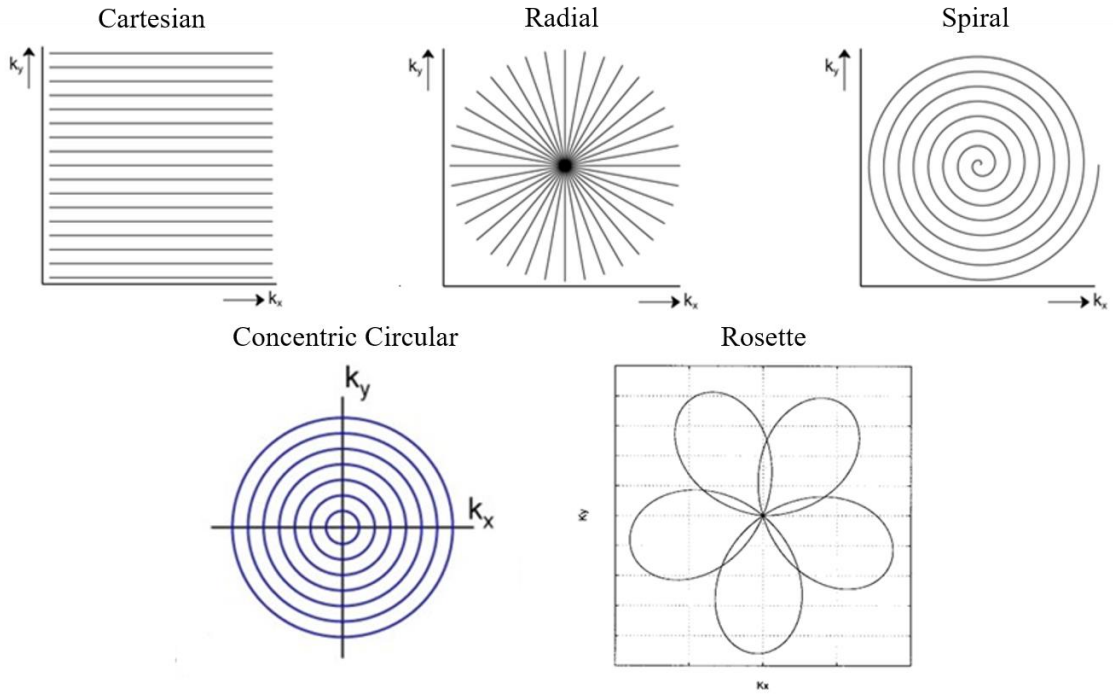

Figure 2-7: Several basic two-dimensional k-space sampling patterns using Cartesian and non-Cartesian trajectories.

2.2 Radial Sampling

2.2.1 Two-dimensional Radial Acquisitions

Radial k-space acquisitions were the first to be implemented for magnetic resonance imaging. The projection reconstruction method previously developed for computed tomography is also applicable to radial MRI acquisitions, since according to the projection-slice theorem, or the Fourier-Radon theorem, the Fourier transform of a spatial projection of an object taken at an angle θ, $P_\theta(r)$, is the k-space data $\widehat{M}(k_r, \theta)$ for the radial spoke at that angle.

$$\mathcal{F}\big(P_\theta(r)\big) = \widehat{M}(k_r, \theta) \tag{2-29}$$

For MRSI, the most practical and time-efficient sampling approach is to acquire "full" radial spokes in k-space, which extend across an entire k-space diameter from -$k_{r,max}$ to $k_{r,max}$, rather than half-spokes, which start at the origin and sample up to $k_{r,max}$. Two common types of radial k-space sampling patterns for 2D acquisitions are: the golden angle and the uniform angle distributions. For the golden angle distribution, each successive spoke $\widehat{M}(k_r, \theta_n)$ is sampled with the projection angle θ_n $(n = 1, 2, \ldots N_p)$ given by

$$\theta_n = \theta_{n-1} + 111.25^\circ \tag{2-30}$$

The starting angle θ_1 can be chosen to be any value, and a total of N_p spokes are acquired. Golden angle distributions have the property that the k-space plane is covered as uniformly as possible for any contiguous subset of the N_p spokes. Therefore, the golden angle distribution has the advantage that a set of spokes can be retrospectively binned or removed in order to select a specific acquisition period or to discard corrupted data. However, if the number of spokes in the golden angle acquisition is not a Fibonacci number, there will be sets of spokes that are separated by large

angular increments relative to other subsets of spokes, which could lead to more coherent aliasing artifacts.

For the uniform angular distribution, the spokes are evenly spaced at an angular increment given by $\Delta\theta = \frac{180^{\circ}}{N_p}$, so that successive spokes are sampled with projection angles given by

$$\theta_n = \theta_{n-1} + \frac{180^{\circ}}{N_p} \tag{2-31}$$

The net readout gradient amplitude $G(t)$ for full-spoke radial acquisitions in the 2D $k_x - k_y$ plane is the same as for Cartesian acquisition with otherwise identical imaging parameters, except that the amplitude is modulated sinusoidally along the G_x and G_y axes as follows

$$\begin{aligned} G_x(t) &= G(t)\cos\theta \\ G_y(t) &= G(t)\sin\theta \end{aligned} \tag{2-32}$$

where θ is the spoke angle. The maximum radius $k_{r,max}$ is the same as the maximum extent in Cartesian space along the readout dimension, i.e., $k_{r,max} = k_{max} = \frac{1}{2\Delta x}$, where $\Delta x = \frac{L}{N}$. The radial acquisitions assume a circular field of view with diameter L. If the matrix size is $N \times N$ then the number of spokes required to satisfy the Nyquist criterion $\Delta k = \frac{1}{L}$ at the k-space edge is

$$N_p = \frac{\pi}{2}N \tag{2-33}$$

Hence, more radial spokes are needed than Cartesian phase-encoding lines to sample an $N \times N$ k-space matrix. In this sense, radial sampling is less efficient than Cartesian sampling. One of the main advantages of radial sampling is that the spoke repeatedly traverses the central k-space region.

This property causes the resulting imaging to be more robust to motion artifacts, as the phase inconsistencies are averaged over every direction in the k-space, in contrast to motion during Cartesian acquisition which causes severe artifacts predominantly along the phase encoding direction.

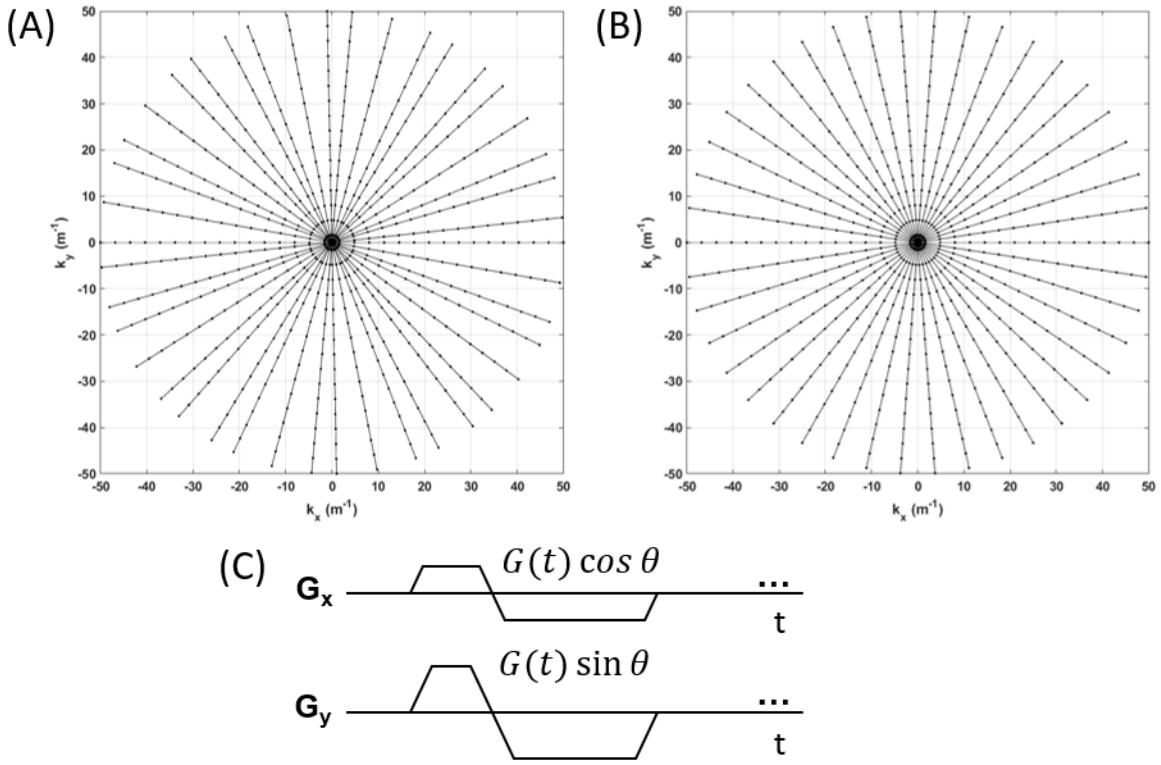

Figure 2-8: (A) An undersampled golden angle distribution of 21 radial spokes for encoding a 32 × 32 matrix (B) An undersampled uniform angular distribution of 21 spokes for encoding a 32 × 32 matrix (C) Readout gradients for encoding the x-y plane along radial spoke at angle θ.

2.2.2 **Three-dimensional (Kooshball) Radial Acquisitions**

In contrast to 2D-based acquisitions in which only the in-plane dimensions (x, y) are frequency-encoded with radial spokes in k-space, and the through-plane dimension (z) is phase-encoded, all three spatial dimensions can be frequency-encoded with radial spokes that extend through the 3D volumetric k-space - (k_x, k_y, k_z). In this case, the radial spokes comprise a

"kooshball" distribution centered at the k-space origin. Using spherical coordinates, in which the polar angle is φ and the azimuthal angle is θ, the necessary gradients to sample data along a spoke with angular coordinates (θ, φ) are given by[6]

$$\begin{aligned} G_x(t) &= G(t)\cos\theta\sin\varphi \\ G_y(t) &= G(t)\sin\theta\sin\varphi \\ G_z(t) &= G(t)\cos\varphi \\ 0 \le\ \theta \le 2\pi, &\qquad 0 \le\ \varphi \le\ \pi \end{aligned} \tag{2-34}$$

The function $G(t)$ is most simply expressed when encoding for an isotropic field-of-view, in which case the magnitude of $\vec{G}(t) = \langle G_x(t), G_y(t), G_z(t)\rangle$ is found in the same manner as described above for 2D acquisitions of a square field-of-view. This type of k-space sampling is only appropriate for three-dimensional volume-selective sequences. The spoke distribution can be uniformly distributed, in which the angles θ and φ are incremented from 0 to 2π and from 0 to π, respectively. More practically, the kooshball acquisitions can be done in a manner similar to a golden-angle 2D distribution, in which specific sets of angles are sampled such that the 3D k-space is covered as much as possible for any given number of spokes. This type of kooshball sampling can be accomplished by finding the angles (θ, φ) according to the spiral phyllotaxis formula

$$\begin{aligned} \theta_q &= \frac{2\pi}{360}\cdot 137.51^\circ \cdot q \\ \varphi_q &= \frac{\pi}{2}\cdot\sqrt{\frac{q}{P}} \end{aligned} \tag{2-35}$$

where q is the q^{th} spoke and P is the total number of spokes. An example of this distribution is shown below, where the endpoints of the spokes are indicated across the outer surface of the spherical k-space boundary.

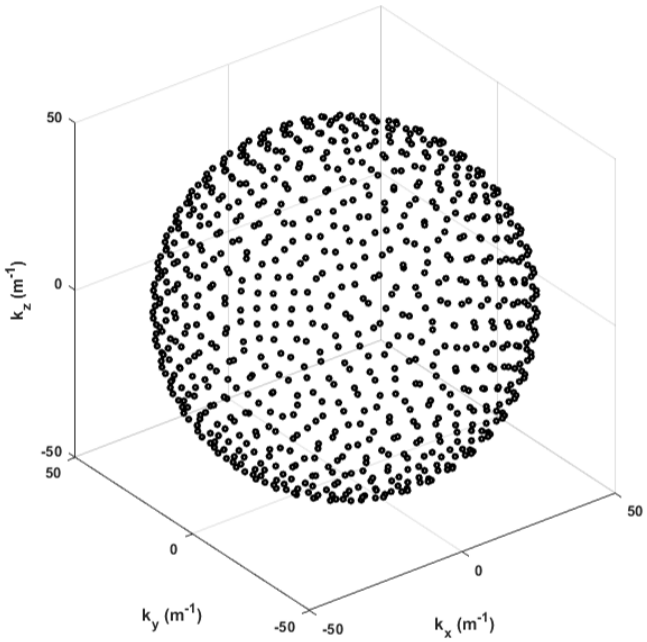

Figure 2-9: The distribution of the end points of spokes around the spherical surface defining the extent of the k-space Kooshball encoding volume. This distribution corresponds to the spiral phyllotaxis pattern.

For a fully-sampled 3D radial acquisition of a $N \times N \times N$ matrix for encoding an isotropic field of view of length L, the required Nyquist number of spokes P_s is

$$P_s = 4\pi(k_{max} \cdot L)^2 \tag{2-36}$$

This number is greater by a factor of π compared to a fully-sampled Cartesian acquisition of the same volume and matrix size. Therefore, Kooshball acquisitions usually must be undersampled for practical applications, limiting their use for only special cases such as low-resolution 3D ^{31}P spectroscopic imaging.

2.2.3 **Stack-of-Stars Radial Acquisitions**

This type of acquisition for a 3D volume is a hybrid between radial and Cartesian encoding, where the in-plane dimensions a frequency-encoded using radial spokes, and the through-plane dimensions are phase-encoded as in a conventional Cartesian acquisition. Unlike for Kooshball radial acquisitions, stack-of-stars is compatible with both slice-selective and volume or slab-selective excitations. In the slice-selective case, no phase-encoding along the slice dimension is

applied, although the end result is a still a hybrid (k_x, k_y, z) space where the radial spokes are stacked in the z direction. With volume-selective excitations, the spokes in the k_x-k_y dimensions are acquired for each phase-encoded along k_z.

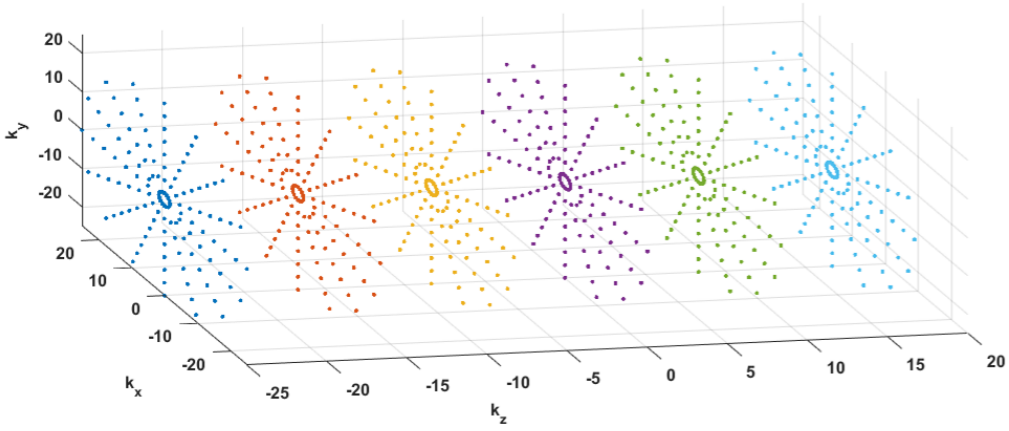

Figure 2-10: Example of a stack-of-stars sampling pattern in k_x-k_y-k_z. For MRSI, this pattern must be acquired for each dwell time along the spectrally-encoded (time) dimension.

The pulse sequence is a simple modification of the one for 2D radial MRSI, as only an extra phase-encoding gradient along the through-plane dimension is needed to encode the 3D space. For practical applications in MRSI, undersampling would usually need to be implemented both along the k_x-k_y and the k_z dimensions to reduce the total scan time. This can be accomplished by skipping phase-encoding steps along k_z and by acquiring few spokes in k_x-k_y.

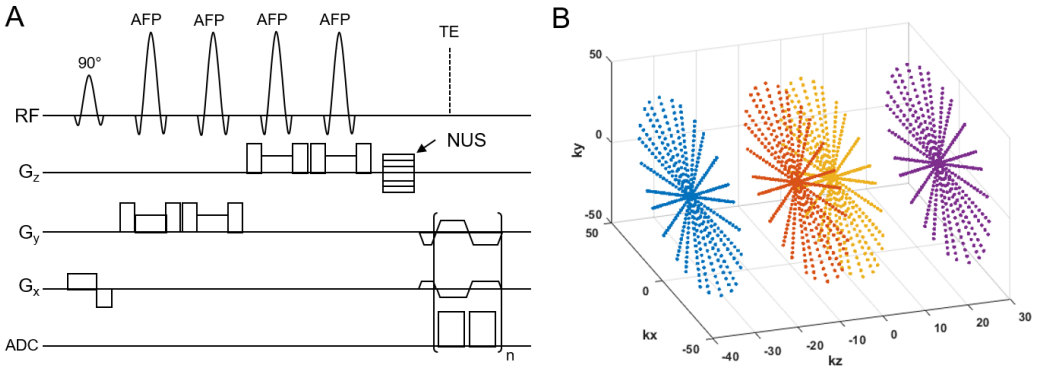

Figure 2-11: (A) Pulse sequence showing radial sampling along the k_x-k_y dimensions and undersampling along the phase encoding in k_z, generating an undersampled stack-of-stars k-space

where the number of spokes in the k_x-k_y dimension is also undersampled. This type of sampling would require a non-linear reconstruction along all dimensions to recover the fully-sampled space.

2.3 Basics of Magnetic Resonance Spectroscopy and Spectroscopic Imaging

2.3.1 Chemical Shift

Magnetic resonance spectroscopy (MRS) is a non-invasive technique that can probe the chemical composition of tissues in vivo. Most clinical MRS measures signals from ^{1}H which have sufficient concentration for the signal to have enough detectable SNR. The fundamental property of chemical shift is exploited to resolve the signal into its constituent chemical components. The hydrogen atoms within a given molecule experience a shielding from the main magnetic field B_0 due to the surrounding electron configurations which are particular to that molecule. If the shielding constant is σ, then the local magnetic field strength experienced by the proton (assuming no other gradients applied) is[7]

$$\boldsymbol{B}_{local} = \boldsymbol{B}_0(1-\sigma) \tag{2-37}$$

Therefore, its modified Larmor frequency is

$$\omega = \omega_0(1-\sigma) \tag{2-38}$$

This shift in frequency is referred to as the chemical shift, denoted by δ, and it is defined independent of the magnetic field strength as

$$\delta = \frac{\omega - \omega_{ref}}{\omega_{ref}} \tag{2-39}$$

where the unit of chemical shift is ppm (parts per million). The reference frequency ω_{ref} is generally taken to be the frequency of chemically inert substance such as water in vivo (4.7 ppm), or tetramethylsilane (TMS) in phantom.

2.3.2 **Single Voxel Spectroscopy (SVS)**

The signal within a voxel S(t) is generated by a volumetric excitation followed by a readout period to sample the signal. At 3T, the spectral width SW necessary to resolve individual metabolite signals over a range of 9ppm, without spectral aliasing, is approximately 1190 Hz. The spectral width determines the spectral dwell time $\Delta\tau = \frac{1}{SW}$. The time-domain signal S(t), which is sampled after the volumetric excitation, can be modeled as the discrete summation

$$S(t) = S(n\Delta\tau) = \sum_{k=1}^{K} A_k e^{i\varphi_k} e^{i2\pi f_k \cdot (n\Delta\tau)} \quad (2\text{-}40)$$

where K is the total number of underlying frequencies in the FID (free induction decay) signal and n = 0, 1, …, N-1, where N is the total number of sampled time points. This model assumes that there are K underlying chemical components each with corresponding a magnitude A_k, phase φ_k, and frequency f_k, although the effect of J-coupling is not adequately considered in Equation 2-40.

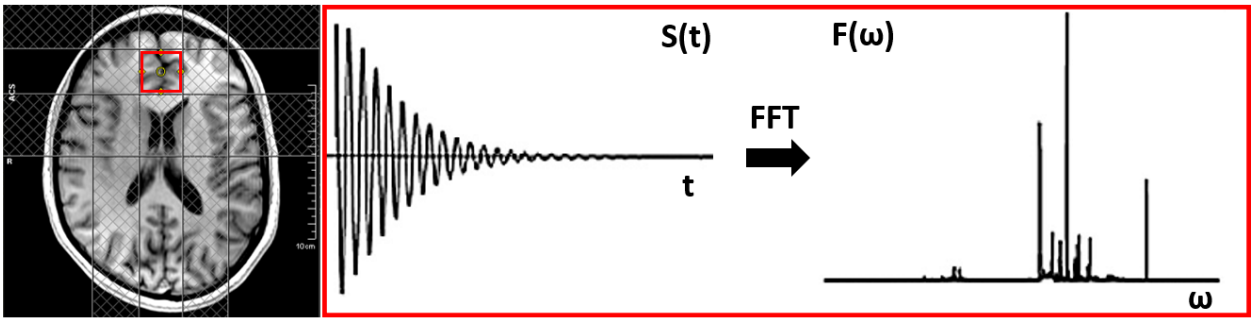

Figure 2-12: A single-voxel volume-of-interest in the frontal lobe of the brain and the corresponding (idealized) time signal S(t) and resulting spectrum F(ω) after Fourier transformation.

All pulse sequences for ^{1}H spectroscopy in vivo require some form of water suppression, either by incorporating a water suppression module before excitation or by advanced post-processing and acquisition methods. The reduction or elimination of the water signal is necessary in order to

adequately resolve the signals near the water peak and to reduce the dynamic range of the signal since the water peak can be as much as 1000 times greater than the metabolite peaks. A common water suppression technique is called WET (water suppression enhanced through T1 effects), which uses three RF pulses tuned to the water frequency combined with spoiler gradients to dephase the magnetization such that the longitudinal component of water is nulled by the time of excitation.

The two most common SVS techniques are PRESS and STEAM. The PRESS pulse sequence consists of one selective 90° excitation pulse along x, followed by two selective 180° refocusing pulses along y and z, to generate a spin echo. If the period between the 90° pulse and the first 180° pulse is τ, then the first echo time (TE_1) is generated a period τ after the first refocusing pulse. The spin echo signal sampled at the second echo time (TE_2), which depends on the temporal separation between TE_1 and the second 180° pulse. Each individual RF pulse in the PRESS localization selects planes whose intersection is the volume of interest (VOI).

The STEAM sequence starts with a selective 90° excitation pulse followed by another two selective 90° pulses, to generate a stimulated echo. This sequence consists of two periods – the mixing time (TM) and the TE. The TM time is between the second and third 90° pulses and it is a period during which the transverse magnetization that was produced by the excitation pulse is converted to longitudinal magnetization and undergoes further signal preparation (e.g, T1-weigthing, diffusion, or chemical exchange saturation transfer) before the start of the third 90° pulses. If the period between the excitation pulse and the second 90° pulse is τ, then the TE is time τ after the last 90° pulse. Generally, one advantage of STEAM is that the TE can be made very

short relative to PRESS-based sequences. However, the signal generated by STEAM has been shown to have a sensitivity one-half that of the signal generated by PRESS.

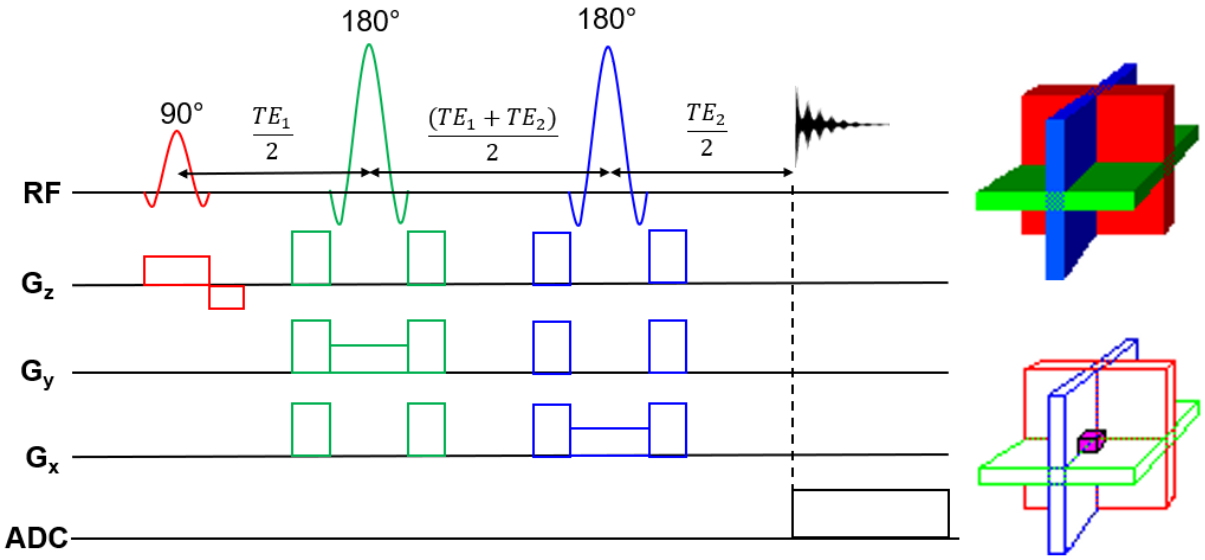

Figure 2-13: Pulse sequence schematic for single-voxel PRESS localization of a volume-of-interest. The action of the three spatially-selective RF pulses results in a volume being selected from the intersection of the three planes. The free induction decay (FID) signal from this volume is then read out during the analog-to-digital (ADC) sampling period.

Due to the localization and crusher gradients, eddy currents are generated which affect the phase and amplitude of the FID, distorting and decreasing the signal intensity of the spectra. An effective way to correct for this eddy-current induced phase error is to acquire a separate scan without water suppression. Without water suppression, the water signal is dominant and captures the phase induced by eddy currents. If the receiver is set to the water resonance, then the water signal can be modeled as $S_w(t) = Ae^{i\varphi_{eddy}(t)}$, where A is the amplitude and $\varphi_{eddy}(t)$ contains the temporal phase effects from eddy currents. After measuring the water suppressed signal $S(t)$, the corrected signal $S_{corr}(t)$ is found by subtracting the phase $\varphi_{eddy}(t)$ from the phase of $S(t)$ as follows: $S_{corr}(t) = S(t)e^{-i\varphi_{eddy}(t)}$.

All pulse sequences that use RF pulses combined with slice or slab selective gradients for localization suffer from chemical shift displacement error (CSDE). Considering the localization along the x dimension, when a gradient of constant amplitude G is on, the precessional frequency as a function of x is

$$\omega(x) = \omega_0 + \gamma G x \tag{2-41}$$

Where $\omega_0 = \gamma B_0$ is the Larmor frequency. An RF pulse with carrier frequency ω_{RF} will then select a slice centered at x' given by

$$x' = \frac{\omega_{RF} - \omega_0}{\gamma G} \tag{2-42}$$

However, if the sample also has spins with precessional frequency $\omega_0 + \Delta\omega$, then for this set of spins, the RF pulses selects a slice that is offset by

$$\Delta x = -\frac{\Delta\omega}{\gamma G} = \frac{\Delta\omega}{BW_{RF}} V_x \tag{2-43}$$

relative to the spins with precessional frequencies at ω_0. The same offset can be expressed in terms of the bandwidth of the RF pulse, BW_{RF} , and the selected voxel dimension along the x axis, V_x. As a result, the generated signal from each metabolite actually originates from different, non-overlapping spatial locations. The only way to reduce this effect is to increase the RF bandwidth, which becomes more challenging at higher fields where the frequency dispersion among metabolites also increases.

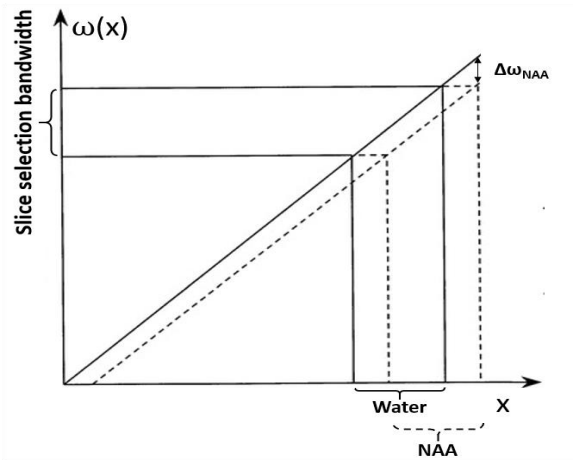

Figure 2-14: Illustration of the relative shift in spatial selection between two species – water and N-acetyl aspartate (NAA) – with different chemical shifts of 4.7 and 2.01 ppm, respectively. The same RF pulse bandwidth selects for water and NAA signal from different spatial locations.

The CSDE problem can be minimized by implementing RF pulses that are insensitive to chemical shift. One class of such pulses are incorporated in MRS sequences that use localization by adiabatic selective refocusing (LASER). In these sequences, adiabatic half passage (AHP) pulses are used for excitation, and adiabatic full passage (AFP) pulses are used for refocusing. The semi-LASER variants do not use an AHP pulse for excitation. These sequences are also insensitive to inhomogeneities in the B_1 field, although one of their limitations is that the RF durations are longer and the specific absorption rate (SAR) is higher, causing more energy deposition in tissues.

2.3.3 **Brain Metabolites**

The major detectable brain metabolites are Choline (Cho), Creatine (Cr), Glutamate (Glu), Glutamine (Gln), γ-aminobutyric acid (GABA), myo-inositol (mI), scyllo-inositol (sI), Lactate (Lac), and N-acetyl aspartate (NAA). At 3T, the frequency separation between glutamine and glutamate is insufficient to differentiate these metabolites, since there is significant overlap in their peaks. For this reason, the combination Glx = Glu + Gln is usually reported at lower field strengths. The signal-to-noise level of the metabolite signal is directly proportional to the concentration, so metabolites that have lower concentration levels such as γ-aminobutyric acid (GABA) are usually not able to be reliably estimated with one-dimensional MRS.

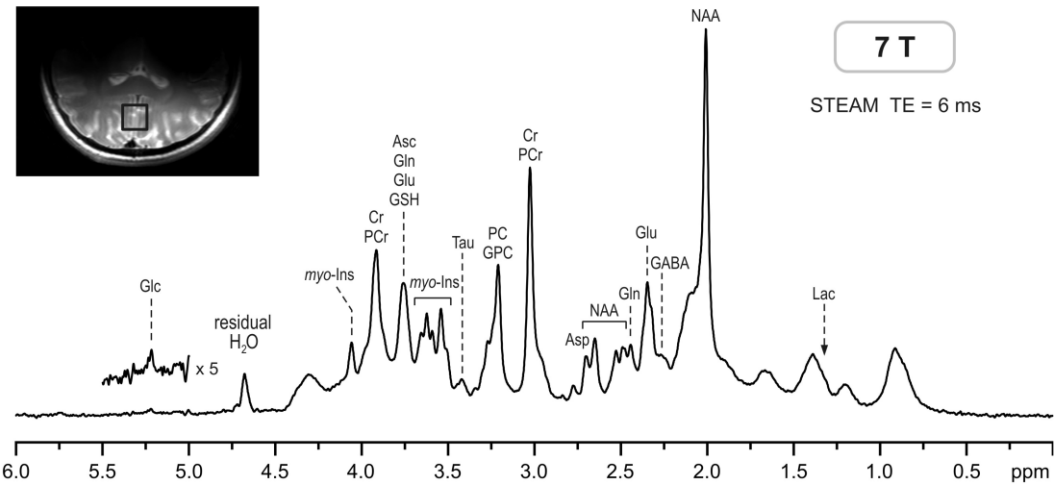

Figure 2-15: Typical ^{1}H spectrum at high field (7T) showing the common metabolites found in the human brain.

Choline

Choline compounds include three main subgroups: glycerophosphorylcholine (GPC), phosphorylcholine (PCh) and free choline (Cho). Total choline (tCho) refers to the sum of these three subgroups and it is often reported when the individual components are estimated with insufficient reliability, which may happen at long echo times or when the signal-to-noise ratio is low. The largest Cho peak is located at a chemical shift 3.2 ppm. This metabolite is associated with the cell-membrane as it is a main component of the phospholipid bilayer. The tCho level can be a good indicator of various underlying pathologies, particularly cancer, where the tCho concentration becomes extremely elevated compared to healthy tissues.

Creatine

Creatine compounds include two major subgroups: creatine and phosphocreatine (PCr). The addition of these two subgroups is referred to as tCr. The largest Cr peaks are those found at chemical shifts of 3ppm and 3.9ppm. Creatine plays a key role in the energy production and

metabolism of the cell. Generally, the creatine concentration is relatively stable across different brain tissue types, and is therefore used as an internal reference signal with respect to which various metabolite ratios are calculated. The singlet peak at 3.9ppm is near water at 4.7ppm so that it can be affected by ineffective water suppression. In some pathologies, the Cr level may also change so the summation of Cr and tCho may be used as an alternative internal reference signal for computing metabolite ratios.

Glutamate and Glutamine

Glutamate is one of the main brain neurotransmitters and its concentration can be altered in various pathologies. Glutamine is a precursor molecule for glutamate and both Glu and Gln are stored in neurons. The Glu functions in the extracellular synapse environment for inducing neuronal impulses, and it is converted back to Gln in glial cells before it can be used again for the neuronal signaling process, during which it converts to Glu. Both Glu and Gln have very similar chemical structures and have significant spectral overlap in the regions at 2.2-2.5ppm and at 3.7ppm, making it difficult to distinguish using 1D MRS techniques, especially at lower field strengths. For most pathologies, Glu plays a more dominant role.

γ-aminobutyric acid (GABA)

GABA is an inhibitory neurotransmitter and plays a role in psychiatric disorders and other pathologies such as sleep apnea. It is a relatively low-concentration metabolite and has three main sets of multiplets centered at 1.9ppm, 2.3ppm, and 3.0ppm, which overlap with the peaks from other, more highly-concentrated metabolites. Therefore, GABA is very difficult to accurately quantify, and more sophisticated, specialized techniques such as spectral editing and two-dimensional spectroscopy have been applied to improve GABA estimation.

Inositol

Inositol compounds have two main subgroups: myo-inositol (mI) and scyllo-inositol (sI). The less abundant form of inositol is sI. Myo-inositol has multiplets within 3.4-3.6ppm, as well as peaks at 3.2 and 4.1ppm, while sI appears as a single peak at 3.35ppm. Both compounds play a role in energy storage and in aiding cell growth, and therefore they can be markers of pathological changes in brain tissues.

Lactate

Lactate (Lac), also known as lactic acid, consists of a characteristic doublet at 1.3ppm and a multiplet at 4.1ppm. Lactate is the final form of energy within the anaerobic metabolic pathway, in which oxygen is lacking. The amount of Lac greatly increases in oxygen-starved tissues found in certain cancers and brain tumors, so this metabolite is used a marker for pathologies that induce hypoxic conditions.

N-acetyl aspartate

N-acetyl aspartate (NAA) is largely localized in neurons and is a marker of neuronal integrity and viability. It is a hydrolysis product of the related compound N-acetyl aspartyl glutamate (NAAG), which is involved in modulating the release of glutamate. Both metabolites have very similar chemical structure and the addition of these two (NAA+NAAG) is referred to as tNAA. In the brain, NAA has a very prominent singlet at 2.0ppm and multiplets in the ranges 2.5-2.8ppm and 4.3-4.4ppm, and it is one of the most reliably quantifiable metabolites due to its strong singlet at 2.0ppm.

Other metabolites

There is a list of many other metabolites that are involved in the structural and functional characteristics in brain tissue whose specific roles are not as clearly defined and whose concentrations are not to the levels necessary for consistent detection and estimation. Certain metabolites such as glutathione (GSH) also happen to have its peaks overlapped with those from multiple major metabolites such as Cr, Glu and Gln. However, these minor metabolites are also of interest and are generally included (depending on the tissue of interest) in MRS quantitation algorithms such as LC Model. This list includes: alanine (Ala), ascorbic acid (Asc), aspartate (Asp), glucose (Glc), glycine (Glyc), phosphoethanolamine (PE), taurine (Tau), and threonine (Thr).

2.3.4 **Chemical Shift Imaging/MR Spectroscopic Imaging**

Magnetic resonance spectroscopic imaging (MRSI) uses spatial-encoding to resolve multiple voxel locations within a volume-of-interest (VOI). The excitation may be slice-selective or may use a volumetric excitation scheme, such as PRESS or STEAM. Conventional MRSI methods use phase-encoding to spatially-resolve one FID per voxel. For 2D or 3D spatial encoding the number of phase-encoding steps is equal to the prescribed matrix size $N_x \times N_y \times N_z$. Hence, the acquisition time may be quite long, depending on the TR. Some variants of phase-encoded MRSI use elliptical encoding schemes to avoid sampling at the corners of k-space, since the loss of this high spatial frequency information is not impactful due to the relatively low resolutions of MRSI. Typical in-plane matrix sizes range from 12 × 12 to 32 × 32, and for 3D acquisitions, the number of through plane points can range from 4 to 12, with FOV's ranging from 120 – 320 mm in each dimension, depending on the anatomy of interest.

For 3D chemical shift imaging, suppose the FOV's along the x, y, and z dimensions are L_x, L_x, and L_x. Then the corresponding k-space sampling increments along these dimensions are

$\Delta k_x = \frac{1}{L_x}$, $\Delta k_y = \frac{1}{L_y}$, and $\Delta k_z = \frac{1}{L_z}$. After the appropriate phase-encoding gradient steps ΔG_x, ΔG_y, and ΔG_z are applied, the FID is modeled as

$$S(t) = \widehat{M}(n_x\Delta k_x, n_y\Delta k_y, n_z\Delta k_z, t) = \int m(x,y,z,f)e^{-i2\pi(n_x\Delta k_x \cdot x + n_y\Delta k_y \cdot y + n_z\Delta k_z \cdot z)}e^{i2\pi f \cdot t}dxdydzdf \quad (2\text{-}44)$$

where $f = \frac{\gamma}{2\pi}\omega$ represents the temporal frequency (Hz) content within the volume. The number of phase-encoding steps along k_x, k_y, and k_z are N_x, N_y, and N_z, respectively. After Fourier transformation along the spatial and temporal dimensions, the resulting data $m(x,y,z,f)$ represents a spectrum for every coordinate in space. The acquisition time T_{acq} for conventional phase-encoded MRSI is $T_{acq} = N_{avg} \times TR \times N_x \times N_y \times N_z$, where N_{avg} is the total number of averages. In addition, a separate water scan must be acquired to perform eddy current phase correction on the FID's from each spatial position.

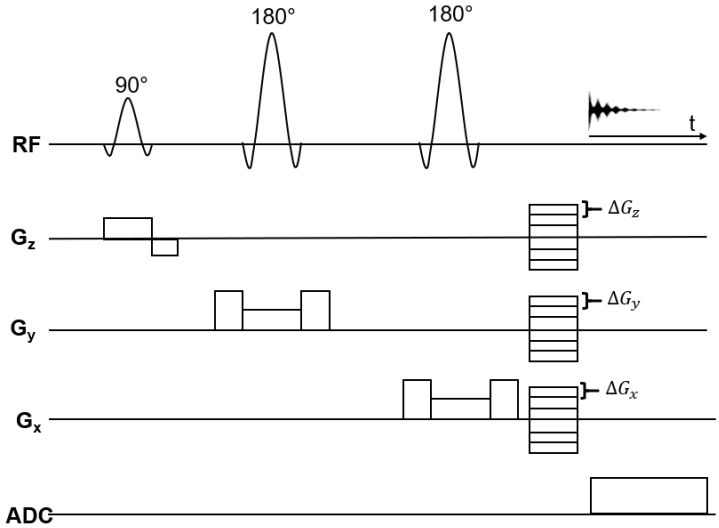

Figure 2-16: Pulse sequence schematic for a conventional chemical-shift imaging pulse sequence based on PRESS localization. After localization of the volume-of-interest with the three slice-selective RF pulses, the signal is spatially-encoded sequentially along each spatial direction. Phase-encoding increments in G_x, G_y, and G_z are needed to generate a dataset with 3D spatial and 1D spectral dimensions.

2.3.5 **Echo Planar Spectroscopic Imaging (EPSI)**

In order to reduce the acquisition time for MRSI, spatial encoding can be interleaved with the temporal sampling of the signal. In the Cartesian case, assuming the readout direction is x, a bipolar gradient echo train $G_x(t)$ is played during which the signal is recorded as the sampling trajectory traverses a zig-zag pattern in the $k_x - t$ plane. If the FOV along x is L_x and the matrix size is N_x, the spatial bandwidth that must be sampled to resolve this FOV is $2k_{max} = \frac{N_x}{L_x}$. As the signal is repeatedly sampled between $-k_{max}$ and k_{max} along each k-space line, the signal is also spectrally-encoded (via time) throughout the readout. Since one k-space dimension is simultaneously sampled with the time dimension, the scan time for EPSI is reduced by an order of magnitude. Compared to conventional 3D phase-encoded MRSI with the same imaging parameters (e.g, matrix size and TR), the scan time is reduced by a factor of N_x, i.e. $T_{acq} = N_{avg} \times TR \times N_y \times N_z$. A water reference scan is also acquired for eddy current phase corrections, and the data sampled during the odd echoes along the readout gradient echo train must be time reversed with respect to the even echoes in order to correctly order them in the $k_x - t$ plane.

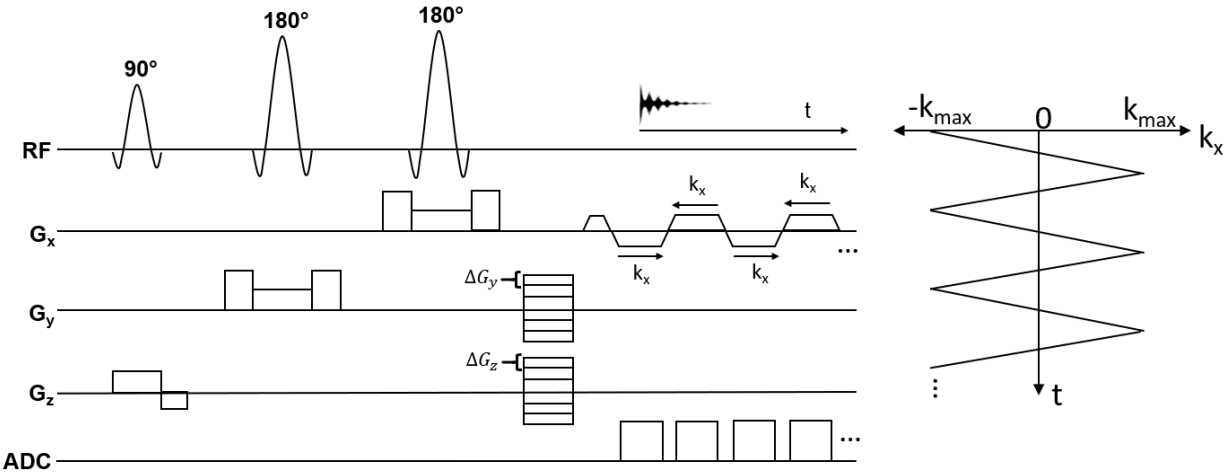

Figure 2-17: Pulse sequence schematic for a three-dimensional Cartesian echo-planar spectroscopic imaging sequence, with the bipolar gradient echo readout played on the G_x gradient axis and conventional phase encoding accomplished with the G_y and G_z gradients. Shown at right

is an illustration of the k-t trajectory created by the bipolar gradient echo train along G_x. The sampling in k-t approximates a zig-zag trajectory, and for simplicity the ADC samples the signal during the gradient plateaus where the k-space increment Δk_x is constant.

During the EPSI readout, spatial encoding is no longer decoupled from the spectral encoding of the signal, as it is for conventional phase-encoded MRSI. For a 2D EPSI acquisition, one of the spatial dimensions, say y, is phase-encoded, while the x and time dimensions are sampled throughout the gradient echo train. Recalling that $k_x(t) = \frac{\gamma}{2\pi}\int_0^t G_x(\tau)d\tau$, the signal during the positive trapezoidal gradient plateaus (with constant amplitude G) can be represented as

$$S(t) = \hat{M}\left(k_x(t), n_y\Delta k_y, t\right) = \int m(x,y,f)e^{-i2\pi n_y \Delta k_y \cdot y}e^{i(2\pi f + \gamma G\cdot x)\cdot t}dxdydf \qquad (2\text{-}45)$$

Hence, besides the spatially-dependent phase distribution caused by the readout gradient $G_x(t)$ alone, there is additional phase accrual due to the chemical shifts (temporal frequencies f) from all metabolites within the sampled volume. This phase contribution leads to a broadening of the spatial point spread function, which can be corrected using the Fourier shift theorem.

2.4 Diffusion-weighted MR Spectroscopy

2.4.1 Diffusion

Diffusion is characterized by the Brownian motion of molecules in a medium, driven my thermal energy. In a fluid medium with no restrictions and with homogenous composition, the mean square displacement of molecules increases linearly with time, that is, the mean square displacement in any single direction is a linear function of time t, with the diffusion coefficient, D, acting as the proportionality constant:

$$\langle (r - r_0)^2 \rangle = 2Dt \qquad (2\text{-}46)$$

where r and r_0 are the final and initial positions of the molecule. For unrestricted (free) diffusion, the diffusion coefficient depends on the temperature and viscosity of the medium as follows:

$$D = \frac{k_B T}{6\pi\eta R_H} \tag{2-47}$$

where k_B is the Boltzmann constant, T is the temperature, η is the viscosity and R_H is the molecular hydrodynamic radius. In the case of free diffusion, the displacement of molecules is isotropic, that is, there is no preferred diffusion direction, and the diffusion is referred to as Gaussian. However, in vivo, water and metabolite molecules encounter restrictive structural environments within tissues, including cellular obstacles (walls and organelles) and fibers organized along a particular direction, which constrain the motion of particles. In this case, the diffusion is anisotropic and the diffusion coefficient is spatially-dependent on the direction in which the molecular motion is measured. The effective diffusion coefficient that is measured, called the apparent diffusion coefficient (ADC), essentially reflects the average of the diffusion coefficients D measured in all directions. This ADC value for a given metabolite is dependent on both the inherent diffusion properties of the metabolite molecule and on the surrounding environmental influences on its diffusion.

2.4.2 **Diffusion-weighting, the diffusion tensor and the b-matrix**

The MR signal can be diffusion-weighted by including diffusion-sensitizing gradients within a given pulse sequence. With either a spin echo- or a gradient echo-based sequence, the resulting signal reflects the amount of gradient-induced phase dispersion that cannot be refocused due to the underlying molecular diffusion in the tissue of interest. For example, in the spin echo case, two gradients of the same polarity straddle the refocusing pulse. The first gradient (prior to the 180° RF pulse) causes a net phase dispersion across the excited volume in the direction of the applied

gradient. After the 180 pulse, a second gradient of equal amplitude and duration is played, which is meant to refocus the phase dispersion caused by the first gradient, except that non-stationary spins undergoing diffusion will have acquired an additional phase accrual due to their motion, which cannot be refocused. The un-refocused phase decreases the measured signal intensity as follows:

$$S(b) = S(0)e^{-bD_i} \tag{2-48}$$

where b is the b-value, D_i is the diffusion coefficient for the direction i specified by the diffusion-sensitizing gradient and $S(0)$ is the signal without diffusion-weighting. The b-value is a user-controlled diffusion-weighting factor which depends on the sequence timing and the diffusion-sensitizing gradient parameters. It is typically reported in units of s/mm^2, while the diffusion coefficient is most conveniently reported in units of $\mu m^2/ms$. The total b-value is derived from the b-matrix and is taken to be the sum of the diagonal entries of this matrix, in practice. In general, the b-matrix is defined as

$$\boldsymbol{b} = \int_0^{TE} \left(\int_0^t \vec{G}(t')dt' \right) \otimes \left(\int_0^t \vec{G}(t')dt' \right) dt \tag{2-49}$$

where $\otimes$ is the outer product operation and $\vec{G}(t) = \left(G_x(t), G_y(t), G_z(t)\right)$ is a vector that represents the time-varying gradients played along all axes in the pulse sequence before the echo time TE. The signal attenuation is generally given by

$$\ln\left(\frac{S(t)}{S(0)}\right) = -\sum_{\alpha,\beta} \boldsymbol{b}_{\alpha\beta}\boldsymbol{D}_{\alpha\beta} \qquad (\alpha, \beta \in \{x, y, z\}) \tag{2-50}$$

where $\boldsymbol{D}$ is the diffusion tensor, which provides information regarding the directionality of the diffusion within the probed voxel. The diffusion tensor is a symmetric 3×3 matrix, written as

$$\boldsymbol{D} = \begin{pmatrix} D_{xx} & D_{xy} & D_{xz} \\ D_{yx} & D_{yy} & D_{yz} \\ D_{zx} & D_{zy} & D_{zz} \end{pmatrix} \tag{2-51}$$

and its estimation requires at least separate measurements along 6 distinct diffusion directions. The diffusion tensor provides several diffusion metrics such as the mean diffusivity (MD), axial diffusivity (AD), radial diffusivity (RD), and the fractional anisotropy. The MD is also known as the trace of the diffusion tensor or the trace ADC. The trace ADC is a rotationally invariant quantity and therefore is theoretically the same regardless of the coordinate system $\{x', y', z'\}$ assumed for representing the diffusion tensor.

2.4.3 **Diffusion-weighted MRS using the PRESS sequence**

The MR signal can be diffusion-weighted by including diffusion-sensitizing gradients in the PRESS pulse sequence. Two primary examples of diffusion-weighting PRESS-based sequences are those with unipolar and bipolar gradient configurations. In the unipolar case, two gradients of the same polarity are placed a time Δ apart, on either side of one of the 180° refocusing pulses. For simplicity, these gradients are assumed to be rectangular and each of duration δ. If the gradient amplitude along a gradient axis is g_d, then the b-value, neglecting all localization and crusher gradients, is given by

$$b = \gamma^2 g_d^2 \delta^2 \left(\Delta - \frac{\delta}{3}\right) \tag{2-52}$$

In the bipolar case, two sets of bipolar gradient pairs are placed within the sequence, with each pair centered around the two refocusing pulses. In this case, the gradient duration is defined as $\frac{\delta}{2}$ and the b-value is given by (again, excluding localization and crusher gradients)

$$b = \gamma^2 g_d^2 \delta^2 \left(\Delta - \frac{\delta}{3} - \frac{\tau}{2}\right) \tag{2-53}$$

where τ is the separation between the bipolar gradients within one pair. More on diffusion-weighted PRESS is explained in greater detail in subsequent chapters.

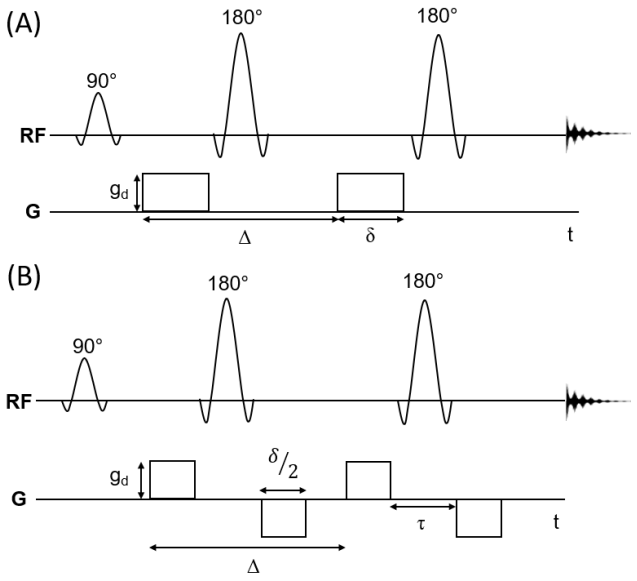

Figure 2-18: (A) Pulse sequence schematic for a PRESS sequence with Unipolar arrangement of diffusion-sensitizing gradients. The gradient amplitude g_d, the duration δ, and the separation Δ determine the b-value. (B) Another PRESS-based sequence with a Bipolar arrangement of diffusion-sensitizing gradients. The time between gradients around each refocusing pulse, τ, is taken into consideration when computing the b-value for this sequence.

The diffusion time t_d is an important parameter for any diffusion-weighted pulse sequence, and it is the effective amount of time that the molecules are allowed to diffuse during the measurement. For long t_d, intracellular molecules have enough time to reach and bounce off of the cellular walls, whereas for short t_d, the effects of restriction are reduced since the molecules have had less time to encounter barriers to its diffusion. Therefore, at long t_d, the ADC appears to be lower than the ADC measured with short t_d, since at short t_d the molecular diffusion more closely approximates free diffusion, where the motion is purely random and causes a maximum degree of phase incoherence and a larger mean square displacement.

Since most metabolites of interest are almost exclusively located within the intracellular environment, metabolite diffusion is highly restricted. Consequently, higher b-values are needed

to observe an adequate signal attenuation due to diffusion. In most cases, b-value greater than approximately 1,500 s/mm^2 have been used in most DW-MRS reports. However, the choice of b-value must also consider the dependence of the apparent diffusion coefficient on the diffusion time. As mentioned earlier, a short t_d leads to larger estimates of the ADC, so that relatively lower b-values are needed to reach the same level of signal attenuation as DW-MRS acquisitions that use higher b-values with longer t_d's.

In contrast to DW-MRI, which can only probe water diffusion, DW-MRS is able to provide information on the microstructure of tissues in pathological states, since metabolite diffusion is mostly intracellular and therefore reflects the underlying cellular structural changes due to disease. Non-diffusion-weighted MRS can only provide information relating metabolite concentration, so DW-MRS is a complementary tool for exploring other aspects of tissue-specific alterations that occur as a result of injury or pathology, such as changes in cell tortuosity or viscosity, cellular damage and breakdown, and interruptions in normal fluid flow and kinetics within and around the cellular environment.

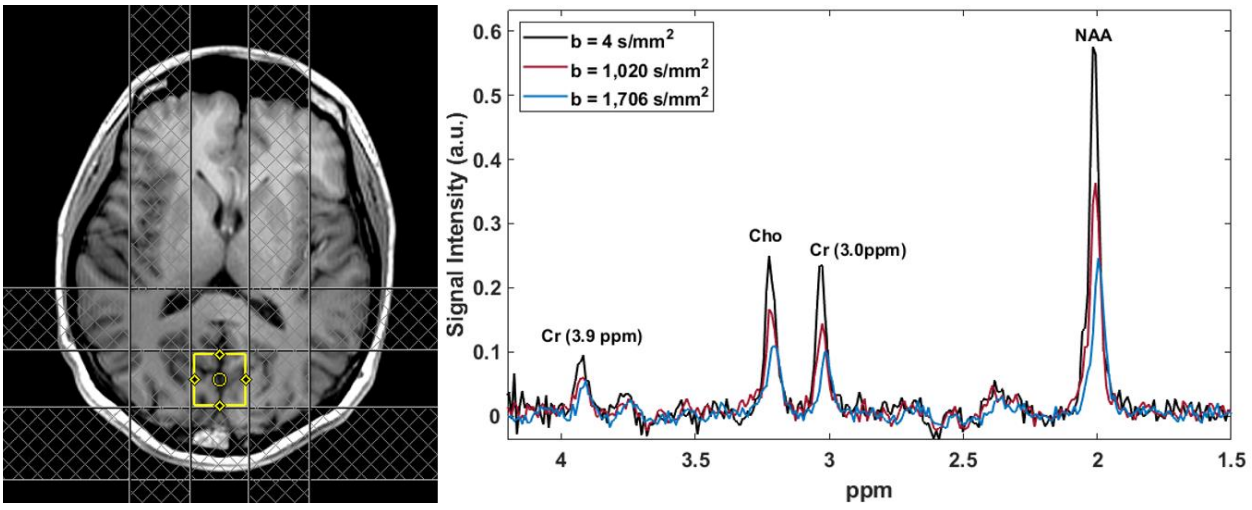

Figure 2-19: Example of diffusion-weighted spectra in the occipital gray matter in human brain in vivo. As the b-value increases, the signal intensity decreases due to greater diffusion-weighting.

The amount of diffusion-weighting and the corresponding signal attenuation also depends on the diffusion time t_d and the specific type of tissue being sampled.

At least two b-values are needed to solve for the ADC using the signal model in Equation 48. Due to the low SNR of metabolites, in addition to the further signal reduction caused by diffusion-weighting, many averages are needed for measuring a signal with enough SNR, causing the acquisition time for DW-MRS experiments to be very long. Besides the long acquisition times, the post-processing of DW-MRS spectra requires careful phase and frequency drift corrective procedures in order to coherently add the signal averages. When acquiring in vivo measurements, it may also be necessary to incorporate cardiac triggering into the pulse sequence to avoid signals that may be overly corrupted by pulsatile motion, however, SNR-based thresholding techniques could also be applied to retrospectively remove spectra that suffer from too much SNR loss or distortion due to motion. Another limitation of DW-MRS is that relatively large voxel volumes (up to approximately 15 mL) are usually required in order to obtain enough SNR, compared to DW-MRI acquisitions. This limitation can make it challenging to study the diffusion of smaller regions of interest with volumes below approximately 0.5 mL without increased averaging or specialized methods to reduce noise.

Currently, the long scan times and the challenging post-processing methods limit the clinical applicability of DW-MRS. So far, no consensus or standardization has been established in the DW-MRS community for data acquisition or post-processing. Up until now, single voxel DW-MRS has been the most reliable approach for measuring the in vivo ADC's from diffusion-weighted spectra, in contrast to multi-voxel DW-MRSI spectroscopic imaging which encounters additional complications due to longer scan time requirements and increased susceptibility to motion-induced artifacts in the spatial encoding.

Chapter 3 Accelerated Radial Echo Planar Spectroscopic Imaging using Golden Angle View Ordering and Compressed Sensing Reconstruction with Total Variation Regularization

3.1 Abstract

Purpose: To implement a novel, accelerated two-dimensional radial echo-planar spectroscopic imaging (REPSI) sequence using undersampled radial k-space trajectories and compressed sensing (CS) reconstruction, and to compare results with those from an undersampled Cartesian spectroscopic sequence.

Methods: The REPSI sequence was implemented using golden-angle view-ordering on a 3T MRI scanner. Radial and Cartesian EPSI data were acquired at 6 acceleration factors (AF), each with time-equivalent scan durations, and reconstructed using compressed sensing with total variation regularization. Results from prospectively and retrospectively undersampled phantom and *in vivo* brain data were compared over estimated concentrations and Cramer-Rao lower bound (CRLB) values, normalized root mean square errors (nRMSE) of reconstructed metabolite maps, and percent absolute differences between fully-sampled and reconstructed spectroscopic images.

Results: REPSI with CS is able to tolerate greater reductions in scan time compared to EPSI. The reconstruction and quantitation metrics – namely spectral nRMSE maps, metabolite map nRMSE values (e.g, for tNAA: REPSI – 9.4% vs. EPSI – 16.3% (AF = 2.5)), percent absolute difference maps, and concentration and CRLB estimates – showed that the scan time can be reduced by a factor of 2.5 while retaining image and quantitation quality.

Conclusion: Accelerated MRSI using undersampled radial echo-planar acquisitions provides greater reconstruction accuracy and more reliable quantitation for a range of acceleration factors compared to time-equivalent CS-reconstructions of undersampled Cartesian EPSI. Compared to the Cartesian approach, radial undersampling with CS could help reduce 2D spectroscopic imaging acquisition time, and offers a better trade-off between imaging speed and quality.

3.2 Introduction

Magnetic resonance spectroscopic imaging (MRSI) is capable of providing metabolic information from multiple locations in biological tissues, allowing biochemical characterization of pathologies, and facilitating the diagnosing and monitoring of disease [8,9]. One of the main challenges in MRSI is to shorten the data acquisition to clinically-feasible scan times without compromising spectroscopic image quality. Conventional MRSI methods require long scan durations due to the sequential phase-encoding of each spatial dimension prior to spectral encoding [10]. More advanced MRSI techniques based on echo-planar *k*-space trajectories significantly reduce the scan time by interleaving the collection of the spatial-spectral data [11]. Apart from rectilinear or Cartesian trajectories, non-Cartesian echo-planar acquisitions using spirals, rosettes, and concentric circles have also been applied for efficient and fast MRSI [12–16], and these offer advantages relative to Cartesian approaches including lower gradient-slew rate demands, greater sampling efficiency, and increased robustness to phase errors caused by motion.

Radial *k*-space sampling techniques have gained widespread use in MRI due to their relatively decreased sensitivity to motion-related artifacts, inherent SNR advantage, and great potential for high acceleration [17,18]. Recently in MRSI, radial trajectories were applied for hyperpolarized ^{13}C imaging due to their repeated traversal of the central k-space, which enhances

the capture of the short-lived image contrast [19]. Three-dimensional radial acquisitions were used for high-field ^{31}P *in vivo* spectroscopic imaging to benefit from the higher signal-to-noise per unit time that radial sampling offers [20]. Most recently, radial sampling was implemented for ^{1}H diffusion-weighted MRSI [21]. However, to date, the application of radial sampling for ^{1}H MRSI remains relatively unexplored [1]. Furthermore, the potential of accelerated acquisitions through radial undersampling and compressed sensing (CS) reconstruction is proven in the MRI field, but has yet to be demonstrated in ^{1}H MRSI.

In general, radial *k*-space undersampling is well-suited for CS reconstruction since it largely avoids dominantly coherent artifacts in the image domain, in contrast to Cartesian *k*-space undersampling. Unlike in the Cartesian case, the aliasing artifacts from radial undersampling are much less pronounced and more noise-like. This property of radial undersampling more closely meets the condition that the *k*-space undersampling pattern produce incoherent noise-like artifacts in the image domain, which is prerequisite for effective CS [22]. Additionally, the high central *k*-space density of radial acquisitions can improve CS reconstructions of the low spatial frequency components of the image, which is particularly advantageous due to the relatively low spatial resolutions that are usually acquired in MRSI. For radial undersampling, the golden-angle (GA) view ordering scheme is ideal since it continuously increments the angle of the radial views, or spokes, by 111.25° throughout the acquisition period, such that the *k*-space is covered as uniformly as possible for any given number of spokes [22,23]. The combination of radial GA undersampling and CS reconstruction has produced diagnostic-quality images from highly undersampled data in various accelerated MRI applications, especially dynamic imaging [24,25]. One of the most widely-used sparsity-promoting transforms in CS reconstructions from undersampled radial data is the

total variation [26,27]. This transform has led to good results in various Cartesian-based accelerated MRSI methods as well [28,29].

Previous studies in accelerated non-Cartesian MRSI have used undersampled spiral trajectories in combination with compressed sensing and parallel imaging, applying other types of regularization based on variants of L_1/TV or low-rank minimization. In Chatnuntawech et al. [30], random spiral-based trajectories were acquired and undersampled spiral *k*-space was reconstructed within a TV-SENSE framework to allow for acceleration factors of up to 4 – 4.5 for single-slice and 3D-MRSI. In [31] and [32], the total generalized variation (TGV), a second-order variant of TV, was used in conjunction with model-based low-rank subspace constraints to reconstruct high-resolution MRSI. Another subspace-based approach was reported in [33], in which high resolution spectra were obtained with the aid of a separate low-resolution scan to model the spatial component of the spatial-temporal signal. Both of the methods in [31] and [33], however, were based on Cartesian trajectories, yet similar studies involving non-Cartesian trajectories have also been the subject of recent research [34].

Radial sampling has some unique advantages compared to other non-Cartesian trajectories. Similar to radial trajectories, spirals and rosettes also repeatedly sample the central portion of *k*-space and can therefore be considered a relatively motion-robust technique. However, fast ^{1}H MRSI using spiral and rosette trajectories at 3T often require spatial and/or spectral interleaves, whereas radial trajectories only require spatial interleaves at 3T [12,14,35]. The additional requirement of spatial and spectral interleaves for spirals and rosettes can limit the achievable spectral bandwidth and makes these trajectories more susceptible to spectral artifacts due to potential inconsistencies between the spectral interleaves. Concentric circular trajectories can sample the *k*-space twice as fast as Cartesian trajectories, and also require fewer spatial interleaves than radial

sampling [13,15,16,36]; however, the main disadvantage of this approach is the loss of motion-robustness because the central k-space is not sampled in each spectral interleaf. However, generally all non-Cartesian trajectories are more susceptible to errors due to off-resonance effects, leading to blurring and other imaging artifacts.

In this study, we evaluated accelerated 2D MRSI using radial echo planar *k*-space trajectories and TV-regularized compressed sensing reconstruction, in both retrospectively and prospectively undersampled acquisitions of phantom and *in vivo* brain data. We evaluated the performance of radial relative to Cartesian EPSI by comparing the spectroscopic image quality and quantitation results obtained from both types of sampling techniques under various rates of undersampling. In the appendix to this chapter, we assess radial sampling of free-breathing, *in vivo* liver spectroscopic image data in terms of robustness to motion-related spectral and spatial artifacts.

3.3 Methods

3.3.1 Pulse Sequence

The REPSI and EPSI pulse sequences were implemented on a Siemens 3T Prisma MR system (Siemens, Munich, Germany) operating in the VE11C platform. For the spatial-spectral readout, a symmetric, bi-polar trapezoidal gradient echo train was utilized, with a spectral bandwidth of 1136 Hz, an ADC bandwidth of 100 kHz, ramp durations of 60 μs, and 32 *k*-space points sampled during the gradient plateaus. Volumetric excitation [37] was achieved using semi-LASER [38] localization, with an initial 90° RF excitation pulse along the slice (*z*) direction followed by two pairs of adiabatic full-passage (AFP) 180° RF pulses along the *x* and *y* directions (Figure 1A) to acquire an axial in-plane orientation. Outer volume suppression bands were placed to suppress signal from lipid-dominant regions and water suppression was done using a three-pulse

WET sequence [39]. For all experiments, the slab thickness of the volume-of-interest (VOI) was set to 15 mm, and the matrix size was 32 × 32 with a field-of-view (FOV) of 320×320 mm^2, resulting in a voxel volume of 1.5 mL.

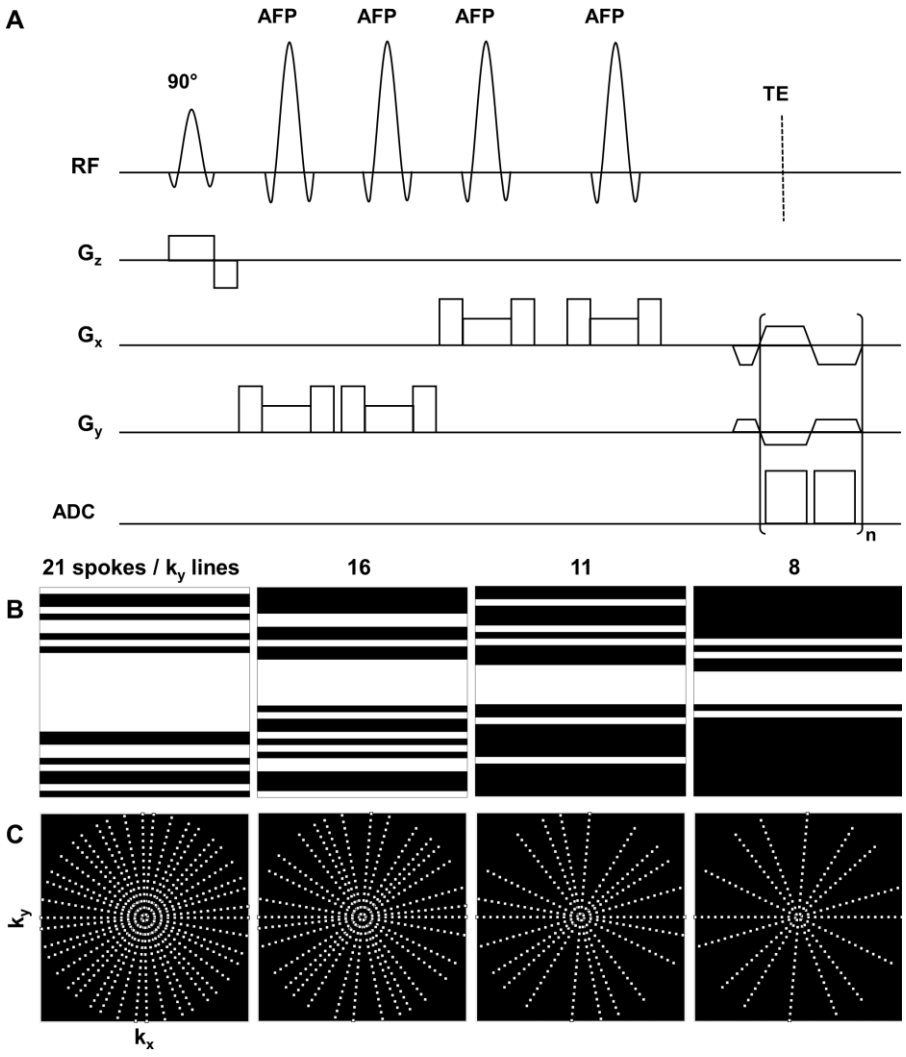

Figure 3-1: (A) Pulse sequence diagram for REPSI in which n t points are acquired during the readout train. A pair of adiabatic full passage (AFP) pulses are played after the first 90° excitation pulse to achieve volumetric localization of an axial slab. (B) Non-uniform undersampling (NUS) masks for a 2D Cartesian 32 × 32 k-space matrix with 21, 16, 11, and 8 k_y-lines, corresponding to acceleration factors (AF) of 1.5, 2.0, 3.0, and 4. (C) Golden-angle radial undersampling distributions with 21, 16, 11, and 8 spokes, corresponding to AF's of 1.5, 2.0, 3.0, and 4.0.

3.3.2 Data Acquisition

Accelerated REPSI and EPSI data were obtained on a time-equivalent basis: for each acceleration factor (AF), the same number of radial spokes and k_y lines (phase-encoding steps) were acquired, resulting in identical scan times for both sequences. Based on the Nyquist sampling criterion for 2D spatial encoding of an N × N image, the radial AF is a factor of $\frac{\pi}{2}$ larger than the Cartesian AF, which is $\frac{N}{k_y\ lines}$. Accordingly, a fully-sampled 32 × 32 *k*-space grid requires 50 spokes and 32 k_y-lines for REPSI and EPSI, respectively. However, for the sake of comparing accelerated REPSI and EPSI data, the AF is defined in terms of the reduced number of spokes or k_y lines acquired relative to 32, which is the number of phase-encoding lines in a fully-sampled 32 × 32 Cartesian *k*-space. This definition of the AF more accurately reflects a comparison between EPSI and REPSI in terms of the scan time instead of the number of sampled *k*-space points.

For undersampled REPSI acquisitions, six different numbers of spokes were acquired using the golden-angle view ordering scheme: 21, 16, 13, 11, 8, and 6. For EPSI, non-uniform sampling (NUS) patterns for the single k_y phase-encoding dimension (Figure 1B) were generated from a Gaussian probability distribution function centered at $k_y = 0$, with at least four fully-sampled central phase-encoding lines. Six Cartesian undersampling masks with 21, 16, 13, 11, 8, and 6 k_y lines were implemented. The AF's for 21, 16, 13, 11, 8, and 6 spokes or k_y-lines are defined as 1.5, 2.0, 2.5, 3.0, 4.0, and 5.0, respectively.

A phantom containing 17 representative brain metabolites at physiological concentrations was used to acquire fully-sampled data for retrospective undersampling experiments. The phantom data was acquired with a 16-channel brain coil, and the VOI was prescribed at isocenter with in-plane dimensions of 80 x 80 mm^2 encompassing a total of 64 voxels. For both REPSI and EPSI,

six retrospectively undersampled data sets were generated at all AF's. In addition, ten fully-sampled and ten prospectively undersampled REPSI and EPSI brain phantom data sets were acquired for each AF, giving a total of 70 data sets each for EPSI and REPSI. For each of these datasets, 25 voxels within the homogenous phantom were extracted, resulting in a total of 250 quantified voxels per AF or fully-sampled set. For all phantom experiments, TR = 2 sec, TE = 40 ms and 8 averages were acquired, resulting in fully-sampled scan times of 8 min 32 sec and 13 min 20 sec for EPSI and REPSI, respectively. Accelerated phantom scan times were 5 min 36 sec, 4 min 16 sec, 3 min 28 sec, 2 min 56 sec, 2 min 8 sec, and 1 min 36 sec for AF's of 1.5, 2.0, 2.5, 3.0, 4.0, and 5.0, respectively. Separately, fully-sampled water reference data was collected with 1 average, taking 1 min 4 sec for EPSI and 1 min 40 sec for REPSI.

Six healthy male volunteers and 1 female volunteer (ages 24 – 42 years) were scanned with approval of the UCLA institutional review broad and written informed consent from each volunteer. Fully-sampled REPSI and EPSI data sets were obtained for all volunteers. In addition, prospectively undersampled data with 11, 8, and 6 k_y encodes or radial spokes were acquired for 3 volunteers; prospectively undersampled datasets with 11 and 8 spokes or k_y encodes were acquired for 2 volunteers; a prospectively undersampled dataset with 16, 11, and 8 spokes or k_y encodes was acquired in one volunteer; and one prospectively undersampled dataset with 16, 13, and 11 spokes was acquired in one volunteer. All *in vivo* data was obtained using a 16-channel brain coil and TR of 1.5 sec, leading to fully-sampled scan times of 6 min 24 sec and 10 minutes for EPSI and REPSI, respectively, and accelerated scan times of 4 min 12 sec, 3 min 32 sec, 2 min 36 sec, 2 min 12 sec, 1 min 36 sec, and 1 min 12 sec for AF's of 1.5, 2.0, 2.5, 3.0, 4.0, and 5.0, respectively. Single-average, fully-sampled water reference scans were acquired in 48 sec for EPSI and 1 min 15 sec for REPSI.

3.3.3 Reconstruction

Optimization Algorithm

Due to the piecewise-smooth nature of spectroscopic images, especially for low-resolutions common in MRSI, the total variation (TV) acts as a natural sparsifying transform for the 2D spatial planes (*x*-*y*) of the acquired data *(k_x-k_y-t*). The TV transform was not applied along the spectral dimension because this dimension was already fully-sampled and is typically not piecewise-smooth, since 1D spectra may consist of several broad, crowded peaks with many non-trivial frequency components. We posed the compressed sensing (CS) reconstruction as the following unconstrained minimization problem:

$$\min_{u} \tfrac{1}{2}\|Fu - d\|_2^2 + \lambda \cdot TV(u) \qquad (3\text{-}1)$$

where *F* is the fast Fourier transform or the non-uniform fast Fourier transform (NUFFT) [40] for Cartesian and non-Cartesian data, respectively, u is the data in *x*-*y*-*f* space, *d* is the acquired undersampled data in polar *k*-space or k_y-k_x space, *TV* is the isotropic total variation transformation, and λ is a regularization parameter that balances the minimization between the data fidelity term and the sparsity-based functional.

The monotone fast iterative soft-thresholding algorithm (MFISTA) [41] was used to solve the above CS reconstruction problem, and the dual formulation of the isotropic TV minimization was implemented as described in [26,41]. The TV transform was applied to each spatial plane in the *x*-*y*-*f* space – separately for each frequency point along the spectral dimension. For all experiments, the CS reconstruction was performed coil-by-coil and all input data was normalized by $mean(u) + 2 \cdot std(u)$, where u is the acquired data in *k*-*t* space and std is the standard deviation. The CS iterations continued until the normalized iterative update (defined as $\|u_{n+1} - u_n\|_2 / \|u_{n+1}\|_2$,

where n is the iteration index) was less than 10^{-3} or until the number of iterations reached a maximum of 100.

For radial-based CS, the data was reconstructed using the NUFFT algorithm from a MATLAB-based (The Math Works, Inc., Natick, MA, USA) image reconstruction toolbox made available by Fessler et al [42]. At each iteration, the algorithm transformed the data from image to polar *k*-space using the NUFFT, and from the temporal to frequency domain using the standard FFT. For density compensation, a ramp filter inversely proportional to the magnitude of the *k*-space radius, $\|\vec{k}\|_2$, was applied to each spoke.

Regularization Parameters

The regularization parameter λ for each coil was defined as $\lambda = \alpha \cdot \sigma$, where σ is the coil noise standard deviation and α is a proportionality factor. The parameter λ essentially defines the value by which the image is denoised in each iterative soft-thresholding step of MFISTA, so λ was adjusted in proportion to the level of the noise in each coil. Accordingly, the proportionality factor α was determined based on estimates of σ for each coil, which were obtained from an in-built pre-scan noise measurement.

Using the fully-sampled phantom and *in vivo* brain data and estimates of σ, the factor α was found by minimizing the l_2-norm of the difference between the fully-sampled spectra and the reconstructed spectra from retrospectively undersampled data:

$$\min_{\alpha} \sqrt{\sum_{i \in VOI} [s_i^{full} - s_i^{rec}(\alpha)]^2} \qquad (3\text{-}2)$$

where s_i^{full} and s_i^{rec} are the fully-sampled and reconstructed spectra between 0.5 – 4.3 ppm at the i^{th} voxel within the VOI, respectively. The minimization was performed by iterating over a range of α values linearly spaced between 0.01 and 1. For both REPSI and EPSI and for all acceleration factors, the value of α that minimized the above metric was approximately 0.10. Thus, the regularization parameter was defined as $\lambda = \sigma \cdot 10^{-1}$ for all REPSI and EPSI reconstructions.

Spectral Pre- and Post-processing

Prior to CS reconstruction, the odd and even echoes from the bi-polar readout were separated into two datasets, and the odd echo data was time-reversed. After Fourier transforming the temporal dimension, a linear phase ramp was applied along the readout in order to correct for chemical-shift displacement caused by the phase accrual of each resonance during k_x-t sampling [43]. Afterward, the data was Fourier transformed back to the time domain, and both the water and non-water suppressed data were averaged. The undersampled, water-suppressed even and odd echo datasets were reconstructed separately. Eddy current and zero-order phase corrections computed from the fully-sampled non-water-suppressed data were applied to the CS-reconstructed data [44]. Coil combination was performed using the singular valued decomposition (SVD) method [45]. After applying a first-order phase correction to the even echoes to account for the difference in echo time relative to the odd echo, and then performing frequency and phase alignment using the FID-A toolbox [46,47], the coil-combined reconstructions from the even and odd echoes were averaged. Finally, the residual water peak was removed using the Hankel-Lanczos SVD method [48].

All reconstructed spectral metabolite maps and quantitation were obtained using LC model (version 6.2-0T) [49]. The basis set for the phantom data was simulated using the VESPA software

package [50] and included the following metabolites: N-acetyl-aspartate (NAA), N-acetylaspartylglutamate (NAAG), γ-aminobutyric acid (GABA), aspartate, choline (Cho), creatine (Cr), glucose, glutamate (Glu), glutamine (Gln), glutathione, myo-inositol (mI), lactate, phosphocholine (PCh), phosphoryl-ethanolamine, alanine, taurine, and threonine. The basis set for *in vivo* datasets included the previously listed metabolites in addition to glycerophosphorylcholine (GSH) and scyllo-inositol.

Comparison across Acceleration Factors

To evaluate the performance of REPSI and EPSI for each AF, five metrics were considered. For retrospectively undersampled data, the reconstruction accuracy was compared using normalized root mean square errors (nRMSE) of the reconstructed spectra and metabolite maps derived from LC Model quantitation. Maps showing the Cramer-Rao lower bounds (CRLB) of the metabolite concentrations for voxels within the VOI were compared, as well as the percent absolute difference (PAD) maps between the fully-sampled and reconstructed metabolite maps. For prospectively undersampled data, the metabolite maps were compared qualitatively with those from the separately-acquired fully-sampled maps, and the CRLB maps for each AF were compared to determine the reliability of the quantified spectra from REPSI versus EPSI reconstructions.

Spectral nRMSE maps were obtained by computing the following metric for each voxel:

$$nRMSE(s_i^{rec}) = \frac{100}{\sqrt{N_s}} \cdot \frac{\left\| s_i^{rec} - s_i^{full} \right\|_2}{\left\| s_i^{full} \right\|_2} \qquad (3\text{-}3)$$

where s_i^{rec} and s_i^{full} are the (complex-valued) reconstructed and fully-sampled spectra, respectively, at the i^{th}voxel within the VOI. Only the range between 0.5 – 4.3 ppm was considered

for this computation and N_s is the number of spectral points within this range. The metabolite map nRMSE value was defined as follows:

$$nRMSE(m) = \frac{100}{\sqrt{N_{VOI}}} \cdot \sqrt{\sum_{i \in VOI} \left(\frac{m_i^{rec} - m_i^{full}}{m_i^{full}} \right)^2} \quad (3\text{-}4)$$

where m_i^{rec} and m_i^{full} is the concentration estimate of metabolite m from the reconstructed and fully-sampled data, respectively. Percent difference maps were also computed as a way to visualize the reconstruction error across the VOI, and the PAD value was computed for each voxel as follows:

$$PAD(m_i^{rec}) = 100 \cdot \frac{\left| m_i^{rec} - m_i^{full} \right|}{m_i^{full}} \quad (3\text{-}5)$$

Finally, the average SNR values of spectra for voxels within the VOI, as measured by LC Model quantitation, were compared.

Comparison between Time-Equivalent Fully-Sampled and Accelerated Acquisitions

To determine the benefit of CS, we compare fully-sampled data acquired with fewer averages to CS reconstructions of time-equivalent, accelerated data obtained with 8 or fewer numbers of averages. One *in vivo* data set was retrospectively undersampled with different numbers of averages to match the scan times of fully-sampled data (AF = 1.0) with 4, 3, 2, and 1 average(s). The following time-equivalent combinations were tested: (1) AF = 1.0 with 4 averages versus AF = 1.5 with 6 averages and AF = 2.0 with 8 averages; (2) AF = 1.0 with 3 averages versus AF = 2.0 with 6 averages; (3) AF = 1.0 with 2 averages versus AF = 1.5 with 3 averages, AF = 2.0 with 4 averages, AF = 2.5 with 5 averages, AF = 3.0 and 6 averages, and AF = 4.0 with 8 averages.

Finally, single-average fully-sampled data is time-equivalent to data acquired at AF = 2.0 with 2 averages, AF = 3.0 with 3 averages, and at AF = 4.0 with 4 averages. For REPSI, fully-sampled data was reduced from 50 to 32 spokes to match the scan time of a fully-sampled EPSI. For each combination, the nRMSE's of the metabolite maps of tNAA, Cr, tCho, Glx, and mI were computed. We applied only TV-denoising to the low-averaged fully-sampled data to compensate for lower SNR, using the same regularization parameter choice as described in Section 2.3.2. The ground truth reconstruction used for computing nRMSE's was taken from the fully-sampled data with 8 averages.

		tCho		Cr		mI		tNAA		Glx	
	AF	**EPSI**	**REPSI**	**EPSI**	**REPSI**	**EPSI**	**REPSI**	**EPSI**	**REPSI**	**EPSI**	**REPSI**
Concentration (mM)	1	1.2 ± 0.1	1.2 ± 0.1	4.3 ± 0.4	4.2 ± 0.3	4.8 ± 0.6	4.7 ± 0.5	7.2 ± 0.7	7.1 ± 0.6	13.6 ± 1.7	13.5 ± 1.5
	1.5	1.2 ± 0.1	1.1 ± 0.1	4.1 ± 0.4	4.0 ± 0.3	4.5 ± 0.5	4.3 ± 0.4	7.0 ± 0.7	6.8 ± 0.6	12.9 ± 1.7	12.5 ± 1.4
	2	1.0 ± 0.1	1.1 ± 0.1	3.8 ± 0.4	3.9 ± 0.3	3.9 ± 0.5	4.1 ± 0.4	6.5 ± 0.7	6.7 ± 0.6	11.4 ± 1.7	12.1 ± 1.4
	2.5	1.0 ± 0.1	1.1 ± 0.1	3.6 ± 0.3	3.8 ± 0.3	3.8 ± 0.4	4.0 ± 0.4	6.2 ± 0.6	6.6 ± 0.5	10.7 ± 1.2	11.9 ± 1.5
	3	1.0 ± 0.1	1.0 ± 0.1	3.5 ± 0.5	3.7 ± 0.4	3.7 ± 0.5	3.9 ± 0.4	6.1 ± 0.7	6.4 ± 0.6	10.8 ± 1.4	11.4 ± 1.6
	4	0.9 ± 0.1	1.0 ± 0.1	3.4 ± 0.5	3.5 ± 0.5	3.7 ± 0.5	3.6 ± 0.5	5.9 ± 1.0	6.2 ± 0.7	10.5 ± 1.5	10.6 ± 1.6
	5	0.9 ± 0.1	0.9 ± 0.1	3.2 ± 0.6	3.3 ± 0.5	3.5 ± 0.5	3.3 ± 0.5	5.4 ± 0.9	5.8 ± 0.7	9.90 ± 1.4	9.50 ± 1.5
CRLBs (%)	1	10.4 ± 2.4	8.7 ± 2.2	7.6 ± 1.6	6.6 ± 1.6	12.0 ± 2.7	10.2 ± 2.6	6.4 ± 1.4	5.6 ± 1.5	10.3 ± 2.4	8.9 ± 1.7
	1.5	9.9 ± 2.1	9.1 ± 2.1	7.4 ± 1.5	6.8 ± 1.6	11.6 ± 2.4	10.8 ± 2.4	6.1 ± 1.3	5.7 ± 1.4	9.9 ± 1.8	9.2 ± 1.7
	2	10 ± 2.1	9.2 ± 2.1	7.3 ± 1.4	6.8 ± 1.6	11.8 ± 2.5	10.8 ± 2.5	5.9 ± 1.2	5.6 ± 1.4	10.1 ± 1.8	9.3 ± 1.7
	2.5	10 ± 1.8	9.2 ± 2.0	7.2 ± 1.3	6.7 ± 1.5	11.7 ± 2.3	10.8 ± 2.4	5.9 ± 1.2	5.5 ± 1.5	10.1 ± 1.5	9.2 ± 1.7
	3	9.8 ± 1.8	9.2 ± 2.0	7.1 ± 1.3	6.7 ± 1.5	11.5 ± 2.1	11.0 ± 2.3	5.7 ± 1.2	5.5 ± 1.4	9.8 ± 1.8	9.4 ± 1.7
	4	9.6 ± 1.9	9.4 ± 1.9	6.9 ± 1.3	6.7 ± 1.3	11.3 ± 2.1	11.3 ± 2.1	5.6 ± 1.2	5.4 ± 1.3	9.8 ± 1.7	9.7 ± 1.8
	5	9.0 ± 1.6	9.8 ± 1.8	6.6 ± 1.0	6.8 ± 1.2	10.6 ± 1.9	11.5 ± 2.2	5.4 ± 0.9	5.4 ± 1.2	9.3 ± 2.1	10.2 ± 2.4

Table 3-1: Concentration estimates and corresponding CRLB (shaded) percentage values of tCho, Cr, mI, tNAA, and Glx quantified from CS reconstructions of prospectively undersampled REPSI and EPSI brain phantom data, for all AFs.

	SNR		FWHM (Hz)	
AF	**EPSI**	**REPSI**	**EPSI**	**REPSI**
1	13.6 ± 1.7	14.5 ± 1.3	2.3 ± 1.0	2.8 ± 1.4
1.5	14.7 ± 1.9	15.5 ± 1.4	2.3 ± 0.9	2.4 ± 1.2
2	15.3 ± 1.9	15.9 ± 1.7	2.2 ± 1.2	2.4 ± 1.3
2.5	15.3 ± 2.2	15.9 ± 1.9	2.2 ± 1.2	2.5 ± 1.7
3	15.2 ± 2.0	16.0 ± 1.7	2.4 ± 1.2	2.5 ± 1.4
4	14.8 ± 2.3	15.9 ± 2.3	2.4 ± 1.2	2.6 ± 1.5
5	14.9 ± 2.4	15.5 ± 2.7	2.6 ± 1.4	2.9 ± 2.0

Table 3-2: The SNR and FHWM values of spectra from CS reconstruction of prospectively undersampled brain phantom data.

3.3.4 In vivo Free-Breathing Liver Scans

Using a body array coil and the same scan parameters used for the *in vivo* brain scans, free-breathing REPSI and EPSI liver datasets were acquired from two healthy male volunteers. For both REPSI and EPSI, 32 k_y-lines or spokes were sampled to maintain the same scan time, so that the REPSI acquisition was technically undersampled, though at a relatively low acceleration factor of 1.5. These experiments were conducted in order to compare the spectral quality resulting from motion-corrupted REPSI and EPSI data. No CS reconstruction was applied to the undersampled REPSI data to avoid the influence of CS-related denoising on the spectrum.

3.3.5 Lipid Contamination in Radial and Cartesian EPSI

It is well-known that lipid signals can cause severe spectroscopic imaging artifacts due to the relatively low resolutions of MRSI and the high intensity of the lipid signal relative to other metabolites, which exacerbates Gibbs ringing artifacts. In order to test and compare the performance of CS-reconstructions of undersampled REPSI and EPSI data to lipid contamination, we performed a separate set of experiments on two subjects in which we expanded the size of volume-of-interest (VOI) to include areas of the intracranial lipid layer (Figure 3A-4). In one subject, we acquired fully-sampled and prospectively-undersampled REPSI and EPSI data, at an acceleration factor (AF) of 3. In another volunteer, we retrospectively undersampled the fully-

sampled data at an AF of 2.5. After CS reconstruction of the lipid-contaminated data using our TV-based regularization, we used a post-processing-based lipid suppression technique [65] to remove the spectral lipid component from each voxel. The lipid and metabolite mask required for Bilgic's L_2-based minimization problem were selected manually, and the regularization parameter was set to $1 \cdot 10^{-3}$ after normalizing the data as described in subsection 3.3.3 of this chapter.

3.3.6 REPSI acquisitions in Obstructive Sleep Apnea

Obstructive Sleep Apnea (OSA) affects over 15% of the adult population and is associated with brain dysfunction. Although the dysfunction is well-identified and presents brain morphological changes as shown with structural imaging, it is unclear what pathology underlies these neural alterations. Magnetic resonance spectroscopic imaging (MRSI) can non-invasively measure several metabolites from multiple brain regions in vivo. However, the clinical practicality of the standard MRSI techniques (Cartesian phase-encoding or echo-planar [EP]) is hindered by long scan times. In order to assess clinical populations, our group developed an alternative MRSI technique, "radial" EP-MRSI. To assess the feasibility and calculate effect sizes we did a pilot study of brain metabolites in OSA using radial EP-MRSI.

Radial EP-MRSI data with a speed-up (undersampling) factor of 2.5 (compared to a fully-sampled Cartesian MRSI scan) were acquired in 5 OSA patients (3 males, 37±11 yrs., Apnea Hypopnea Index (AHI): 8.2±5.5) and 10 healthy controls (5 males, 28±7 yrs.). Spectra from twelve brain regions were selected from each subject and five metabolites–total choline, myo-inositol (mI), total N-acetylaspartate, glutamine+glutamate (Glx) and lactate (Lac)–were quantified as ratios with respect to creatine (Cr), using LC Model. The brain regions include left/right of: basal ganglia, insula, and gray/white of the frontal and occipital regions. Mean group differences were calculated and compared with independent samples t-tests.

3.3.7 Accelerated REPSI in Healthy Prostate with a Reduced Field-of-View

Radial echo planar spectroscopic imaging (REPSI) is applied in healthy prostate and compared to Cartesian EPSI acquisitions. Due to the small spatial extent of the anatomy-of-interest, REPSI is well-suited for acceleration in a reduced-field-of-view context. In this proof-of-concept study, we acquired both prospectively and retrospectively undersampled REPSI and Cartesian EPSI datasets in prostate phantom and in vivo, at multiple acceleration factors, and we compared both quantitative and qualitative results.

Monitoring of prostate tumor grade and progression is important for both the diagnosis and treatment of prostate cancer. Multi-parametric MRI and biopsy are widely used for detection and grading of prostate cancer although both techniques can be limited by small tumor size and sampling error bias[66,67], respectively. Magnetic resonance spectroscopy (MRS) can complement these modalities by providing further chemical characterization of prostate tumors. In contrast to single-voxel techniques, spectroscopic imaging (MRSI) measures a greater spatial coverage within a single scan, yet requires long acquisitions times which can be clinically impractical[68]. Faster alternatives based on echo planar (EPSI) trajectories have been proposed to decrease the scan time by an order of magnitude[11]. More recently, radial EPSI has been proposed as an alternative which can tolerate higher degrees of under-sampling compared to Cartesian EPSI[4]. Additionally, radial acquisitions in prostate are well-suited for reduced field-of-view (FoV) imaging[51], since the anatomy-of-interest is constrained to a relatively small region. In such cases, reduced FoV spectroscopic imaging can further decrease the scan time by enabling greater acceleration factors. In this proof-of-concept study, we accelerate REPSI in the prostate by reducing the number of acquired spokes and applying compressed sensing (CS) with total variation (TV) regularization, resulting in reduced FoV's and shortened scan times that are within clinically-feasible durations.

Prospectively under-sampled radial data sets from in vivo prostate and in a phantom were acquired, as well as data using the more conventional Cartesian EPSI for comparison.

In both the in vivo and prostate phantom experiments, a radial echo planar spectroscopic imaging (REPSI) sequence with semi-LASER volume excitation was used to acquire a 40 × 40 × 15 mm^3 volume-of-interest (VoI) within a 320 × 320 mm^2 field-of-view, using a 32 × 32 matrix size (1.5 mL voxel volume), a flyback gradient echo train[69] (1562.5 Hz spectral width and 512 time points), TE = 100 ms, TR = 1.5 s and 8 averages. No lipid suppression modules were included in the sequence, however, the lipids were removed from the reference water signal in post-processing using HLSVD[48] for eddy current phase correction. Fully-sampled Cartesian EPSI and REPSI datasets acquired in three healthy male volunteers were retrospectively undersampled with acceleration factors (AF) of 1.5 (21 k_y-lines/spokes), 2 (16 k_y-lines/spokes), and 2.5 (13 k_y-lines/spokes). An external body coil with a maximum of 30 coils was used for the in vivo acquisitions. At AF = 1.0, time equivalent datasets with 32 k_y-lines or spokes were acquired. One prospectively undersampled REPSI dataset was acquired in a fourth volunteer with AF's of 1.5, 2, and 2.5. Fully-sampled and prospectively undersampled Cartesian EPSI and REPSI datasets (AF's of 1.5, 2, 2.5) were acquired in a prostate phantom containing choline (Cho), citrate (Cit), creatine (Cr), myo-inositol (mI), and spermine (Spm) at physiological concentrations. All undersampled data was reconstructed with a CS-TV algorithm[4]. Scan times for AF's of 1, 1.5, 2, and 2.5 were 7 min 30 sec, 5 min, 3 min 45 sec, and 3 min, respectively. The prostate phantom reconstructions were quantified in LCModel[49] using simulated basis sets generated in VESPA[50]. Ratios with respect to Cho were computed in the prostate phantom and compared as a function of AF, and the percent difference with respect to the fully-sampled Cho ratio was also determined. Citrate maps

and multi-voxel spectra were reconstructed in the retrospectively and prospectively undersampled in vivo data sets and were compared qualitatively.

3.4 Results

3.4.1 Accelerated REPSI and EPSI Reconstructions

Table 3-1 shows the means and standard deviations (SD) of the estimated concentrations of tNAA (total NAA: NAA + NAAG), tCho (total Cho: Cho + PCh), Glx (Glu + Gln), Cr and mI from reconstructions of prospectively undersampled brain phantom data, as well as the means and SD's of the corresponding CRLB's. Generally, the concentrations were more underestimated as the AF increased, but for REPSI, the estimates remained closer to those from the fully-sampled data. For example, the difference between the fully-sampled and reconstructed Cr concentration were 0.4 mM and 0.7 mM for REPSI and EPSI undersampled with 13 spokes or k_y-lines, respectively. REPSI also had lower SD's of the concentration values, indicating a greater consistency in the quantitation compared to EPSI. It can be inferred that the coefficients of variation (CV) of the concentration estimates from REPSI were lower for all metabolites and AF's. The lower CRLB values confirmed that the concentration estimates from REPSI were more reliable than those from EPSI. Increased SNR from radial acquisitions is shown in Table 3-2. For all AF's, REPSI CS reconstructions data had greater SNR, although the estimates of the full-width-at-half-maximum (FWHM) values of reconstructed REPSI spectra were slightly higher than those of the EPSI spectra.

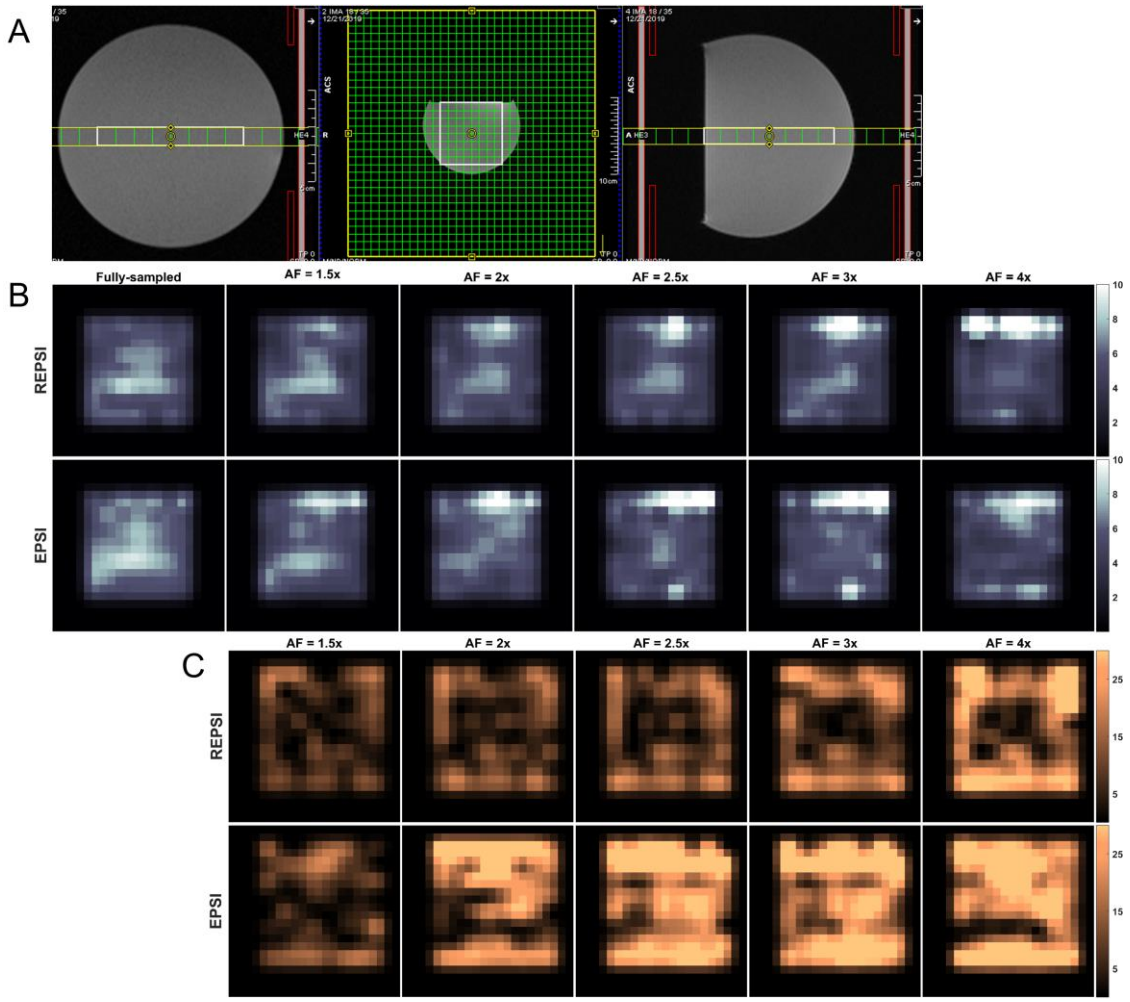

Figure 3-2: **(A)** Localization image for brain phantom acquisitions. **(B)** Maps of the Cramer-Rao lower bounds (CRLBs) as percentages of the estimated total NAA concentrations (tNAA), from fully sampled and compressed sensing (CS)–reconstructed REPSI and echo-planar spectroscopic imaging (EPSI) brain phantom data. **(C)** Percent absolute difference (PAD) maps of tNAA from CS reconstructions of retrospectively undersampled REPSI and EPSI brain phantom data, for all AFs corresponding to 21 (1.5×), 16 (2×), 13 (2.5×), 11 (3×), and 8 (4×) radial spokes or k_y-lines. All maps are interpolated by a factor of two.

Figure 3-2C displays the PAD maps of tNAA from CS reconstructions of retrospectively undersampled REPSI and EPSI data. Clearly, the REPSI tNAA maps contain lower values across most of the VOI. Due to effects from chemical shift displacement, the edges of the VOI are more susceptible to error in both radial and Cartesian acquisitions, but as the AF increases, EPSI has higher reconstruction errors as measured by the PAD, particularly in the central portion of the VOI.

In contrast, REPSI reconstructions maintain relatively low PAD values within the center of the VOI, even for data acquired with as few as 8 spokes. Figure 3-2B shows the CLRB maps for the tNAA concentrations. Similar to the PAD maps, the CRLB maps show overall lower values across large portions of the VOI in comparison the EPSI tNAA CRLB maps, except for the highest AF's corresponding to 8 spokes and in some peripheral voxels.

Table 3-2 lists the nRMSE's of the metabolite maps of tNAA, tCho, Cr, Glx, and mI from CS reconstructions of *in vivo* data. For almost all AF's considered, the nRMSE values from REPSI reconstructions were much lower, indicating higher reconstruction accuracy. Figure 3-3(A,B) shows the spectral nRMSE maps for CS reconstructions of retrospectively undersampled REPSI and EPSI in vivo data. As with the PAD, CRLB, and metabolite map nRMSE's, the spectral nRMSE maps show that the REPSI spectra have higher reconstruction accuracy for all acceleration factors. For both *in vivo* brain datasets, the spectral nRMSE values from REPSI do not increase as sharply as those from EPSI, which demonstrates that REPSI is much more robust to higher AF's. Similarly, Table 3-3 shows lower CRLB values for REPSI, indicating more reliable *in vivo* quantitation compared to EPSI for all AF's.

		tNAA		**tCho**		**Glx**		**mI**		**Cr**	
	AF	**REPSI**	**EPSI**	**REPSI**	**EPSI**	**REPSI**	**EPSI**	**REPSI**	**EPSI**	**REPSI**	**EPSI**
Mean nRMSEs	1.5	11.9	**10.3**	**16.4**	32.5	**22.7**	31.6	75.4	**36.5**	**14.1**	14.6
	2	**13.6**	18.7	**18.6**	34.1	**25.3**	76.8	75.1	**46.4**	**16**	23.7
	2.5	**15.3**	24.2	**19.7**	31.1	**26.7**	37	72.1	**49.1**	**18.4**	29.7
	3	**18.3**	26.2	**22.8**	32.4	**28.9**	37.3	**46.1**	56.9	**20.6**	30.6
	4	**21.9**	22.5	**26.4**	28.8	**34.5**	38.1	69.7	**48.2**	**24.4**	30.5
	5	**25.9**	32.2	**27.8**	36.3	**35.1**	42.3	85.8	**56.5**	**25.6**	41
Mean CRLBs	1	**8.4**	9	**11.6**	13.7	**16.9**	19.8	37.8	**28.2**	**7.8**	9.5
	1.5	**8**	8.5	**12.3**	13.3	**17.6**	18.7	**22.3**	30.2	**7.7**	8.8
	2	**8**	11.1	**12.3**	15.7	**18.6**	20.6	**19.5**	41.9	**7.7**	9.9
	2.5	**8.1**	11.8	**12.4**	17	**16.8**	22.8	**24.3**	64.2	**7.6**	11.8
	3	**8.3**	11.6	**13.8**	17.3	**17.1**	24.6	**29.5**	40.8	**7.9**	10.5
	4	**8.8**	10	**13.8**	15	**17.5**	23.1	33.1	**32.8**	**8.1**	9.5
	5	**9.5**	11.1	**15**	17	**18.9**	23.8	**34.9**	36.4	**8.8**	9.6

Table 3-3: Mean nRMSE values of metabolite maps obtained from LCModel quantitations of CS-reconstructed, retrospectively undersampled, in vivo brain data (top) and mean CRLB values from both REPSI and EPSI CS reconstructed, averaged across 7 healthy volunteers (bottom). Note: The mean values across 7 healthy volunteers are shown for AFs of 1.5, 2, 2.5, 3, 4 and 5. The bold numbers in the top half indicate a lower mean nRMSE value for that particular AF and metabolite. The bold numbers in the bottom half indicate a lower mean CRLB for that particular AF and metabolite.

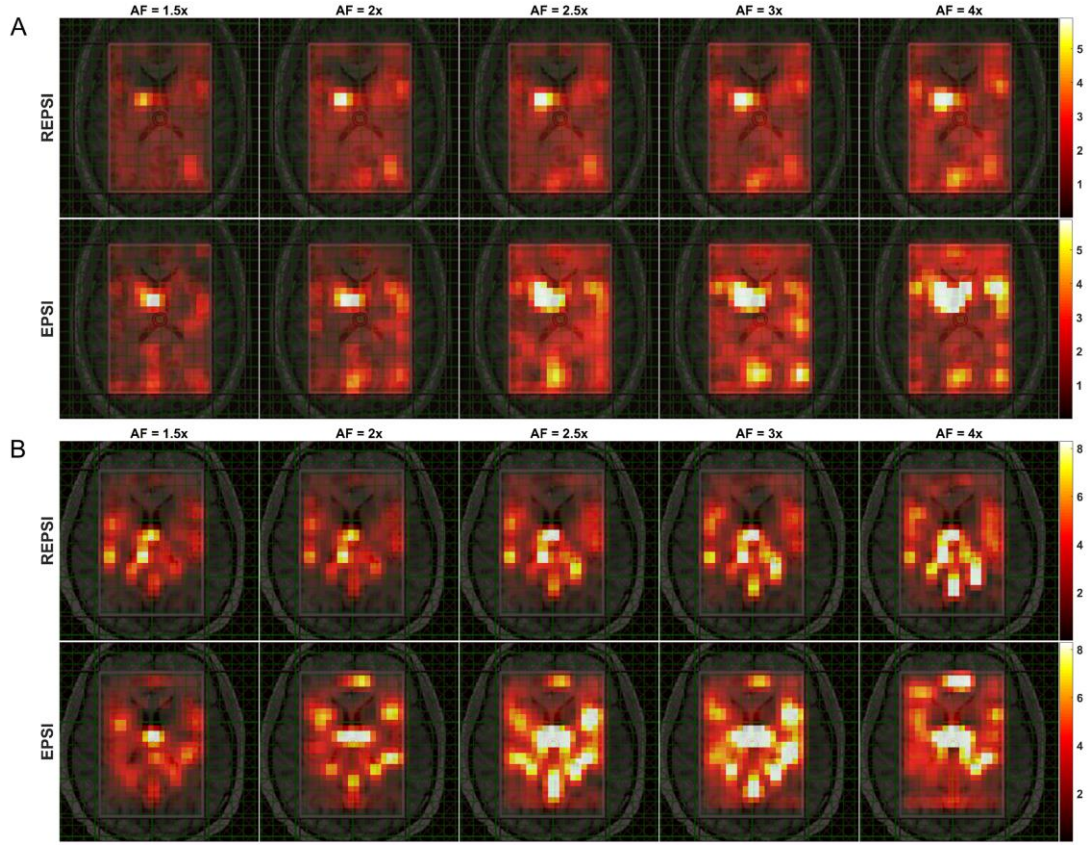

Figure 3-3: **(A)** Maps of the spectral normalized RMS error (nRMSE) computed from CS reconstructions of retrospectively undersampled REPSI and EPSI in vivo data from a 26-year-old healthy volunteer, shown for AFs corresponding to 21 (1.5×), 16 (2×), 13 (2.5×), 11 (3×), and 8 (4×) radial spokes or k_y-lines. **(B)** Spectral nRMSE maps from CS reconstructions of retrospectively undersampled REPSI and EPSI in vivo brain data acquired from a healthy 33-year-old male volunteer, shown for AFs of 1.5, 2, 2.5, 3, and 4. All maps are interpolated by a factor of two

Metabolite and CRLB maps from reconstructions of prospectively undersampled *in vivo* REPSI and EPSI brain data are shown in Figure 3-4. The tNAA map from EPSI reconstructions degraded significantly starting at the relatively low AF of 2 (16 k_y-lines), while the maps from

REPSI retain the underlying brain morphology, such as the outlines of the ventricles, even at the highest AF's. Overall, reconstruction artifacts were significantly less prominent in the REPSI tNAA maps. The corresponding CRLB maps in Figure 3-4B show that the concentration estimates from REPSI data have lower CRLB's across most of the VOI, except in voxels near the frontal cortex where EPSI also has increased CRLB's. In both areas surrounding the ventricles and in the posterior regions of the brain, REPSI maintains more reliable estimates of the tNAA concentrations.

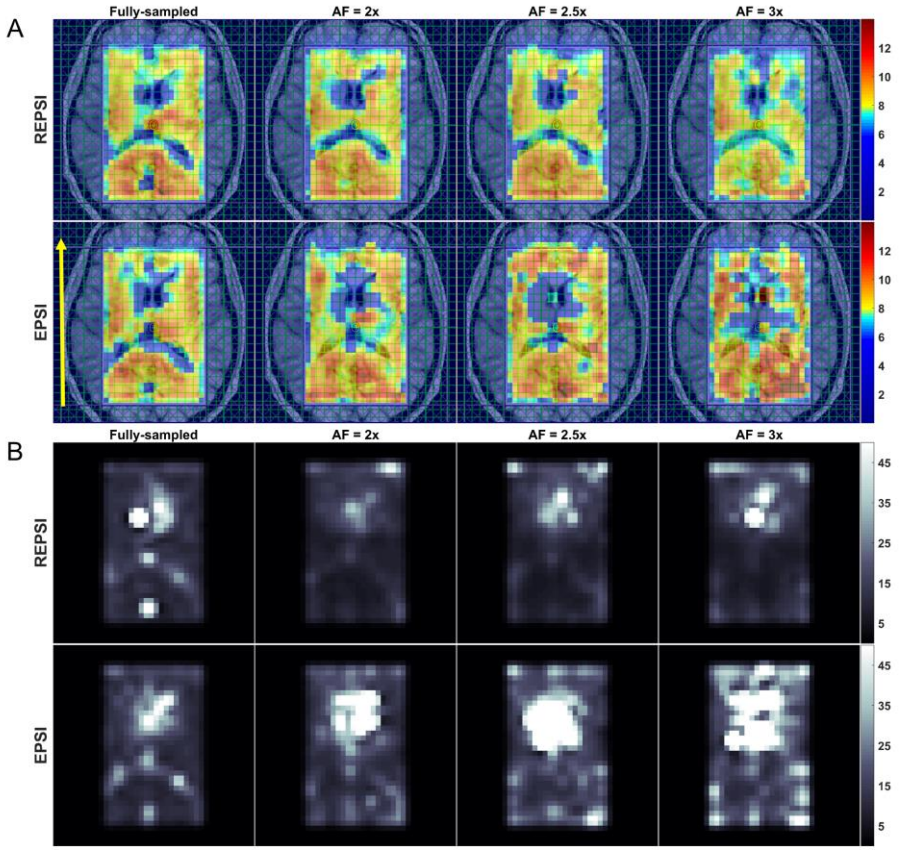

Figure 3-4: Brain MRSI scan of a 33-year-old healthy male volunteer. **(A)** The tNAA maps from fully sampled (AF = 1.0) REPSI and EPSI brain data (leftmost column), and tNAA maps from CS reconstructions of prospectively undersampled brain data acquired with 16, 13, and 11 radial spokes or k_y-lines. **(B)** The CRLB maps for the tNAA maps shown in (A). The phase-encoding direction is indicated by the yellow arrow in the leftmost image of the EPSI row in (A). All maps are interpolated by a factor of two.

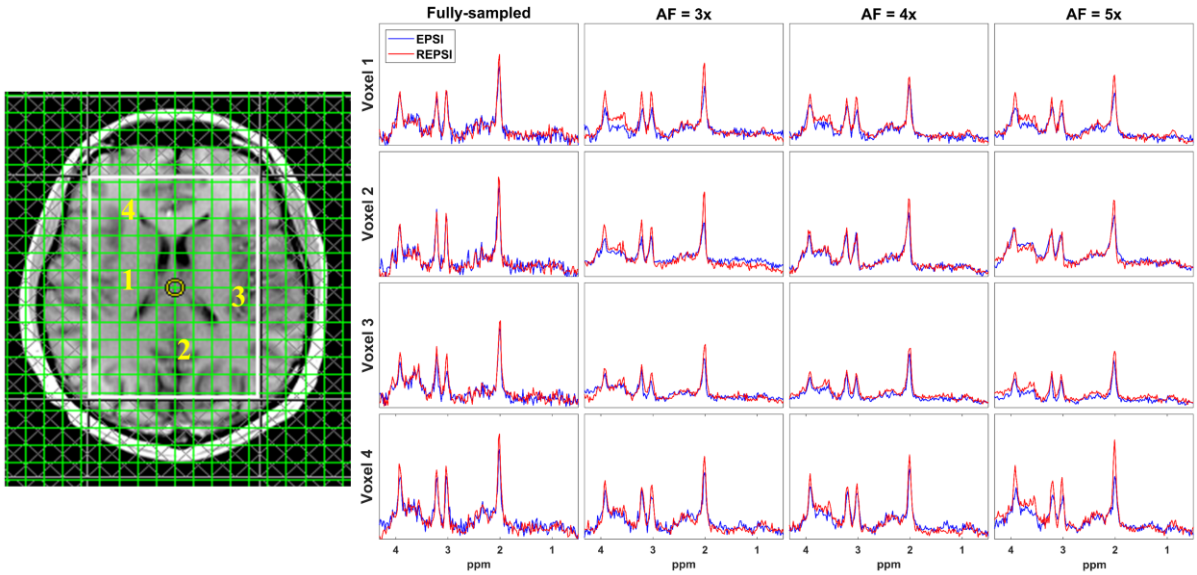

Figure 3-5: Representative spectra from fully sampled and CS reconstructions of prospectively undersampled in vivo brain data from a 32-year- old healthy male volunteer. Spectra extracted from four brain locations are shown: 1, right putamen to corona radiata; 2, occipital gray matter; 3, left posterior insular cortex; and 4, frontal white matter. Both the REPSI and EPSI data were prospectively undersampled with 11 (AF = 3), 8 (AF = 4), and 6 (AF = 5) acquired radial spokes or k_y-lines, respectively. Baselines of the REPSI and EPSI spectra between 0.5 and 4.3 ppm were matched. The NAA peak (2.01 ppm) intensity from fully sampled REPSI spectra (red) had an approximately 16% increase in peak intensity compared with the EPSI spectra (blue) from the selected voxels. All spectra are shown in real mode (phase sensitive) and share the same scale.

Figure 3-5 shows extracted spectra from CS reconstructions of prospectively undersampled data in four brain areas – (1) right putamen to corona radiata, (2) occipital gray matter, (3) left posterior insular cortex, and (4) frontal white matter, as indicated in the axial brain localization image. As mentioned previously, REPSI has a greater SNR advantage over EPSI, which is evident from the higher peak amplitudes of REPSI spectra relative to those from EPSI. Due to the denoising effect from the CS reconstruction, both REPSI and EPSI spectra, however, were able to provide spectra with well-resolved NAA, Cr, mI and tCho peaks up to the highest AF factors, although, expectedly, the peak intensity decreased as the AF increases. This slight reduction in

intensity is caused by a decrease in SNR due to fewer k-space points sampled as the AF increases, although the central k-space remains densely sampled. However, the radial undersampling patterns at high AF's retain a greater concentration of the lower spatial frequency data compared to the undersampled Cartesian masks for high AF's, in which more samples are taken along the k_x direction and fewer along k_y. For the spectra shown in Figure 3-5, the tNAA peak height above the noise floor reduced by approximately 10% and 16% in REPSI and EPSI spectra at AF = 3.0, respectively, compared to the fully-sampled spectra.

Figure 3-6 shows metabolite maps of tNAA, Cr, tCho, Glx, and mI from fully-sampled (A) and CS reconstructions (B) of accelerated (AF = 2.5) REPSI and EPSI data. The morphological features in the accelerated REPSI maps more closely match those of the fully-sampled data, while the EPSI maps show severe degradation. Figure 3-7 demonstrates the degree of reconstruction error, where the PAD maps clearly indicate that CS reconstructions from undersampled REPSI data are more accurate. Figure 3-10 shows the fully-sampled metabolite maps (A) and the corresponding CRLB maps (B), indicating that REPSI is better able to reliably estimate the concentrations of tNAA, Cr, tCho, Glx, and mI.

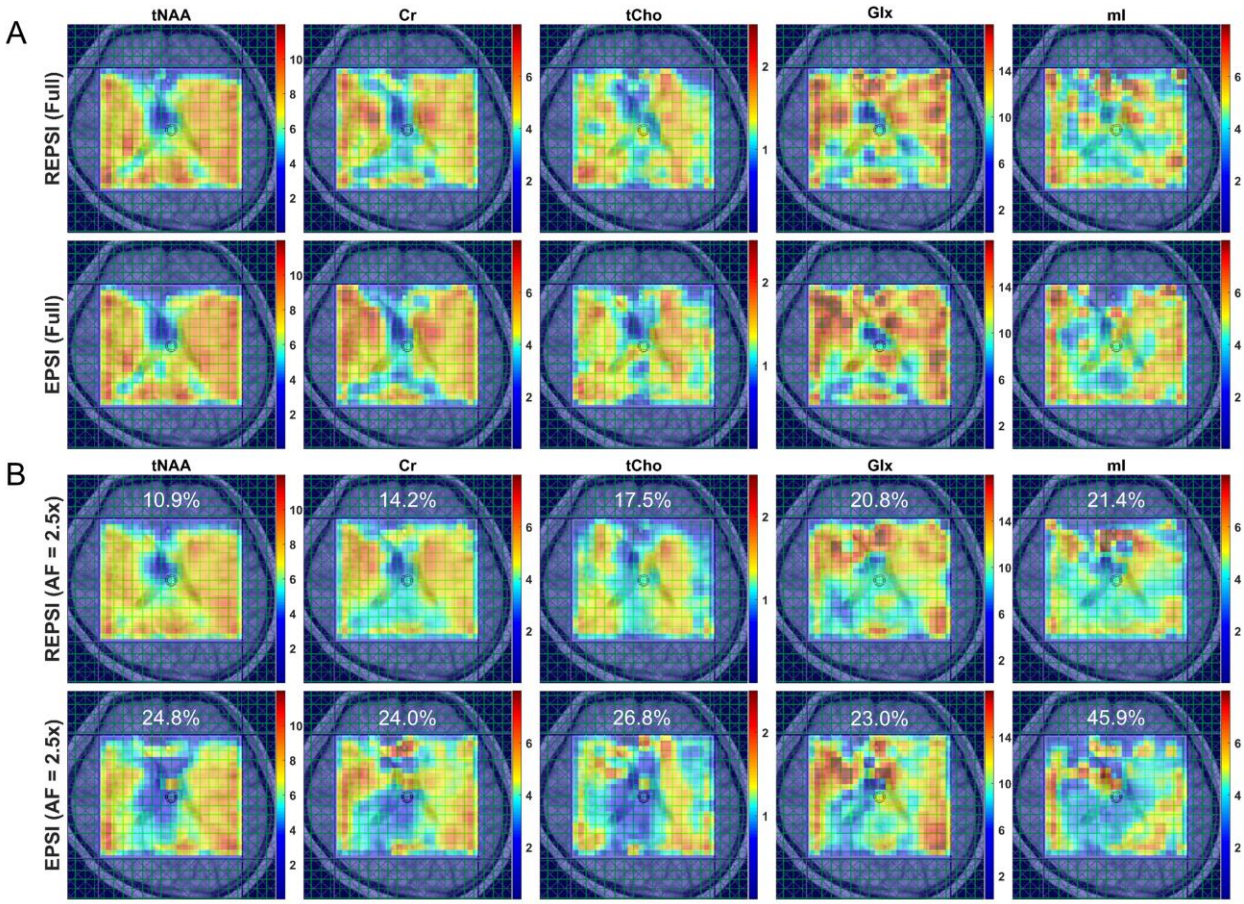

Figure 3-6: **(A)** Metabolite maps of tNAA, Cr, total choline (tCho), Glx (glutamate + glutamine), and myo-inositol (mI) from fully sampled REPSI (top row) and EPSI (bottom row) reconstructions of in vivo brain data from a healthy 24-year-old healthy female volunteer. **(B)** Metabolite maps of tNAA, Cr, tCho, Glx, and mI from CS reconstructions of retrospectively undersampled (AF = 2.5) REPSI (top row) and EPSI (bottom row) data. Note that the REPSI reconstructions at AF = 2.5 show greater similarity to the fully sampled metabolite maps, compared with the EPSIreconstructions. The nRMSEs of the metabolite maps are also shown. All maps are interpolated by a factor of two.

Table 3-4 shows the metabolite map nRMSE's from reconstructions of time-equivalent, fully-sampled and accelerated REPSI and EPSI data with different numbers of averages. Generally, the CS-reconstructed data, particularly from REPSI, had lower metabolite map nRMSE's than the time-equivalent, denoised fully-sampled data. Additionally, the nRMSE values from REPSI were, in most cases, lower than those from the time-equivalent EPSI reconstructions. Therefore, it may

be more beneficial to apply CS reconstruction to data with more averages than to acquire a time-equivalent, fully-sampled data with fewer averages.

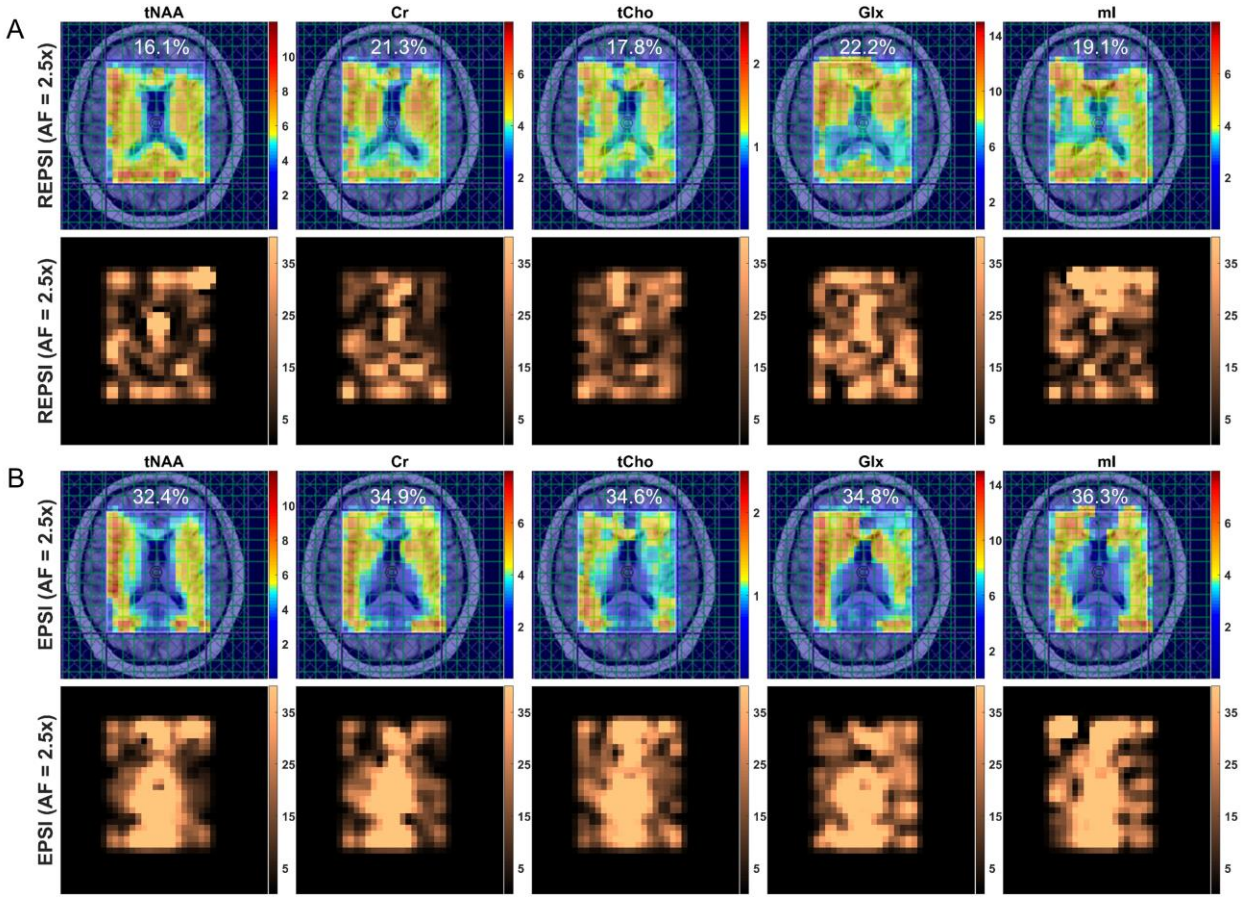

Figure 3-7: Metabolite maps of tNAA, Cr, tCho, Glx, and mI (top row) from CS reconstructions of retrospectively undersampled in vivo brain data (AF = 2.5) from a 34-year-old healthy male volunteer. The corresponding percent absolute difference (PAD) maps are shown in the bottom row. The maps in **(A)** correspond to an AF of 2.5 for REPSI reconstructions. **(B)** Metabolite maps of tNAA, Cr, tCho, Glx, and mI (top row) and corresponding PAD maps (bottom row) from EPSI reconstructions of retrospectively undersampled data (AF = 2.5). The nRMSEs of the metabolite maps are also shown. All maps are interpolated by a factor of two.

3.4.2 In vivo Free-Breathing Liver Scans

The motion-robustness of REPSI is shown in Figure 3-8. Breathing motion causes severe artifacts in the fully-sampled EPSI spectrum (Figure 3-8). These spurious, oscillating peaks mostly emanate from the water signal and decrease in intensity toward the opposite end of the spectrum

near the poly-methylene lipid peak in the high-field region. The dominant lipid peak also appears to have a broadened line width and surrounding peak artifacts similar to those near the water signal. Although the REPSI spectrum is reconstructed from (spatially) undersampled data (Figure 3-8), it is clear that the motion-related artifacts are much less severe and that the line width of the main lipid peak is relatively smaller compared to the EPSI spectrum. It is also possible to observe traces of other peaks in the spectrum such as choline at 3.2 ppm, since there are no overlapping motion-induced spectral artifacts in that range. Finally, the water and lipid maps from EPSI show severe motion-related artifacts along the phase-encoding dimension, whereas the REPSI water and lipid maps remain relatively artifact-free (Figure 3-9). These results demonstrate that radial sampling can produce more reliable measurements in motion-prone organs.

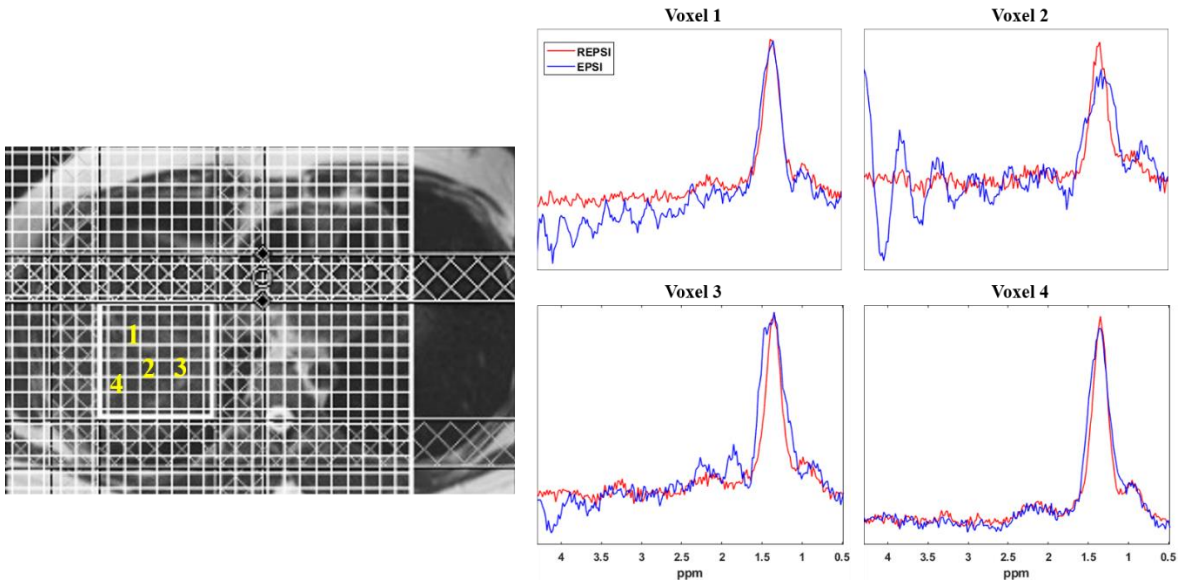

Figure 3-8**:** (Left) VOI localization for a free-breathing REPSI and ESPI liver scan from a healthy 33 year-old male volunteer. (Right) REPSI (red) and EPSI (blue) liver spectra extracted from four voxel locations numbered in yellow on the left.

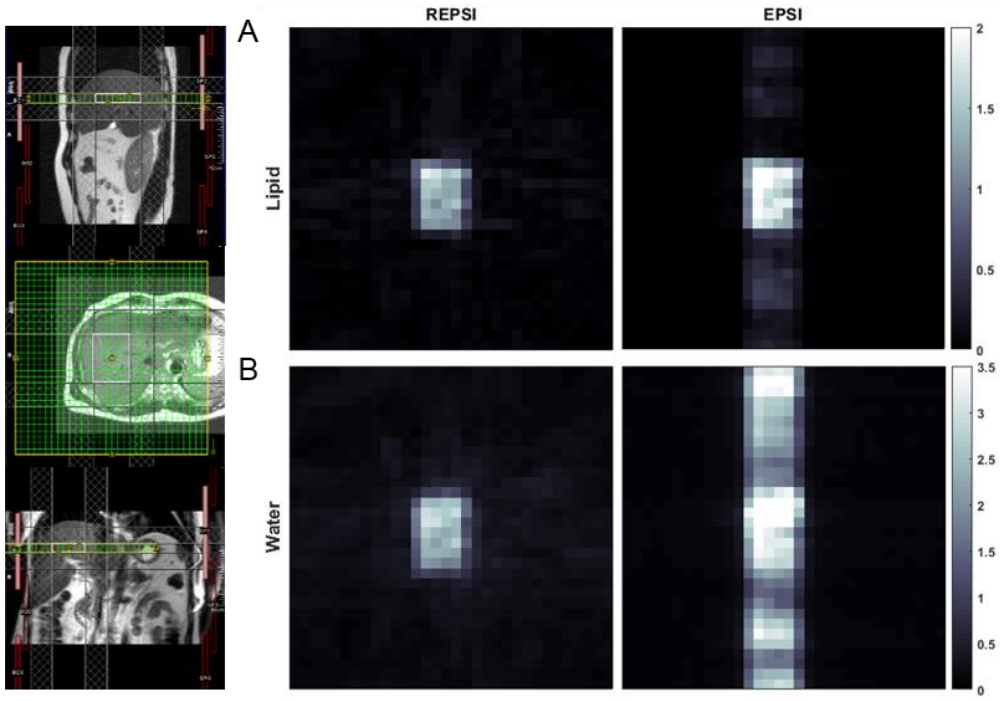

Figure 3-9**:** (Left) VOI localization for a free-breathing REPSI and ESPI liver scan from a healthy 42 year-old male volunteer. (A) REPSI and EPSI maps of the poly-methylene lipids at approximately 1.35 ppm, measured in the liver. (B) Water maps of the liver from REPSI (left) and EPSI (right). Note the strong ghosting artifacts present along the phase-encoding dimension in the EPSI maps.

3.4.3 Comparison between Time-Equivalent Fully-Sampled & Accelerated Acquisitions

Table 3-4 shows the nRMSE's of metabolite maps from reconstructions of time-equivalent, fully-sampled and accelerated REPSI and EPSI data with varying numbers of averages. Generally, the CS-reconstructed data, particularly from REPSI, had lower nRMSE's than the time-equivalent, denoised fully-sampled data. The nRMSE values from REPSI were also, in most cases, lower than those from the time-equivalent EPSI reconstructions. Based on the improved nRMSE values in the CS-reconstructed data, it is preferable to reconstruct accelerated REPSI with more averages than to acquire a time-equivalent, fully-sampled dataset with fewer averages. It can also be seen that REPSI retains lower nRMSE values than EPSI in essentially all cases. Figure 3-13 shows EPSI and REPSI tNAA maps resulting from the following time-equivalent cases: (A) Fully-sampled

with 2 averages versus AF = 2.5 with 5 averages, and (B) Fully-sampled with 2 averages versus AF = 4.0 with 8 averages. The CS-reconstructed maps in both cases showed improved SNR and greater similarity to the fully-sampled reference (8 averages) compared to the denoised fully-sampled data, especially for REPSI.

	Full (4 avg., denoised)		AF = 1.5x (6 avg)		AF = 2x (8 avg)	
	REPSI	EPSI	REPSI	EPSI	REPSI	EPSI
tNAA	27.1	30.6	13.2	16.7	13.4	21.7
Cr	25.7	43.0	12.7	16.0	12.7	23.9
tCho	25.5	98.5	11.5	103.0	14.0	93.3
Glx	38.3	92.4	21.3	84.3	21.6	67.1
mI	30.6	27.7	18.3	17.0	17.4	28.1
SNR	9.2 ± 7.8	7.4 ± 5.3	4.7 ± 4.1	5.2 ± 3.4	5.5 ± 4.6	5.6 ± 3.9

	Full (3 avg., denoised)		AF = 2x (6 avg)	
	REPSI	EPSI	REPSI	EPSI
tNAA	28.7	21.2	14.2	22.5
Cr	27.2	26.7	15.3	29.7
tCho	27.6	38.3	16.3	270.7
Glx	43.6	35.9	23.1	26.8
mI	32.1	28.6	15.6	31.8
SNR	8.5 ± 7.7	6.5 ± 5.1	5.3 ± 4.3	4.8 ± 3.6

	Full (2 avg., denoised)		AF = 1.5x (3 avg)		AF = 2x (4 avg)		AF = 2.5x (5 avg)		AF = 3x (6 avg)		AF = 4x (8 avg)	
	REPSI	EPSI	REPSI	EPSI	REPSI	EPSI	REPSI	EPSI	REPSI	EPSI	REPSI	EPSI
tNAA	31.9	23.6	17.9	16.5	15.5	20.2	18.5	31.9	18.5	35.5	26.5	22.1
Cr	32.1	28.4	13.5	21.8	19.2	24.5	16.8	36.1	21.4	34.7	27.3	24.0
tCho	29.6	41.9	19.9	29.4	19.3	66.0	20.1	34.4	22.0	46.5	23.9	31.4
Glx	43.1	38.2	21.9	347.8	25.0	27.1	27.7	36.1	27.7	42.5	29.7	33.3
mI	33.9	32.3	18.8	28.1	19.3	22.9	19.6	42.4	22.2	40.0	26.1	27.6
SNR	7.2 ± 7.1	5.5 ± 4.3	3.2 ± 3	3.4 ± 2.6	4 ± 3.7	4.3 ± 3	4.8 ± 4.1	4 ± 3.3	5.2 ± 4.7	4.2 ± 3.7	6.5 ± 5.2	5.9 ± 5

	Full (1 avg., denoised)		AF = 2x (2 avg)		AF = 3x (3 avg)		AF = 4x (4 avg)	
	REPSI	EPSI	REPSI	EPSI	REPSI	EPSI	REPSI	EPSI
tNAA	34.9	27.0	18.7	23.7	22.7	34.2	30.8	26.4
Cr	35.5	33.2	22.7	22.3	27.1	33.4	30.9	42.6
tCho	36.0	188.5	22.2	31.6	25.1	133.7	26.7	157.3
Glx	51.4	309.5	23.0	161.6	27.0	38.7	29.2	111.2
mI	37.5	36.7	26.1	33.7	23.2	46.3	29.4	28.5
SNR	5.7 ± 5.7	4.3 ± 3.3	2.9 ± 2.8	2.9 ± 2.2	3.9 ± 3.4	3.4 ± 2.9	4.3 ± 4.1	5 ± 3.7

Table 3-4**:** Normalized root-mean square error (nRMSE) values of reconstructions from time-equivalent, fully-sampled EPSI and REPSI acquisitions versus nRMSE values from CS reconstruction of time-equivalent accelerated data with different numbers of averages.

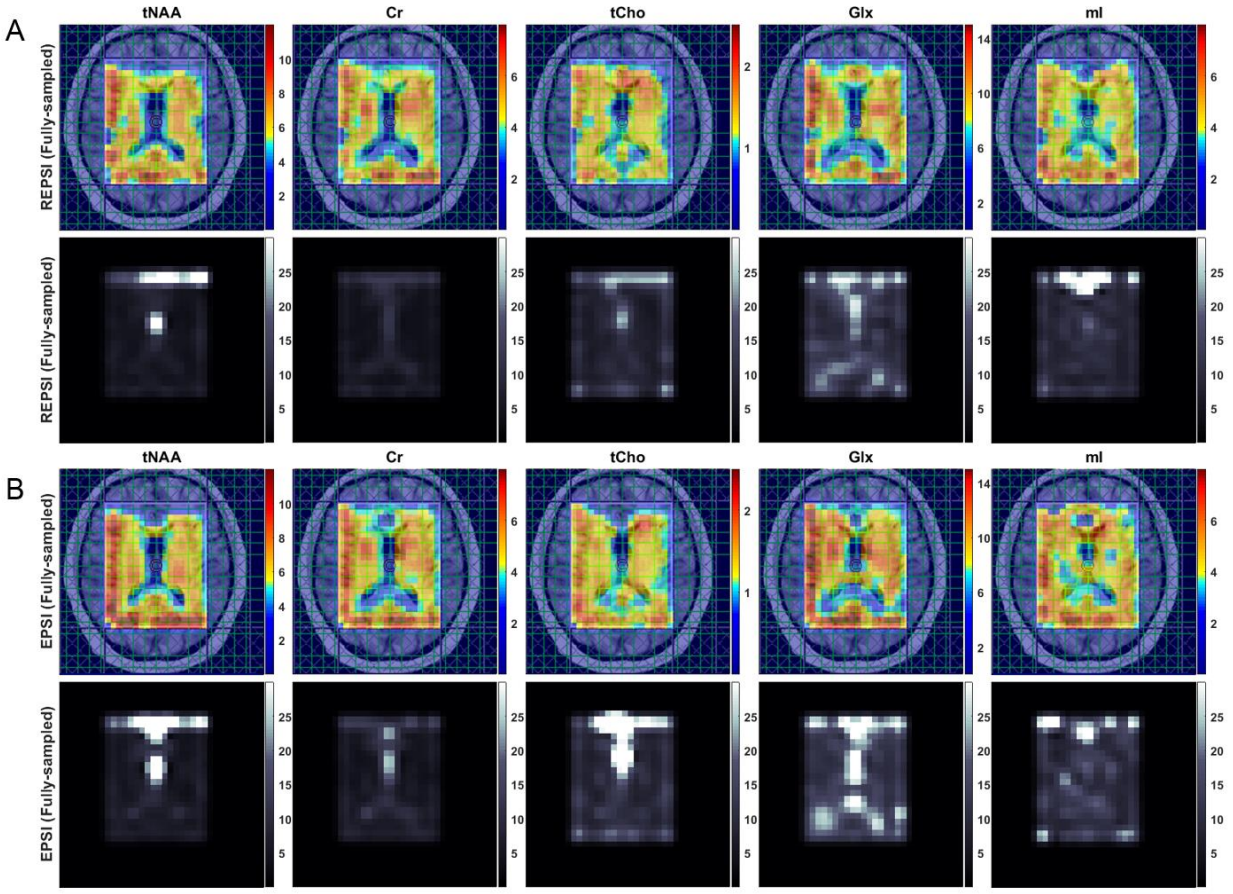

Figure 3-10**:** (A) Metabolite maps of tNAA, Cr, tCho, Glx, and mI (upper row) from fully-sampled reconstructions of REPSI brain data from a healthy 34 year-old male volunteer, and the respective CRLB maps (bottom row). (B) Fully-sampled EPSI reconstructions of tNAA, Cr, tCho, Glx, and mI metabolite maps (upper row) with the corresponding CRLB maps (bottom row). Note the higher intensities in the EPSI CRLB maps, indicating that REPSI produces more reliable metabolite concentration estimates, in part due a relatively high SNR's. All maps are interpolated by a factor of two.

3.4.4 Lipid Contamination in Radial and Cartesian EPSI

We show the tNAA map and a representative spectrum before and after the lipid-suppression from the EPSI (Figure 3-11(A)) and the REPSI (Figure 3-11(B)) reconstructions. As seen in both cases, the metabolite maps improve in both the CS-reconstructed and fully-sampled data, where more frontal voxels in the REPSI tNAA maps were able to be quantified by LC model

after the lipid-suppression. The spectra also show significant reductions of the lipid peak near NAA, especially in the REPSI case. Notably, the tNAA maps before and after lipid-removal are qualitatively very similar, for both the fully-sampled and CS reconstructions, and the lipid signal did not result in prominent artifacts. The CS algorithm applied to the lipid-contaminated data did not produce spectra in which the non-lipid signals are excessively attenuated. Since the proposed CS method avoids applying the TV operation along the spectral domain, the tendency of the reconstruction to weight the larger lipid or residual water signals more strongly than the lower SNR metabolites is reduced. This can be seen by the REPSI reconstruction of the prospectively undersampled data in Figure 3-12 (and Figure 3-5), where the CS-reconstructed spectra retain good fidelity to the fully-sampled spectra, before and after lipid-removal.

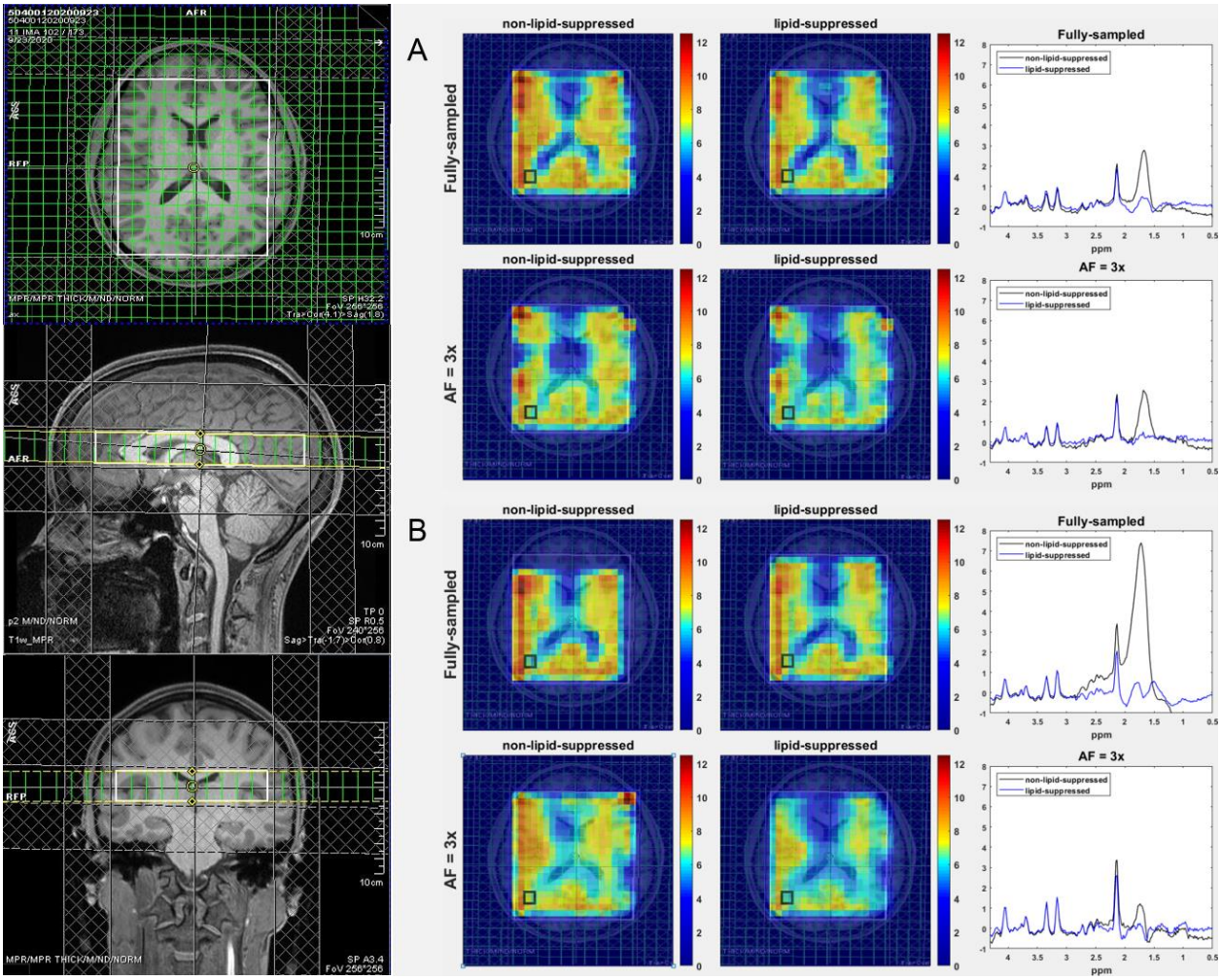

Figure 3-11**:** (A) (Left column): Fully sampled and accelerated (AF = 3x) non-lipid-suppressed EPSI tNAA metabolite map reconstructions from an in vivo brain dataset acquired with a larger VOI that encompasses the intracranial lipids at the corners. (Middle column): metabolite maps reconstructed after using an L_2-minimization-based lipid suppression algorithm by Bilgic et al. (Right column): reconstructed spectra for fully-sampled and accelerated acquisitions (AF = 3x) before and after lipid-suppression in post-processing. (B) Same as (A) except for REPSI. The metabolite maps are interpolated by a factor of two.

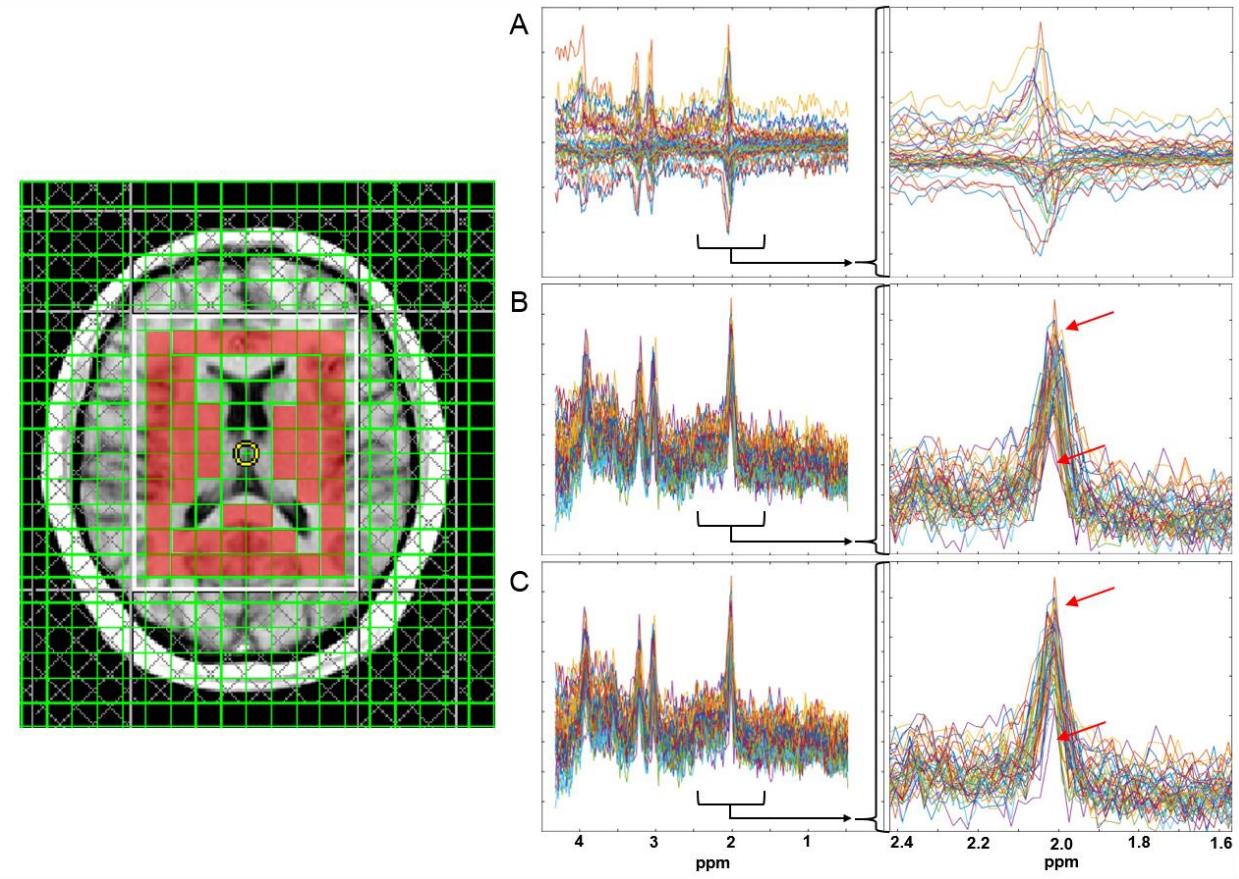

Figure 3-12**:** Overlaid in vivo brain spectra from the voxels within the volume-of-interest (highlighted in red), shown on the localization image (left). (A) Spectra with no eddy current or frequency drift corrections. (B) Spectra shown with only eddy current phase correction using Klose's method. (C) Spectra shown with eddy current phase correction and with frequency and phase drift corrections using FID-A.

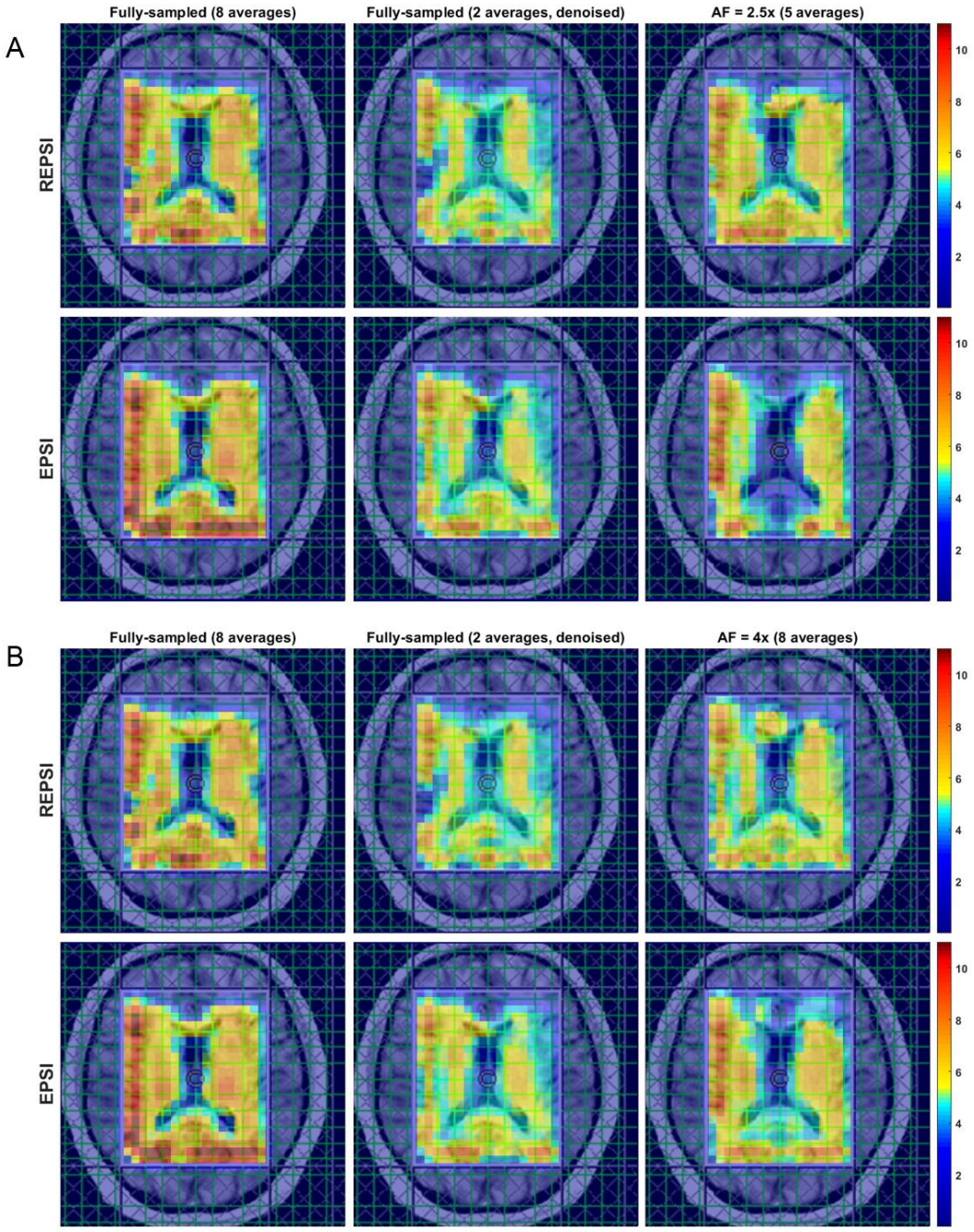

Figure 3-13**:** (A) (Left) REPSI and EPSI metabolite maps of tNAA from the fully-sampled reference (8 averages) compared to the maps from the fully-sampled, denoised reconstructions (middle) with 2 averages (denoised), and the maps from CS-reconstructions (right) at AF = 2.5 with 5 averages (B) (Left) Fully-sampled reference metabolite maps of tNAA (8averages), compared to the fully-sampled, denoised map (middle) with 2 averages versus the map from CS-reconstruction at AF = 4.0 with 8 averages. The CS-reconstructed maps in both cases showed improved SNR and greater similarity to the fully-sampled reference (8 averages) compared to the denoised fully-sampled data, especially for REPSI. All maps are interpolated by a factor of two.

3.4.5 REPSI acquisitions in Obstructive Sleep Apnea

Glx/Cr was significantly decreased (27%; $p<0.05$) in OSA vs. control in the left posterior insula. Other metabolites did not show significant differences. mI/Cr trends were consistent with previous findings (higher in OSA) and Lac/Cr trended higher in OSA.

This feasibility study showed that it is possible to measure multiple metabolites in multiple regions and detect effects of OSA. The accelerated technique enabled measurements to be completed in under 4 minutes.

3.4.6 Accelerated REPSI in Healthy Prostate with a Reduced Field-of-View

Table 3-5 shows that the Cho ratios from prospectively undersampled REPSI acquisitions are more consistent with those from the fully-sampled scans, compared to Cartesian EPSI. In a few cases, the percent errors are higher for REPSI but overall this error does not exceed 14%, whereas the percent error from Cartesian EPSI are as high as 76%. Overestimation and underestimation of the Cho ratios (e.g, Cr/Cho ~ 2.0 and Cit/Cho ~ 17) is possibly due to T_1 saturation and T_2 losses in the phantom. Figure 3-14 shows good REPSI and EPSI reconstructions from prospectively undersampled data, however the peak intensity decreases less in the REPSI case when AF = 2.0 & 2.5. The in vivo spectra and citrate maps in Figure 3-15 and Figure 3-16 also show greater stability in the reconstructions from retrospectively undersampled REPSI, with more benign undersampling artifacts in REPSI. The Cartesian EPSI maps degrade faster as the AF increases, particularly along the phase-encoding dimension, and can be more susceptible artifacts from subject motion. In Figure 3-15, the spectra and the citrate map in the VoI show good consistency with the fully-sampled results. Even at AF = 2.5, the REPSI citrate maps in Figure 3-16 and maintains the basic structures in the fully-sampled map, whereas the EPSI map at AF = 2.5 suffers an obvious signal loss in the lower right region.

(A)	AF = 1.0		AF = 1.5		AF = 2.0		AF = 2.5	
	REPSI	EPSI	REPSI	EPSI	REPSI	EPSI	REPSI	EPSI
Cr/Cho	0.9 ± 0.18	0.97 ± 0.27	0.81 ± 0.21	0.9 ± 0.2	0.89 ± 0.24	1.7 ± 2.89	0.92 ± 0.3	0.77 ± 0.28
mI/Cho	3.72 ± 0.48	3.46 ± 0.48	3.19 ± 0.88	3.36 ± 0.77	3.3 ± 1.21	6.09 ± 8.16	3.44 ± 1.11	3.3 ± 1.12
Spm/Cho	0.86 ± 0.32	0.71 ± 0.51	0.8 ± 0.3	0.9 ± 0.4	0.78 ± 0.27	0.66 ± 0.45	0.84 ± 0.36	0.62 ± 0.27
Cit/Cho	31.82 ± 2.48	28.71 ± 13.49	33.54 ± 5.27	34.38 ± 3.44	34.57 ± 3.9	30.29 ± 13.54	34.33 ± 4.03	37.12 ± 4.87

(B)	AF = 1.5		AF = 2.0		AF = 2.5	
	REPSI	EPSI	REPSI	EPSI	REPSI	EPSI
Cr/Cho	10.0	**7.2**	**1.1**	75.3	**2.2**	20.6
mI/Cho	14.2	**2.9**	**11.3**	76.0	7.5	**4.6**
Spm/Cho	**7.0**	26.8	9.3	**7.0**	**2.3**	12.7
Cit/Cho	**5.4**	19.7	8.6	**5.5**	**7.9**	29.3

Table 3-5: (A) Ratios of citrate (Cit), spermine (Spm), creatine (Cr), and myo-inositol (mI) with respect to choline (Cho), and their standard deviations, computed from CS-TV reconstructions of fully-sampled and prospectively undersampled REPSI and Cartesian EPSI datasets acquired in a prostate phantom. Note that the REPSI values are more consistent across all acceleration factors (AF). (B) Percent differences for the Cho ratios, taken with respect to the fully-sampled value.

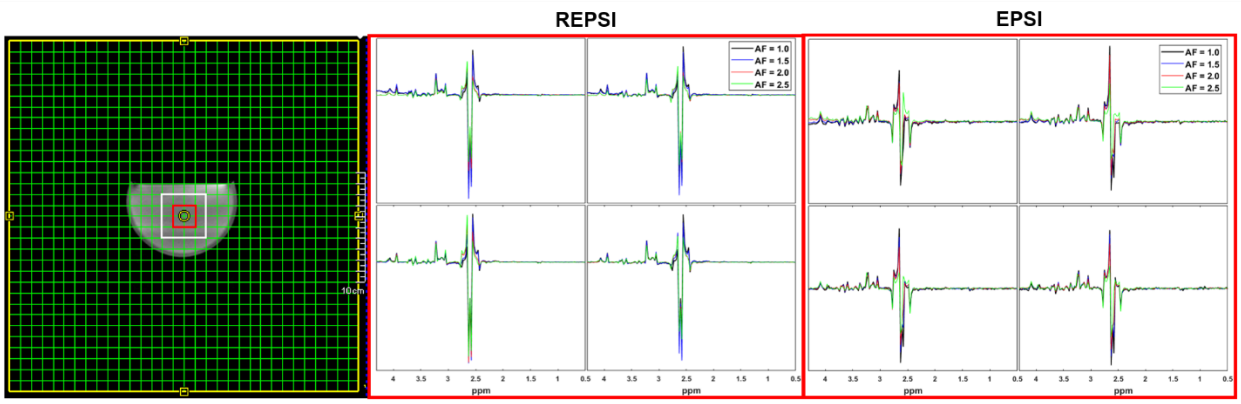

Figure 3-14: (Left panel) Localization image for the prostate phantom, showing a 320 x 320 mm^2 field-of-view and the inner 40 x 40 mm^2 volume-of-interest (VOI). The red box contains the inner 2 x 2 region whose spectra are shown at the right, to avoid signal variations at the edges of the VOI. (Middle and right panels) Multi-voxel spectra from CS-TV reconstructions of prospectively undersampled REPSI and EPSI phantom datasets, respectively, acquired at acceleration factors (AF) of 1.0 (fully-sampled), 1.5 (21 k_y-lines/spokes), 2 (16 ky-lines/spokes), and 2.5 (13 ky-lines/spokes).

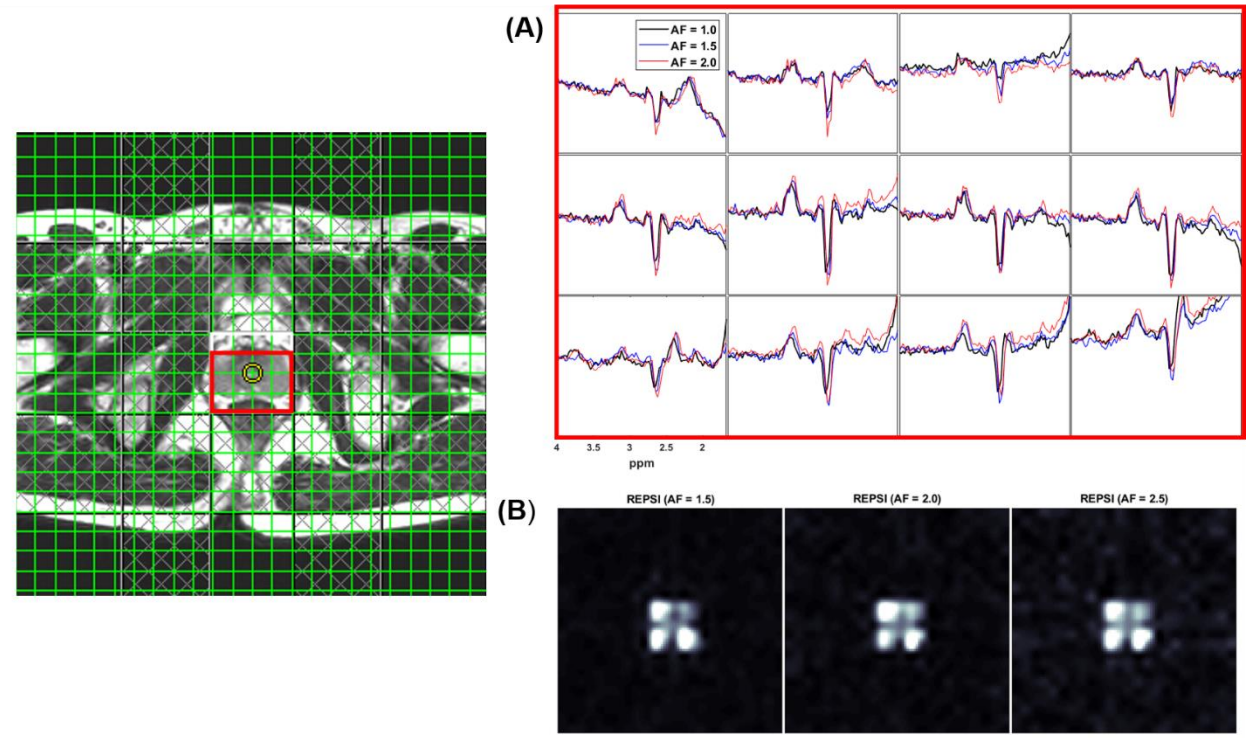

Figure 3-15: (A) Multi-voxel spectra from CS-TV reconstructions of prospectively undersampled REPSI data from an in vivo healthy prostate (31 year-old healthy volunteer), acquired with acceleration factors (AF) of 1.5, 2, and 2.5. The spectra correspond to the 3 x 4 region shown in the localization image, where the fat signal is least dominant. (B) Citrate maps (with baseline of fat subtracted) from CS-TV reconstructions of prospectively undersampled REPSI data, acquired with AF's of 1.5, 2, and 2.5.

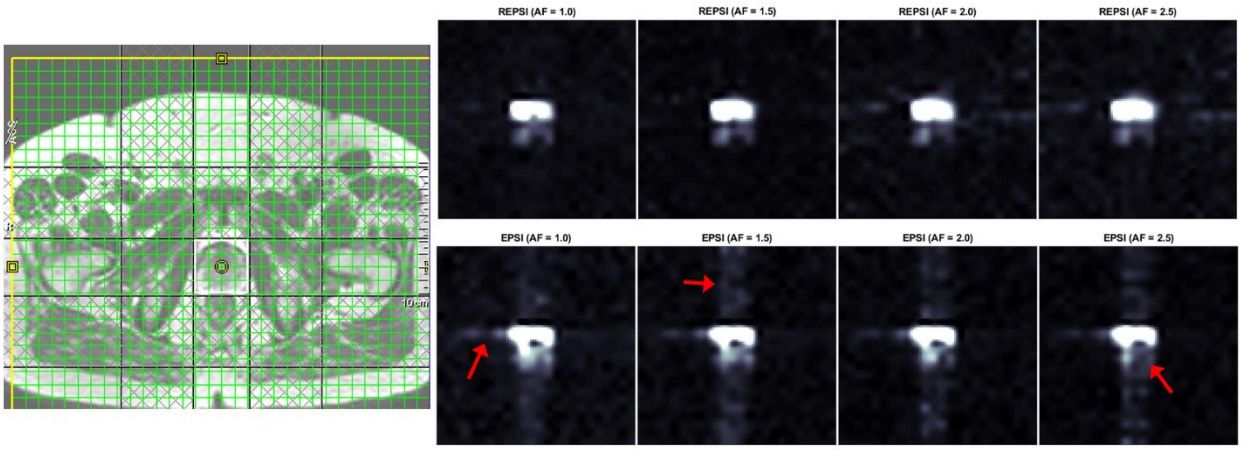

Figure 3-16: (Left) Localization image of the prostate from a 65 year-old healthy volunteer. (Right) Citrate maps from CS-TV reconstructions of retrospectively undersampled REPSI (top) and Cartesian EPSI (bottom), with acceleration factors (AF) of 1.0 (fully-sampled), 1.5, 2, and 2.5. The red arrows show that EPSI reconstructions have prominent aliasing artifacts across the phase-encoding dimension, especially as the AF increases, whereas the REPSI

reconstructions show relatively benign streaking. The REPSI citrate maps appear more consistent with the fully-sampled map.

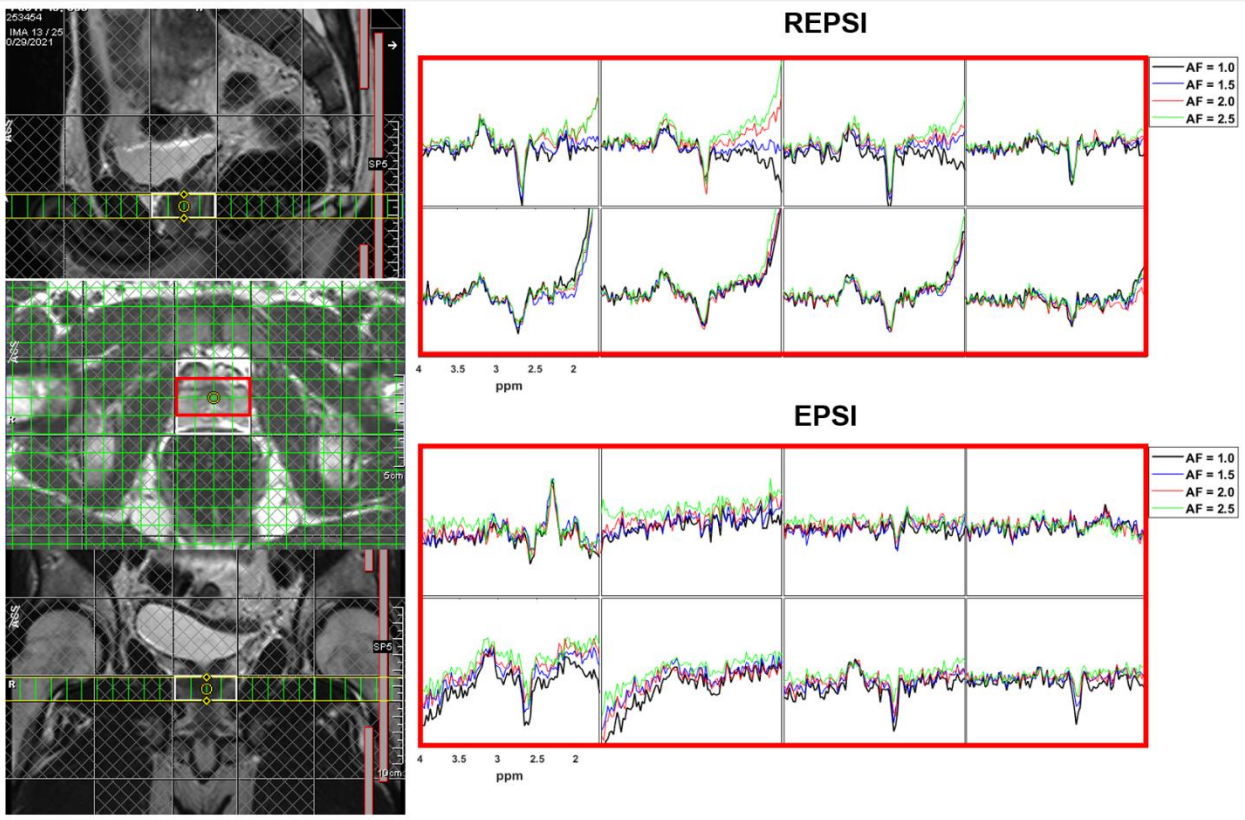

Figure 3-17: (Left) Localization images of the prostate from a 28 year-old healthy volunteer. The 2 × 4 box shows the region in which the spectra are shown (at right), where signal is least dominated by fat. (Right) Multi-voxel spectra from CS-TV reconstructions of retrospectively undersampled REPSI (top) and Cartesian EPSI (bottom), with acceleration factors (AF) of 1.0 (fully-sampled), 1.5, 2, and 2.5. Note that the REPSI spectra show and more prominent citrate peaks and are more consistent with the fully-sampled acquisition.

Evidently, REPSI can tolerate more acceleration and therefore may be better suited for faster acquisitions in the prostate, in which the anatomy is small compared to the nominal FoV. In the examples shown in the study, the scan time of 2D REPSI can be decreased from 7.5 minutes to 3-3.5 minutes without much loss in spectral quality, demonstrating the potential of reduced FoV MRSI for clinical prostate scans.

3.5 Discussion

3.5.1 Validation of REPSI for Accelerated ^{1}H Spectroscopic Imaging

We have shown that, in combination with CS, REPSI is able to tolerate greater reductions in scan time compared to EPSI. The findings confirm the potential of utilizing radial echo-planar *k*-space trajectories and compressed sensing for accelerated spectroscopic imaging. Quantitation of metabolites and spectroscopic imaging results from radial data were compared with those from CS-reconstructions of undersampled Cartesian echo-planar spectroscopic data, on a time-equivalent basis. Thus, the degree of reconstruction and quantitation accuracy as well as spectroscopic image quality of CS-reconstructions from undersampled EPSI and REPSI data were determined as a function of the scan time duration. All reconstruction and quantitation metrics – including spectral nRMSE maps, metabolite map nRMSE values, percent absolute difference maps, and concentration and CLRB estimates – show that accelerated REPSI provides a better trade-off between imaging speed and spectroscopic imaging quality, compared to the EPSI approach.

The comparisons are in the context of 2D spatial MRSI. Highly undersampling the 2D *k*-space along the single phase-encoding dimension produces imaging artifacts that spread predominantly along that dimension. In contrast, the undersampled radial *k*-space results in streaking artifacts that are distributed uniformly outside of a reduced field-of-view [51]. Thus, radially-undersampled 2D *k*-space is better suited for CS reconstruction, since these streaking artifacts are more similar to incoherent noise [22]. An additional advantage of radial sampling is that each spoke contains equal amounts of low and high spatial frequencies over k_y-k_x, unlike in Cartesian sampling which consistently samples the lowest spatial frequencies only along the readout direction. For these reasons, it is expected that the CS reconstructions of REPSI data would produce better results than those from EPSI data, particularly in the 2D case. However, radial

imaging is relatively more susceptible to spatial blurring due to off-resonance effects [52]. The slightly higher FWHM values of REPSI, particularly for fully-sampled data, is probably due to this limitation. Future studies need to be conducted to compare results from accelerated radial undersampling with those of Cartesian undersampling of two phase-encoding dimensions in 3D MRSI.

The *in vivo* brain REPSI results demonstrate the applicability of radial echo-planar trajectories for fast MRSI on a clinical scanner. Qualitatively, the tNAA metabolite map from the CS-reconstruction of radial data undersampled with 13 spokes still appears very similar to the fully-sampled tNAA map, while the EPSI result contains severe spatial artifacts. Further reductions in spokes or k_y-lines worsens both the REPSI and EPSI reconstructions. This observation implies that spectroscopic 2D imaging time can be reduced by approximately a factor of 2.5 relative to a fully-sampled Cartesian acquisition, but this can only be achieved with radial undersampling. Moreover, as shown in free-breathing liver acquisitions, the motion-robustness of radial sampling allows for measuring spectra with minimal motion-related artifacts from a free-breathing liver scan. This property, along with the self-navigating ability of radial sampling, allows for the possibility of mitigating spectral artifacts in applications affected by motion-induced phase errors, such as diffusion-weighted spectroscopic imaging [21].

One limitation of this work is that the reconstructions were done coil-by-coil, and separately for each odd and even echo. The reconstruction time was approximately 1.5 – 2 hours for a single 16-channel *in vivo* dataset. Previous reports in accelerated MRSI, such as in Chatnuntawech et al. [30] and Nassirpour et al. [29] utilized a combination of parallel imaging (PI) and CS to obtain good quality, high-resolution MRSI at high acceleration factors in relatively short reconstruction times. The work in [30] used spiral undersampling schemes to measure 3D MRSI at AF's of 4 – 4.5 with

high-resolution (voxel size 0.5 cc) and in [29] Cartesian undersampled FID-MRSI was applied to reconstruct matrices of up to 64 × 64 in 3 – 3.75 minutes. In our case, it is possible to use parallel computing and coil-compression [53] to reduce the computation overhead, and to adopt flyback trajectories [54,55] to avoid separate echo reconstructions. Future implementations will utilize a joint CS-PI approach [56], which requires a calibration scan. An advantage of radial sampling is that it is self-calibrating because it densely samples the central *k*-space, which is the most important data for estimating the coil sensitivities [57].

Another limitation of this work is that errors due to field inhomogeneity were not corrected in the CS reconstruction. Correction for B_0 inhomogeneity in non-Cartesian undersampled data has been shown in [58–61], in which the B_0 map can be incorporated into the undersampling operator to simultaneously correct for field inhomogeneity while performing the CS iterations. This approach requires a good low-resolution estimate of the field inhomogeneity map, which can be computed from the densely sampled central region of radial *k*-space. Future implementations will incorporate the B_0 map into the CS reconstruction pipeline. Some effects of B_0 inhomogeneity, such as frequency drift, can be corrected during post-processing [62,63(p),64]. In Figure 3A-5 in the Appendix, we show that a combination of Klose's correction for eddy-current-induced phase distortion, and frequency and phase alignment using the FID-A toolbox, can significantly improve the quality of the spectra and remove the frequency drifts among all spectra. Although lipid contamination is largely preventable with VOI-based excitation, it is possible to remove the lipid signal in post-processing using the L_2-based minimization technique by Bilgic et al. [65]. In Section 2 of the Appendix, we demonstrate the robustness of our CS technique to lipid signals originating from large prescriptions of the VOI that include the intracranial lipid layer.

3.5.2 Other Potential Acceleration Techniques using REPSI: Parallel Imaging

While this chapter demonstrated a compressed sensing technique for undersampled REPSI reconstructions, there are other acceleration methods that can be applied, such as parallel imaging. Parallel imaging techniques are often categorized as operating either in the image domain or in the k-space domain. Both types of approaches are related by the use of coil sensitivities or linear relationships among local k-space neighborhoods to estimate the missing k-space samples. With respect to the k-space based methods, calibration data is often required to estimate the k-space kernels that are used for synthesizing the missing data. This calibration data is usually acquired from the central k-space region, which corresponds to the lowest spatial frequencies that are also the most important for characterizing coil sensitivities. Therefore, since radial trajectories provide highly densely sampled central k-space acquisitions, REPSI is highly compatible with any type of parallel imaging method, without necessitating a separate calibration scan.

In the Appendix, we discuss an image domain-based parallel imaging method that exploits the local correlations among the coil images. The local correlations are modeled an enforced as low rank matrices. Since these image correlations are based on the underlying coil sensitivities, whose dominant spatial information is contained within the central, low-frequency k-space region, the application of this type of this parallel imaging approach is highly suitable for radial acquisitions, for which the balance between data consistency and local low-rankness can be more readily met due to the dense radial sampling of the central k-space. Although the Appendix focuses on the application of this technique to MRI acquisitions, the same conceptual framework can be applied for REPSI acquisitions, in which the low-rank enforcement of local coil images can be iterated across the spectral dimension. Chapter 6 proposes future work for adopting this locally low-rank, image domain-based parallel imaging method for accelerated spectroscopic imaging.

3.6 Conclusion

We demonstrated the potential benefits of accelerated 2D spectroscopic imaging using radial *k*-space undersampling and compressed sensing reconstruction with total variation regularization. Compared to CS-reconstructions of undersampled Cartesian EPSI data, REPSI provided greater reconstruction accuracy and more reliable quantitation for essentially all acceleration factors. Reconstruction results in the brain indicate that EPSI-based metabolite maps are much more degraded at the acceleration factor corresponding to 13 acquired k_y-lines, while REPSI still maintains reasonable image quality from the same number of spokes. The consequence is that the minimum scan time can be reduced by using the REPSI sequence, in the present example from 6 min 24 sec to 2 min 36 sec. Compared to the standard Cartesian approach and in combination with CS, radial undersampling is a promising approach to reduce scan time for 2D spectroscopic imaging.

Chapter 4 Single-Shot Diffusion Trace-Weighted MR Spectroscopy: Comparison with Unipolar and Bipolar DW-PRESS

4.1 Abstract

Purpose: Demonstrate the feasibility and performance of the PRESS-based, single-shot diffusion trace-weighted sequence in quantifying the trace apparent diffusion coefficient (ADC) in phantom and in vivo using a 3T MRI/MRS scanner, and compare results to trace ADC's derived from conventional diffusion-weighted PRESS sequences acquired with unipolar and bipolar diffusion gradient configurations.

Methods: The single-shot diffusion trace-weighted PRESS sequence was implemented and compared to DW-PRESS variants using bipolar and unipolar diffusion-sensitizing gradients, in vivo and in phantom. Nine phantom data sets were acquired using each sequence, and seven volunteers were scanned in three different brain regions to determine the range and variability of trace ADC values, and to allow a comparison of trace ADC's among the sequences.

Results: The single-shot trace sequence results in relatively stable range of trace ADC values that are statistically significantly higher than those produced from the unipolar and bipolar DW-PRESS sequences. Only tNAA, tCr, and tCho were reliably estimated in all sequences with CRLB's of at most 20%. The larger trace ADC from the single-shot sequences are likely due to the shorter diffusion time relative to the other sequences.

Conclusion: This study presents the first demonstration of the single-shot diffusion trace-weighted sequence in a clinical scanner at 3T, and we compare the trace ADC values obtained with this sequence to those computed from conventional DW-PRESS sequences with bipolar and unipolar diffusion gradients. Results show excellent agreement of phantom trace ADC's computed with all sequences, and in vivo ADC's agree well with the expected differences between gray and white matter. The diffusion trace-weighted sequence could provide an estimate of the trace ADC in a much shorter scan time (by nearly a factor of three) compared to conventional DW-PRESS approaches that require three separate orthogonal directions.

4.2 Introduction

Diffusion-weighted magnetic resonance spectroscopy (DW-MRS) is a powerful tool that is capable of non-invasively measuring the diffusion properties of various intra-cellular metabolites in vivo. Unlike water, which permeates both the intra- and extra-cellular spaces, most metabolites are confined within the intracellular space, so that their diffusion reflects the structure and function of tissues at the microscopic scale. Quantifying metabolite diffusion therefore provides information pertaining to cellular compartment size and chemical transport, and the degree of tissue tortuosity and viscosity [70,71]. Single voxel DW-MRS has shown changes in the apparent diffusion coefficients (ADC) of metabolites due to various pathologies such as ischemia and brain tumors [72–75], multiple sclerosis [76,77], and psychiatric disorders [78].

One of the major confounding factors in measuring the ADC is the effect of diffusion anisotropy. Generally, the ADC along any diffusion direction depends on the orientation of the subject with respect to the scanner frame of reference. To eliminate this bias, several studies have instead reported the trace of the diffusion tensor, which is an invariant quantity independent of the relative

orientation between the gradient axes and the volume of interest [79–81]. Conventional DW-MRS methods require at least three separate measurements along orthogonal diffusion directions to determine the trace ADC. This can be accomplished by applying the diffusion gradients separately along each gradient axis or by scaling the amplitude simultaneously along multiple axes according to the desired directions [74,79–82].

The additional diffusion-weighting from cross-term interactions between the diffusion-sensitizing, localization, and other background gradients can also bias the ADC quantitation [83,84]. One straightforward, although time-consuming, technique for removing this bias is to acquire an additional measurement with diffusion gradient amplitudes of opposite polarities [82]. The geometric mean of the diffusion-weighted signal from both polarities eliminates the cross-term contribution to the signal attenuation [84], thereby improving the accuracy of the estimated ADC. This approach can be used for any conventional DW-MRS sequence, including those incorporating bipolar (Figure 4-1A) or unipolar (Figure 4-1B) diffusion-sensitizing gradients within the PRESS [37] localization module. The bipolar scheme is known to minimize the cross-term contributions as well as eddy current effects, whereas the unipolar configuration (Figure 4-1B) generally does not share the same benefits [85–87]. A PRESS-based variant of the bipolar DW-MRS sequence has also been implemented using semi-LASER localization [81].

DW-MRS sequences based on PRESS, as opposed to sequences that use other localization schemes such as STEAM [88], are of particular interest because this class of sequences allows for a diffusion gradient configuration that generates a signal weighted by the trace of the diffusion tensor, within a single shot or TR. This single-shot diffusion trace-weighted scheme was originally proposed by Mori et al. for DW-MRI [89], and was later extended for DW-MRS by de Graaf [90]. The single-shot diffusion trace-weighted MRS sequence (from here on also referred to as “Trace DW-

PRESS") is able to eliminate all cross terms between diffusion gradients and any background gradients while providing a diffusion trace-weighted signal that is suitable for directly estimating the trace ADC, without any additional measurements along orthogonal diffusion directions. A version of this sequence using localization by adiabatic selective refocusing (LASER) was proposed by Valette et al. [2] using a small bore animal scanner. However, to date, the validation and performance of trace DW-MRS in humans has not been shown, although it has been implemented on a clinical scanner for DW-MRI only [91].

Another important consideration in DW-MRS is the dependence of the measured ADC on the diffusion time. Shorter diffusion times are known to produce higher estimates of metabolite ADC's in vivo. As the diffusion time decreases, the impact of structural restrictions on diffusion is reduced, and the mean displacements of the metabolites tend to approach those found in environments with unrestricted, free diffusion, resulting in a greater degree of signal attenuation [92]. Several reports have explored DW-MRS at short diffusion times (typically 1 – 10 ms or less) using oscillating sinusoidal gradients and have measured this relative increase in the trace ADC compared to DW-MRS with long diffusion times [93–95]. In the category of DW-MRS using pulsed gradients, the trace DW-MRS sequence is capable of much shorter diffusion times relative to the bipolar and unipolar alternatives, especially at long echo times. Generally, the echo times for trace DW-MRS must be relatively long (~140 ms) in order to accommodate the diffusion-sensitizing gradients within the PRESS localization module, and consequently the number of reliably detected metabolites is limited to the main groups of total n-acetylaspartate (tNAA), total creatine (tCr), and total choline (tCho).

In this chapter, we validate the single shot diffusion-trace pulse sequence in vivo and in a phantom on a clinical 3T scanner. This study presents the first demonstration of DW-MRS using

the single-shot diffusion trace sequence proposed by de Graaf [90], but which until recently had not been testable in humans due to earlier hardware limitations of clinical scanners. We report the in vivo trace ADC values of three main metabolite groups – total NAA, total Cr, and total Cho – and water, as well as six metabolites (NAA, Cr, Cho, Glu, mI, Lac) from a brain phantom, and compare these values to those measured with unipolar and bipolar PRESS DW-MRS schemes acquired with three orthogonal diffusion directions and positive and negative gradient polarities. In vivo results are shown from three different brain regions, and we tested for differences in trace ADC values across the different brain regions and pulse sequence variants.

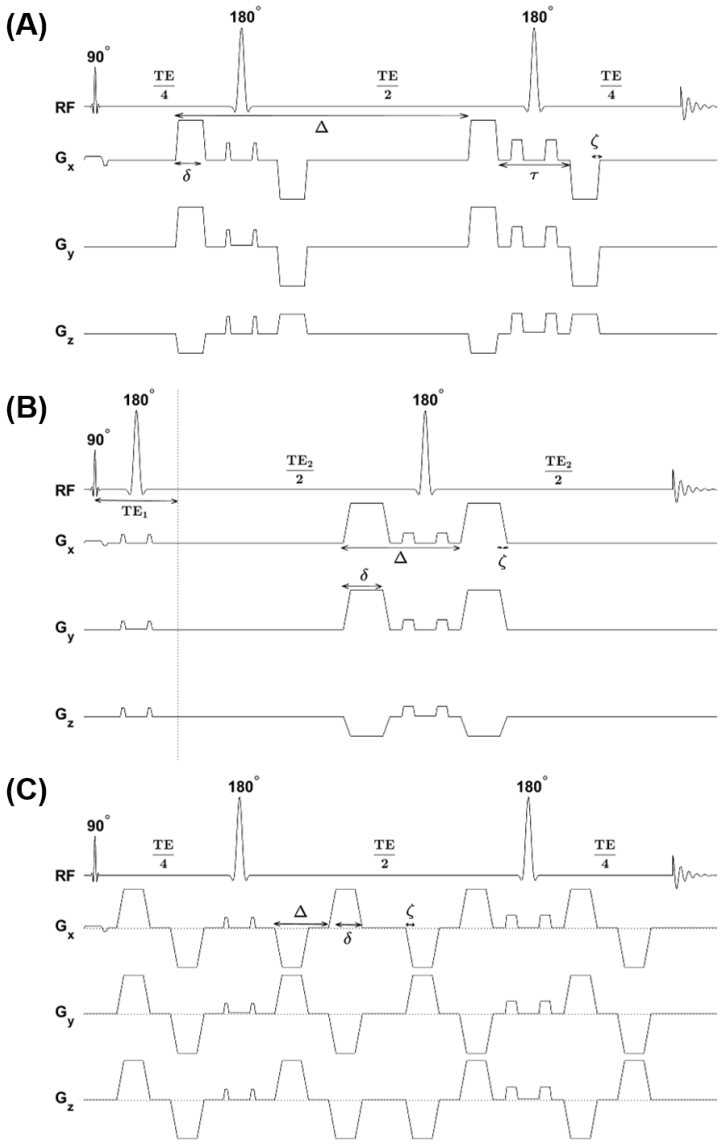

Figure 4-1: Pulse sequence diagrams for the **(A)** Bipolar, **(B)** Unipolar, and **(C)** the single-shot diffusion trace-weighted (Trace) DW-PRESS sequences. The configuration for direction 1 ([1.0, 1.0, -0.5]) is shown here for the Bipolar and Unipolar DW-PRESS sequences. In general, TE = TE_1 + TE_2 for PRESS sequences. For the Bipolar and Trace DW-PRESS sequences, TE_1 = TE_2 = TE/2. The unipolar sequence was implemented with the minimum TE_1 and the rest of the time evenly distributed within the TE_2 period.

4.3 Theory

4.3.1 The b-matrix and the Diffusion Tensor

The degree of signal attenuation from diffusing molecules is achieved by varying the b-value, which is primarily a function of the durations, amplitudes and temporal separations between the diffusion-sensitizing gradients, as well as all other localization and crusher gradients. A key component of the b-value computation is the gradient moment $\vec{F}(t')$:

$$\vec{F}(t') = \int_0^{t'} \vec{G}(t)\, dt \tag{4-1}$$

where $\vec{G}(t) \coloneqq \langle G_x(t), G_y(t), G_z(t) \rangle$ is defined as the vector of the applied time-varying gradients [96]. The matrix of b-values, $\boldsymbol{b}$, can then be defined as

$$\boldsymbol{b} = \gamma^2 \int_0^{\tau} \vec{F}(t') \otimes \vec{F}(t')\, dt' \tag{4-2}$$

where $\otimes$ denotes the outer product operation. Using this definition, the signal attenuation $S(\tau)$, after a time τ, can be described as

$$\ln\left(\frac{S(\tau)}{S_0}\right) = -\sum_{\alpha,\beta} \boldsymbol{b}_{\alpha\beta}\boldsymbol{D}_{\alpha\beta} \qquad \alpha, \beta \in \{x, y, z\} \tag{4-3}$$

where S_0 is the signal amplitude without diffusion-weighting and $\boldsymbol{D}$ is the diffusion tensor. It is important to note that both $\boldsymbol{b}$ and $\boldsymbol{D}$ are defined with respect to the same reference frame. For any arbitrary rotation, represented by matrix $\boldsymbol{R}$, the trace of the rotated diffusion tensor $\boldsymbol{D}'$ is preserved:

$$Tr(\boldsymbol{D}') = Tr(\boldsymbol{R}\boldsymbol{D}) = D'_{xx} + D'_{yy} + D'_{zz} = D_{xx} + D_{yy} + D_{zz} = Tr(\boldsymbol{D}) \tag{4-5}$$

This invariance under any unitary transformation makes the trace of the diffusion tensor a quantity which can more consistently reflect the diffusion characteristics of metabolites, regardless of the relative orientation of the patient with respect to the scanner frame of reference.

4.3.2 Cross Term Contribution to Diffusion-weighting

Apart from the applied diffusion-sensitizing gradients, other background gradients, such as those from B_0 inhomogeneity and susceptibility, as well as localization and crusher gradients, can cause an additional, unwanted diffusion-weighting. The total gradient $\vec{G}(t)$ can be represented as a summation of the diffusion-sensitizing ($\vec{G}_d(t)$) and the localization and background gradients ($\vec{G}_a(t)$): $\vec{G}(t) = \vec{G}_d(t) + \vec{G}_a(t)$. In Equation 4-2, the b-matrix becomes

$$\boldsymbol{b} = \gamma^2 \int_0^\tau \left[\vec{F}_d(t') \otimes \vec{F}_d(t') + \vec{F}_a(t') \otimes \vec{F}_d(t') + \vec{F}_d(t') \otimes \vec{F}_a(t') + \vec{F}_a(t') \otimes \vec{F}_a(t')\right] dt' \qquad (4\text{-}6)$$

The two inner terms are commonly referred to as cross terms between the diffusion and all other background gradients, which further contribute to the diffusion-weighting of the signal. The last term is usually relatively small and is considered negligible in practice [97]. Therefore, the b-matrix simplifies to

$$\boldsymbol{b} = \boldsymbol{b_d} + \boldsymbol{b_{ct}} \qquad (4\text{-}7)$$

where $\boldsymbol{b_d} = \gamma^2 \int_0^\tau \vec{F}_d(t') \otimes \vec{F}_d(t') dt'$ and $\boldsymbol{b_{ct}} = \gamma^2 \int_0^\tau \left[\vec{F}_a(t') \otimes \vec{F}_d(t') + \vec{F}_d(t') \otimes \vec{F}_a(t')\right] dt'$. The procedure for undoing this extra term in the diffusion-weighting is to compute the geometric mean of the signals (peak integrals) acquired with diffusion-sensitizing gradients of opposite polarities, since the sign of the $\boldsymbol{b_{ct}}$ term becomes negated and cancels out:

$$S_{geo}(b) = \left[S_{pos}(b) \cdot S_{neg}(b)\right]^{1/2} = \left[S_0 e^{-(b_d^+ + b_{ct})D} \cdot S_0 e^{-(b_d^- - b_{ct})D}\right]^{1/2}$$
$$= S_0 e^{-\frac{1}{2}(b_d^+ + b_d^-)D} \quad (4\text{-}8)$$

The effective b-value for the geometric mean is the average of the b-values from the negative and positive diffusion gradient polarities, b_d^- and b_d^+, respectively.

4.3.3 Diffusion Trace-weighted PRESS

Signal-weighting by the trace of the diffusion tensor provides an orientation-independent ADC measurement. Conventional DW-MRS approaches require relatively long scan times to acquire separate measurements along three orthogonal diffusion directions to determine the trace ADC. On the other hand, the single shot technique achieves diffusion-trace weighting in only one measurement, thereby reducing the total necessary scan time for trace ADC measurements.

The scheme first introduced by Mori et al. [89] applies sets of bipolar diffusion gradients of specific polarities such that any signal weighted by off-diagonal diffusion tensor elements is cancelled within a single TR. It can be shown that the particular configuration of the 12 sets of bipolar gradient lobes (interleaved with the PRESS localization) leads to the cancellation of signal weighted by off-diagonal terms in the diffusion tensor, i.e., in Equation 4-3, diffusion-weighting involving terms in the set $\{\boldsymbol{D}_{\alpha\beta} \mid \alpha \neq \beta\}$ are cancelled. Further details and examples of how these off-diagonal terms are cancelled in the computation in Equation 4-3 can be found in the aforementioned reports [2,89,90].

The contribution to the total diffusion-weighting from the cross terms between the diffusion-sensitizing and the localization and crusher gradients can heavily bias the ADC estimation, so it is important to minimize or eliminate this confounding factor when measuring

this quantity, especially in vivo. Since the bipolar diffusion gradient pairs in the Trace DW-PRESS sequence are isolated from the localization and crusher gradients, and the gradient-induced phase is rebalanced after each pair, the diffusion-weighting originating from cross-terms due to localization and crusher gradients is effectively null. Another feature of Trace DW-PRESS is that the inclusion of a second refocusing pulse allows for the elimination of any cross-terms originating between the static background gradients (such as those arising from B_0 inhomogeneity and susceptibility) and the diffusion-sensitizing gradients. The bipolar DW-MRS sequence (Figure 4-1A) also is known to minimize (not eliminate) cross terms [98], while the unipolar DW-MRS retains a large contribution from cross-terms due to any static background gradients (Figure 4-5).

4.3.4 Computing the b-matrix with respect to a given frame of reference

As mentioned previously, the conventional approach for estimating the trace ADC requires measurements along three orthogonal diffusion directions. For a given diffusion-sensitizing gradient amplitude G_d, a particular diffusion direction is achieved by scaling this amplitude along each gradient axis according to a directional vector, $\vec{n} = (n_x, n_y, n_z)$. As such, the diffusion gradient along the direction specified by $\vec{n}$ can be written as $\vec{G}_d = G_d \cdot \vec{n}$. When scaling the diffusion gradient amplitudes on each axis according to each vector within a given basis set, the diffusion tensor and b-matrix are consequently described with respect to that basis.

Usually, the three directional vectors are chosen to be an orthogonal basis, with a common set being $\beta = \{(1.0, 1.0, -0.5),\ (1, -0.5, 1),\ (-0.5, 1.0, 1.0)\}$. This set makes more efficient use of the gradients to reach a given b-value, compared to other choices such as the standard basis $\beta_0 = \{(1,0,0), (0,1,0), (0,0,1)\}$, for which the diffusion gradient is applied only along a single gradient axis per measurement. This standard basis is equivalent to the scanner frame of reference

in which the physical gradients are defined. The unitary transformation (change of basis) matrix $[Q]^{\beta}_{\beta_0}$ from the β_0 to β frame is

$$[Q]^{\beta}_{\beta_0} = \frac{1}{3}\begin{pmatrix} 2 & 2 & -1 \\ 2 & -1 & 2 \\ -1 & 2 & 2 \end{pmatrix}$$

The b-matrix, $\boldsymbol{b}$, for the trace DW-PRESS sequence, computed with respect to β_0, is a diagonal matrix when neglecting all non-diffusion-sensitizing gradients, since all off-diagonal diffusion tensor terms are cancelled. Inclusion of localization and crusher gradients only adds extremely small off-diagonal terms as the amplitudes of these gradients are usually much smaller than those of the diffusion-sensitizing gradients.

However, it is important to note that when performing the computation in Equation 4-2 with respect to the β frame, by replacing $\vec{G}(t)$ with $\vec{G}'(t) = Q\vec{G}(t)$, the b-matrix for the trace DW-PRESS is preserved. That is,

$$[\boldsymbol{b}]_{\boldsymbol{\beta}} = \gamma^2 \int_0^{TE} \left(\int_0^{t'} Q\vec{G}(t)dt\right) \otimes \left(\int_0^{t'} Q\vec{G}(t)dt\right) dt' = \gamma^2 \int_0^{TE} \left(\int_0^{t'} \vec{G}(t)dt\right) \otimes \left(\int_0^{t'} \vec{G}(t)dt\right) dt' = [\boldsymbol{b}]_{\boldsymbol{\beta_0}}$$

This is generally not the case for the b-matrices computed for the bipolar and unipolar DW-PRESS sequences. The b-matrix for these sequences have diagonal and off-diagonal entries when computed in the standard β_0 frame, although these matrices naturally become diagonal in the β frame, with only one diagonal entry, depending on the particular diffusion direction $\vec{n} \in \beta$ assumed in Equation 4-2.

4.3.5 Diffusion times and b-values for the Bipolar, Unipolar, and Trace DW-PRESS

Based on the formalism presented in [96], and referring to Figure 4-1, the analytic b-value for the bipolar sequence (neglecting the localization and crusher gradients) can be derived (see Appendix) as

$$b = \gamma^2 \left\|\vec{G}_d\right\|^2 (2\delta)^2 \left\{\left(\Delta - \frac{2\delta}{3} - \frac{\tau}{2}\right) - \frac{\zeta}{6\delta}\left[\left(3\delta + \frac{\zeta}{2}\right) - \frac{\zeta^2}{5\delta}\right]\right\} \quad (4\text{-}9)$$

where $\left\|\vec{G}_d\right\|$ is the magnitude of the diffusion gradient vector applied along the direction specified by $\vec{n}$ ($\vec{G}_d = G_d \cdot \vec{n}$), and G_d is the amplitude. Based on this formula, the effective diffusion time is

$$t_d = \left(\Delta - \frac{2\delta}{3} - \frac{\tau}{2}\right) - \frac{\zeta}{6\delta}\left[\left(3\delta + \frac{\zeta}{2}\right) - \frac{\zeta^2}{5\delta}\right] \quad (4\text{-}10)$$

The following formula

$$b = N \gamma^2 \left\|\vec{G}_d\right\|^2 \delta^2 \left[\left(\Delta - \frac{\delta}{3}\right) - \frac{1}{6}\left(\frac{\zeta}{\delta}\right)^2 \left(\delta - \frac{\zeta}{5}\right)\right] \quad (4\text{-}11)$$

gives the analytic b-value for the unipolar (N = 1) and the single-shot trace-weighted (N = 4) sequences. For the trace-weighted sequence, the directional vector is always $\vec{n} = (1.0, 1.0, 1.0)$, since the diffusion gradient amplitudes must be the same along all axes. For the unipolar and trace-weighted sequences (Figure 4-1B and 4-1C), the diffusion time can be derived analytically from the generic b-value equation for a pair of trapezoidal gradients [6]:

$$t_d = \left(\Delta - \frac{\delta}{3}\right) - \frac{1}{6}\left(\frac{\zeta}{\delta}\right)^2 \left(\delta - \frac{\zeta}{5}\right) \quad (4\text{-}12)$$

The analytic b-value formulas presented above assume no localization and crusher gradients. The diffusion times given above are effectively the "reduced" diffusion times that are appropriate for trapezoidal diffusion-sensitizing gradients [99,100].

4.4 Methods

All measurements were made using a Siemens Prisma 3T scanner (Siemens Healthcare, Munich, Germany) with a maximum net slew rate limit of 200 mT/m/ms and a maximum gradient amplitude limit of 80 mT/m per axis. A 16-channel receive head coil was used for both the phantom and in vivo acquisitions. Localization of the entire phantom or brain volume was achieved with T_1-weighted axial, coronal, and sagittal two-dimensional MRI's acquired with TR/TE = 250 ms/2.49 ms, FOV = 240 × 240 mm^2, 1.25 × 1.25 mm^2 in-plane resolution, and 35 slices of 4 mm thickness each.

For all DW-PRESS acquisitions, the voxel size was 25 × 25 × 25 mm^3, TR = 2 s, and TE = 140 ms. The spectral width was 1250 Hz with 1024 time points. The offset frequency for the RF pulses was set at -2.3 ppm relative to water to minimize chemical shift misregistration. Global water suppression was achieved using a WET module [39]. Non-water suppressed data was acquired for eddy current phase correction [44], coil sensitivity estimation, and for computing the water ADC.

For Bipolar and Unipolar DW-PRESS, three orthogonal diffusion directions were measured. These directions correspond to the vectors [1.0, 1.0, -0.5] (direction 1), [1.0, -0.5, 1.0] (direction 2), and [-0.5, 1.0, 1.0] (direction 3). To eliminate bias due to cross terms, both negative and positive gradient polarities were acquired. The average of the b-values from the negative and positive gradient polarities were taken for calculating the cross-term compensated trace ADC's

from the geometric means of the signals. All b-values were computed with numerical integration using the actual chronograms and gradient parameters implemented in the sequences.

		b-values (s/mm^2)				
		b_0	b_1		b_2	
			pos	neg	pos	neg
BIPOLAR	dir 1	4	1006	1026	1704	1731
	dir 2		1005	1027	1703	1732
	dir 3		1006	1026	1705	1731
UNIPOLAR	dir 1	4	1034	954	1749	1644
	dir 2		1034	953	1750	1643
	dir 3		1034	953	1750	1644
TRACE		4	1020		1707	

Table 4-1: Table of b-values for each sequence used in this study. Note the relatively large difference in the computed b-values between the positive and negative diffusion gradient polarities for the Unipolar DW-PRESS sequence. For calculating the ADC in each direction, the average of the b-values from the positive and negative gradient polarities were used for fitting the geometric mean of the corresponding diffusion-weighted signals.

4.4.1 Phantom Data Acquisitions

The GE "Braino" phantom (GE Medical Systems, Milwaukee, WI, USA), containing N-acetylasparate (NAA, 12.5 mM), creatine (Cr, 10.0 mM), choline (Cho, 3.0 mM), Glutamate (Glu, 12.5 mM), myo-inositol (mI, 5.0 mM), and Lactate (Lac, 5.0 mM) was used for all phantom acquisitions. The ADC's of the GE Braino metabolites were reported by Landheer et al. [101]. The voxel was positioned at the center of the phantom which was placed at isocenter.

Three b-values – null (b_0), medium (b_1), and high (b_2) – were measured for phantom scans: b_0 = 4 s/mm^2, b_1 = 994 – 1,021 s/mm^2, and b_2 = 1,697 – 1,718 s/mm^2. For these b-values, the corresponding diffusion-sensitizing gradient amplitudes for each sequence were as follows: (i)

Bipolar – 0, 24.9, 32.4 mT/m; (ii) Unipolar – 0, 52, and 68 mT/m; (iii) Trace – 0, 51, 66 mT/m. For a fixed TE, the trace-weighted sequence is less efficient at reaching higher b-values than the other sequences. The unipolar sequence has marked differences in the computed b-value from the negative and positive diffusion gradient polarities (Table 4-1).

The diffusion gradient parameters for each sequence (Figure 4-1) were as follows: (i) Bipolar – ζ = 700 μs, δ = 6.7 ms, Δ = 70 ms, τ = 17.6 ms; (ii) Unipolar – ζ = 1.5 ms, δ = 9.5 ms, Δ = 28.6 ms; (iii) Trace – ζ = 1.5 ms, δ = 6.5 ms, Δ = 13 ms. At the largest b-value, the bipolar and unipolar DW-PRESS sequences had net slew rates of 69.4 mT/m/ms and 68 mT/m/ms, respectively, while the trace-weighted sequence had a net slew rate of 76.2 mT/m/ms. For the given gradient amplitudes, the ramp times were chosen to in order to limit the slew rate of the Unipolar and Trace DW-PRESS sequences, which could not exceed 79.6 mT/m/ms due to scanner-imposed nerve stimulation limits for in vivo scans.

The diffusion times for the bipolar and unipolar sequences were 58.8 ms and 25.2 ms, respectively, and the diffusion time for the trace-weighted sequence was 10.8 ms.

The water-suppressed acquisitions had 20, 36, and 52 averages with corresponding non-water suppressed averages of 4, 6, and 8 averages, for the null, medium, and high b-values, respectively. The average linewidth of the water magnitude peak after manual shimming was 4.6 Hz.

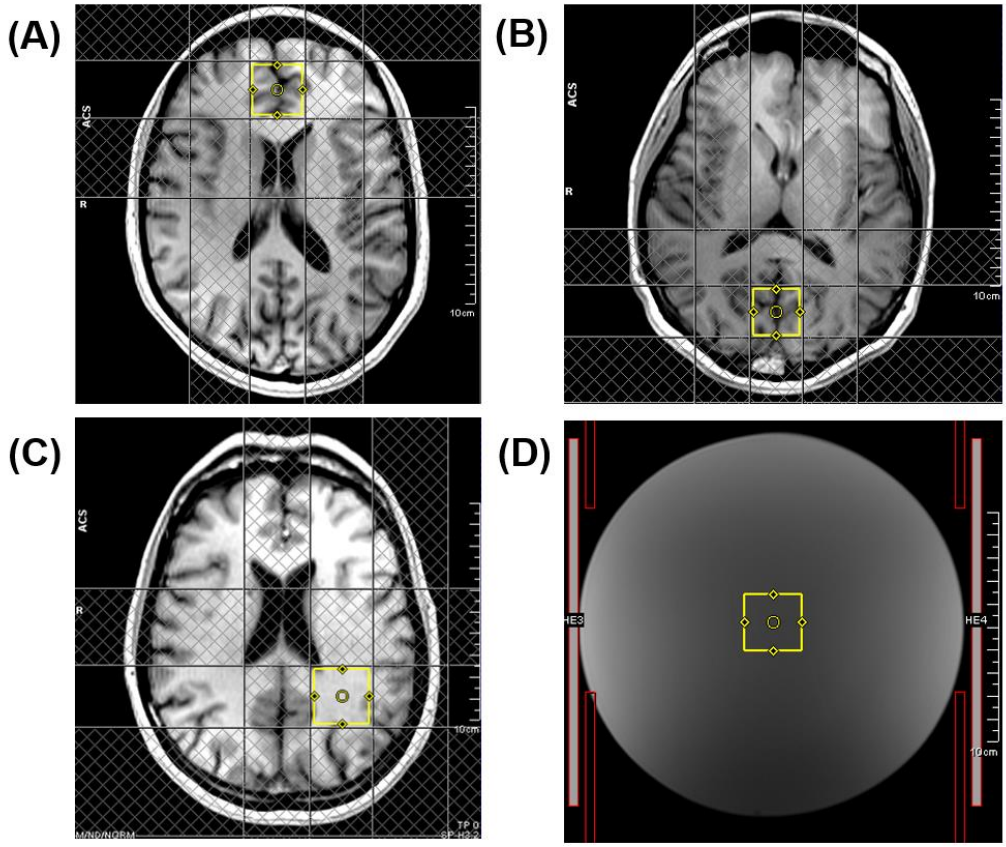

Figure 4-2: In vivo localization images for **(A)** frontal gray matter (FG) **(B)** occipital gray matter (OG), and **(C)** occipital (subcortical) white matter (OW). The panel in **(D)** shows voxel placement in the GE Braino phantom.

4.4.2 In Vivo Data Acquisitions

A total of 14 healthy volunteers (6 females and 8 males, ages = 39.9 ± 16 years) were recruited to participate in this study and gave informed consent according to local institutional review board guidelines. A subset of these volunteers was scanned no more than two times but in different brain regions. Three different brain regions (Figure 4-2) were probed with each sequence – the frontal gray (FG) matter from the prefrontal lobe, occipital gray (OG) matter, and occipital (subcortical) white (OW) matter.

Data from all three sequences were acquired during the same scan session. Only two b-values were acquired from the Bipolar and Unipolar DW-PRESS sequences, due to scan time limitations – one null b-value of approximately 4 s/mm^2 (b_0) and a higher b-value (b_2) of 1,697 – 1,718 s/mm^2. The null b-value data (with diffusion gradients set to zero) were acquired with 28 and 4 averages for water-suppressed and non-water-suppressed data, respectively. Diffusion-weighted spectra were acquired with 56 and 8 averages for the water-suppressed and non-water-suppressed data, respectively. For the Bipolar and Unipolar DW-PRESS sequences, spectra from three orthogonal directions and with negative and positive diffusion gradient polarities were acquired, resulting in a scan time of 13 minutes, 52 seconds for 7 measurements (1 null and 6 diffusion-weighted).

In contrast, three b-values were acquired for the diffusion trace-weighted sequence – one null b-value of approximately 4 s/mm^2 (b_0), a medium b-value of 1,021 s/mm^2 (b_1), and a higher b-value (b_2) of 1,707 s/mm^2. The same number of averages were acquired as for the Bipolar and Unipolar DW-PRESS sequences for b_0 and b_2. For b_1, 44 and 6 averages were acquired for the water-suppressed and non-water-suppressed data, respectively. The scan time for the Trace DW-PRESS acquisition was 4 minutes, 45 seconds.

The average linewidths of the water magnitude peak after manual shimming was 18.2 Hz, 13.8 Hz, and 12.8 Hz, for the frontal gray, occipital gray, and occipital (subcortical) white matter brain regions, respectively.

The total scan time for one in vivo session (Bipolar, Unipolar, and Trace DW-PRESS acquisitions) - including localization, shimming, and other sequence preparations – was approximately 50 minutes

4.4.3 Determining the effects of eddy-currents

The extent of the influence of eddy currents on the signal was quantified by measuring the standard deviation (SD) of first order phase correction for the NAA peak before subtracting the reference water phase from the FID, and before coil-combination. The spectrum from the dominant coil element was used. The maximum coil element was determined as the coil with the greatest water peak integral in the water-unsuppressed data, which also had sufficient NAA SNR to allow a reliable phase determination. A similar approach for measuring eddy current effects was taken recently by Hanstock et al. [102].

This analysis was done on phantom data from all sequence types, since the phantom measurements were not influenced by confounding factors such as thermal noise, motion, and variability in localization – all of which could present additional sources of phase variation in vivo. Additionally, only the spectrum from the coil with maximum signal was used, since this analysis was done on uncombined coil data. Using a least-squares algorithm, the optimal phase φ_0 for placing the real part of the NAA peak in absorptive mode was formulated as the minimization

$$\varphi_0 = \underset{\varphi}{\operatorname{argmin}} \frac{1}{2} \left\| |Y| - Ye^{i\varphi} \right\|_2^2 \tag{4-13}$$

where Y is the portion of the measured spectrum in the range of the NAA singlet (1.8 – 2.2 ppm) and $|Y|$ is the magnitude. Prior to the least-squares procedure, linear baseline was subtracted. The SD of the zero-order phase φ_0 was computed from across all measurement for each type of sequence and for each b-value.

4.4.4 Determining the effects of diffusion-weighting from cross terms

The water-unsuppressed phantom data from the bipolar and unipolar DW-PRESS sequences was used for determining the degree to which cross-terms cause additional signal attenuation. The water peak in magnitude mode was integrated over a frequency range containing a water signal level above at least 1% the maximum peak height. This integral was computed for all three directions and for both polarities. Large differences in the water peak area between negative and positive polarities would indicate a strong contribution from cross terms. This approach for determining the effects due to cross terms is similar to those found in other reports [82,103].

4.4.5 Post-processing

Several reports have emphasized the importance of correcting the diffusion-weighted signal before any quantitative analysis [79,80,104–109]. The diffusion-sensitizing gradients, along with pulsatile motion in the brain, render the signal more susceptible to large phase variations from shot to shot. Therefore, it is crucial to apply 0^{th} order phase corrections as well as frequency drift corrections to the data before signal averaging (Figure 4-3). The residual water or another dominant peak, such as the NAA singlet, can serve as a reference for phasing the signal and determining the amount of frequency drift. No cardiac gating or ECG triggering was used in this study, similar to other reports [79,80,102].

Initially, eddy current phase correction was implemented using the non-water-suppressed data [44]. Using a least squares algorithm [Equation 4-13], the optimal zero-order phase for the NAA peak was determined for each average and coil, and this constant phase was subsequently applied to the entire spectrum. The coil sensitivities were estimated from the water peak integrals of the water-unsuppressed data. Generalized least squares coil combination [110] was then applied. The

amount of frequency shift was estimated using a cross-correlation algorithm with the NAA peak from the first average as a reference. Following the frequency drift correction, the individual averages with NAA peak SNR's less than 90% of the average NAA peak SNR were removed. Before averaging, a final frequency drift Δf_i and zero-order phase φ_i correction for each average were computed using a non-linear least squares algorithm [46]

$$\Delta f_i, \varphi_i = \underset{\Delta f, \varphi}{\operatorname{argmin}} \frac{1}{2} \left\| \tilde{y} - y_i e^{i\varphi + i2\pi\Delta f t} \right\|_2^2 \tag{4-14}$$

where y_i is the time signal of the i^{th} average, and $\tilde{y}$ is the average that is most similar (in terms of room mean square error) to the other averages within the same set.

Finally, the signals were averaged and the residual water was removed using the Hankel-Lanczos singular value decomposition algorithm [48]. These corrective procedures were necessary to phase and frequency align each individual spectrum to maximize the SNR before the final averaging and quantitation and to remove, by signal SNR thresholding, spectra overly affected my motion and other artifacts. All spectra were processed using MATLAB (MathWorks, Natick, MA, USA).

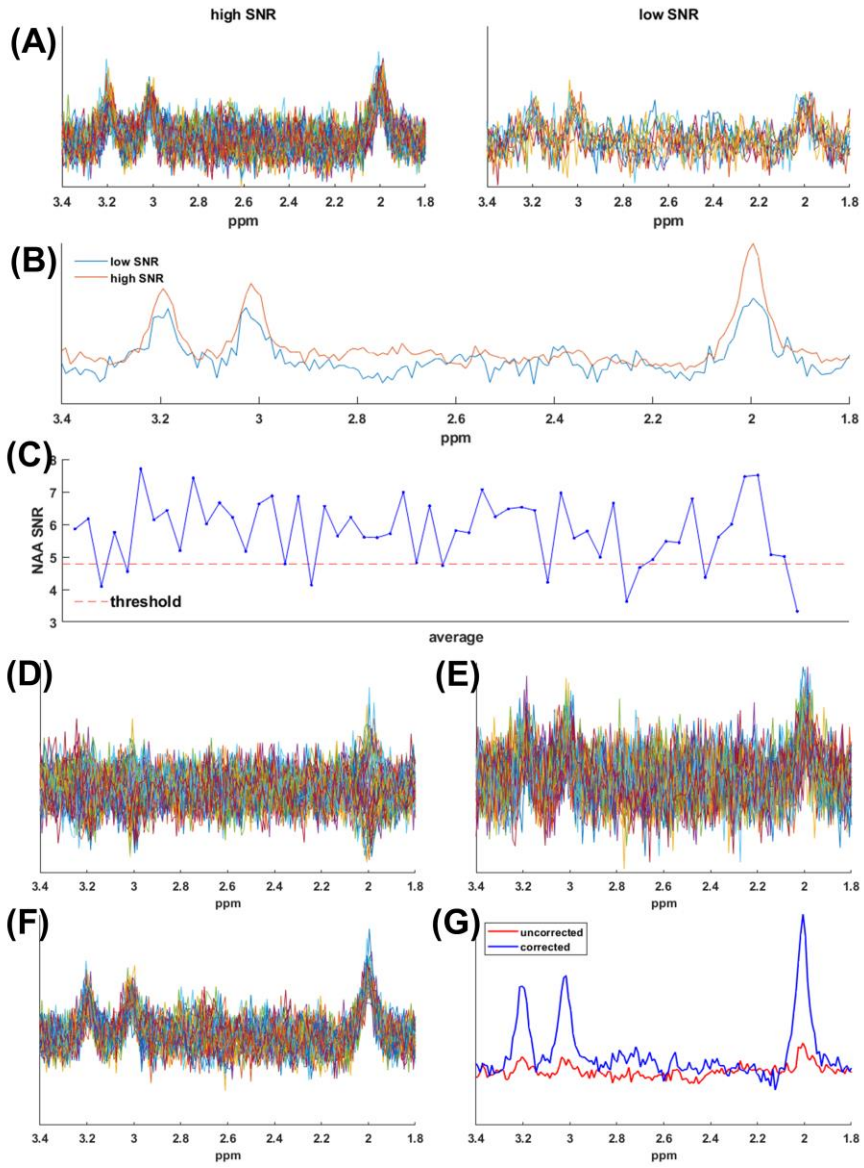

Figure 4-3: Post-processing procedures: **(A)** Separation of the low- and high-SNR averages. **(B)** Comparison of the averaged spectra from the sets of low-SNR and high-SNR averages, showing that a reduction in peak intensities will result if the low-SNR averages are not removed. **(C)** The threshold criterion based on the SNR of the NAA singlet determines which specific averages to remove. **(D)** Raw spectra before zero-order phase correction. **(E)** The spectra after zero-order phase correction. **(F)** Frequency-drift correction after zero-order phasing. **(G)** Comparison between the uncorrected and corrected spectra.

4.4.6 Signal Quantitation and Determination of ADC

Prior-knowledge basis spectra were simulated with VESPA[50], using the exact sequence timings of each DW-PRESS variant, but with ideal 90° and 180° RF pulses. For in vivo data sets, the basis set included the following metabolites: alanine, ascorbate, aspartate, choline (Cho), creatine (Cr), γ-aminobutyric acid, glucose, glutamine (Gln), glutamate (Glu), glycerophosphorylcholine, glutathione, lactate (Lac), myo-inositol (mI), n-acetylaspartate (NAA), n-acetylaspartylglutamate (NAAG), phosphorylcholine (PCh), phosphocreatine (PCr), phosphorylethanolamine, scyllo-inositol, and taurine.

The post-processed MRS signal was quantified using LC Model (version 6.2-0T) [111] and the resulting LC model concentration estimates, which are proportional to the metabolite peak integrals, were assumed to fit the general model:

$$S\left(b_k^{\pm}\right) = S(b_0)e^{-b_k^{\pm}\cdot ADC_k^{\pm}} \tag{4-15}$$

where $b_k^{\pm}$ and $ADC_k^{\pm}$ is the b-value and the ADC in the k^{th} direction, for either the positive or negative polarities, respectively. Only estimates with Cramer-Rao lower bounds (CRLB's) ≤ 20% were considered for further analysis. For DW-PRESS acquisitions with three directions and two polarities, the ADC's from the negative, positive, and geometric means of the two polarities were also determined. The geometric mean, $S_{geo}(b_k)$, of the peak area values was computed as:

$$S_{geo}(b_k) = \sqrt{S(b_k^{+}) \cdot S(b_k^{-})} \tag{4-16}$$

The final trace ADC from positive, negative, or geometric means was computed as the average of the corresponding ADC's from all three directions.

$$Trace\ ADC^{\{+,-,geo\}} = \frac{1}{3}\sum_{k=1}^{3}\left(ADC_k^{\{+,-,geo\}}\right) \quad (4\text{-}17)$$

The above model also holds for the trace DW-PRESS sequence, where $k = 1$ and a single polarity is applicable.

For estimation of water ADC's, the water peak from the non-water suppressed data was first zero-order phased into absorptive mode. The peak was then 4× interpolated followed by numerical integration to estimate the area. These water peak areas were subsequently used for computing the ADC using the same model stated above.

4.4.7 Statistical Analysis

Phantom

A repeated measures analysis of variance was conducted to determine any significant differences in the trace ADC values of NAA, Cr, Cho, Glu, mI, and Lac from the brain phantom, among the Bipolar, Unipolar and Trace DW-PRESS sequences. Differences were considered statistically significant if $p < 0.05$.

Paired samples t-test were conducted to determine any statistically significant differences in the trace ADC values of NAA, Cr, Cho, Glu, mI, and Lac from the brain phantom, between acquisitions with negative (ADC-) and positive (ADC+) gradient polarities. This analysis was done separately for the Bipolar and Unipolar sequences.

In vivo

A repeated measures analysis of variance was conducted to determine any significant differences in the trace ADC values of tNAA, tCr, tCho and Water, for each brain region (FG, OG,

and OW), among the Bipolar, Unipolar and Trace DW-PRESS sequences. Differences were considered statistically significant if $p < 0.05$, with Bonferroni correction for multiple comparisons.

Paired samples t-tests were conducted to determine any statistically significant differences in the trace ADC values of tNAA, tCr, tCho, and Water between the occipital gray (OG) and occipital white (OW) matter, for each type of pulse sequence. A p-value of 0.05 was set for statistical significance.

Paired samples t-test were conducted to determine any statistically significant differences in the trace ADC values of tNAA, tCr, tCho, and water measured from acquisitions with negative (ADC-) and positive (ADC+) gradient polarities. This analysis was done separately for the Bipolar and Unipolar sequences, and for each brain region (FG, OG, and OW).

Two volunteers were each scanned three separate times – one in the frontal gray (FG) matter and the other in the occipital gray (OG) matter. The means, standard deviations, and coefficients of variance (CV) of the trace ADC's of tNAA, tCr, tCho, and water were computed across the three sessions.

4.5 Results

The importance of post-processing procedures is illustrated in Figure 4-3, where SNR-based thresholding was key in excluding averages that were significantly affected by motion. Frequency drift and phase corrections prior to summation also ensured that the diffusion-weighted signal was not overly biased towards higher ADC's. Without these corrective procedures, the signal quantitation would inaccurately reflect the actual signal attenuation due to diffusion.

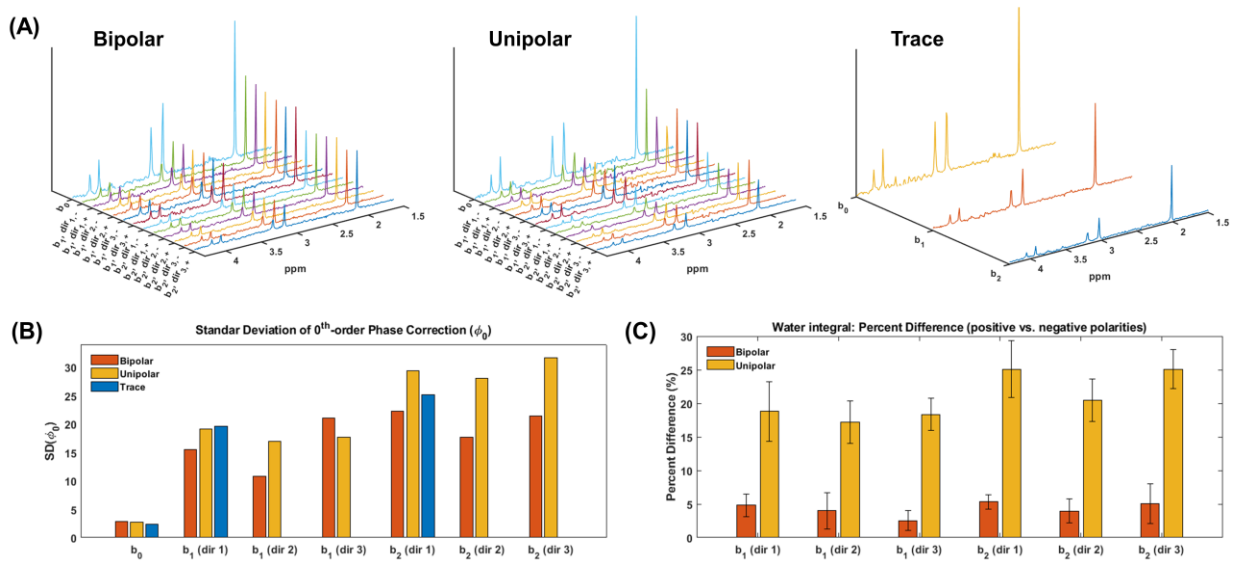

Figure 4-4: **(A)** Representative spectra acquired with the Bipolar, Unipolar, and diffusion-trace weighted (Trace) DW-PRESS sequences. Spectra from all three b-values (b_0, b_1, b_2) are shown. The spectra from the Bipolar and Unipolar DW-PRESS sequences acquired at all three directions with positive (dir_{1+}, dir_{2+}, dir_{3+}) and negative (dir_{1-} , dir_{2-}, dir_{3-}) polarities are shown. **(B)** The standard deviations (SD) of the zero-order phase corrections for the NAA peak (before application of eddy current phase correction). This SD is a measure of the effect of eddy currents on the acquired signal. **(C)** Percent difference of the water peak integral values between water spectra acquired with negative and positive polarities – mean and standard deviations (error bars) are shown for all three directions and for the two b-values greater than the b_0. The unipolar sequence has markedly higher differences in b-values between the two polarities.

Figure 4-4A presents representative spectra acquired with the bipolar, unipolar, and trace-weighted sequences in the GE Braino phantom. The amplitudes of the NAA peaks in the unipolar sequences tend to vary more compared to the NAA spectra from the bipolar sequence, both as a function of direction and polarity. In Figure 4-4B, the standard deviations of the zero-order phase correction on the NAA singlet, shows that the bipolar sequence experiences a lower degree of eddy current-induced phase fluctuations. However, the unipolar and trace sequences have a larger standard deviation, indicating greater influence of eddy currents, as expected since these sequences require a greater diffusion amplitude to reach a given b-value, compared to the bipolar sequence. Figure 4-4C also shows that the unipolar sequence does not compensate for cross-terms as well as

the bipolar sequence, as the percent differences between the water peaks acquired with positive and negative polarities is greater than the bipolar sequence.

	GE Braino Trace ADC values: mean ± standard deviation [μm²/ms]							
	Bipolar			Unipolar			Trace	Reference Values
	ADC-	ADC+	ADC*	ADC-	ADC+	ADC*	ADC	
NAA	0.59 ± 0.01	0.61 ± 0.02	0.6 ± 0.01	0.6 ± 0.02	0.6 ± 0.02	0.6 ± 0.02	0.6 ± 0.02	0.59 ± 0.01
Cr	0.77 ± 0.01	0.78 ± 0.01	0.78 ± 0.01	0.78 ± 0.03	0.78 ± 0.02	0.78 ± 0.02	0.78 ± 0.02	0.78 ± 0.02/0.84 ± 0.1
Cho	0.93 ± 0.01	0.94 ± 0.02	0.93 ± 0.01	0.95 ± 0.04	0.95 ± 0.03	0.95 ± 0.03	0.93 ± 0.03	0.91 ± 0.03
Glu	0.78 ± 0.06	0.77 ± 0.04	0.78 ± 0.04	0.64 ± 0.06	0.65 ± 0.06	0.64 ± 0.06	0.73 ± 0.07	0.76 ± 0.03
Lac	0.75 ± 0.13	0.8 ± 0.14	0.78 ± 0.12	0.82 ± 0.08	0.8 ± 0.08	0.81 ± 0.06	0.76 ± 0.1	0.64 ± 0.13
mI	0.78 ± 0.16	0.79 ± 0.13	0.79 ± 0.14	0.72 ± 0.12	0.72 ± 0.14	0.72 ± 0.13	0.76 ± 0.11	0.76 ± 0.1

Table 4-2: GE Braino trace ADC values averaged over 9 measurements from DW-PRESS acquisitions using the Bipolar, Unipolar, and Single-shot Trace-weighted sequences. All phantom measurements agree well with reference values [101].

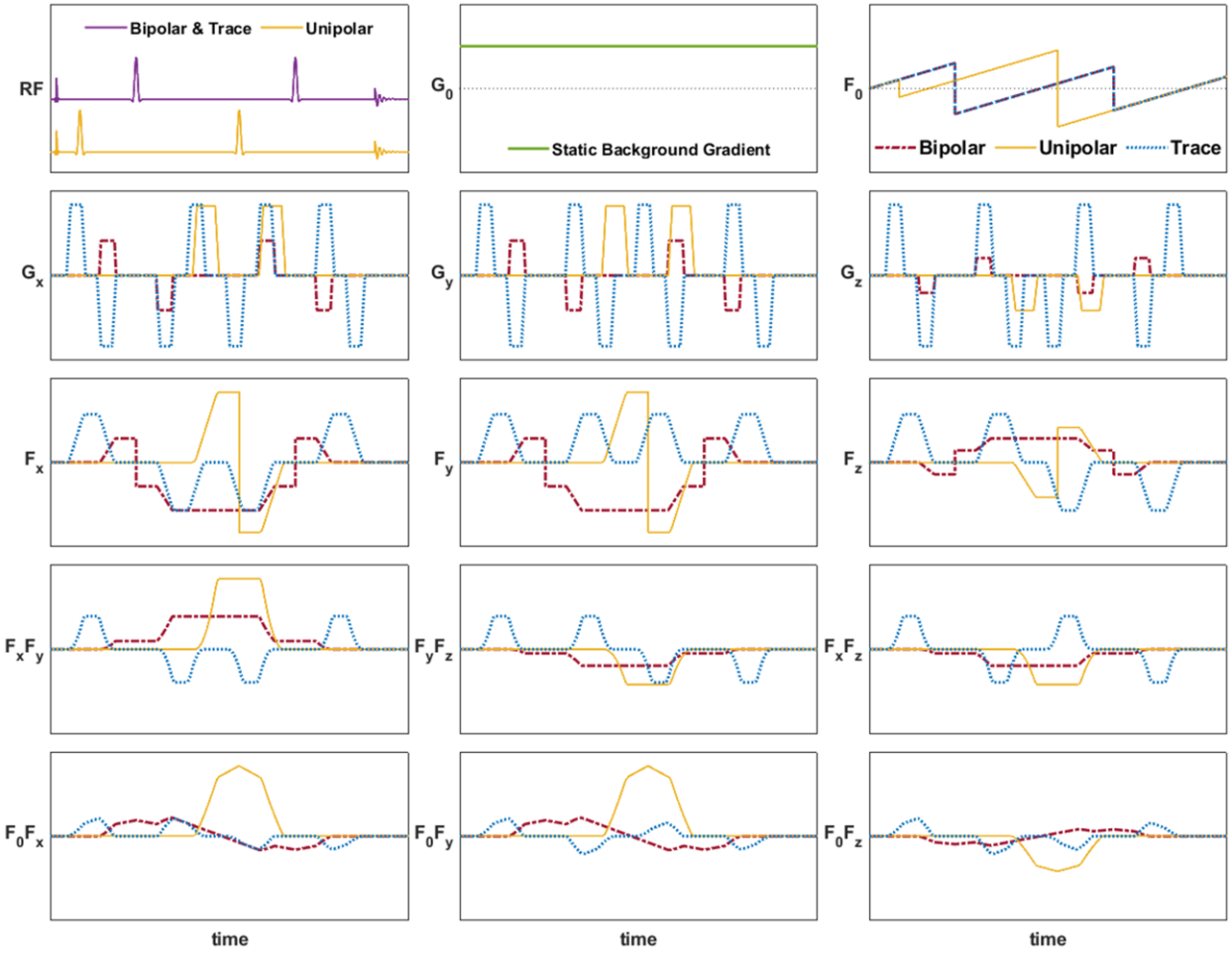

Figure 4-5: Effect of cross-terms originating from the interaction of the diffusion-sensitizing gradients with a static background gradient G_0 (shown in green). The diffusion direction

corresponding to the vector [1.0, 1.0, -0.5] is shown. The gradient moments (F_0, F_x, F_y, and F_z) are plotted along with the cross terms (F_0F_x, F_0F_y, and F_0F_z), for the Bipolar, Unipolar, and Trace (diffusion trace-weighted) DW-PRESS sequences. The cross terms F_xF_y, F_yFz, and F_xF_z that contribute to off-diagonal elements in the b-matrix are also shown. Note that the Bipolar and Trace DW-PRESS sequences have equal contributions of negative and positive areas in the F_0F_x, F_0F_y, and F_0F_z plots, leading to cancellation of cross terms originating from the G_0. The Unipolar DW-PRESS sequences, in contrast, retains a large net cross term contribution. For simplicity, the localization and crusher gradients were omitted in the computation of F_0, F_j, and F_0F_j (j = x, y, z).

As seen in Figure 4-5, cross terms due to static background gradients are compensated for in the Bipolar and Trace DW-PRESS sequences. However, the Unipolar sequence has an inherent greater net signal attenuation due to cross terms from the background gradient. This effect explains the large differences in the computed b-value between the negative and positive diffusion gradient polarities in the Unipolar DW-PRESS sequences (Table 4-1). The cross terms F_xF_y, F_xF_z, and F_yF_z correspond to the off-diagonal elements of the b-matrix. Evidently, the time integrals of these terms are essentially nulled only for the Trace DW-PRESS sequence. Figure 4-6 shows representative spectra in the FG, OG, and OW regions, indicating good linewidths (averages of 12-18 Hz for the magnitude water peak in vivo) and SNR's suitable for quantitation, as well as Cramer-Rao lower bound values (CRLB's) no greater than 20% (Table 4-4). Spectra from Trace DW-PRESS experience the largest drop in signal amplitude at the highest b-value tested, compared to the Bipolar and Unipolar DW-PRESS acquisitions.

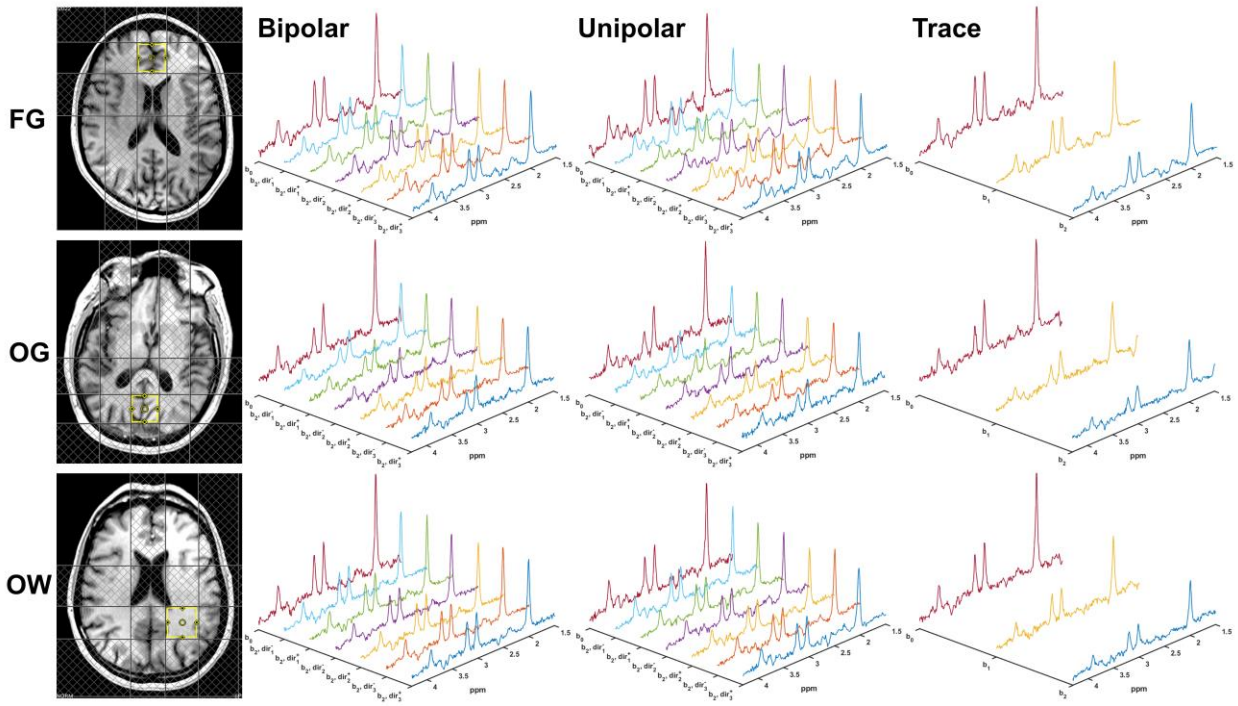

Figure 4-6: In vivo spectra from Bipolar, Unipolar, and Trace DW-PRESS sequences, shown from acquisitions in frontal gray matter (FG), occipital gray matter (OG), and subcortical white matter (OW). For Bipolar and Unipolar DW-PRESS, spectra are shown for both gradient polarities and all three directions, at b_0 (null) and b_2. An additional b-value (b_1) was acquired for Trace DW-PRESS.

Figure 4-7 demonstrates the average trace ADC's computed from the three sequences in each brain region. The difference in ADC's between the Trace and Unipolar and Bipolar DW-PRESS sequences were statistically significant for most metabolites (see subsection below). The significantly increased trace ADC values of water is quite evident in the Trace DW-PRESS acquisitions, indicating the effect of the shorter diffusion time. This effect is also seen in Figure 4-9, where the signal ratios $S(b)/S_0$ in the Trace DW-PRESS sequence are evidently lower than the Bipolar and Unipolar DW-PRESS acquisitions, for any given b-value.

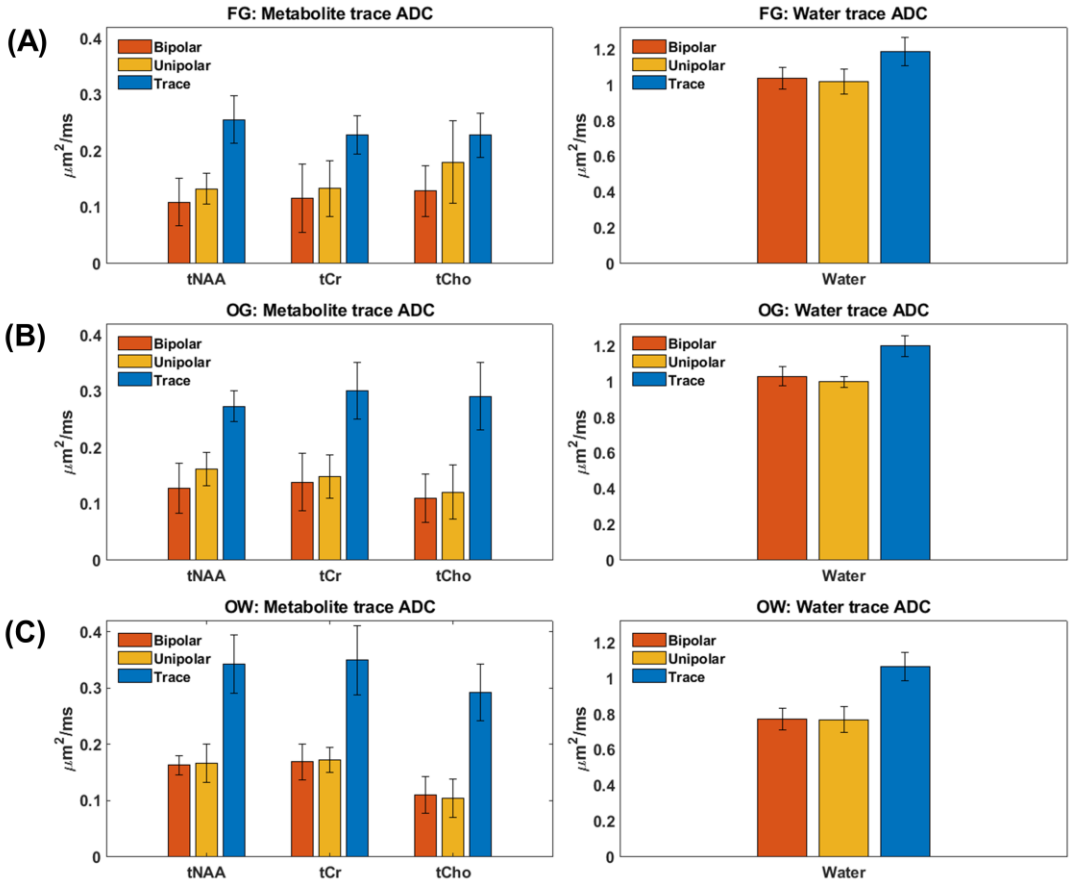

Figure 4-7: Average trace ADC values for the three main metabolite groups (tNAA, tCr, and tCho) and Water in **(A)** frontal gray (FG) matter, **(B)** occipital gray (OG) matter, and **(C)** occipital (subcortical) white (OW) matter. Note the overall larger trace ADC's of water and metabolites from Trace DW-PRESS compared to the other sequences (Bipolar and Unipolar).

Figure 4-8 illustrates representative spectra for each sequence in the occipital gray matter region of the brain. The difference in the spectra from negative and positive polarities, as well as from different diffusion directions, is quite small, as seen from the NAA singlet from the Bipolar and Unipolar DW-PRESS acquisitions. However, the extent of signal attenuation is less than that of the Trace DW-PRESS sequence, which shows more reduction at the highest b-value (1707 s/mm^2) compared to the other sequences. This effect is largely due to the shorter diffusion time of the Trace DW-PRESS sequences. In contrast to the in vivo spectra, the phantom spectra from all sequences experience a similar reduction of signal intensity as a function of b-value, as seen in

Figure 4-10A. In vivo, these relative signal intensity reductions are not the same as a function of the lowest (b_0) and highest (b_2) b-value, between the Bipolar and Unipolar and the Trace DW-PRESS sequence (Figure 4-10B), showing that the restriction of the metabolites is affected differently depending on the diffusion time.

		In Vivo Trace ADC values: mean ± standard deviation [μm²/ms]						
		BIPOLAR			UNIPOLAR			TRACE
		ADC-	ADC+	ADC (gm)	ADC-	ADC+	ADC (gm)	ADC
FG	tNAA	0.11 ± 0.04	0.11 ± 0.04	0.11 ± 0.04	0.12 ± 0.03	0.15 ± 0.04	0.13 ± 0.03	0.26 ± 0.04
	tCr	0.11 ± 0.06	0.12 ± 0.06	0.12 ± 0.06	0.12 ± 0.04	0.14 ± 0.06	0.13 ± 0.05	0.23 ± 0.03
	tCho	0.12 ± 0.05	0.14 ± 0.05	0.13 ± 0.04	0.18 ± 0.08	0.18 ± 0.07	0.18 ± 0.07	0.23 ± 0.04
	Water	1.03 ± 0.06	1.05 ± 0.06	1.04 ± 0.06	1.02 ± 0.07	1.02 ± 0.07	1.02 ± 0.07	1.19 ± 0.08
OG	tNAA	0.13 ± 0.05	0.13 ± 0.04	0.13 ± 0.04	0.16 ± 0.03	0.17 ± 0.03	0.16 ± 0.03	0.27 ± 0.03
	tCr	0.14 ± 0.05	0.14 ± 0.05	0.14 ± 0.05	0.15 ± 0.03	0.15 ± 0.05	0.15 ± 0.04	0.3 ± 0.05
	tCho	0.11 ± 0.05	0.11 ± 0.04	0.11 ± 0.04	0.14 ± 0.04	0.11 ± 0.06	0.12 ± 0.05	0.29 ± 0.06
	Water	1.02 ± 0.05	1.04 ± 0.06	1.03 ± 0.05	1.01 ± 0.04	0.99 ± 0.03	1.00 ± 0.03	1.20 ± 0.06
OW	tNAA	0.16 ± 0.02	0.17 ± 0.02	0.16 ± 0.02	0.16 ± 0.04	0.17 ± 0.04	0.17 ± 0.03	0.34 ± 0.05
	tCr	0.17 ± 0.03	0.17 ± 0.04	0.17 ± 0.03	0.17 ± 0.03	0.17 ± 0.02	0.17 ± 0.02	0.35 ± 0.06
	tCho	0.11 ± 0.04	0.11 ± 0.03	0.11 ± 0.03	0.10 ± 0.04	0.11 ± 0.03	0.1 ± 0.03	0.29 ± 0.05
	Water	0.77 ± 0.06	0.77 ± 0.06	0.77 ± 0.06	0.78 ± 0.07	0.76 ± 0.07	0.77 ± 0.07	1.06 ± 0.08

Table 4-3: Table of in vivo ADC values for the Bipolar, Unipolar, and Trace DW-PRESS sequences. For the Bipolar and Unipolar DW-PRESS sequences, the trace ADC's from negative (ADC-) and positive (ADC+) polarities were computed, as well as the trace ADC from the geometric mean, ADC (geo), of the signals from positive and negative diffusion gradient polarities. In the rightmost column, the trace ADC values from the Trace DW-PRESS sequence are shown.

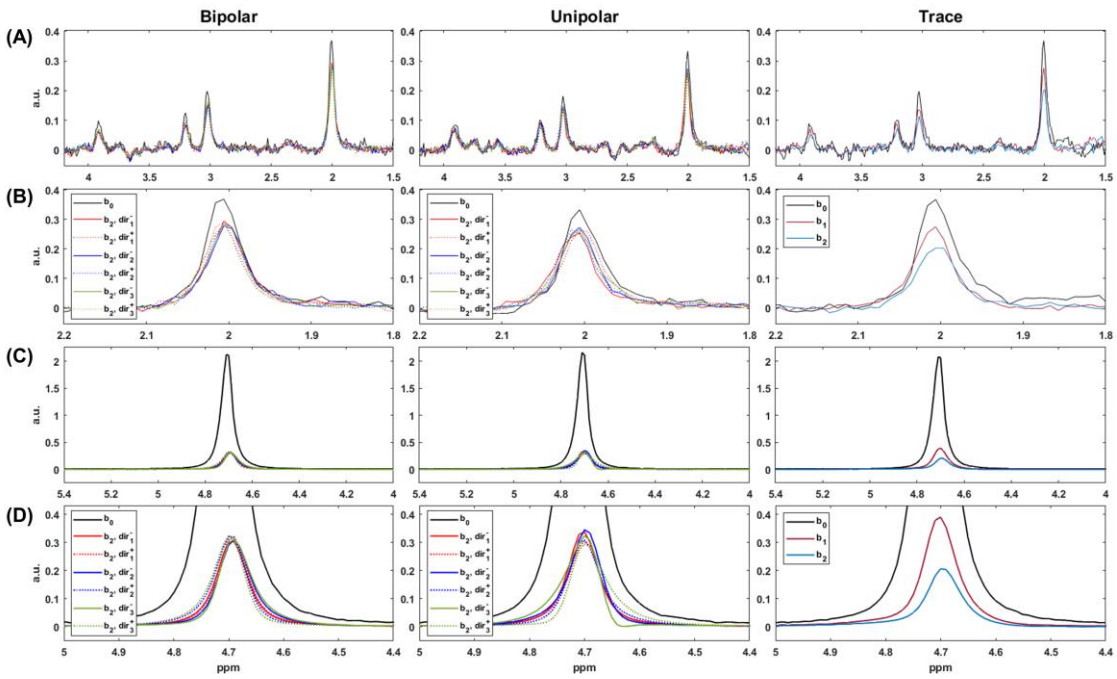

Figure 4-8: **(A)** Representative spectra from the Bipolar, Unipolar and Trace DW-PRESS acquisitions, from a healthy volunteer in the occipital gray (OG) matter region. **(B)** Plots of the NAA singlet at 2.01 ppm. For the Unipolar and Bipolar DW-PRESS sequences, the various spectra from both gradient polarities and three diffusion directions (dir_1^-, dir_1^+, dir_2^-, dir_2^+, dir_3^-, dir_3^+) are overlaid. The NAA singlet is shown for the Trace DW-PRESS sequence at three b-values. **(C)** The water peak from the null to the highest diffusion-weighting. Note the greater degree of signal attenuation in the Trace DW-PRESS acquisitions, for the same b-value range (b_0 and b_2) as those shown for the Unipolar and Bipolar DW-PRESS spectra. **(D)** Zoom-in on the water spectra, indicating the greater reduction in water signal in the Trace DW-PRESS acquisitions.

4.5.1 Statistical Analysis

Phantom

No significant differences were found in the trace ADC values of NAA, Cr, Cho, Lac, and mI among the Bipolar, Unipolar, and Trace DW-PRESS phantom acquisitions (Table 4-2). The trace ADC values of Glu were significantly different only between the Bipolar (0.78 ± 0.05 $\mu m^2/ms$) and Unipolar (0.64 ± 0.06 $\mu m^2/ms$) sequences ($p = 0.006$). For Unipolar DW-PRESS, the trace ADC of Glu from the negative gradient polarities ($ADC- = 0.64 \pm 0.06$ $\mu m^2/ms$) is significantly different ($p < 0.001$) from the one from the positive polarities ($ADC+ = 0.65 \pm 0.07$ $\mu m^2/ms$). For

the Bipolar sequence, the trace ADC+ of Glu (0.77 ± 0.04 $\mu m^2/ms$) was also significantly different from the trace ADC- (0.78 ± 0.07 $\mu m^2/ms$). All other trace ADC+ and ADC- values are not statistically significantly different for any other metabolites from either the Unipolar or Bipolar sequences.

Coefficients of variance percentages (CV%) are largest for the trace ADC estimates of Glu (6 – 10%), Lac (8 – 18%), and mI (15 – 21%) in all sequences, while the CV%'s of NAA, Cr, and Cho are all below 4%. The CV%'s of trace ADC estimates of Lac and mI are largest from the Bipolar acquisitions (16-19% and 19-21%, respectively). The CV% value for Lac is lowest from the Unipolar sequence (8-10%).

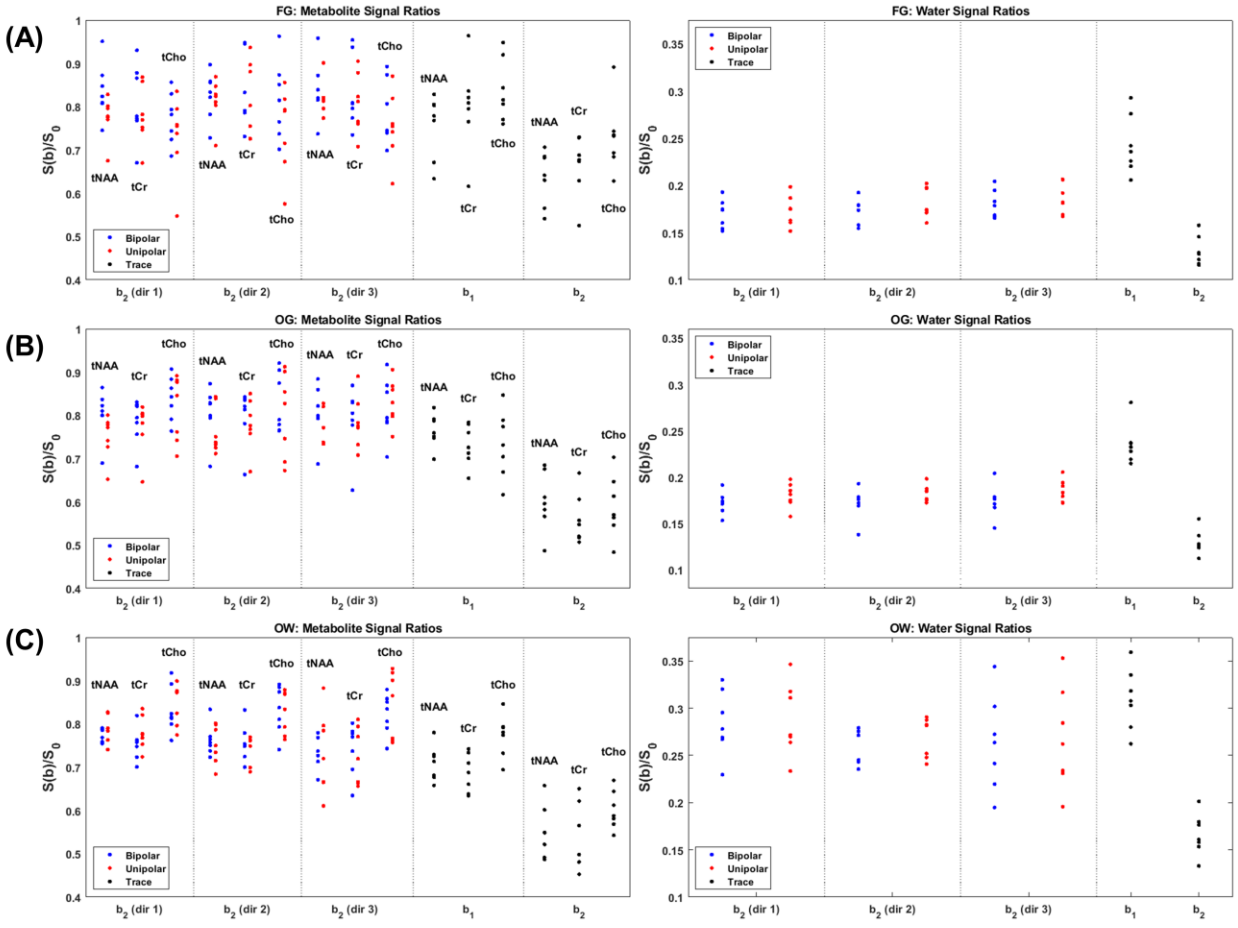

Figure 4-9: Signal Ratios (S/S_0) for the Bipolar, Unipolar, and Trace DW-PRESS acquisitions in **(A)** frontal gray (FG) matter, **(B)** occipital gray (OG) matter, and **(C)** occipital (subcortical) white (OW) matter. For the Bipolar and Unipolar sequences, the ratios of the high to null b-value signals ($S(b_2)/S(b_0)$) are shown for all three diffusion directions. The ratios of $S(b_1)/S(b_0)$ and $S(b_2)/S(b_0)$ are shown for the trace DW-PRESS sequence in the third column Only the lowest (null – b_0 = 4 s/mm^2) and the highest (b_2 = 1,697 – 1,718 s/mm^2) b-values were acquired for in vivo Bipolar and Unipolar DW-PRESS. The Trace DW-PRESS measurements were acquired with an additional b-value (b_1 = 994 - 1021 s/mm^2). Note the lower signal ratios in the Trace DW-PRESS measurements compared to the Bipolar and Unipolar DW-PRESS acquisitions, indicating a greater reduction of the metabolite and water signals for the same b-value range.

In vivo

In the frontal gray matter, the trace ADC of tNAA from Trace DW-PRESS (0.26 ± 0.04 μm^2/ms) is significantly different from the trace ADC's of tNAA measured with the Unipolar (0.13 ± 0.03 μm^2/ms) and Bipolar (0.11 ± 0.04 μm^2/ms) sequences ($p = 0.002$ for both). The trace ADC of tCr from Trace DW-PRESS (0.23 ± 0.03 μm^2/ms) sequence is also significantly different from the trace ADC's of tCr measured with the Unipolar (0.13 ± 0.05 μm^2/ms) and Bipolar sequences (0.12 ± 0.06 μm^2/ms), with $p = 0.023$ and $p = 0.027$, respectively. For tCho, the trace ADC's are only significantly different between the Bipolar and Trace DW-PRESS acquisitions ($p = 0.029$). Water trace ADC's were significantly different between the Unipolar and Trace ($p = 0.047$), between the Unipolar and Bipolar ($p = 0.005$), and between the Bipolar and Trace DW-PRESS acquisitions ($p = 0.001$).

In the occipital gray matter, the trace ADC of tNAA from the Trace DW-PRESS sequence was significantly different from the trace ADC's of tNAA measured with the Unipolar ($p = 0.001$) and Bipolar sequences ($p < 0.001$). The trace ADC of tCr from the Trace DW-PRESS sequence was also significantly different from the trace ADC's of tCr measured with the Unipolar and Bipolar sequences ($p = 0.002$ and $p < 0.001$, respectively). The trace ADC's of tCho from Trace

DW-PRESS are significantly different from the values measured with Unipolar and Bipolar DW-PRESS ($p = 0.006$ and $p = 0.001$, respectively). The same pattern occurs with the water trace ADC, as the values from Trace DW-PRESS are significantly different from those measured with the Unipolar and Bipolar acquisitions ($p < 0.001$ and $p = 0.001$, respectively).

In the occipital white matter, the trace ADC of tNAA measured with Trace DW-PRESS was significantly different from the trace ADC's of tNAA measured with the Unipolar and Bipolar sequences (both at $p < 0.001$). The trace ADC of tCr from the Trace DW-PRESS sequence is also significantly different from the trace ADC's of tCr measured with the Unipolar and Bipolar sequences (both at $p < 0.001$). Similarly, the trace ADC's of tCho from Trace DW-PRESS are significantly different from the values measured with Unipolar and Bipolar DW-PRESS (both at $p < 0.001$). The same pattern occurs with the water trace ADC, as the values from Trace DW-PRESS are significantly different from those measured with the Unipolar and Bipolar acquisitions (both at $p < 0.001$) in OW.

When comparing the trace ADC's between the OG and OW regions, statistically significant differences were found in the trace ADC's of water in OG vs. OW, measured with all three sequences (Table 4-3). Only the trace ADC of tNAA measured with Trace DW-PRESS was significantly different in OW vs. OG ($p = 0.040$).

In occipital white matter, statistically significant differences were found in the trace ADC+ and ADC- values of water measured with Bipolar and Unipolar DW-PRESS ($p = 0.025$ and $p = 0.002$, respectively). In occipital gray matter, only the water trace ADC+ and ADC- values were statistically significant in the measurements using Unipolar DW-PRESS ($p = 0.004$), although the water trace ADC+ and ADC- values were nearly significantly different in the Bipolar DW-PRESS

acquisitions (p = 0.066). In frontal gray matter, the difference in the trace ADC+ and ADC- of water measured with Bipolar DW-PRESS was significant (p = 0.008), and only the trace ADC+ and ADC- values of tNAA were significantly different in the Unipolar DW-PRESS measurements (p = 0.048).

		In Vivo CRLB Values: mean ± standard deviation						
		BIPOLAR		UNIPOLAR		TRACE		
		b_0	b_2	b_0	b_2	b_0	b_1	b_2
FG	tNAA	3.5 ± 1.2	2.2 ± 0.5	3.2 ± 1.4	2.3 ± 0.5	3.6 ± 1.4	2.8 ± 0.6	2.6 ± 0.7
	tCr	4.8 ± 1.1	3.2 ± 0.5	4.6 ± 1.7	3.5 ± 0.8	4.7 ± 1.6	3.9 ± 0.8	3.6 ± 0.9
	tCho	7.7 ± 1.8	5.6 ± 1.3	6.4 ± 2.3	5.6 ± 1.4	8.4 ± 2.8	7.4 ± 2.6	6.3 ± 2.2
OG	tNAA	3.0 ± 0	2.1 ± 0.3	2.8 ± 0.4	2.6 ± 0.5	3 ± 0	3.3 ± 0.5	3.4 ± 1.2
	tCr	4.3 ± 0.7	3.4 ± 0.5	3.9 ± 0.6	3.9 ± 0.6	4.1 ± 0.3	4.9 ± 0.8	5.1 ± 1.8
	tCho	12 ± 4.1	9.7 ± 2	11.3 ± 3.3	10.5 ± 3.3	9.8 ± 3	13.2 ± 5.4	12.6 ± 6.3
OW	tNAA	2.3 ± 0.8	2.1 ± 0.5	2.4 ± 0.8	2.1 ± 0.5	2.1 ± 0.4	2.3 ± 0.5	2.4 ± 0.5
	tCr	3.6 ± 0.8	3.4 ± 0.7	3.6 ± 0.8	3.3 ± 0.7	3.6 ± 0.8	3.8 ± 0.4	4.1 ± 0.7
	tCho	6.6 ± 2.3	4.7 ± 1.5	7.1 ± 3.3	5.3 ± 1.8	6.7 ± 2.1	5.5 ± 2.1	5.1 ± 1.1

Table 4-4: Average CRLB values (and standard deviations) for the three main singlets measured with each sequence. Due to the long TE (140 ms) the CRLB values for mI and Glx (Glu+Gln) often exceeded 20%. These values are recorded for the three b-values used in this study (b_0, b_1, and b_2). Only the lowest (b_0) and the highest (b_2) b-values were used for the in vivo Unipolar and Bipolar DW-PRESS acquisitions due to scan time limitations.

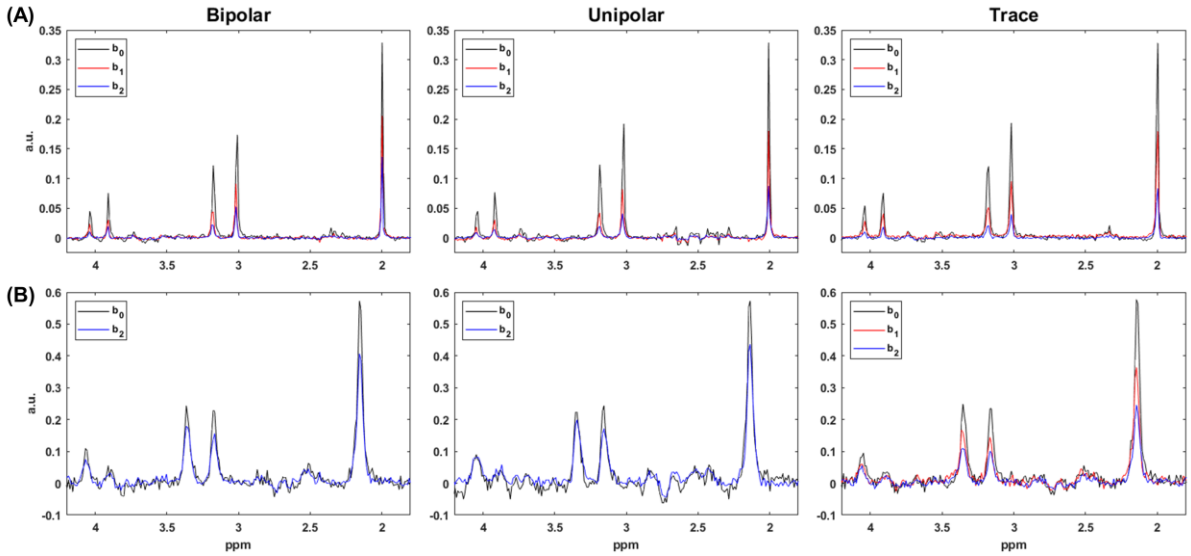

Figure 4-10: **(A)** Diffusion-weighted phantom spectra at three b-values b_0, b_1, and b_2. Only the lowest (null – b_0 = 4 s/mm^2) and the highest (b_2 = 1,697 – 1,718 s/mm^2) b-values were acquired for in vivo Bipolar and Unipolar DW-PRESS. The Trace DW-PRESS measurements were acquired

with an additional b-value (b_1 = 994 - 1021 s/mm^2). Note that the signals from all sequences have similar reduction in signal intensity for all b-values. **(B)** Diffusion-weighted in vivo spectra from the occipital white matter. Note that the in vivo Trace DW-PRESS signal acquired at b_2 has a greater attenuation than the corresponding spectra from Bipolar and Unipolar DW-PRESS acquired at b_2, showing that the restriction of the metabolites is affected differently depending on the diffusion time.

4.5.2 Repeatability of three in vivo measurements in two volunteers

The repeatability of measuring the trace ADC's of tNAA, tCr, tCho, and water was estimated with the coefficient of variance (CV). Table 4-5 lists the means, standard deviations, and CV's (%) of these metabolites measured across three sessions in two volunteers, one in the frontal gray and the other in the occipital gray matter. Water has the lowest CV's (3-4%) in all methods and regions. The FG region generally had higher CV's compared to the OG region for nearly all metabolites, except tCho. The trace ADC of tCho also carried the highest CV within both the FG (45-58%) and OG (15-62%) regions. In the FG region, the Trace DW-PRESS measurements had the lowest CV's except for water, while in the OG region, they were also lowest except for tNAA, where Bipolar DW-PRESS resulted in the lowest CV (8% vs. 11%).

		Trace ADC's across 3 sessions in two volunteers mean ± standard deviation (CV%) (μm^2/ms)		
		BIPOLAR	UNIPOLAR	TRACE
FG	tNAA	0.10 ± 0.04 (36%)	0.11 ± 0.05 (41%)	0.32 ± 0.06 (19%)
	tCr	0.11 ± 0.04 (36%)	0.08 ± 0.03 (44%)	0.26 ± 0.03 (11%)
	tCho	0.11 ± 0.06 (58%)	0.09 ± 0.05 (51%)	0.18 ± 0.08 (45%)
	Water	1.12 ± 0.03 (3%)	1.11 ± 0.03 (3%)	1.32 ± 0.05 (4%)
OG	tNAA	0.12 ± 0.01 (8%)	0.13 ± 0.02 (19%)	0.28 ± 0.03 (11%)
	tCr	0.12 ± 0.01 (12%)	0.14 ± 0.02 (18%)	0.32 ± 0.02 (8%)
	tCho	0.15 ± 0.04 (24%)	0.10 ± 0.06 (62%)	0.34 ± 0.05 (15%)
	Water	1.04 ± 0.03 (3%)	1.02 ± 0.02 (2%)	1.23 ± 0.05 (4%)

Table 4-5: Trace ADC values of the main metabolite groups and water from two volunteers across three scan sessions, one measured in the frontal gray (FG) and the other in the occipital gray (OG) matter. Means, standard deviations, and coefficients of variance (CV%) are reported for each volunteer. The CV is a measure of the repeatability of the trace ADC values over the three measurements.

4.6 Discussion

Trace ADC values were estimated in vivo and in phantom using the single-shot diffusion trace-weighted sequence in a clinical scanner at 3T, and these values were compared to those computed from the conventional DW-PRESS techniques using bipolar and unipolar diffusion gradients applied at three orthogonal diffusion directions with positive and negative gradient polarities. All sequence variants are generally in agreement with one another in terms of average trace ADC values in phantom, except for Glu for which the Bipolar and Unipolar sequence have slightly different ADC's (Table 4-2). Overall, the trace ADC's in phantom agree remarkably well with those reported previously in the same standardized phantom [101], except for mI, Lac, and Glu, since the report by Landheer et al. used shorter TE values (minimum of 74 ms) at which the signals from these metabolites are more distinguishable and have higher SNR's. The phantom trace ADC values for NAA, Cr, Cho have low coefficients of variance while those for mI, Glu, and Lac are higher, due to long TE.

One of the limitations of the single-shot sequence is that the long TE leads to reliability in only tNAA, tCr, tCho. Strong diffusion gradients could potentially render any DW-MRS sequence more susceptible to motion, possibly leading to more signal loss and resulting in an overestimation of ADC. However, the phantom results indicate that eddy current effects may not be a significant factor for the particular sequence parameters used in the experiments, since the values from the Trace, Bipolar, and Unipolar DW-PRESS sequence are stable and agree well with reference values. The combination of large gradients and long TE also puts a constraint on the highest achievable b-value for the single-shot trace-weighted sequence.

Cross-terms found from the water signal indicated a greater cross-term contribution in the unipolar DW-PRESS sequence compared to the bipolar variant. The standard deviations of the zero-order phase correction show that the Trace and Unipolar sequences are more susceptible to eddy-current induced phase fluctuations. The report by Hanstock [102] did not use a water reference in order to reduce the scan time and because of the high b-values tested which greatly attenuate the water signal. In that report, the phase variation was also measured via the standard deviation of the zero-order phase correction on a reference peak. However, in this study, the eddy current phase correction [44] using the water data apparently corrects for these effects in all the sequences, since the phantom data remains relatively stable (low CV%) for all sequences. Additionally, for the Unipolar DW-PRESS acquisitions, the taking of the geometric mean of the signals from both polarities evidently reduces the effect of the cross terms, as the trace ADC values in the phantom are quite stable and comparable to those from the Bipolar and Trace DW-PRESS acquisitions.

A general limitation of this study is that no cardiac gating or ECG triggering was implemented, which could avoid further signal losses. However, other DW-MRS reports [79,80,102] have similarly excluded the use of triggering and gating without overestimating the ADC's by implementing careful post-processing procedures, as was done in this study. Another limitation is chemical shift displacement which is inherent to the basic PRESS sequence and causes misregistration of the metabolite signals with respect to the target volume-of-interest. Also, no more than two b-values were able to be practically acquired in one scan session for the Bipolar and Unipolar DW-PRESS in vivo measurements, as opposed to Trace DW-PRESS, for which there was sufficient time to acquire three b-values. A similar, two b-value approach for Bipolar DW-PRESS was taken in the report by Deelchand et al. [80], however, three b-values could further

improve the estimation of the ADC's for the Bipolar and Unipolar DW-PRESS acquisitions, albeit at a considerable increase in scan duration.

Results show that the trace ADC of water in white matter is significantly higher than the trace ADC of water in gray matter, as measured with the unipolar, bipolar, and trace-weighted sequences. Also, the tNAA trace ADC value in white matter is significantly higher that the value in gray matter for Trace DW-PRESS acquisitions only. The tCr trace ADC value measured with Unipolar DW-PRESS is nearly significantly higher in OW vs. OG ($p = 0.088$), indicating that more subjects are needed to establish this difference. The difference in ADC's in OW and OG are due to structural differences in the composition between gray and white matter, and higher ADC's of the three main metabolite groups in white matter compared to gray matter have been reported [103]. The trace ADC's in frontal gray matter have greater coefficients of variation (CV%), likely due to challenges experienced with acquiring the spectra near the sinus regions, where effects from B_0 inhomogeneity are greater and water suppression is less effective. It is known that tCho tends to have lower trace ADC's than tCr and tNAA [103]. This trend can be seen from all acquisitions in occipital gray and white matter, as the trace ADC of tCho are lower in those regions, except for Trace DW-PRESS in OG where it is comparable to the values for tNAA and tCr. The trend is also apparent in the frontal gray matter for Trace DW-PRESS, but not for the Bipolar or Unipolar measurements, likely partly due to the complicating factors in frontal lobe MRS acquisitions mentioned above.

With a diffusion time of 10.8 ms, the trace-weighted sequence implemented for this study approaches the short diffusion time regime ($t_d \approx 10$ ms or less), resulting in higher estimates of ADC's compared to those found with the Unipolar ($t_d = 25.6$ ms) and Bipolar ($t_d = 58.8$ ms) DW-

PRESS. Figures 4-8, 4-9, and 4-10 show that the in vivo metabolite and water spectra measured with Trace DW-PRESS sequence experience a larger signal drop compared to the other sequences, for the same b-value range. Previous reports have shown this trend in animals and to some extent in humans [92–95,112]. Although the diffusion time of Unipolar sequence is only slightly greater than twice that of Trace DW-PRESS, the signal attenuation of the spectra more closely resembles that of the Bipolar sequence, even for water. This finding indicates that there may be a certain threshold in the diffusion time under which the metabolite diffusivity becomes less restricted. The general range of trace ADC values found in this study are within a reasonable range of those reported at shorter diffusion times (0.20 to 0.30 μm^2/ms), although the values in occipital white matter tend to be higher, with the highest average at approximately 0.35 μm^2/ms (Table 4-3). These higher values, however, may be expected as the ADC's in white matter tend to be higher than those found in the gray matter regions, for which the highest average trace ADC value found is approximately 0.30 μm^2/ms.

4.7 Conclusion

This study presents the first demonstration of the single-shot diffusion trace-weighted sequence in a clinical scanner at 3T, and we compare the trace ADC values obtained with this sequence to those computed from the conventional bipolar and unipolar DW-PRESS sequences acquired with three orthogonal directions and negative and positive diffusion gradient polarities. Results show excellent agreement of phantom trace ADC's computed with all sequences, and in vivo ADC's agree well in both the difference between OG and OW matter, as well as the overestimation of metabolite and water ADC's due to a shorter diffusion time. The diffusion trace-weighted sequence could provide an estimate of the trace ADC of the main metabolite groups

(tNAA, tCr, and tCho) in a much shorter scan time (by nearly a factor of three) compared to conventional DW-PRESS acquisitions.

4.8 Appendix

4.8.1 Derivation of b-value formula for Bipolar DW-PRESS

Referring to Figure 4-1A, the diffusion-sensitizing gradient $G(t)$ along a single gradient axis, with maximum amplitude G, can be defined in a piecewise fashion over 15 time intervals. Each time interval T_i $(i = 1, 2, \dots, 15)$ is defined as the set

$$T_i = \{t \mid t_{i-1} \leq t \leq t_i\}$$

and each segment $G_i(t)$ of the piecewise gradient function $G(t)$ is defined over the interval T_i.

For simplicity of the calculation, assume the starting time point $t_0 = 0$, which is at the start of the first gradient lobe before the first 180° RF pulse. The set of time points t_i can then be listed as follows:

$t_0 = 0, t_1 = \zeta, t_2 = \delta, t_3 = \delta + \zeta, t_4 = \delta + \tau + \zeta, t_5 = \delta + \tau + 2\zeta, t_6 = 2\delta + \tau + \zeta, t_7 = 2(\delta + \zeta) + \tau, t_8 = \Delta, t_9 = \Delta + \zeta, t_{10} = \Delta + \delta, t_{11} = \Delta + \delta + \zeta, t_{12} = \Delta + \delta + \tau + \zeta, t_{13} = \Delta + \delta + \tau + 2\zeta, t_{14} = \Delta + 2\delta + \zeta + \tau, t_{15} = \Delta + 2(\delta + \zeta) + \tau$

The piecewise gradient is then defined as

$G_1(t) = \frac{G}{\zeta}t$, $G_2(t) = G$, $G_3(t) = -\frac{G}{\zeta}\big(t - (\delta + \zeta)\big)$, $G_4(t) = 0$, $G_5(t) = -\frac{G}{\zeta}\big(t - (\delta + \zeta + \tau)\big)$, $G_6(t) = -G$, $G_7(t) = -\frac{G}{\zeta}(t - (2(\delta + \zeta) + \tau))$, $G_8(t) = 0$, $G_9(t) = \frac{G}{\zeta}(t - \Delta)$, $G_{10}(t) = G$, $G_{11}(t) = -\frac{G}{\zeta}(t - (\Delta + \delta + \zeta))$, $G_{12}(t) = 0$, $G_{13}(t) = -\frac{G}{\zeta}(t - (\Delta + \delta + \zeta + \tau))$, $G_{14}(t) = -G$, $G_{15}(t) = \frac{G}{\zeta}(t - (\Delta + 2(\delta + \zeta) + \tau))$

The corresponding gradient moments $F_i(t) = \int G_i(t')dt'$ are computed for each interval T_i as

$F_1(t) = \frac{G}{2\zeta}t^2$, $F_2(t) = G(t - \frac{\zeta}{2})$, $F_3(t) = -\frac{G}{2\zeta}[(t - (\delta + \zeta))^2 - 2\delta\zeta]$, $F_4(t) = G\delta$, $F_5(t) = \frac{G}{2\zeta}[(t - (\delta + \zeta + \tau))^2 + 2\delta\zeta]$, $F_6(t) = G\left[t - \frac{1}{2}(3\zeta + 2\tau)\right]$, $F_7(t) = -\frac{G}{2\zeta}[(t - (2(\delta +$

$\zeta) + \tau))^2 - 4\delta\zeta]$, $F_8(t) = 2G\delta$, $F_9(t) = -\frac{G}{2\zeta}[(t-\Delta)^2 - 4\delta\zeta]$, $F_{10}(t) = -G\left[t - \frac{1}{2}(2\Delta + \zeta + 4\delta)\right]$, $F_{11}(t) = \frac{G}{2\zeta}[(t-(\Delta+\delta+\zeta))^2 + 2\delta\zeta]$, $F_{12}(t) = G\delta$, $F_{13}(t) = -\frac{G}{2\zeta}[(t-(\Delta+\delta+\zeta+\tau))^2 - 2\delta\zeta]$, $F_{14}(t) = -G\left[t - \frac{1}{2}(2(\Delta+\tau)+3\zeta+4\delta)\right]$, $F_{15}(t) = \frac{G}{2\zeta}(t-(\Delta+2(\delta+\zeta)+\tau))^2$

For simplicity, no reversal of sign due to the refocusing pulses is considered in the gradient moment expressions above, as the b-value calculation in the end only involves the squares of the gradient moments, $F_i^2(t)$.

Now, the following integral can be defined, which is the integration of the square of the gradient moment $F_i(t)$ over the appropriate time interval T_i:

$$H_i = \int_{t_{i-1}}^{t_i} F_i^2(t)dt$$

The b-value is then the summation

$$b = \sum_{i=1}^{15} H_i$$

The values of H_i can found by straightforward integration and are listed as follows:

$H_1 = \frac{G^2\zeta^3}{20}$, $H_2 = \frac{G^2(\delta-\zeta)}{3}\left[\delta^2 + \frac{\zeta^2}{4} - \frac{\delta\zeta}{2}\right]$, $H_3 = G^2\zeta\left[\delta^2 + \frac{\zeta^2}{20} - \frac{\delta\zeta}{3}\right]$, $H_4 = G^2\delta^2\tau$, $H_5 = G^2\zeta\left[\delta^2 + \frac{\zeta^2}{20} + \frac{\delta\zeta}{3}\right]$, $H_6 = \frac{G^2(\delta-\zeta)}{3}\left[7\delta^2 + \frac{\zeta^2}{4} - \frac{\delta\zeta}{2}\right]$, $H_7 = G^2\zeta\left[4\delta^2 + \frac{\zeta^2}{20} - \frac{2\delta\zeta}{3}\right]$, $H_8 = 4G^2\delta^2(\Delta - 2(\delta+\zeta) - \tau)$, $H_9 = H_7$, $H_{10} = H_6$, $H_{11} = H_5$, $H_{12} = H_4$, $H_{13} = H_3$, $H_{14} = H_2$, $H_{15} = H_1$

Adding these terms, the final formula for the b-value of the Bipolar DW-PRESS sequence is

$$b_{Bipolar} = \gamma^2 G^2 (2\delta)^2 \left\{\Delta - \frac{2\delta}{3} - \frac{(\tau-\zeta)}{2} - \frac{1}{12}\left(\frac{\zeta}{\delta}\right)^2\left(\delta - \frac{\zeta}{5}\right)\right\}$$

The above formula assumed a gradient applied along a single axis. If the diffusion-sensitizing gradient is applied along all axes, with a directional scaling vector $\vec{n} = (n_x, n_y, n_z)$, then the squared gradient amplitude above is replaced by $G^2 = \| G \cdot \vec{n}\|^2 = \left\|\vec{G}_d\right\|^2$, giving the general formula shown in the main text.

4.8.2 Derivation of b-value formula for Unipolar and Trace DW-PRESS

For Unipolar DW-PRESS (Figure 4-1B), the diffusion-sensitizing gradient $G(t)$ along a single gradient axis, with maximum amplitude G, is defined a piecewise fashion over 7 time intervals, where each time interval T_i $(i = 1, 2, \dots, 7)$ is defined as the set

$$T_i = \{t \mid t_{i-1} \leq t \leq t_i\}$$

and each segment $G_i(t)$ of the piecewise gradient function $G(t)$ is defined over the interval T_i.

For simplicity of the calculation, assume the starting time point $t_0 = 0$, which at the start of the first gradient lobe. In the Unipolar DW-PRESS case, no reversal of sign due the refocusing pulse is considered in the expressions for the gradient moments, since the b-value calculation will only consider the square of the gradient moments, $F_i^2(t)$.

In the case for Trace DW-PRESS (Figure 4-1C), the same time intervals apply for a single bipolar gradient pair, of which there are four along a single gradient axis. Therefore, the following derivation applies for both types of sequences, except that the final result is multiplied by 4 for Trace DW-PRESS.

The set of time points t_i are listed as follows:

$$t_0 = 0, t_1 = \zeta, t_2 = \delta, t_3 = \delta + \zeta, t_4 = \Delta, t_5 = \Delta + \zeta, t_6 = \Delta + \delta, t_7 = \Delta + \delta + \zeta$$

The piecewise gradient is then defined as

$$G_1(t) = \frac{G}{\zeta}t\ ,\ G_2(t) = G\ ,\ G_3(t) = -\frac{G}{\zeta}\big(t - (\delta + \zeta)\big)\ ,\ G_4(t) = 0\ ,\ G_5(t) = -\frac{G}{\zeta}(t - \Delta)\ ,$$

$$G_6(t) = -G, G_7(t) = \frac{G}{\zeta}(t - (\Delta + \delta + \zeta))$$

The corresponding gradient moments $F_i(t)$ are the computed for each interval T_i as

$$F_1(t) = \frac{G}{2\zeta}t^2\ ,\ F_2(t) = G(t - \frac{\zeta}{2})\ ,\ F_3(t) = -\frac{G}{2\zeta}[(t - (\delta + \zeta))^2 - 2\delta\zeta]\ ,\ F_4(t) = G\delta\ ,$$

$$F_5(t) = -\frac{G}{2\zeta}[(t - \Delta)^2 - 2\delta\zeta], F_6(t) = -G\left[t - \left(\Delta + \delta + \frac{\zeta}{2}\right)\right], F_7(t) = \frac{G}{2\zeta}\big(t - (\Delta + \delta + \zeta)\big)^2,$$

Using the same definition of H_i given in the previous section, the b-value is the summation

$$b = \sum_{i=1}^{7} H_i$$

The values of H_i can found by straightforward integration and are listed as follows:

$H_1 = \frac{G^2\zeta^3}{20}$, $H_2 = \frac{G^2\delta^3}{3} - \frac{G^2\zeta^3}{12} + \frac{G^2\zeta^2\delta}{4} - \frac{G^2\zeta\delta^2}{2}$, $H_3 = \frac{G^2\zeta^3}{20} - \frac{G^2\zeta^2\delta}{3} + G^2\zeta\delta^2$, $H_4 = G^2\delta^2(\Delta - \delta - \zeta)$, $H_5 = H_3$, $H_6 = H_2$, $H_7 = H_1$

Adding these terms, the final formula for b-value of the Unipolar DW-PRESS sequence is

$$b_{Unipolar} = \gamma^2 G^2 \delta^2 \left[\left(\Delta - \frac{\delta}{3}\right) - \frac{1}{6}\left(\frac{\zeta}{\delta}\right)^2 \left(\delta - \frac{\zeta}{5}\right)\right]$$

Again, the above formula assumed a gradient applied along a single axis. If the diffusion-sensitizing gradient is applied along all axes, with a directional scaling vector $\vec{n}$, then the squared gradient amplitude above is replaced by $G^2 = \| G \cdot \vec{n}\|^2 = \left\|\vec{G}_d\right\|^2$, giving the general formula shown in the main text.

The b-value formula for Trace DW-PRESS is 4 times the b-value formula for the Unipolar case, since there are 4 bipolar pairs of gradients along each gradient axis, as compared to only one for Unipolar DW-PRESS. Hence, if the diffusion gradient is played along all axes, the b-value for Trace DW-PRESS is

$$b_{Trace} = 4\gamma^2 \left\|\vec{G}_d\right\|^2 \delta^2 \left[\left(\Delta - \frac{\delta}{3}\right) - \frac{1}{6}\left(\frac{\zeta}{\delta}\right)^2 \left(\delta - \frac{\zeta}{5}\right)\right]$$

Chapter 5 Single-Shot Diffusion Trace Spectroscopic Imaging using Radial Echo Planar Trajectories

5.1 Abstract

Purpose: Demonstrate the feasibility and evaluate the performance of single-shot diffusion trace-weighted radial echo planar spectroscopic imaging (Trace DW-REPSI) for quantifying the trace apparent diffusion coefficient (ADC) in phantom and *in vivo* using a 3T clinical scanner.

Methods: Trace DW-REPSI datasets were acquired in ten phantom and ten healthy volunteers, with a maximum b-value of 1,601 s/mm^2 and diffusion time of 10.75 ms. The self-navigation properties of radial acquisitions were used for corrections of shot-to-shot phase and frequency shift fluctuations of the raw data. *In vivo* trace ADCs of total N-acetyl-aspartate (tNAA), total creatine (tCr), and total choline (tCho) extrapolated to pure gray and white matter fractions were compared, as well as trace ADCs estimated in voxels within white or gray matter-dominant regions.

Results: Trace ADCs in phantom show excellent agreement with reported values, and *in vivo* ADC's agree well with the expected differences between gray and white matter. For tNAA, tCr, and tCho, the trace ADCs extrapolated to pure gray and white matter ranged from 0.18–0.27 and 0.26–0.38 μm^2/ms, respectively. In sets of gray and white matter-dominant voxels, the values ranged from 0.21–0.27 and 0.24–0.31 μm^2/ms, respectively. The overestimated trace ADCs from this sequence can be attributed to the short diffusion time.

Conclusion: This study presents the first demonstration of the single-shot diffusion trace-weighted spectroscopic imaging sequence using radial echo planar trajectories. The Trace DW-REPSI sequence could provide an estimate of the trace ADC in a much shorter scan time compared to conventional approaches that require three separate measurements.

5.2 Introduction

Diffusion-weighted magnetic resonance spectroscopy (DW-MRS) is able to explore the microstructural characteristics of in vivo tissues due to the predominantly intracellular compartmentalization of metabolites. In contrast, DW-MRI is only capable of probing water diffusion, which occurs throughout both the intra- and extra-cellular spaces. Since the majority of detectable metabolites reside within the cell where most biochemical processes occur, metabolite diffusion can directly reflect the tissue-specific structural and, to some extent, functional environment at the cellular level[70,71]. This compartment-specific assessment of tissue structure enables a clearer understanding of the cellular-level conditions and alterations that underlie various pathologies, such as cerebral ischemia and tumors[72–75], multiple sclerosis[76,77], and psychiatric disorders[78]. Therefore, DW-MRS provides a promising tool for further improving the etiology, diagnosis and monitoring of disease.

DW-MRS is challenging due to the diffusion-sensitization of the inherently low-SNR metabolite signals, requiring careful shot-to-shot phase and frequency corrections and multiple signal averages for accurate ADC quantification. Singe-voxel DW-MRS has generated reproducible in vivo ADC's of several major metabolites in human brain such as N-acetyl aspartate, creatine, and choline[79,103,113]. However, a major limitation of the single-voxel approach is that it can only be applied to relatively small anatomical regions per measurement. Few reports have

explored diffusion-weighted MR spectroscopic imaging (DW-MRSI), either using conventional phase-encoding or echo-planar k-space trajectories[114–116]. Compared to single-voxel methods, DW-MRSI faces greater technical challenges as it requires longer acquisition times and is more susceptible to motion-induced phase inconsistencies and other temporal instabilities among the spatially-encoded signal averages. Large diffusion gradients can also induce strong eddy currents that may influence the fidelity of phase and frequency encoding.

Both acquisition-based and post-processing procedures have been implemented for DW-MRSI to avoid and/or correct the corrupted signal averages and inconsistencies in phase- and frequency-encoding[105,114,115]. During acquisition, cardiac gating or electrocardiogram (ECG) triggering discards signal averages corrupted by pulsatile motion in real time, thus avoiding further signal attenuation not caused by the diffusion-sensitizing gradients alone[81]. Line-scan acquisitions with echo-planar readouts were implemented to more easily track and correct for phase inconsistencies in the diffusion-weighted data[117]. Navigator echoes can also be implemented in the pulse sequence to monitor the signal for relative phase inconsistencies, which can be retrospectively corrected in post-processing[104,114,115]. Further processing steps include those also commonly implemented for single-voxel DW-MRS, such as SNR thresholding, zero- and first-order phase corrections, and frequency drift corrections on the individual spectra[79,80,102,106,109]. The majority of these DW-MRSI techniques have relied on Cartesian sampling of k-space, including those using conventional phase-encoding or echo-planar trajectories.

Recently, radial ^{1}H echo planar spectroscopic imaging (REPSI) was demonstrated in the human brain and was shown to be more compatible with higher under-sampling factors compared to Cartesian EPSI for two-dimensional (2D) spatial acquisitions[4]. A key advantage of REPSI is that the radial trajectory allows for self-navigation of the readout signal and is less sensitive to

motion, due to the repeated traversal of the low spatial frequency region and k-space origin. The central k-space points ($k_x = k_y = 0$) are considered free of any spatial encoding and can therefore be used to construct a navigator signal to monitor the intershot phase and frequency inconsistencies of the radial projections. This approach was first shown by Kim et al. for motion-correction of spiral MRSI[118], and it was applied by Boer et al. for diffusion-weighted 2D REPSI with semi-LASER localization[21]. Therefore, unlike Cartesian DW-MRSI, it is possible to track the readout data without implementing a separate navigator echo within the pulse sequence. This self-navigation feature of radial sampling has been exploited for many MRI applications as well[24,119,120].

Apart from the acquisition and signal processing challenges in DW-MRSI, diffusion anisotropy of tissues can bias the in vivo ADC quantitation. Generally, the estimated ADC along any diffusion direction depends on the orientation of the subject with respect to the gradient frame of reference. To avoid this confounding factor, several studies have instead reported the trace of the diffusion tensor, which is an invariant quantity independent of the relative orientation between the gradient axes and the anatomy of interest[79–81,89,90]. Conventional methods require measurements along three orthogonal diffusion directions to determine the trace ADC[74,80,82], which could be time-consuming. Another potential source of bias is the additional, unintended diffusion-weighting caused by the interactions (cross terms) between the diffusion-sensitizing gradients and the localization, crusher, and other background gradients[83]. Such cross-term contributions can be eliminated by acquiring additional measurements with gradients of opposite polarity[80,82,84], however, also at the cost of longer scan time.

DW-MRSI based on PRESS localization[37], as opposed to other localization schemes such as STEAM[88], allows for a particular diffusion gradient configuration that can generate a signal weighted by the trace of the diffusion tensor within a single shot or TR. First proposed by Mori et

al. for DW-MRI[89] and later extended to single voxel DW-MRS by de Graaf et al.[90], the single-shot diffusion trace-weighted sequence is able to eliminate all cross terms between diffusion gradients and any background gradients while providing a diffusion trace-weighted signal that is suitable for directly estimating the trace ADC, without any additional measurements along orthogonal diffusion directions. A version of this sequence using localization by adiabatic selective refocusing (LASER) was proposed by Valette et al.[2] using a small bore animal scanner. However, to date, the validation and performance of this sequence for DW-MRSI in humans has not been shown, although it has been implemented on a clinical scanner for DW-MRI only[91,121].

In this work, we validated single shot diffusion-trace weighted MRSI using radial echo planar trajectories, both in vivo and in a phantom on a clinical 3T scanner. This study presents the first demonstration of DW-REPSI using the single-shot diffusion trace-weighted scheme proposed by de Graaf et al.[90], but which until recently had not been testable in humans due to earlier hardware limitations of clinical scanners. We report the in vivo trace ADC values of three main metabolite groups – total NAA, total Cr, and total Cho – and water, as well as six metabolites (NAA, Cr, Cho, Glu, mI, Lac) from a brain phantom. We also demonstrate the utility of self-navigation of the radial spokes, and demonstrate corrections for gradient delays based on calibration scans. A preliminary account of this work has been previously presented as an abstract[122].

5.3 Theory

5.3.1 Signal weighting with the b-matrix and the diffusion tensor

The b-matrix is primarily a function of the durations, amplitudes and timing parameters of the diffusion-sensitizing gradients, as well as all other localization, crusher, and background gradients. A key component of the b-matrix computation is the zero-order gradient moment $\vec{F}(t')$

$$\vec{F}(t') = \int_0^{t'} \vec{G}(t)\, dt \tag{5-1}$$

where $\vec{G}(t) \coloneqq \langle G_x(t), G_y(t), G_z(t) \rangle$ is defined as the vector of the applied time-varying gradients [96]. The matrix of b-values, $\boldsymbol{b}$, can then be defined as

$$\boldsymbol{b} = \gamma^2 \int_0^{\tau} \vec{F}(t') \otimes \vec{F}(t')\, dt' \tag{5-2}$$

where $\otimes$ denotes the outer product operation. Using this definition, the signal attenuation $S(\tau)$, after a time τ, can be described as

$$\ln\left(\frac{S(\tau)}{S_0}\right) = -\sum_{\alpha,\beta} \boldsymbol{b}_{\alpha\beta}\boldsymbol{D}_{\alpha\beta} \qquad \alpha, \beta \in \{x, y, z\} \tag{5-3}$$

where S_0 is the signal amplitude without diffusion-weighting and $\boldsymbol{D}$ is the diffusion tensor [89].

5.3.2 Diffusion-sensitizing gradient configuration for trace-weighting in PRESS

Building on the theory first proposed by Mori et al., Graaf et al. showed that a particular configuration of 12 sets of bipolar diffusion-sensitizing gradient lobes interleaved within the PRESS localization (Figure 5-1) leads to: (1) cancellation of signal weighted by off-diagonal terms in the diffusion tensor, and (2) elimination of any cross-terms originating between any static

background gradients (such as those arising from B_0 inhomogeneity) and the diffusion-sensitizing gradients. In contrast to spin-echo slice selection, the second refocusing pulse in the volumetric PRESS excitation is crucial for eliminating the cross-term contribution from background gradients. The resulting sequence achieves diffusion-trace weighting in only one measurement while simultaneously avoiding bias from cross-term contributions in the diffusion-weighting. Further details and examples of how these off-diagonal terms are cancelled in Equation 5-3 can be found in the aforementioned reports[2,89,90].

In a subsequent section, it is shown that the b-matrix for this trace-weighted sequence (excluding localization and crusher gradients) is invariant with respect to any unitary transformation, most importantly rotations. This key property is largely dependent on the fact that the off-diagonal terms in the b-matrix, i.e., $\boldsymbol{b}_{\alpha\beta}$ $(\alpha \neq \beta)$, are zero when only the diffusion-sensitizing gradients are considered. Inclusion of localization and crusher gradients adds only a very small contribution since these gradients are usually much smaller than the diffusion-sensitizing gradients.

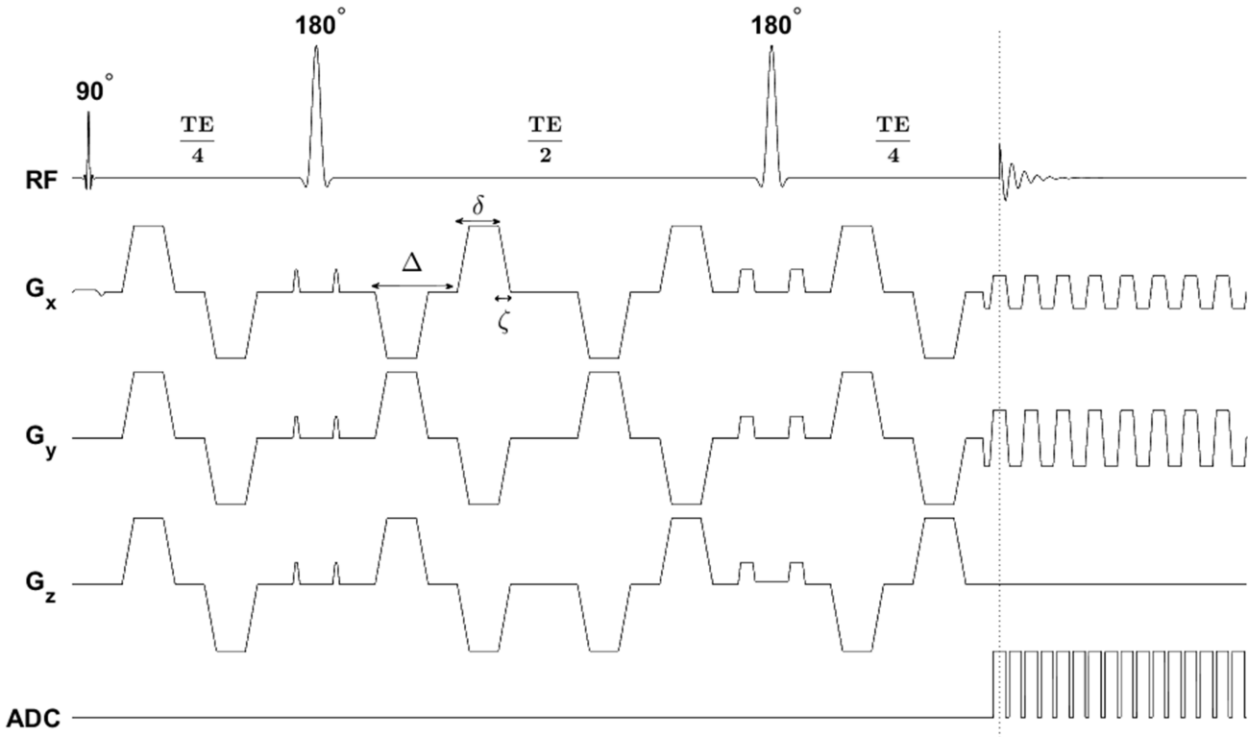

Figure 5-1: Pulse sequence diagram for Trace DW-REPSI. The water suppression module and outer volume saturation bands preceding the excitation pulse are not shown. Four pairs of bipolar diffusion-sensitizing gradients are placed along each gradient axis (12 in total) in a particular configuration that cancels the contribution of off-diagonal diffusion tensor elements to the signal attenuation. Cross terms between static background gradients and the diffusion-sensitizing gradients are also eliminated. The bipolar readout gradients spatially encode the signal along a radial projection while temporally encoding the chemical shift. For a single bipolar pair, the separation between the two trapezoidal gradients of opposite polarity is Δ. The gradient ramp time is ζ, and the flat top duration is (δ - ζ). This sequence requires that $TE_1 = TE_2$ with symmetric placement of the diffusion-sensitizing gradients around each 180° refocusing pulse.

5.3.3 Diffusion time and b-value for Trace DW-REPSI

The b-value for this sequence was reported for rectangular bipolar pairs in the original work by Mori et al.[89]. For trapezoidal gradients, used in this work (Figure 5-1), the b-value for the trace-weighted sequence (neglecting localization and crusher gradients) can be derived as

$$b = 12\,\gamma^2 G^2 \delta^2 \left[\left(\Delta - \frac{\delta}{3}\right) - \frac{1}{6}\left(\frac{\zeta}{\delta}\right)^2 \left(\delta - \frac{\zeta}{5}\right)\right] \quad (5\text{-}4)$$

where G is the amplitude of the diffusion-sensitizing gradient, ζ is the ramp time, and $(\delta - \zeta)$ is the flat top duration.

The use of bipolar diffusion-sensitizing gradient pairs leads to a relatively short diffusion time compared to other diffusion-weighted PRESS sequences that use bipolar pairs around each refocusing pulse[80,103], or a single unipolar pair around one of the refocusing pulses[102,115]. The diffusion time t_d can be inferred from the expression for the b-value, and is given by

$$t_d = \left(\Delta - \frac{\delta}{3}\right) - \frac{1}{6}\left(\frac{\zeta}{\delta}\right)^2 \left(\delta - \frac{\zeta}{5}\right) \tag{5-5}$$

5.3.4 Invariance of the b-matrix for Single-Shot Diffusion Trace-weighted PRESS

Given the diffusion-sensitizing gradients $G_x(t)$, $G_y(t)$, and $G_z(t)$ with the particular configurations shown in Figure 5-1, it can be shown from Equation 5-2 that the off-diagonal terms in the b-matrix are zero when neglecting crusher and localization gradients, i.e., $\boldsymbol{b}_{\alpha\beta} = 0$ $(\alpha \neq \beta)$. This property can be easily seen in Figure 5-2, which shows the gradient moments $F_x(t)$, $F_y(t)$, and $F_z(t)$, as well as the associated cross multiplicative functions $F_x(t) \cdot F_y(t)$, $F_y(t) \cdot F_z(t)$, and $F_x(t) \cdot F_z(t)$. For the trace-weighted sequence, the key property is that the functions $F_\alpha(t) \cdot F_\beta(t)$ (for $\alpha \neq \beta$) have equal contributions of positive and negative areas that sum to zero after integrating over the TE period[89]:

$$\boldsymbol{b}_{\alpha\beta} = \gamma^2 \int_0^{TE} F_\alpha(t) \cdot F_\beta(t)\, dt = 0 \quad (\alpha \neq \beta) \tag{5-6}$$

Because the gradient amplitudes are equal along all axes, it is straightforward to note that

$$\boldsymbol{b}_{xx} = \boldsymbol{b}_{yy} = \boldsymbol{b}_{zz} = \gamma^2 \int_0^{TE} F_\alpha^2(t)\, dt \quad \{\alpha = x, y, z\} \tag{5-7}$$

Hence, the b-matrix is a diagonal matrix with identical entries, again provided that only the diffusion-sensitizing gradients are considered in Equation 5-2.

Now, suppose that the matrix $Q_{\Omega_0}^{\Omega'}$ represents a unitary transformation, such as a rotation from the scanner frame Ω_0 to a new frame Ω'. The vector of time-varying gradients $\vec{G}(t)$ can then be represented in the Ω' frame as $\vec{G}'(t) = Q\vec{G}(t)$. Correspondingly, the vector of gradient moments is transformed in the same manner: $\vec{F}'(t) = Q\vec{F}(t)$. So, in this new frame, the elements of transformed b-matrix $\boldsymbol{b}' = [\boldsymbol{b}]_{\boldsymbol{\Omega}'}$ are:

$$\boldsymbol{b}'_{\alpha\beta} = \gamma^2 \int_0^{TE} F'_\alpha(t) \cdot F'_\beta(t)\, dt = \gamma^2 \int_0^{TE} \left(\sum_\epsilon Q_{\alpha\epsilon} \cdot F_\epsilon(t)\right)\left(\sum_\sigma Q_{\beta\sigma} \cdot F_\sigma(t)\right) dt \tag{5-8}$$

Expanding these terms and using Equation 5-6 and Equation 5-7,

$$\boldsymbol{b}'_{\alpha\beta} = \gamma^2 \left(Q_{\alpha x}Q_{\beta x} + Q_{\alpha y}Q_{\beta y} + Q_{\alpha z}Q_{\beta z}\right) \int_0^{TE} F_\alpha^2(t)\, dt \tag{5-9}$$

Now, a general property of any real unitary matrix Q is that

$$\begin{aligned} \sum_\epsilon Q_{\alpha\epsilon}Q_{\alpha\epsilon} &= 1 \\ \sum_\epsilon Q_{\alpha\epsilon}Q_{\beta\epsilon} &= 0 \end{aligned} \tag{5-10}$$

Hence, from Equation 5-9, $\boldsymbol{b}'_{\alpha\beta} = 0$ for $\alpha \neq \beta$, and $\boldsymbol{b}'_{\alpha\alpha} = \gamma^2 \int_0^{TE} F_\alpha^2(t)\, dt = \boldsymbol{b}_{\alpha\alpha}$. Therefore,

$$[\boldsymbol{b}]_{\Omega_0} = [\boldsymbol{b}]_{\Omega'} \tag{5-11}$$

This shows that the b-matrix for any PRESS-based single-shot trace-weighted sequence is preserved under any rotation or unitary transformation of the scanner frame of reference. Because the b-matrix is diagonal, the signal weighting in Equation 5-3 involves only the diagonal elements of the diffusion tensor.

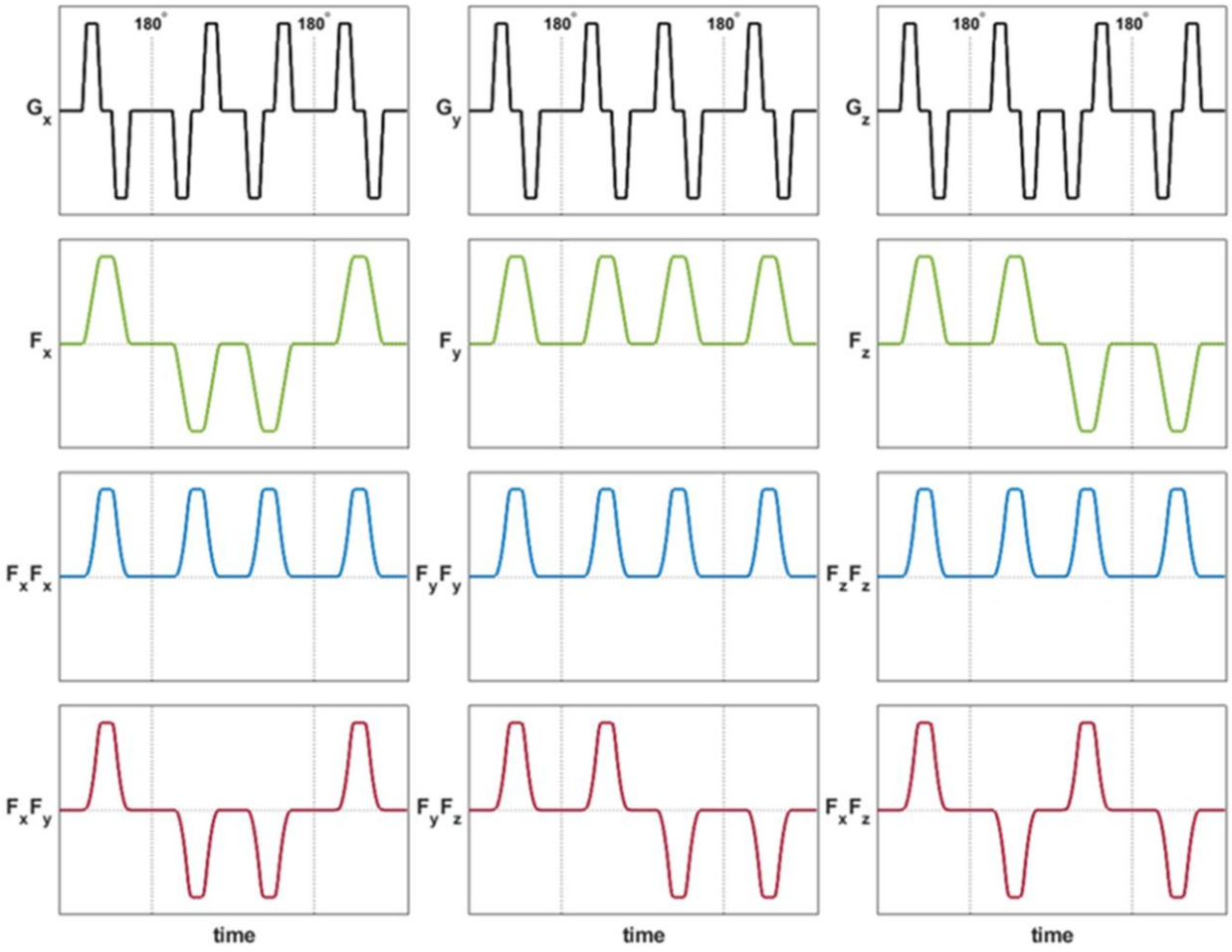

Figure 5-2: Gradients (G_x, G_y, and G_z) and zero-order gradient moments (F_x, F_y, and F_z) are shown along with the functions F_iF_j (i, j = x, y, z), whose integrals determine the diagonal and off-diagonal entries of the b-matrix (slice-select and crusher gradients are omitted). Note that the functions F_xF_y, F_yF_z, and F_xF_z (shown in red) have equal portions of negative and positive areas, which lead to a net integral of zero for these functions at the TE. Consequently, the off-diagonal terms b_{xy}, b_{yz}, and b_{xz} of the symmetric b-matrix are zero. Only the functions F_xF_x, F_yF_y and F_zF_z (shown in blue) have non-zero net positive integrals that contribute to the diagonal terms b_{xx}, b_{yy}, and b_{zz}, respectively.

5.4 Methods

All measurements were made using a Siemens Prisma 3T scanner (Siemens Healthcare, Munich, Germany) with a maximum net slew rate limit of 200 mT/m/ms and a maximum gradient amplitude limit of 80 mT/m per axis. A 16-channel receive head coil was used for both the phantom and in vivo acquisitions. Localization of the entire phantom or brain volume was achieved with T_1-weighted axial, coronal, and sagittal two-dimensional MRI's acquired with TR/TE = 250 ms/2.49 ms, field-of-view (FOV) = 240 × 240 mm^2, 1.25 × 1.25 mm^2 in-plane resolution, and 35 slices of 4 mm thickness each.

Both phantom and in vivo acquisitions were acquired with TE = 144 ms and TR = 2.25 s, FOV of 320 × 320 mm^2 with a 32 × 32 matrix size (in-plane resolution = 1 × 1 cm^2), and PRESS-based volumetric excitation[37,90]. The slab thickness and in-plane dimension of the volume-of-interest (VOI) differed between phantom and in vivo acquisitions, and these details are reported in subsequent sections. Global water suppression was achieved using a WET module[39]. Non-water suppressed data was acquired for coil sensitivity estimation, eddy current phase correction, and for computing water ADC maps.

Spectroscopic imaging data was sampled with radial echo-planar trajectories using a symmetric bipolar gradient echo train. The ADC bandwidth was 100 kHz with 32 radial k-space points acquired per spoke. Each readout gradient lobe had a ramp time of 50 μs and flat top duration of 320 μs, leading to spectral width of 1190 Hz after separation of odd and even echoes. Radial datasets consisted of 33 spokes with uniform angular sampling, i.e., the angular spacing between the spokes was $180°/33 \approx 5.45°$. This acquisition is technically undersampled at an acceleration factor (AF) of 1.52, as the required number of spokes for a Nyquist-sampled 32 × 32 k-space

matrix is $\frac{\pi}{2}(32) \approx 50$. An odd number of uniformly-spaced spokes reduces coherent aliasing and thereby further reduces the degree of undersampling artifacts[123], which are anyway constrained outside of the resulting (reduced) circular field-of-view[51]. The nominal reduced circular FOV with this number of spokes has a diameter of $\frac{33}{32} \cdot \frac{2}{\pi} \cdot 320\ mm \approx 210\ mm$, which is more than sufficient to resolve the signal without streaking artifacts within the VOI whose maximal dimension was 120 mm in the anterior-posterior direction.

All diffusion-weighted acquisitions used trapezoidal gradients with ramp time ζ = 1.9 ms and flat top duration of 4.6 ms (δ = 6.5 ms). The time gap between the two lobes of a single bipolar pair was 4.6 ms (Δ = 13 ms). The diffusion time (t_d) was 10.75 ms.

5.4.1 Phantom Experiments

The GE "Braino" phantom (GE Medical Systems, Milwaukee, WI, USA), containing N-acetylasparate (NAA, 12.5 mM), creatine (Cr, 10.0 mM), choline (Cho, 3.0 mM), Glutamate (Glu, 12.5 mM), myo-inositol (mI, 5.0 mM), and Lactate (Lac, 5.0 mM) was used for all phantom acquisitions.

The in-plane dimensions of the VOI for phantom acquisitions was 10 × 10 cm^2 and the slab thickness was 1.5 cm, resulting in an individual voxel volume of 1.5 mL (Figure 5-3). Two b-values were acquired: one null b-value (no diffusion-sensitizing gradients) and the other at b = 1,500 s/mm^2, corresponding to a gradient amplitude of 63.4 mT/m. For the null b-value, the number of averages was 5 and 1 for water-suppressed and non-water-suppressed acquisitions, respectively. For the high b-value, the number of averages was 10 and 2 for water-suppressed and non-water-suppressed acquisitions, respectively. The average linewidths of the water magnitude

peak after manual shimming was 5.2 Hz. The total scan time for one measurement was approximately 30 minutes.

The means and standard deviations of the phantom ADC values were determined in five areas within the VOI to assess the degree of the homogeneity of ADC values across the VOI (Figure 5-6(B)). The VOI matrix was divided into 5 central subregions with 10×10, 8×8, 6×6, 4×4, and 2×2 voxels to measure the variation of ADC values over these areas within the VOI.

To further assess the accuracy of ADC estimates from Trace DW-REPSI, ten measurements from a single-voxel variant of the diffusion trace-weighted sequence (Trace DW-PRESS) were acquired in the phantom to compare against the ADC values derived from the Trace DW-REPSI sequence. The voxel size was $2.5 \times 2.5 \times 2.5$ cm^3 and three b-values were acquired: 4 s/mm^2, 1,021 s/mm^2, and 1,707 s/mm^2 with a corresponding number of 18, 36 and 52 averages and 2, 4, and 6 averages for the water and non-water-suppressed acquisitions, respectively. All ADC values in the GE Braino phantom were compared with the reference values reported by Landheer et al.[101].

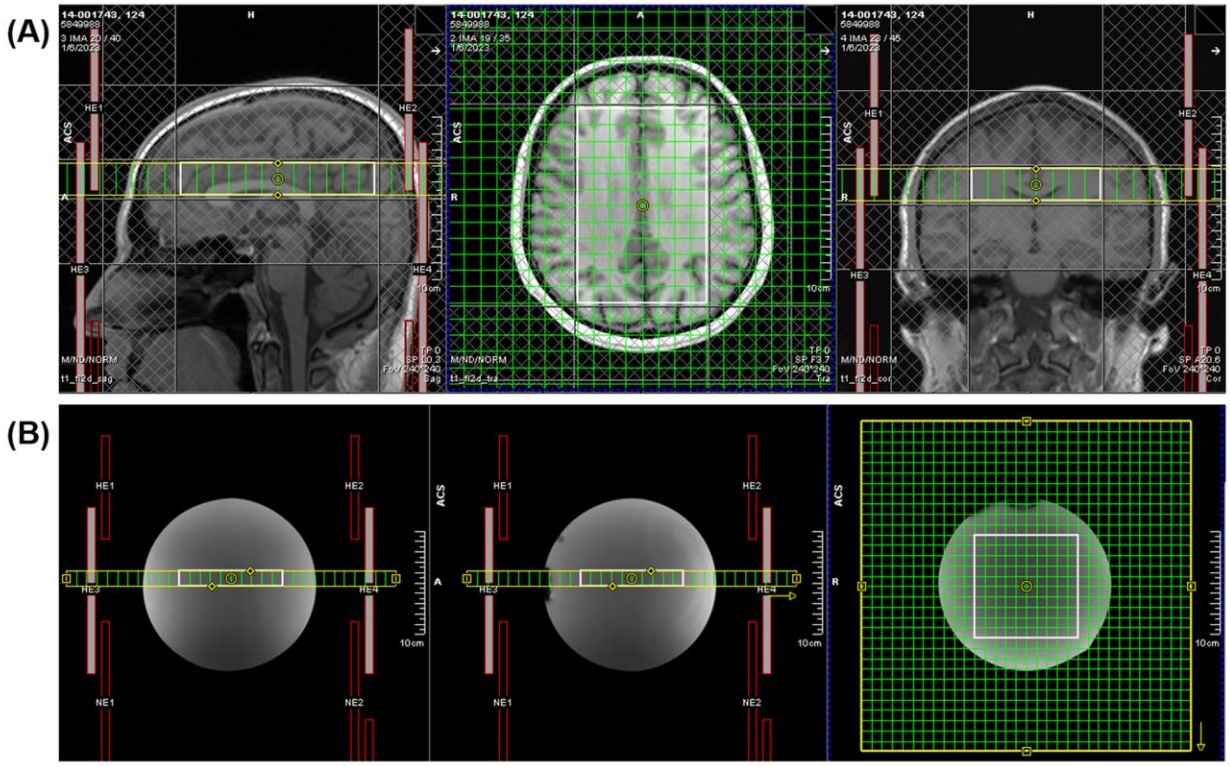

Figure 5-3: **(A)** Localization the volume-of-interest (VOI) in a healthy volunteer. With a transversal orientation, the VOI was placed superior to the ventricle region, partially covering the corpus callosum. The slab thickness was 2 cm in the superior-inferior (SI) direction, and the dimensions in the left-to-right (LR) and anterior-posterior (AP) directions was typically 75-80 mm and 115-120 mm, respectively, resulting in an individual voxel volume of 2 mL. Outer volume saturation bands (centered at -3.4 ppm from water) were placed around the VOI and over the intracranial lipid layer to suppress contamination from fat signal. **(B)** Localization for the GE Braino phantom. The VOI in-plane dimensions were 10 × 10 cm^2 with slab thickness of 1.5 cm (voxel volume of 1.5 mL).

5.4.2 In Vivo Experiments

Twelve healthy volunteers (4 females and 8 males, ages = 39.9 ± 16 years) were recruited to participate in this study and gave informed consent according to local institutional review board guidelines. Of these twelve, data from two volunteers was excluded due to inadequate spectral quality.

The in-plane dimensions of the VOI for in vivo acquisitions ranged from 75 – 80 mm in the left-to-right dimension (x), and 115-120 mm in the anterior-posterior dimension (y). The slab thickness was 2 cm, resulting in an individual voxel volume of 2 mL. The VOI orientation was transversal and the slab was placed superior to the ventricle region, partially covering the corpus callosum (Figure 5-3). Six outer volume saturation bands, centered at -3.4 ppm from water, were placed around the VOI to suppress the predominant fat signal from the intracranial lipid layer. The average linewidth of the water magnitude peak after manual shimming was 22.1 Hz. Sufficient in vivo water signal was available at the highest b-value to allow for adequate eddy current phase corrections, water ADC estimations, and navigator-based corrections[95].

Data sets for two b-values were acquired: one low b-value at 51 s/mm^2 and a higher b-value at 1,601 s/mm^2, corresponding to diffusion-sensitizing gradient amplitudes of 11 mT/m and 64 mT/m, respectively. For the low b-value, the number of averages was 6 and 1 for water-suppressed and non-water-suppressed acquisitions, respectively. For the high b-value, the number of averages was 14 and 2 for water-suppressed and non-water-suppressed acquisitions, respectively. The total scan time – including localization, shimming, water suppression adjustments and other preparatory procedures – was approximately 50 minutes. Due to scan time restrictions, an additional single voxel Trace DW-PRESS acquisition was infeasible within the same scan session.

Trace DW-REPSI data from one healthy volunteer was scan twice to determine the reproducibility of metabolite and ADC maps across the two scan sessions.

5.4.3 Data Processing

Gradient Delay Calibration and Correction

Uecker and Block presented a method for determining the k-space shifts caused by gradient delays along the y and x gradient axes[124]. Two pairs of calibration spokes were acquired: one pair at the projection angles of 0° and 180° and the other at 90° and 270° to determine the k-space shifts $\Delta\kappa_x$ and $\Delta\kappa_y$, respectively, for each channel and for all even and odd echoes along the entire bipolar readout. The values of $\Delta\kappa_x$ and $\Delta\kappa_y$ for the echoes over the first 12 ms (corresponding to approximately 16 time points) were averaged and then used for correcting the k-space shift of rest of the time points. This extrapolation was done to avoid the influence of noise and other instabilities (e.g., motion) in the cross-correlation analysis used for computing the relative offset between the echo peaks of spokes acquired at opposite angles (Figure 5-4).

Let $S(k_\rho, \theta)$ be the k-space signal for the spoke at projection angle θ, and let $\mathcal{F}_\rho$ denote the forward Fourier transform along the spatial dimension. The spatial projection at angle θ can then be written as $s(\rho, \theta) = \mathcal{F}_\rho^{-1}\left(S(k_\rho, \theta)\right)$. The raw data can be corrected for k-space shifts due to the gradient delay as follows:

$$s(\rho[m], \theta[n])^{corr} = s(\rho[m], \theta[n]) \cdot e^{-i2\pi\,(\Delta\kappa(\theta[n])\cdot\rho[m])} \tag{5-12}$$

where ρ represents the vector of spatial coordinates, m represents the number of samples per projection, and n represents the number of projection angles. The k-space shift $\Delta\kappa(\theta[n])$ for the spoke at angle $\theta[n]$, is computed from $\Delta\kappa_x$ and $\Delta\kappa_y$ as follows

$$\Delta\kappa(\theta[n]) = \Delta\kappa_x \cdot \cos^2(\theta[n]) + \Delta\kappa_y \cdot \sin^2(\theta[n]) \tag{5-13}$$

This correction was applied for all time points and channels, separately for the even and odd echoes[125]. Afterwards, the signal was transformed back to the k-space domain, i.e., $S(k_\rho, \theta)^{corr} = \mathcal{F}_\rho(s(\rho, \theta)^{corr})$, and the even echoes were then time-reversed relative to the odd echoes.

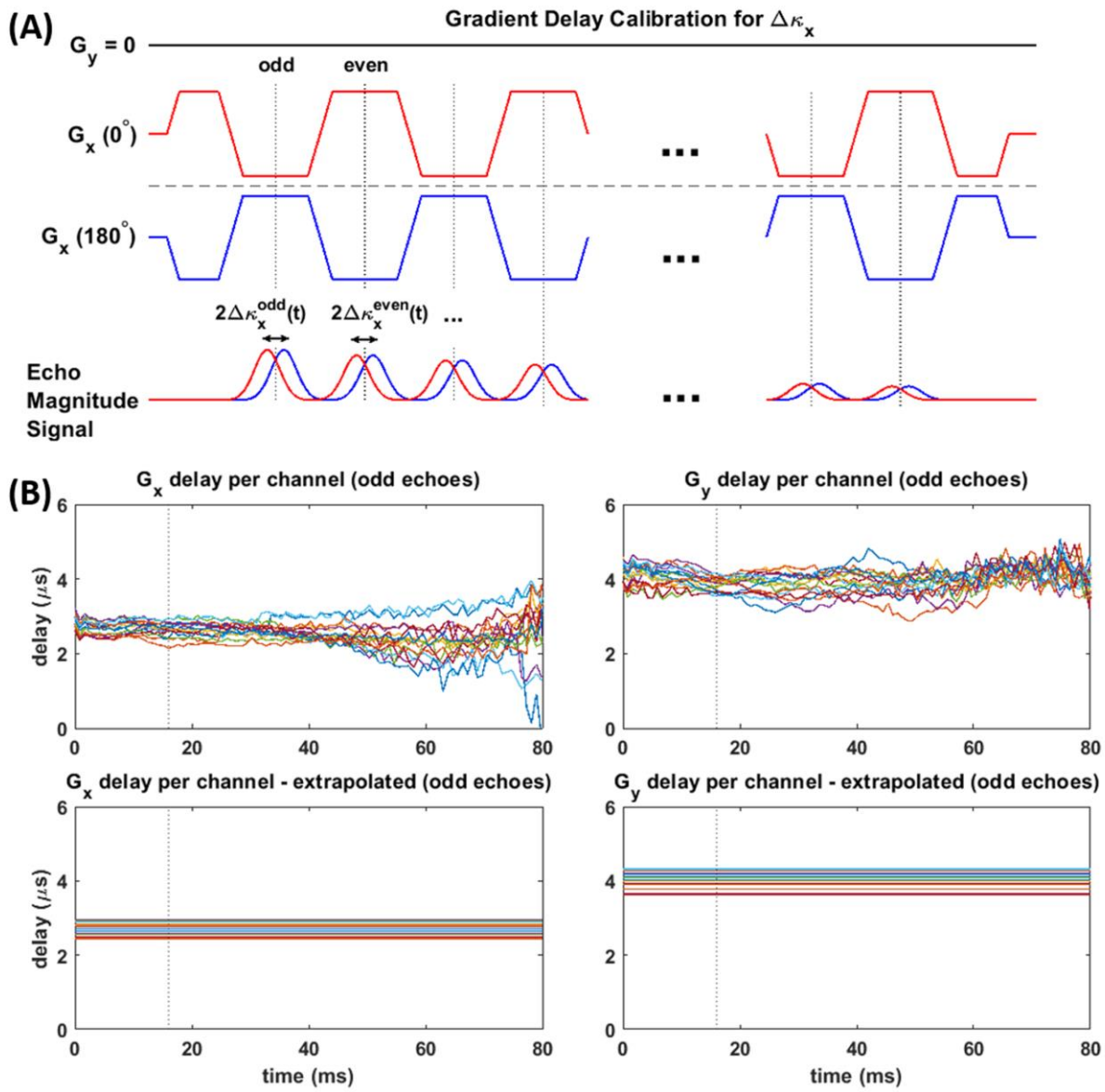

Figure 5-4: **(A)** Gradient echo trains used for acquiring spokes at 0° (red) and 180° (blue) to calibrate the k-space shift $\Delta\kappa_x$ caused by gradient delay in G_x. The gradient G_y is maintained at zero. The same procedure is done for determining $\Delta\kappa_y$ where $G_x = 0$ and the G_y echo train samples spokes at angles 90° and 270°. The difference in echo peak maxima from echoes of spokes at opposing angles is used for computing the k-space shift. **(B)** Gradient delay per channel as a function of time (only the odd echoes of the symmetric bipolar readout are shown for simplicity). Each color represents a separate coil out of a total of 16. The average gradient delay per channel is determined from the first 16 ms (up to the dotted line), and this value is used for the correcting all 512 time points echoes for each spoke. The total readout duration is approximately 430 ms.

Echo-Planar Phase Correction and Combination of Even and Odd Echoes

Besides the phase evolution induced by the readout gradients, phase accrual due to chemical shift is also present throughout the frequency-encoding period. Consequently, the even and odd echoes acquire an apparent spatial shift in opposite directions. To correct for this effect, a linear frequency-dependent phase correction is applied to the spokes acquired from the even and odd echoes[43,126,127], $S_{even}(k_\rho[m], \theta[n], t[q])$ and $S_{odd}(k_\rho[m], \theta[n], t[q])$, respectively, where q represents the number of time points.

Let $\mathcal{F}_\tau$ denote the forward Fourier transform along the time dimension. Then, for a particular spoke at angle $\theta[n]$, the raw data matrix in the $k - f$ dimensions is $\hat{s}(k_\rho, \theta, f) = \mathcal{F}_\tau(S(k_\rho, \theta, \tau))$. The correction is then applied as follows:

$$\begin{aligned} \hat{s}_{even}(k_\rho[m], \theta[n], f[q])^{corr} &= \hat{s}(k_\rho[m], \theta[n], f[q]) \cdot e^{+i2\pi\,(m\Delta t \cdot f[q])} \\ \hat{s}_{odd}(k_\rho[m], \theta[n], f[q])^{corr} &= \hat{s}(k_\rho[m], \theta[n], f[q]) \cdot e^{-i2\pi\,(m\Delta t \cdot f[q])} \end{aligned} \tag{5-14}$$

where f is the vector of spectral frequencies and Δt is the ADC dwell time.

Following this correction (done for all spokes, channels, and averages), a time shift is applied to the even echoes in order to coherently add the signals from the even and odd echoes. The time shift between the odd and even echoes is exactly half the spectral dwell time $\Delta\tau$, therefore, the time signal from the even echoes is shifted by this amount before addition with the odd echo signal

$$\hat{s}(k_\rho[m], \theta[n], f[q])^{corr}$$

$$= \frac{1}{2}\Big(\hat{s}_{even}\big(k_\rho[m], \theta[n], f[q]\big)^{corr} \cdot e^{i2\pi\,(\frac{1}{2}\Delta\tau \cdot f[q])} \tag{5-15}$$

$$+ \hat{s}_{odd}\big(k_\rho[m], \theta[n], f[q]\big)^{corr}\Big)$$

Subsequent processing is done on the resulting signal in the time domain: $S(k_\rho, \theta, \tau)^{corr} = \mathcal{F}_\tau^{-1}\big(\hat{s}\big(k_\rho, \theta, f\big)^{corr}\big)$.

Self-Navigation

The self-navigation property of REPSI derives from the periodic traversal of the radial trajectory through the k-space origin during the readout[118]. The navigator FID's are extracted from the central k_0 points (Figure 5-5). The navigator FID for the spoke acquired at angle θ is written as

$$\tilde{S}_\theta(\tau[q]) = S(k_0, \theta, q\Delta\tau)^{corr} \tag{5-16}$$

where $k_0 = k_\rho[0]$ is the k-space origin. The j^{th} average of each spoke therefore has a corresponding navigator signal $\tilde{S}_{\theta,j}(\tau[q])$. For each channel, the (corrected) raw data $S_j(k_\rho, \theta, \tau)^{corr}$ undergoes further corrections in two stages.

The first stage involves phase alignment of the averages for a single spoke. This is done by first selecting the navigator signal $\tilde{S}_{\theta,P}(\tau)$ of the single average (denoted by P) which is most similar, in a least squares sense, to the median of the navigator signals of all averages, $med(\tilde{S}_\theta(\tau)) = median(\{\tilde{S}_{\theta,j}(\tau),\ j = 1, \dots, N_{avg}\})$, where N_{avg} is the number of averages per spoke. Then the zero-order phase correction $\varphi_{\theta,j}$ is:

$$\varphi_{\theta,j} = \underset{\varphi}{\operatorname{argmin}} \frac{1}{2} \left\| \tilde{S}_{\theta,P} - \tilde{S}_{\theta,j} e^{i\varphi} \right\|_2^2 \tag{5-17}$$

This phase correction is applied to the j^{th} average of the raw data as follows:

$$S_j^{(1)}(k_\rho, \theta, \tau) = S_j(k_\rho, \theta, \tau)^{corr} \cdot e^{i\varphi_{\theta,j}} \tag{5-18}$$

where $S^{(1)}(k_\rho, \theta, \tau)$ denotes the corrected data after the first stage. The navigator FID's must be re-calculated after the first stage, $\tilde{S}_\theta(\tau) \rightarrow \tilde{S}_\theta^{(1)}(\tau)$.

The second stage involves phase and frequency alignment of the spokes. For this step, a reference spoke at angle $\theta[M]$ is chosen with which to phase and frequency align the rest of the spokes. In this work, the spoke at angle $\theta = 0^\circ$ was chosen, although other spoke angles are possible, although this choice must be consistent. The navigator FID's for this reference spoke at angle $\theta[M]$ are averaged, and the rest of the averaged navigator FID's for all other angles are phase and frequency aligned with respect to the averaged reference navigator FID, $\tilde{S}_{\theta[M]}^{(1),avg}(\tau)$. For the spoke at angle $\theta[n]$, the zero-order phase and frequency shifts, $\varphi_{\theta[n]}$ and $\Delta f_{\theta[n]}$, are found as follows[46]:

$$\Delta f_{\theta[n]}, \varphi_{\theta[n]} = \underset{\Delta f, \varphi}{\operatorname{argmin}} \frac{1}{2} \left\| \tilde{S}_{\theta[M]}^{(1),avg}(\tau) - \tilde{S}_{\theta[n]}^{(1),avg} e^{i\varphi + i2\pi\Delta f \cdot \tau} \right\|_2^2 \tag{5-19}$$

These phase and frequency corrections are applied to the j^{th} average and spoke at angle $\theta[n]$ of the raw data (following the 1st stage) as follows

$$S_j^{(2)}(k_\rho, \theta[n], \tau[q]) = S_j^{(1)}(k_\rho, \theta[n], \tau[q]) \cdot e^{i\varphi_{\theta[n]}} \cdot e^{i2\pi(\Delta f_{\theta[n]}) \cdot \tau[q]} \tag{5-20}$$

Subsequent reconstruction is performed on the averaged signal, $S^{(2),avg}(k_\rho, \theta, \tau)$.

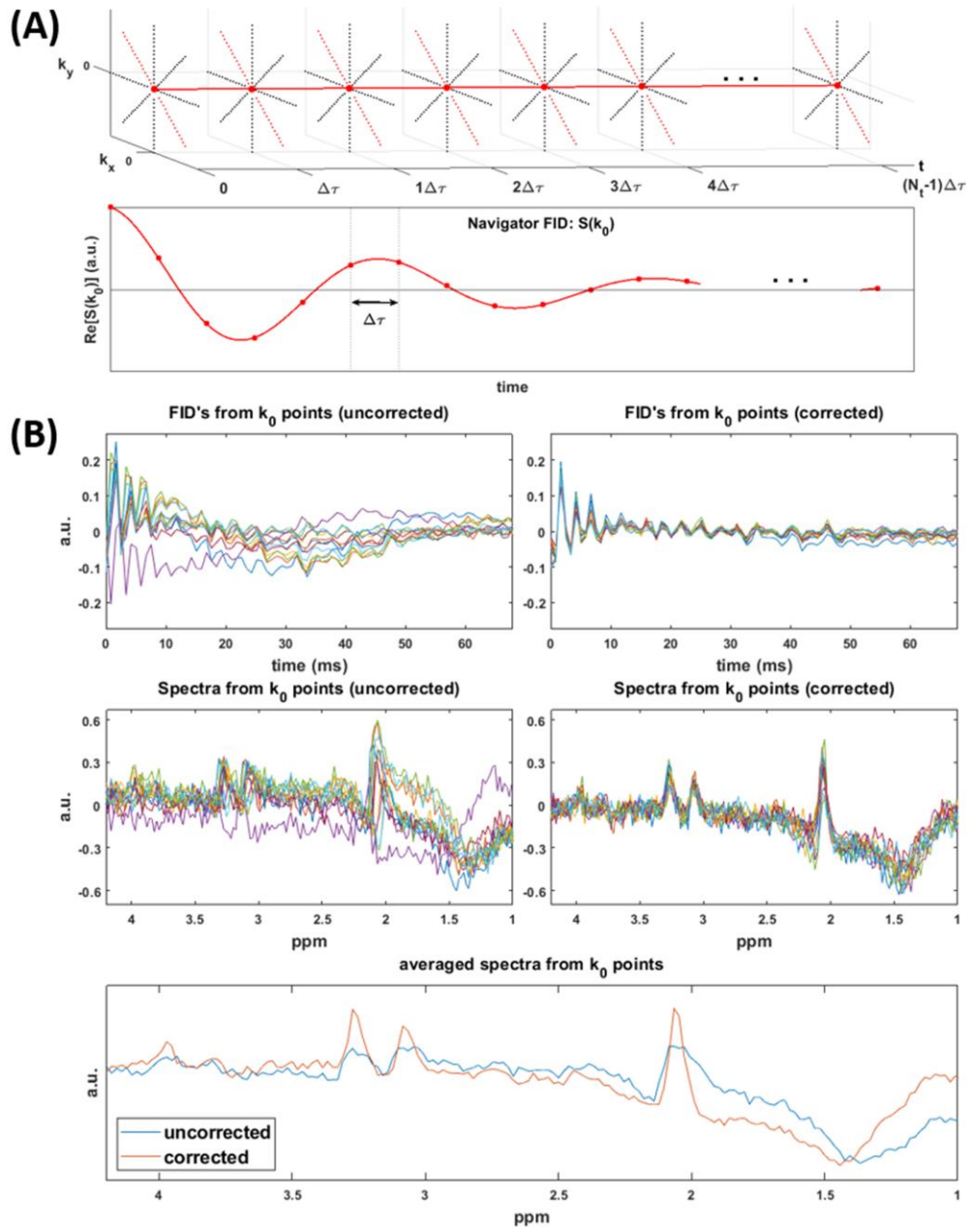

Figure 5-5: **(A)** The navigator FID for each spoke consists of the central k-space points (k_0) from all N_t time points, sampled with dwell time $\Delta\tau$. The number of odd and even echoes is $N_t = 512$ and $\Delta\tau = 840$ μs **(B)** *(Top)* Navigator FID's from each average. The navigator FID's are built from the central k-space points (k_0) sampled at the dwell time increment $\Delta\tau$. Only the time points from 0 – 70 ms are shown, although the total readout duration is approximately 430 ms. The necessary values for the phase and frequency drift corrections are determined from these navigator FID's, and these values are applied to the raw data. *(Middle)* The spectra corresponding the navigator FID's before and after corrections. To exclude averages overly corrupted by motion, signals with NAA SNR's below 1.2 standard deviations of the average SNR of the NAA peak were removed prior to further processing. *(Bottom)* The averaged uncorrected and corrected spectra. Note that

the uncorrected spectra suffer a loss of signal intensity due to the varying phases and frequency shifts of the individual averages.

Reconstruction and Post-Processing

After phase and frequency alignment of the averages in the first stage of pre-processing described above, the signal-to-noise ratio (SNR) of the NAA peak was determined, and the individual averages with NAA SNR's below 1.2 standard deviations away from the average NAA SNR were excluded from the data. This SNR threshold, similar to the methodology presented in other studies[80], ensures that averages overly corrupted by motion are excluded from further reducing the signal intensity in the reconstructed data. Following this step, the second pre-processing stage was preformed and the data was finally averaged and reconstructed on a coil-by-coil basis. The radial data was reconstructed using the non-uniform Fourier transform (NUFFT)[40]. The interpolation kernel size for the NUFFT was 5×5 and a ramp filter inversely proportional to the k-space radius was applied for density compensation. After reconstruction, eddy-current phase correction was applied using the water unsuppressed data[44]. Coil sensitivities were estimated from the water peak integrals of the low or null b-value acquisitions, followed by generalized least squares coil combination[110].

On a voxel-by-voxel basis, the reconstructed spectra were zero-order phase corrected to bring the NAA singlet at 2 ppm into absorptive mode and, for the in vivo data, the residual water signal and any remaining fat lipids around 1.35 ppm were removed using the Hankel-Lanczos singular value decomposition method[48]. Subsequently, a linear baseline, estimated from the noise regions between -0.5-1 ppm and 7.5-9 ppm, was subtracted from the spectrum.

5.4.4 Quantitation

Spectra were quantified using LC Model[49] (version 6.2-0T) with basis sets simulated in VESPA[50]. Exact timings with ideal 90° and 180° RF pulses were used in the pulse sequence simulation. For in vivo data sets, the basis set included the following metabolites: alanine, ascorbate, aspartate, choline (Cho), creatine (Cr), γ-aminobutyric acid, glucose, glutamine (Gln), glutamate (Glu), glycerophosphorylcholine, glutathione, lactate (Lac), myo-inositol (mI), n-acetylaspartate (NAA), n-acetylaspartylglutamate (NAAG), phosphorylcholine (PCh), phosphocreatine (PCr), phosphorylethanolamine, scyllo-inositol, and taurine. In vivo spectra were fitted between 0.8 to 4.2 ppm.

The LC Model concentration estimate, S_m, which is proportional to the peak integral of the particular metabolite m, was assumed to fit the standard model

$$S_m(b_k) = S_m^0 e^{-b_k \cdot ADC_m} \tag{5-21}$$

where b_k is the kth b-value and S_m^0 is the non-diffusion-weighted signal. With two b-values, the ADC for metabolite m was computed as

$$ADC_m = -\frac{\ln[S_m(b_2)/S_m(b_1)]}{(b_2 - b_1)} \tag{5-22}$$

For in vivo data, only concentration estimates with Cramer-Rao lower bounds (CRLB's) ≤ 20% were considered for further analysis. Voxels in the metabolite maps that did not intersect with the water VOI were also excluded in order to avoid spectra with inadequate eddy current phase corrections[114].

For phantom data, all estimates were taken into consideration and the average CRLB's across all measurements for each metabolite and b-value are reported in Table 5-1 and briefly summarized in the Results section.

	Measurements 1- 10: Phantom CRLB Values (%)	
	Null b-value (4 s/mm^2)	**High b-value (1,500 s/mm^2)**
NAA	5 ± 1 (16%)	5 ± 1 (15%)
Cr	6 ± 1 (14%)	7 ± 1 (12%)
Cho	7 ± 1 (13%)	10 ± 1 (13%)
Glu	24 ± 6 (25%)	31 ± 12 (38%)
Lac	20 ± 5 (26%)	27 ± 8 (31%)
mI	31 ± 10 (33%)	38 ± 13 (35%)

Table 5-1: Means, standard deviations, and coefficient of variance (CV%) of Cramer-Rao Lower Bound (CRLB) values of metabolite quantitation in the GE Braino phantom.

The water ADC map was derived from the non-water suppressed reconstructions. For each voxel, the water peak was zero-order phased into absorptive mode and 4× interpolated followed by numerical integration to estimate the area. These water peak areas were then used for computing the voxel-wise ADC's using the above model.

Estimates of ADCs in Pure White and Gray Matter

Voxel-wise estimations of the gray and white matter fractions were made based on the T_1-weighted localization images, using an in-house MATLAB (Mathworks, Natick, MA, USA) routine. Cerebral ventricle regions, containing dominant water signal from cerebral spinal fluid, were segmented and excluded from further quantitative analysis of metabolite ADC's. Regions on the T_1-weighted images corresponding to each voxel within the VOI were individually extracted

and segmented between the white and gray matter regions (Figure 5-10). The masks for distinguishing between the gray and white matter regions were determined automatically based on a pixel value threshold that separated these two regions. Based on these masks, the number of pixels n_{GM} and n_{WM} in the gray and white matter, respectively, were counted in each spectroscopic voxel. The fractions for gray and white matter were then defined as $f_{GM} = n_{GM}/(n_{GM} + n_{WM})$ and $f_{WM} = n_{WM}/(n_{GM} + n_{WM})$, respectively. For total NAA (tNAA = NAA + NAAG), total creatine (tCr = Cr + PCr), total choline (tCho = Cho + PCh), and water, linear regression was applied to estimate each respective metabolite ADC as a function tissue gray or white matter fraction[114,128,129]. Based on this regression, the ADC values for pure gray matter was estimated based on an extrapolation to $f_{GM} = 1$. The values for pure white matter correspond to ADC's extrapolated to $f_{GM} = 0$.

Distribution of ADCs in selected voxels in Gray and White Matter Regions

Eight specific voxels were selected to determine the distributions of ADC values in gray and white matter-dominant locations, as an alternative to the above analysis which provided extrapolated pure gray and white matter ADC values based on the correlations between the multi-voxel ADC's and corresponding gray and white matter fractions in those voxels.

Four voxels in gray matter- and four in white matter-dominant regions were extracted (Figure 5-10). In gray matter, these voxels were located in the following regions: (1) – right anterior cingulate cortex (RACC), (2) – left anterior cingulate cortex (LACC), (3) – right superior precuneus (RSP), and (4) – left superior precuneus (LSP). The white matter voxels were located in the following regions: (5) – right anterior corona radiata (RACR); (6) – right posterior corona radiata (RPCR); (7) – left anterior corona radiata (LACR); and (8) – left posterior corona radiata

(LPCR). The average ADC's and WM and GM fractions in each of these voxels are listed in Table 5-4.

The ADC's of tNAA, tCr, tCho, and water were compared between the white and gray matter locations, and with the values obtained from the regression analysis.

5.4.5 Statistical Analysis

Phantom

One-way ANOVA's were performed separately for each metabolite to assess the homogeneity of values across the five VOI subregions, and multiple comparisons tests with Bonferroni corrections were done to determine the specific regions that were significantly different from each other. An alpha level of $\alpha = 0.05$ was adopted to test of significance

Two-sample t-tests were conducted for each metabolite to determine any significant differences between the ten Trace DW-REPSI measurements of the 2×2 subregion (with cumulative volume of 6 mL and 40 individual values in total), and 10 measurements from single voxel DW-PRESS (voxel volume 15.6 mL).

Coefficients of variance for NAA, Cr, Cho, Glu, Lac, and mI were determined from the ten Trace DW-REPSI measurements in phantom. Percent errors were computed between the ADC values derived from the Trace DW-REPSI and the reference values reported in the literature.

In Vivo

For the ADC values extrapolated to pure gray and white matter fractions, separate one-way ANOVA's were performed to test for differences among the ADC's of tNAA, tCr, and tCho in gray matter and in white matter. A multiple comparisons analysis with Bonferroni correction was

done to determine the specific significant differences in the ADC values from these three metabolites. Paired t-tests were done separately for tNAA, tCr, and tCho to determine any significant differences in ADC's between gray and white matter.

For the ADC values extracted from the gray and white matter-dominant voxels, separate one-way ANOVA's were performed to test for difference among the ADC's of tNAA, tCr, and tCho in gray matter and in white matter locations. A multiple comparisons analysis with Bonferroni correction was done to determine the specific significant differences in the ADC values from these three metabolites. Paired t-tests were done separately for tNAA, tCr, and tCho to determine any significant differences in ADC's between gray and white matter.

To test for reproducibility of Trace DW-REPSI, the Pearson correlation coefficients were computed for the metabolite and ADC maps for tNAA, tCr, and tCho between two scan sessions for the same volunteer.

5.5 Results

5.5.1 Phantom

The ADC values of all six metabolites from Trace DW-REPSI acquisitions in phantom are shown in Table 5-2. The average ADC values of NAA, Cr, Cho, and Glu, and mI over the entirety of the VOI (10×10 voxel region) are consistent with values reported in the literature[101] and with values obtained with the single-voxel DW-PRESS. Mean values from other subregions (8×8 to 2×2) agree with values from valued derived from the entire VOI.

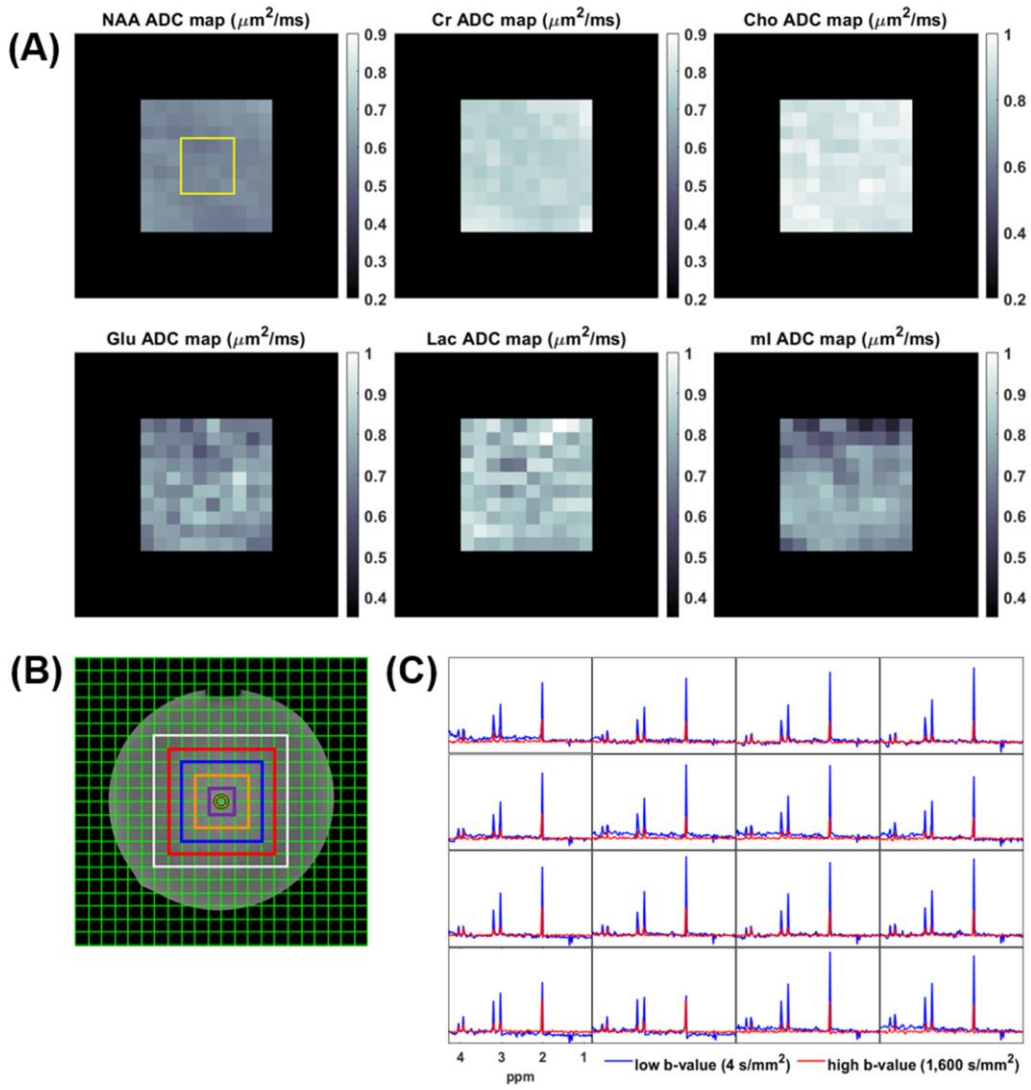

Figure 5-6: **(A)** Trace ADC maps computed from single shot diffusion trace-weighted REPSI in the GE "Braino" phantom. The NAA, Cr, and Cho maps have the least spatial inhomogeneity of trace ADC values, while the maps for Glu, mI, and Lac show greater variations across the volume-of-interest. **(B)** The 5 regions in which average ADC values were computed for assessing the degree of spatial homogeneity of the ADC values across the volume-of-interest. **(C)** Representative diffusion-weighted spectra, acquired with a null (4 s/mm^2) and high b-value (1,500 s/mm^2), are shown within the 4×4 voxel region within the yellow box on the ADC map of tNAA shown in (A). The average linewidths of the water magnitude peak after manual shimming was 5.2 Hz.

The means and standard deviations of the CRLB percentage values for NAA, Cr, Cho, Glu, Lac, and mI from the null b-value acquisition were 5 ± 1%, 6 ± 1%, 7 ± 1%, 24 ± 1%, 20 ± 1%,

and 31 ± 1%, respectively, and at the higher b-value, these values were 5 ± 1%, 7 ± 1%, 10 ± 1%, 31 ± 12%, 27 ± 8%, and 38 ± 13%, respectively.

With respect to reference values, the percent errors for NAA, Cr, Cho, Glu, mI, and Lac (from values averaged over the 10×10 region) are 2%, 1%, 1%, 4%, 29%, and 4%, respectively. The three main peaks of NAA, Cr, and Cho are the best quantified of all the metabolites, and their ADC's agree well with expected values and show the most homogeneity across the VOI, as shown in Table 5-2.

	Measurements 1-10: Braino Trace ADC values [mean ± standard deviation (CV%)] ($\mu m^2/ms$)					**Measurements 1-10: Single voxel ADC values**	**Reference ADC values**
	Voxel subregions within Volume-of-interest (VOI)						
	10×10	**8×8**	**6×6**	**4×4**	**2×2**		
NAA	0.58 ± 0.05 (8%)	0.58 ± 0.05 (8%)	0.57 ± 0.05 (9%)	0.57 ± 0.05 (9%)	0.58 ± 0.04 (7%)	0.61 ± 0.02 (3.89 %)	0.59 ± 0.01
Cr	0.77 ± 0.06 (8%)	0.76 ± 0.06 (7%)	0.76 ± 0.06 (8%)	0.76 ± 0.06 (8%)	0.76 ± 0.06 (8%)	0.78 ± 0.02 (3%)	0.78 ± 0.02 (Cr3.1)/0.84 ± 0.1 (Cr3.9)
Cho	0.92 ± 0.07 (8%)	0.91 ± 0.07 (8%)	0.91 ± 0.08 (9%)	0.9 ± 0.08 (9%)	0.92 ± 0.08 (8%)	0.93 ± 0.03 (3%)	0.91 ± 0.03
Glu	0.73 ± 0.16 (22%)	0.74 ± 0.18 (24%)	0.75 ± 0.21 (28%)	0.74 ± 0.23 (31%)	0.77 ± 0.23 (30%)	0.73 ± 0.07 (10%)	0.76 ± 0.03
Lac	0.84 ± 0.17 (20%)	0.84 ± 0.16 (19%)	0.82 ± 0.17 (21%)	0.81 ± 0.2 (24%)	0.82 ± 0.2 (24%)	0.77 ± 0.11 (14%)	0.64 ± 0.13
mI	0.73 ± 0.26 (36%)	0.75 ± 0.26 (35%)	0.77 ± 0.27 (35%)	0.76 ± 0.28 (37%)	0.72 ± 0.24 (33%)	0.76 ± 0.11 (15%)	0.76 ± 0.1

Table 5-2: Mean, standard deviation, and coefficient of variance (CV%) values of brain phantom trace ADC's, estimated from Trace DW-REPSI data. These values are calculated from sets of voxels within five subregions (Figure 5-6) of the volume-of-interest (VOI) – 10×10 (entire VOI: white box), 8×8 (red box), 6×6 (blue box), 4×4 (yellow box), and 2×2 (purple box). Reference values are shown in the rightmost table.

The coefficients of variance (CV%) are highest for Glu, mI, and Lac, ranging between 22 – 31%, 33 – 37%, and 19 – 24%, respectively. The larger standard deviation of mI ADC's is apparent in the ADC maps shown in Figure 5-6 as well as in the histogram in Figure 5-7, even though the mean value agrees well with the reference, as indicated by a percent error value of 4%. This pattern is the same for Glu, however the CRLB and CV values for this metabolite indicate a better quantitation compared to mI. The ADC's of Lac are more elevated relative to the reference

and Trace DW-PRESS values by approximately 30% and 9%, respectively, although its CRLB's at both b-values are lower than those for Glu and mI.

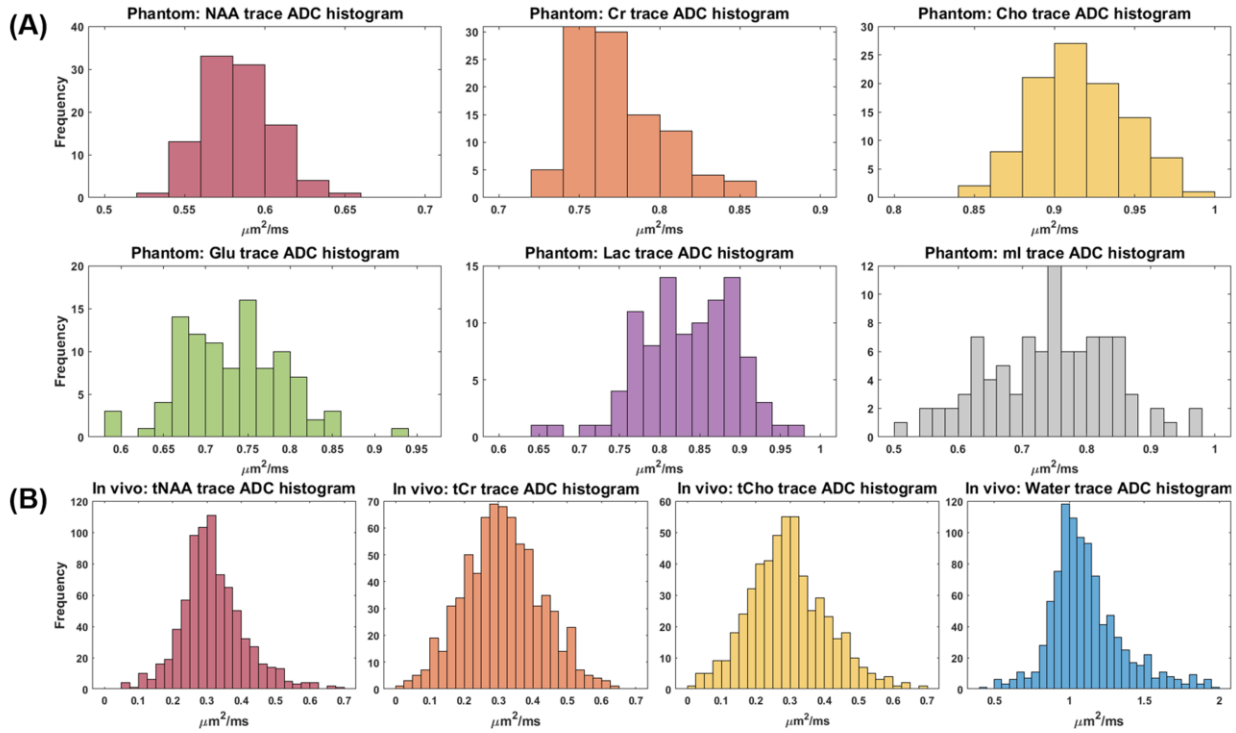

Figure 5-7: **(A)** Histograms of trace ADC values in the GE Braino phantom for NAA, Cr, Cho, Glu, mI, and Lac. **(B)** Histograms of in vivo brain trace ADC values. These include the ADC's of all voxels (with CRLB's ≥ 20% and outside of ventricle regions) in the volume-of-interest (VOI).

Statistical Analysis

Within the 10 x 10 voxel region of the VOI and all its subregions, the highest CV's found for NAA, Cr, Cho, Glu, Lac, and mI were 9%, 8%, 9%, 31%, 24%, and 37%, respectively. For the single voxel acquisition, the CV's were 4%, 3%, 4%, 10%, 14%, and 15%, respectively.

The one-way ANOVA's for testing differences in the means among all VOI subregions, taken across 10 measurements (done for each metabolite), showed no statistically significant differences for Cho ($p = 0.4364$), Glu ($p = 0.4277$), Lac ($p = 0.0552$), and mI ($p = 0.1519$). For

NAA, the values between the 10×10 and 4×4 subregions were significantly different ($p = 0.0252$). For Cr, the values between the 10×10 subregion and the 8×8, 6×6, and 4×4 subregions were also significantly different with p-values of 0.0236, 0.0432, and 0.0023, respectively.

The two-sample t-tests between the 10 measurements within the smallest 2 × 2 subregion of the VOI (4×10 values for each metabolite) and the 10 single-voxel DW-PRESS measurements indicated no statistically significant difference in the means from these two acquisition types. The closest indication of any potential significant difference occurred for NAA ($p = 0.054$).

5.5.2 In Vivo

The effect of navigator-based phase and frequency shift corrections are shown in Figure 5-5. The zero-order phase and frequency shift values needed to phase and frequency align all averages are determined from the set of navigator spokes from the averages. These values are then subsequently applied to the corresponding raw data, ensuring that the radial spokes are coherently averaged for maximum signal retention, as seen in the averaged uncorrected and corrected navigator spectra. Before averaging, the SNR thresholding step typically eliminated 1-3 averages out of total of 14 in vivo.

Figure 5-8(A) shows in vivo NAA metabolite maps, taken with $b = 1{,}600$ s/mm^2, before and after corrections. Without any navigator-based corrections on the raw data, the final NAA map shows a marked decrease in signal intensity and greater appearance of streaking artifacts. After corrections, the spectral signal intensity is restored and the degree of streaking is greatly reduced. Improvements in spectral intensities of NAA, Cr, and Cho, and an overall increase in SNR is also evident in the spectra shown in Figure 5-8(B).

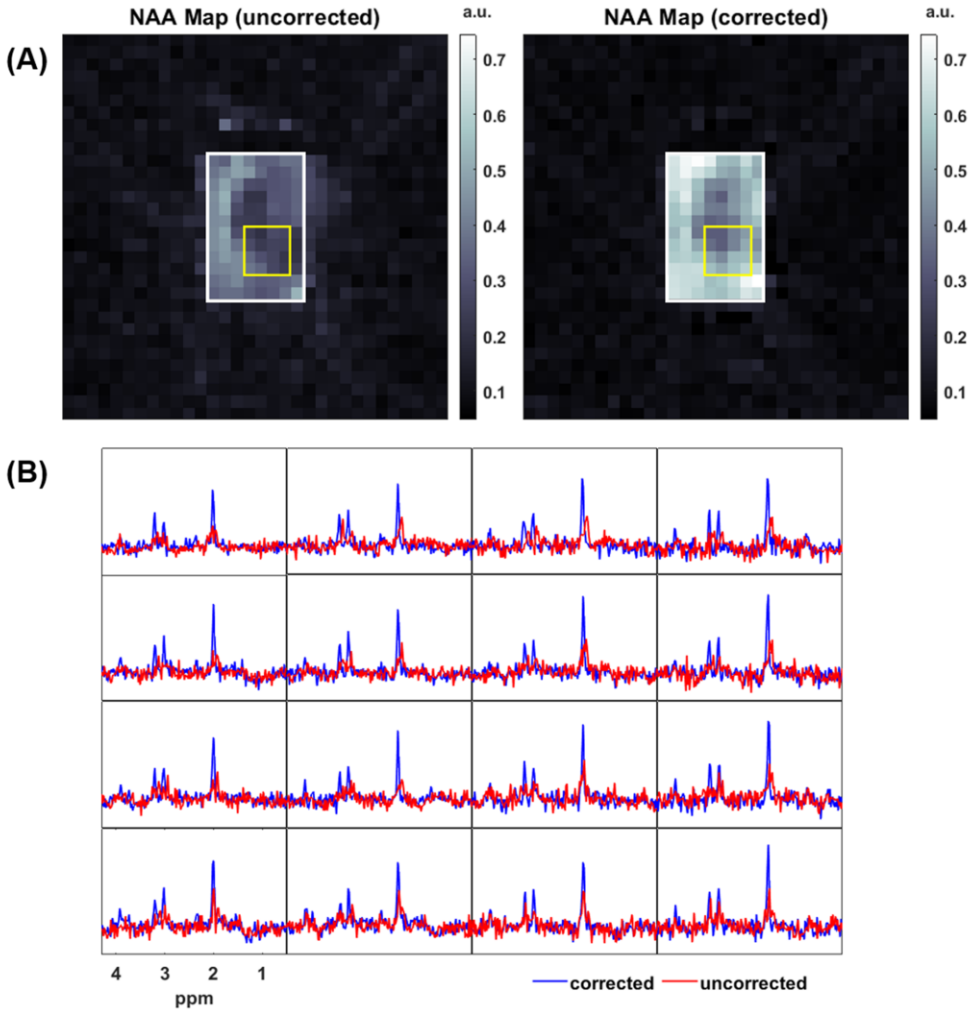

Figure 5-8: **(A) (Left)** NAA map from reconstructions without navigator-based phase and frequency shift corrections. The raw data was uncorrected although eddy-current phase correction was still applied using the (uncorrected) water-unsuppressed data. **(Right)** NAA map after navigator-based corrections. The signal intensity is increased and the degree of streaking artifacts is substantially reduced in the corrected NAA map. **(B)** Uncorrected (red) and corrected (blue) diffusion-weighted spectra taken with b-value of 1,601 s/mm^2, shown within the yellow box indicated in the NAA maps. The spectral linewidths and signal intensities are greatly improved after applying the navigator-based phase and frequency drift corrections on the raw data before reconstruction.

Figure 5-9 shows trace ADC maps of tNAA, tCr, tCho and water. The water VOI was displaced relative to the metabolite maps due to chemical shift misregistration. Voxels in the metabolite maps that overlapped with the water VOI were considered for further analysis of ADC's

in white and gray matter regions. The metabolite ADC maps share common regions of high and low ranges of ADC values, and are consistent with the underlying anatomy, as also seen in the water ADC map. Typically, the CRLB's in the periphery of the VOI, particularly in the leftmost column and bottom row had values greater than 20%. Across the 10 healthy volunteers, the average proportion of voxels excluded for tNAA, tCr, and tCho was 5%, 8%, and 10%, respectively.

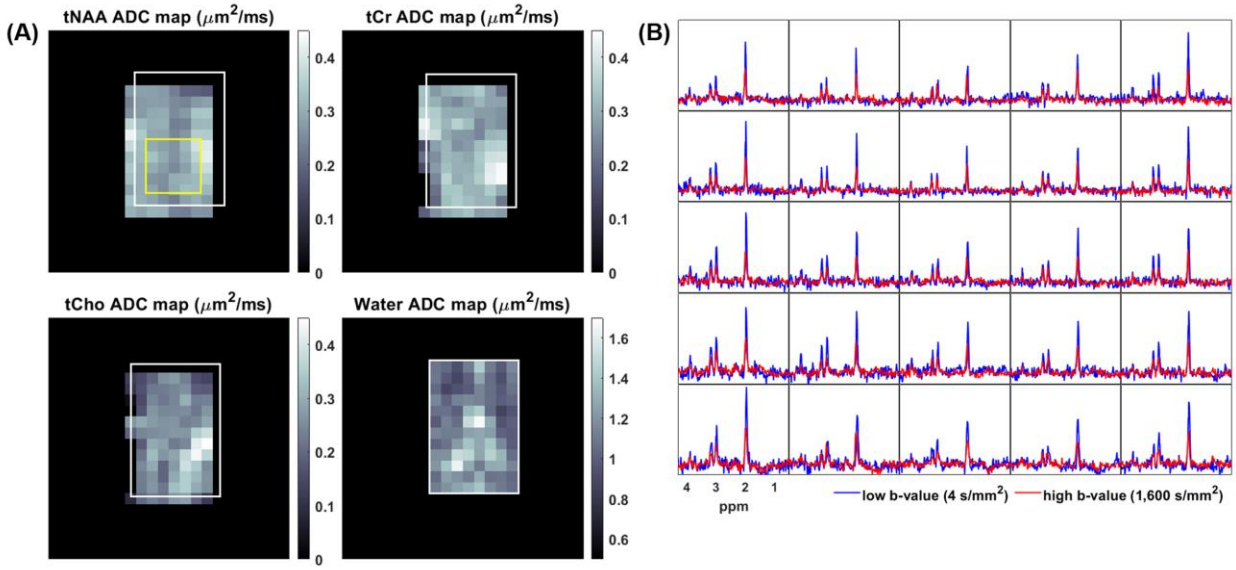

Figure 5-9: **(A)** Trace ADC maps of total NAA (tNAA), total Creatine (tCr), total Choline (tCho), and water. Estimated tNAA ADCs ranged between 0.25-0.35 μm^2/ms, which agree with reports probing short diffusion times. Most water trace ADC's ranged between 1.0 – 1.4 μm^2/ms. The water VOI (white box) is displaced relative to the metabolite maps due to chemical shift misregistration. Regions where CRLB values exceeded 20% usually occurred in the leftmost column and lowest row of the multi-voxel VOI grid. **(B)** Representative diffusion-weighted spectra within the yellow box placed on the tNAA ADC map in (A) are shown. The diffusion-weighted spectra from the low (51 s/mm^2) and high b-value (1,601 s/mm^2) are overlaid for comparison.

Estimates of ADCs in Pure White and Gray Matter

Figure 5-10(B) shows fits of the ADC values of tNAA, tCr, tCho, and water as a function of gray matter fraction, for a single volunteer. The Pearson correlation coefficient ρ shows moderate correlation (0.47 – 0.53) between the GM fraction and metabolite ADC's. The water ADC has the low degree of correlation with ρ = 0.17. Extrapolations to pure WM or GM were made by evaluating the linear fit at the values of f_{GM} to 0 and 1, respectively. Table 5-3 shows the ADC estimates of pure GM and WM, based on these extrapolations. The corresponding Pearson correlations coefficients and associated p-values less than α = 0.05 are also listed. In general, the metabolite ADC's in GM tend to be greater than those in WM, except for water, which has white matter ADC's slightly than those in gray matter. The ranges of ADC's in pure GM for tNAA, tCr, tCho and water were 0.23 – 0.27, 0.20 – 0.33, 0.18 – 0.26, and 0.96 – 1.24 μm^2/ms, respectively, and for pure WM, the ADC ranges were 0.31 – 0.38, 0.29 – 0.38, 0.26 – 0.34, and 0.97 – 1.08 μm^2/ms, respectively.

	Extrapolated ADC's to Pure Gray and White Matter (μm²/ms)											
	tNAA			**tCr**			**tCho**			**Water**		
	GM	**WM**	**ρ (*p*-value)**	**GM**	**WM**	**ρ (*p*-value)**	**GM**	**WM**	**ρ (*p*-value)**	**GM**	**WM**	**ρ (*p*-value)**
1	0.24	0.32	-0.28 (0.015)	0.22	0.32	-0.22 (NS)	0.2	0.27	-0.22 (NS)	1.05	1.05	0.09 (NS)
2	0.23	0.38	-0.44 (< 0.001)	0.29	0.36	-0.21 (NS)	0.22	0.31	-0.28 (NS)	1.1	1.02	0.09 (NS)
3	0.24	0.33	-0.43 (< 0.001)	0.22	0.35	-0.48 (< 0.001)	0.22	0.31	-0.28 (0.044)	1.05	1.08	0.1 (NS)
4	0.24	0.32	-0.17 (NS)	0.24	0.33	-0.14 (NS)	0.24	0.34	-0.14 (NS)	1.03	1.04	0.11 (NS)
5	0.27	0.33	-0.26 (0.032)	0.26	0.34	-0.24 (NS)	0.2	0.32	-0.32 (0.021)	1.19	1	0.29 (0.012)
6	0.26	0.33	-0.29 (0.012)	0.28	0.36	-0.23 (0.048)	0.26	0.3	-0.08 (NS)	1.08	1.07	0.1 (NS)
7	0.27	0.35	-0.35 (0.002)	0.2	0.32	-0.38 (0.001)	0.21	0.31	-0.32 (0.009)	1.13	0.98	0.37 (< 0.001)
8	0.24	0.33	-0.33 (0.012)	0.33	0.29	-0.19 (NS)	0.21	0.32	-0.21 (NS)	1.06	0.97	0.12 (NS)
9	0.25	0.36	-0.53 (< 0.001)	0.24	0.38	-0.47 (< 0.001)	0.18	0.33	-0.53 (< 0.001)	0.96	1.05	0.17 (NS)
10	0.26	0.31	-0.2 (NS)	0.29	0.33	-0.15 (NS)	0.24	0.26	-0.06 (NS)	1.24	1.07	0.4 (< 0.001)
Group*	0.25 ± 0.01 (6%)	0.34 ± 0.02 (6%)	-0.33 ± 0.11 (35%)	0.26 ± 0.04 (16%)	0.34 ± 0.03 (8%)	-0.27 ± 0.13 (47%)	0.22 ± 0.02 (11%)	0.31 ± 0.02 (8%)	-0.24 ± 0.14 (56%)	1.09 ± 0.08 (7%)	1.03 ± 0.04 (4%)	0.18 ± 0.12 (66%)

NS: not significant

* Data from two volunteers was excluded due to inadequate spectral quality

Table 5-3: Mean, standard deviation, and CV% values of estimated in vivo brain trace ADC's in pure gray matter (GM) and pure white matter (WM). These estimated values were extrapolated from linear regression fits of ADC vs. GM or WM fraction. The correlation coefficient (ρ) and the corresponding *p*-value is also shown.

Statistical Analysis

For ADC estimates in pure GM, one-way ANOVA test indicated no significant differences in the mean values between tNAA (0.25 $\mu m^2/ms$) and tCr (0.26 $\mu m^2/ms$) ($p = 1.0$), nor between tNAA and Cho (0.22 $\mu m^2/ms$) ($p = 0.0511$). However, the mean pure GM ADC's of tCr and tCho were significantly different ($p = 0.0135$).

For ADC estimates in pure WM, no significant differences in the mean values between tNAA (0.34 $\mu m^2/ms$) and tCr (0.34 $\mu m^2/ms$) ($p = 1.0$) were found. However, the mean ADC's of tNAA and tCho (0.31 $\mu m^2/ms$) in pure WM were significantly different ($p = 0.0357$). In addition, the mean ADC's of tCr and tCho in pure WM were also significantly different ($p = 0.0229$).

Paired t-test showed significant differences in the ADC's of tNAA, tCr, and tCho between GM and WM, all with $p < 0.001$. However, no significant differences were found in the water ADC's between gray and white matter ($p = 0.0928$).

Distribution of ADCs in selected voxels in Gray and White matter regions

Table 5-4 shows the means, standard deviations, and coefficients of variance of the ADC's of tNAA, tCr, tCho, and water in the four gray matter-dominant and four white matter-dominant voxels selected as indicated in Figure 5-10(C). The respective average gray matter and white matter fractions are also reported for each of these voxel locations. Consistent with the trend seen in the extrapolated ADC's for pure GM and WM, the ADC's in the gray matter are higher than those in white matter, except for water where the values fall within a similar range. For example, for tNAA, tCr, and tCho, the range of ADC's in the gray matter voxels was 0.25 – 0.27, 0.22 – 0.3, and 0.21-0.27 $\mu m^2/ms$, respectively, whereas in the white matter voxels the ADC ranges of these

metabolites were 0.28 – 0.31, 0.27-0.31, and 0.24 – 0.30 μm^2/ms, respectively. The ADC' of tCho have the highest coefficients of variance, ranging from 33-50% in gray and 21-30% in white matter, while the CV's of tNAA and water tend to me the lowest, not exceeding 19% in either gray or white matter locations.

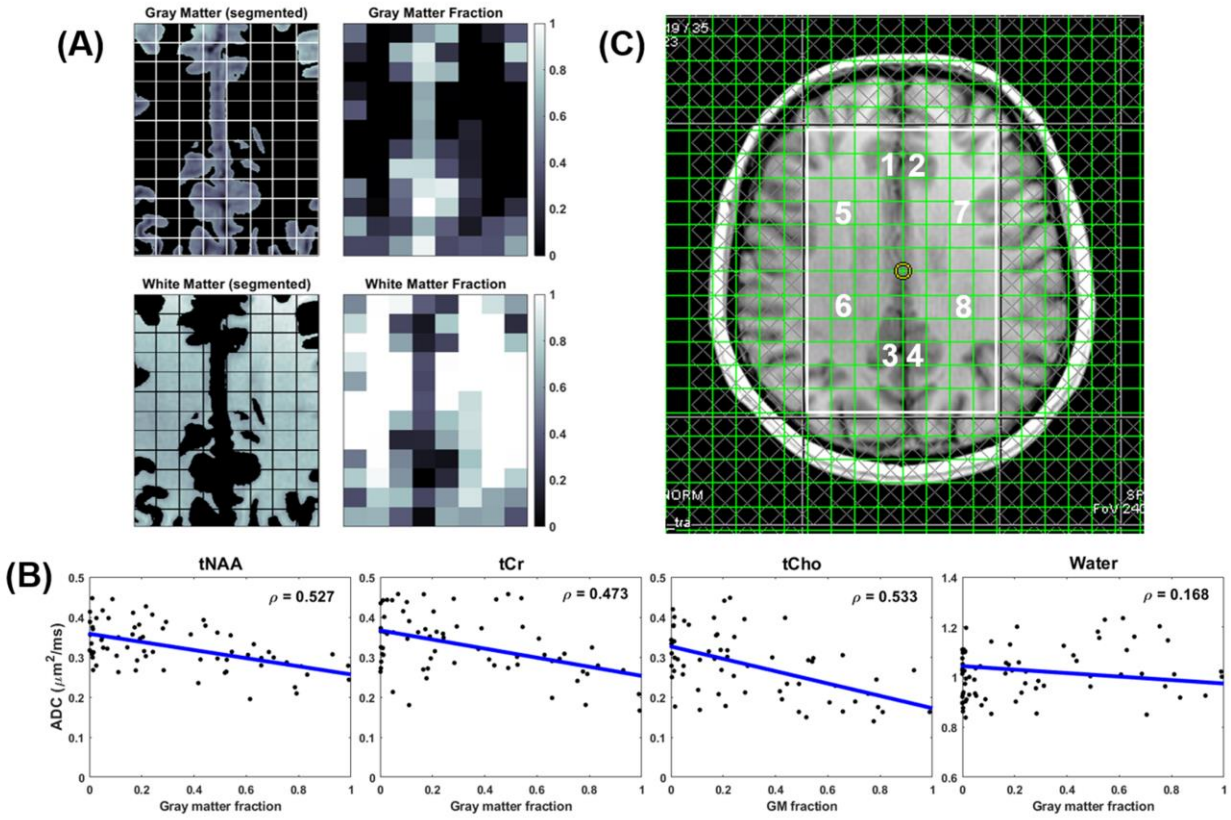

Figure 5-10: **(A)** Segmentation process for determining the relative contributions of white and gray matter within the VOI. Only a representative slice from the set of T_1-weighted images is shown. The areas of white and gray matter within the VOI is delineated within each voxel. The relative number of pixels in the white and gray matter regions is then used for determining the gray matter (GM) and white matter (WM) fraction. **(B)** Linear regression fits of ADC values as a function of the GM fraction. The Pearson correlation coefficient ρ is shown next the linear fit. **(C)** Specific voxels in gray matter (1-4) and white matter (5-8) dominant locations were selected for further analysis of the relative ADC distributions of tNAA, tCr, tCho, and water within and between GM and WM regions. The specific voxels are located in: (1) – right anterior cingulate cortex (RACC); (2) – left anterior cingulate cortex (LACC); (3) – right superior precuneus (RSP); (4) – left superior precuneus (LSP); (5) – right anterior corona radiata (RACR); (6) – right posterior corona radiata (RPCR); (7) – left anterior corona radiata (LACR); and (8) – left posterior corona radiata (LPCR).

Statistical Analysis

Paired t-tests, for each metabolite, indicated significant differences in the ADC's of tNAA ($p < 0.001$) and tCr ($p = 0.0264$) between gray and white matter. However, no statistically significant differences between GM and WM were found in the ADC's of tCho or water.

In gray matter voxels, one-way ANOVA tests showed no significant differences in the ADC values of tNAA, tCr, tCho and water. However, in white matter voxels, the only significant difference found was between the ADC's of tNAA and tCho ($p = 0.039$).

		ADC's in Selected Voxel Locations ($\mu m^2/ms$)					
		tNAA	**tCr**	**tCho**	**Water**	**Gray Matter Fraction**	**White Matter Fraction**
Gray Matter Locations	**RACC**	0.27 ± 0.03 (13%)	0.22 ± 0.08 (34%)	0.23 ± 0.08 (33%)	1.13 ± 0.14 (12%)	0.74 ± 0.16 (22%)	0.26 ± 0.16 (62%)
	LACC	0.25 ± 0.04 (17%)	0.24 ± 0.09 (40%)	0.21 ± 0.06 (29%)	1.18 ± 0.15 (12%)	0.74 ± 0.22 (30%)	0.26 ± 0.22 (86%)
	RSP	0.27 ± 0.02 (9%)	0.3 ± 0.07 (23%)	0.27 ± 0.1 (39%)	1.16 ± 0.25 (21%)	0.8 ± 0.16 (20%)	0.2 ± 0.16 (79%)
	LSP	0.27 ± 0.05 (19%)	0.26 ± 0.05 (20%)	0.27 ± 0.13 (50%)	1.15 ± 0.2 (18%)	0.84 ± 0.15 (17%)	0.16 ± 0.7 (43%)
White Matter Locations	**RACR**	0.31 ± 0.03 (9%)	0.31 ± 0.04 (13%)	0.24 ± 0.07 (30%)	1 ± 0.11 (11%)	0.04 ± 0.03 (61%)	0.96 ± 0.03 (3%)
	RPCR	0.31 ± 0.04 (14%)	0.29 ± 0.04 (13%)	0.29 ± 0.06 (19%)	1.11 ± 0.17 (15%)	0.2 ± 0.1 (50%)	0.8 ± 0.25 (32%)
	LACR	0.31 ± 0.04 (14%)	0.31 ± 0.07 (24%)	0.3 ± 0.06 (21%)	1.01 ± 0.12 (12%)	0.06 ± 0.03 (50%)	0.94 ± 0.1 (11%)
	LPCR	0.28 ± 0.04 (13%)	0.27 ± 0.05 (17%)	0.26 ± 0.08 (29%)	1.24 ± 0.17 (14%)	0.35 ± 0.17 (49%)	0.65 ± 0.28 (43%)

Table 5-4: Mean, standard deviation, and CV% values of *in vivo* brain trace ADC's in the four selected voxels in the gray matter (GM) locations and in the four selected voxels in the white matter (WM) locations. The corresponding GM and WM fractions within each respective voxel in the gray or white matter regions are shown in the rightmost portion of the table. The locations of the voxels are shown in Figure 5-10(C), and the abbreviations are defined as follows: RACC – right anterior cingulate cortex; LACC – left anterior cingulate cortex; RSP – right superior precuneus; LSP – left superior precuneus; RACR – right anterior corona radiata; RPCR – right posterior corona radiata; LACR – left anterior corona radiata; LPCR – left posterior corona radiata

Reproducibility across two scan session for a single volunteer

One volunteer was scanned twice on separate days and the Pearson's linear correlation coefficient, ρ, was taken as measure of reproducibility of the ADC and metabolite maps between the scan sessions.

For the low b-value (11 s/mm^2) metabolite maps, ρ = 0.86, 0.84, and 0.80, and 0.94 for tNAA, tCr, tCho and water, respectively. For metabolite maps acquired at the higher b-value (1,600 s/mm^2), the correlation coefficient for tNAA, tCr, tCho, and water was ρ = 0.86, 0.86, 0.81, and 0.92, respectively.

For ADC maps, the correlation coefficient was 0.43, 0.35, 0.31, and 0.68, for tNAA, tCr, tCho, and water, respectively.

5.6 Discussion

This study evaluated diffusion-weighted spectroscopic imaging using the single-shot trace-weighted scheme with radial echo-planar trajectories, in both in vivo and phantom data. The radial acquisition enabled a self-navigating approach for retrospective corrections on the raw data before reconstruction. These corrections improved SNR retention and fidelity of spatial encoding, allowing for multi-voxel in vivo trace ADC estimations that show consistent trends with previous DW-MRS/MRSI reports. The trace DW-REPSI sequence also enables the estimation of the trace ADC within a single measurement, potentially reducing the influence of motion and other inconsistencies on the trace ADC estimation from three separate measurements, as done in conventional DW-MRSI sequences.

5.6.1 Phantom validation

The trace ADCs in phantom agree remarkably well with reported values, except for overestimation of Lac. The coefficients of variance are also higher in Lac, mI, and Glu compared to the NAA, Cr, and Cho, indicating that the former three metabolites are not as reliably quantified. These discrepancies could be due to the TE of 144 ms, which is much longer than the (minimum) TE of 74 ms used in the report by Landheer et al.[101]. At long TE's, the effects of SNR loss, T_2 decay and phase modulations due to J-coupling are more pronounced and can cause the signals of mI, Glu, and Lac to have lower inherent SNR and to add incoherently during the averaging process. These effects explain the relative inhomogeneity of values across the ADC maps of mI, Lac, and Glu compared to non-J-coupled main singlets of NAA, Cr, and Cho, all of which retain fairly homogenous mean ADCs and low CVs for the various VOI subregions. Overall, the accurate ADC estimation from Trace DW-REPSI validates the performance of this sequence in phantom.

5.6.2 In vivo validation and comparison of ADCs with other studies

In vivo ADC's from this study are generally slightly higher than those reported in the literature. One key contribution to this effect is the diffusion time t_d. Most other reports have used diffusion-weighted single-voxel or spectroscopic imaging sequences with long diffusion times greater or equal to 36 ms[114–116]. The current study used a diffusion time of 10.75 ms, which is one the shortest reported for DW-MRSI to the best of our knowledge. It is well known that *in vivo* brain ADCs are larger when measured with short diffusion times. Several studies have reported this ADC overestimation at short diffusion times in rodent and human brain *in vivo*[92,93,95].

In healthy adults, the single-voxel study by Ellegood et al.[79] (t_d = 117 ms) reported trace ADC ranges of 0.15–0.20 μm^2/ms in gray matter and 0.19–0.30 μm^2/ms in white matter for tNAA, tCr, and tCho. The report by Ercan et al.[114] (t_d = 50 ms) found these metabolites to have trace ADC ranges of 0.11–0.13 μm^2/ms in gray matter and 0.13–0.17 μm^2/ms in white matter. Fotso et al.[115]

($t_d \approx 36.6$ ms) reported an ADC range of 0.17–0.20 $\mu m^2/ms$ or 0.09–0.11 $\mu m^2/ms$ (for gray-white mixtures), depending on the degree of corrections for phase-encoding ghosting. In contrast, in our study, the trace ADC values in extrapolated to pure GM and WM ranged between 0.18–0.27 and 0.26–0.38 $\mu m^2/ms$, respectively. However, in the selected gray and white matter-dominant voxels, ranges of 0.21–0.27 and 0.24–0.31 $\mu m^2/ms$, respectively, were quantified. The larger ADC values in white matter found in our study is consistent with the report by Kan et al.[103] and the trends found in the aforementioned reports. We found significant differences in the extrapolated ADCs of tNAA, tCr, and tCho between pure GM and WM. For the selected gray and white matter locations, only tNAA and tCr were significantly different between in gray versus white matter.

With regard to water, our study shows that the differences in ADC's between gray and white matter are not significant. However, there is a trend of higher mean values in the extrapolated water ADCs of gray matter (1.09 $\mu m^2/ms$) versus white matter (1.03 $\mu m^2/ms$). In the analysis of selected gray and white matter voxels, this trend also holds, with an average water trace ADC of 1.16 and 1.09 $\mu m^2/ms$ in gray and white matter, respectively. The higher water ADCs in gray compared to white matter is consistent with literature[130].

5.6.3 Limitations

The diffusion trace-weighted pulse sequence has several limitations. Firstly, the TE must be relatively long to accommodate the diffusion-sensitizing gradients and consequently the number of reliably detected metabolites is limited to tNAA, tCr, and tCho. Secondly, high b-values require large gradients amplitudes, which could increase the influence of eddy currents and potentially exceed scanner slew rate and nerve stimulation limits. With all other parameters fixed, the current sequence could reach b-values up to approximately 3,100 s/mm^2, however, only at the maximum

amplitude of 80 mT/m. The b-value of 1,601 s/mm^2 was chosen for two reasons: (1) to allow sufficient water for eddy current phase correction of the high b-value data, and (2) to allow enough residual water for the navigator-based corrections. Thirdly, the PRESS localization uses non-adiabatic pulses which are not robust to chemical shift displacement, and volumetric excitation prevents whole-brain coverage.

Regarding other limitations, firstly, the *in vivo* voxel size is large at 2 mL, which could worsen the partial volume effects in the spectra. This large volume was selected to maximize the SNR. Although the linear correlation of ADC vs. gray and white matter fraction could somewhat compensate for partial volume effects, it is difficult to isolate the ADC coming from only gray or white matter. Secondly, the scan time is rather long, taking approximately 25-30 minutes alone for the diffusion-weighted acquisitions. The long scan time is partially due to the use of a relatively large number of spokes and the need for averaging. However, the high concentration of radial samples within the higher-SNR central k-space helps to increase the sensitivity of the signal. Alternatively, golden angle acquisitions could be used for prospectively undersampled data, however, in this study, we chose uniform undersampling with a prescribed odd number of spokes as this type of sampling minimizes the azimuthal gaps between the spokes compared to a non-Fibonacci number of spokes in a golden angle distribution[22]. A third limitation is that only two b-values were able to be practically acquired within a one-hour scan session. The use of three or more b-values could further improve the ADC estimation. Lastly, no cardiac gating was implemented, although other studies have also omitted its use by depending on post-processing methods to minimize the effects of pulsatile motion in the brain[79,80,102]. In this study, the acquired radial data itself was used via a self-navigating approach to retrospectively remove data that was

overly corrupted by motion. This approach is in contrast to other studies that report the importance of cardiac gating for accurately estimating the ADC[81].

5.6.4 Other Considerations in Trace DW-REPSI

Besides self-navigation, other types of signal tracking have been implemented for DW-MRSI, in addition to those first introduced by Posse et al.[104,105], which involve separate built-in readout gradients interspersed within the sequence to track shot-to-shot phase and frequency changes[114,115]. Motion correction approaches using real-time and volumetric navigators[131,132] could also be used for diffusion-weighted MRSI. In contrast to other DW-MRSI reports mentioned above, this study exploited the self-navigating properties of radial trajectories to retrospectively correct or remove data, as done in other reports in radial MRI[24,119,120].

In addition to navigator-based pre-processing corrections, gradient delay corrections were also applied on the raw data. The gradient delay calibration and correction in this study only considers the k-space offset parallel to the radial direction, and does not account for the perpendicular displacement of the spoke away from the k-space center[133]. However, the overall apparent effect of this gradient delay correction may be minimal at low spectroscopic imaging resolutions. Further improvements in trajectory misalignment can be done by estimating the actual trajectory with additional calibration scans[134].

To improve the potential clinical applicability of this sequence, future studies are needed to determine the effects of radial undersampling on the ADC estimation. In this study, the amount of under-sampling was conservative (acceleration factor of 1.52 with 33 spokes) in order to acquire the data during a time comparable to that of a fully-sampled Cartesian acquisition with the same matrix size (32×32), and to ensure a sufficiently large reduced FOV unaffected by undersampling

artifacts, such as streaking[51]. In principle, compressed sensing reconstruction may be used for this mildly undersampled radial data[4]. However, in some cases with suboptimal parameter tuning, the compressed sensing algorithm could inadvertently introduce a further reduction in the diffusion-weighted spectral amplitudes, especially as the lower concentrated diffusion-weighted spectra may be already highly attenuated and near the noise level. Future work involves evaluating the use of CS and parallel imaging techniques for accelerated DW-MRSI and their effects on ADC quantitation.

5.7 Conclusion

This study presents the first demonstration of the single-shot diffusion trace-weighted spectroscopic imaging sequence using radial echo planar trajectories in a clinical scanner at 3T. We evaluate the performance of this sequence in phantom and *in vivo*, and demonstrate the utility of self-navigation-based corrections of the radial data. Results show excellent agreement of phantom trace ADC's computed with Trace DW-REPSI and reference values. *In vivo* ADC's agree well in both the difference between gray and white matter, as well as the overestimation of metabolite and water ADC's due to a shorter diffusion time. The diffusion trace-weighted sequence could provide an estimate of the trace ADC of the main metabolite groups (tNAA, tCr, and tCho) in a much shorter scan time compared to conventional diffusion-weighted spectroscopic imaging techniques that require separate measurement along three orthogonal diffusion directions.

Chapter 6 Conclusion

In this dissertation, we implemented radial echo planar spectroscopic imaging and demonstrated its application for accelerated MRSI acquisitions and its utility for diffusion-weighted MRSI owing to its robustness to motion, self-navigation capability, and excellent tolerance to high undersampling factors. In Chapter 3, accelerated REPSI was applied for 2D brain ^{1}H MRSI and was compared to time-equivalent Cartesian EPSI acquisitions, showing that the REPSI with compressed sensing reconstruction can outperform Cartesian EPSI in terms of quantitation and imaging quality as a function of acceleration factor and in terms of its robustness to motion-induced artifacts. In Chapter 4, we implemented a single voxel version of the single-shot diffusion trace-weighted pulse sequence and were the first to demonstrate this technique for in vivo trace ADC estimates in human brain. In Chapter 5, we extended the single voxel diffusion trace-weighted sequence for diffusion-weighted spectroscopic imaging using REPSI and demonstrated the inherent capability of the self-navigated radial trajectories for implementing crucial post-processing corrections of the diffusion-weighted spatially-encoded data. Finally, in the Appendix, a study improving the computation efficiency of locally low-rank-based parallel imaging reconstruction is presented.

6.1 Summary of Technical Development

6.1.1 Accelerated Radial Echo Planar Spectroscopic Imaging

In Chapter 3, we demonstrated one of the first studies of ^{1}H radial echo planar spectroscopic imaging using acceleration based on compressed sensing reconstruction with total variation regularization. Comparisons of results with reconstructions of undersampled Cartesian EPSI acquisitions, at various reduction factors, show that REPSI is more tolerant of high acceleration of

2D MRSI and can be applied to free-breathing liver and prostate acquisitions with minimal motion-induced artifacts, which can more significantly affect Cartesian EPSI. Reconstruction results in the brain indicate that EPSI-based metabolite maps are much more degraded at the acceleration factor corresponding to 13 acquired k_y-lines, while REPSI still maintains reasonable image quality from the same number of spokes. The consequence is that the minimum scan time can be reduced by using the REPSI sequence, in the present example from 6 min 24 sec to 2 min 36 sec. Compared to the standard Cartesian approach and in combination with CS, radial undersampling is a promising approach to reduce scan time for 2D spectroscopic imaging.

6.1.2 Single-shot Diffusion Trace-weighted DW-PRESS

In chapter 4, we present the first demonstration of the single-shot diffusion trace-weighted sequence in a clinical scanner at 3T, and we compare the trace ADC values obtained with this sequence to those computed from the conventional bipolar and unipolar DW-PRESS sequences acquired with three orthogonal directions and negative and positive diffusion gradient polarities. Results show excellent agreement of phantom trace ADC's computed with all sequences, and in vivo ADC's agree well in both the difference between OG and OW matter, as well as the overestimation of metabolite and water ADC's due to a shorter diffusion time. The diffusion trace-weighted sequence could provide an estimate of the trace ADC of the main metabolite groups (tNAA, tCr, and tCho) in a much shorter scan time (by nearly a factor of three) compared to conventional DW-PRESS acquisitions.

6.1.3 Single-shot Diffusion Trace-weighted REPSI

In Chapter 5, we present the first demonstration of the single-shot diffusion trace-weighted spectroscopic imaging sequence using radial echo planar trajectories in a clinical scanner at 3T. We evaluate the performance of this sequence in phantom and *in vivo*, and demonstrate the utility of self-navigation-based corrections of the radial data. Results show excellent agreement of phantom trace ADC's computed with Trace DW-REPSI and reference values. *In vivo* ADC's agree well in both the difference between gray and white matter, as well as the overestimation of metabolite and water ADC's due to a shorter diffusion time. The diffusion trace-weighted sequence could provide an estimate of the trace ADC of the main metabolite groups (tNAA, tCr, and tCho) in a much shorter scan time compared to conventional diffusion-weighted spectroscopic imaging techniques that require separate measurement along three orthogonal diffusion directions.

6.1.4 Improved Computation Efficiency of Locally Low-Rank Parallel Imaging Reconstruction

In the Appendix, we show that locally low rank reconstruction using random iterative patch adjustments (LLR-IRPA) retains the same level of image reconstruction and quantitative parameter mapping results compared to overlapping patch-based LLR regularization, in terms of image quality and normalize root mean square error, but with the distinct advantage of substantially reduced computational load. We describe this patch adjustment strategy for LLR regularization and set a theoretical framework for formulating this novel development in the context of patch-based image reconstruction techniques. This technique is an improvement over conventional LLR-based algorithms such as CLEAR, since the computational load is substantially reduced without promoting block artifacts. Experimental results and theoretical analysis of the proposed method, including a proof of convergence for this algorithm, support these findings. The

implications of LLR-IRPA is to facilitate the application of LLR-based regularization for clinical MRI applications.

6.2 Future outlook

6.2.1 Accelerated Radial Echo Planar Spectroscopic Imaging

In this work, we implemented a radial echo planar spectroscopic imaging sequence along with undersampling scheme based on golden angle view ordering and reconstruction with compressed sensing using total variation regularization. This sequence can be applied currently, although only for accelerated two-dimensional MRSI in human brain. Although promising results were shown in free-breathing liver and prostate scans, further validation is needed to assess the repeatability of metabolite quantitation for these types of acquisitions. The same sequence can be extended for three-dimensional MRSI by including phase-encoding steps for the slice dimension, resulting in a stack-of-stars acquisition. However, the optimization algorithm would need to be modified to reconstruct two non-Cartesian (k_x-k_y) and one Cartesian (k_z) dimensions. For three-dimensional acquisitions, there is also the challenge of requiring a long scan time to acquire the water reference scan, therefore an interleaved water acquisition would be the most practical way to obtain water reference data for eddy current phase correction.

6.2.2 Single-shot Diffusion Trace-weighted DW-PRESS

In this work, we mainly focused on demonstrating the feasibility of the single voxel diffusion trace-weighted PRESS sequence (Trace DW-PRESS) for in vivo human brain acquisitions, and on comparing trace ADC estimates from this sequence to those obtained from conventional DW-PRESS acquisitions using bipolar and unipolar diffusion-sensitizing gradient configurations. Compared to current protocols for measuring the trace ADC, the Trace DW-PRESS sequence can

in principle reduce the necessary scan time for estimating the trace ADC, however, due to the long TE, only the main singlets of total N-acetyl aspartate, total choline, and total creatine can be reliably estimated, thus limiting the ability of this technique to probe other metabolites of interest such as glutamate + glutamine and myo-inositol. For this sequence to be clinically practical, the in-built scanner software must include advanced phase- and frequency-aligning subroutines to ensure optimal signal combination for reliable trace ADC estimation. Further optimization of these sequence in terms of the optimal trade-off between TE and b-value may also need to be explored.

6.2.3 Single-shot Diffusion Trace-weighted REPSI

In this work, we demonstrated that Trace DW-REPSI is able to provide estimates of the trace ADCs of the three main metabolite groups of total N-acetyl aspartate, total choline, and total creatine, similar to the single voxel case, using only two measurements as opposed to the six that would be required using conventional DW-MRSI. However, the acquisition is still quite long at approximately 30 minutes for 2 b-values, largely due to the acquisition of a relatively high number of 33 spokes, corresponding to an acceleration factor of roughly 1.52. Therefore, future studies must be conducted to show the effect of further undersampling on the resulting trace ADC estimation. This study used a high number of spokes, although still short of the 50 required to meet the Nyquist sampling criterion, to validate the technique while minimizing the influence of spatial undersampling. Further undersampling could make this technique more clinically feasible, although other complications due to chemical shift misregistration which is inherent to the foundational PRESS sequence are less avoidable.

6.2.4 Improved Computation Efficiency of Locally Low-Rank Parallel Imaging Reconstruction

In this work, the locally low rank (LLR) technique for image domain-based parallel imaging is improved by significantly reducing the computational load without promoting block artifacts. In fact, the amount of acceleration from using random shifting of image patches has been shown to reach up to a factor of 3 to 4. The iterative random patch adjustment strategy is experimentally shown to suppress block artifacts while retaining the convergence rate of more computationally expensive conventional LLR algorithms. The implications of LLR-IRPA is to facilitate the application of LLR-based regularization for clinical MRI applications. Currently, a similar techniques is offered as a standard function within the Berkeley Advanced Reconstruction Toolbox (BART)[135].

For accelerated spectroscopic imaging, the same LLR-IRPA framework can be applied for each frequency component of the spectrum. The computational load can be reduced by reconstructing only the undersampled spatial data within the spectral range of interest. It is also possible to simultaneously reconstruct multiple low-rank matrices for a broad range of frequencies using parallel computing techniques, making the LLR-IRPA method more feasible for fast MRSI. Since the resolutions for MRSI are relatively low compared to MRI, it would also be possible to increase the patch size without further compromising the low rank property of the matrices formed by the local image patches. Hence, the LLR-IRPA method can use a much reduced number of local patches, thereby offsetting the increased number of frequency-by-frequency reconstruction that are needed in the context of MRSI.

APPENDIX: Improved Computational Efficiency of Locally Low Rank MRI Reconstruction Using Iterative Random Patch Adjustments

A.1 Abstract

This chapter presents and analyzes an alternative formulation of the locally low-rank (LLR) regularization framework for magnetic resonance image (MRI) reconstruction. Generally, LLR-based MRI reconstruction techniques operate by dividing the underlying image into a collection of matrices formed from image patches. Each of these matrices is assumed to have low rank due to the inherent correlations among the data, whether along the coil, temporal, or multi-contrast dimensions. LLR regularization has been successful for various MRI applications such as parallel imaging and accelerated quantitative parameter mapping. However, a major limitation of most conventional implementations of LLR regularization is the use of multiple sets of overlapping patches. Although the use of overlapping patches leads to effective shift-invariance, it also results in high computational load, which limits the practical utility of LLR regularization for MRI. To circumvent this problem, alternative LLR-based algorithms instead shift a single set of non-overlapping patches at each iteration, thereby achieving shift-invariance and avoiding block artifacts. A novel contribution of this paper is to provide a mathematical framework and justification of LLR regularization with iterative random patch adjustments (LLR-IRPA). This method is compared with a state-of-the-art LLR regularization algorithm based on overlapping patches, and it is shown experimentally that results are similar but with the advantage of much reduced computational load. We also present theoretical results demonstrating the effective shift

invariance of the LLR-IRPA approach, and we show reconstruction examples and comparisons in both retrospectively and prospectively undersampled MRI acquisitions.

A.2 **Introduction**

Current medical magnetic resonance imaging (MRI) largely depends on undersampled data acquisitions, combined with specialized reconstruction techniques, to reach the levels of spatio-temporal resolutions and volumetric coverage necessary for practical clinical purposes[136–138]. These accelerated imaging methods recover images from highly reduced k-space samples by implementing optimization schemes that incorporate *a priori* knowledge of the underlying image information. Parallel imaging takes advantage of the inherent data redundancy available from multiple coil measurements, while compressed sensing (CS) exploits the low-dimensional representation of spatiotemporal image characteristics with respect to suitable sparsifying transforms or matrix decompositions[139,140]. One of the most recently developed ideas in CS includes the notion of low-rank constrained reconstruction, which is based on the fact that image data tends to be highly correlated across, for example, the temporal and/or coil dimensions[141]. In the globally low-rank (GLR) model, a time series or multi-coil image set, when treated jointly in matricized form, can be accurately represented by a matrix of much lower rank relative to the number of time points or coils[142]. The reconstruction of such an undersampled image set is generally posed as a low-rank constrained matrix completion optimization problem. Several researchers have demonstrated significant advantages in image quality and improved temporal resolution from utilizing this low-rank optimization framework in dynamic imaging[143–145], parallel imaging[146], functional imaging[147], real-time imaging[148], and accelerated quantitative parameter mapping[149].

Despite the success of the GLR approach, recent studies have shown that adopting a locally low-rank (LLR) model---which assumes correlations across multiple images only within a relatively small neighborhood of pixels---yields more favorable results and involves less computational load than the GLR approach. Studies by Trzasko et al.[150] have shown that the LLR framework may provide better performance in terms of the trade-off between imaging speed and data fidelity. This framework has been applied in parallel imaging, where Tzrasko and Manduca introduced an image domain-based calibration-free method that is based on the observation that coil sensitivities vary smoothly in space, such that images are locally-correlated along the coil dimension[151]. Zhang et al.[152] demonstrated accelerated T_1 and T_2 mapping using a similar concept, except that the local image correlations are assumed to exist across images taken with different pulse-sequence parameters. Locally low-rank constraints have facilitated the combination of both compressed sensing and parallel imaging reconstruction techniques, most notably in the case of dynamic cardiac and contrast-enhanced imaging[153]. Importantly, LLR-based reconstruction has the distinct advantage of requiring considerably less computational load and memory requirements than its GLR counterpart[151].

The LLR approach, although very useful and effective, has certain drawbacks that result from the particular way of defining the set of patches into which the underlying image is decomposed. The collection of patches, or partition, delineates the local regions in the image series where low-rank 'submatrices' may be formed. Like most patch-based reconstruction methods, LLR-based reconstruction can be implemented by using sets of either overlapping or non-overlapping patches. A partition consisting of overlapping patches can minimize the appearance of block artifacts as the transform becomes approximately shift-invariant, but it comes with the disadvantage of high computational cost due to the large number of patches involved. In contrast,

a partition composed of non-overlapping, covering patches can greatly reduce the computational load, but it inevitably leads to block artifacts. Both of these strategies, therefore, limit the utility of LLR regularization for practical MRI applications.

Here, we present an implementation of LLR regularization with iterative random patch adjustments (LLR-IRPA) that utilizes an effectively shift-invariant, patch-based transform without high computational cost. This paper promotes the case of using partitions consisting of non-overlapping patches, since these types of partitions require the computation of a much smaller number of singular-value matrix decompositions (SVD)[154], in comparison to using partitions formed from overlapping patches. Inspired by the work of Xu and Yin[155], we propose to randomly shift the partition at each iteration of the iterative singular value soft-thresholding algorithm that is used for solving the associated optimization problem[156]. We compare LLR-IRPA with one of the state-of-the-art LLR regularization methods, CLEAR[151], which uses multiple sets of overlapping patches. We show that LLR-IRPA performs equivalently or even better than CLEAR but with the added advantage of substantially reduced computational load. This strategy is not limited strictly to parallel MRI, but can be extended within the context of MR quantitative parameter mapping. As also shown in the results, the LLR-IRPA approach applies equally well to accelerated T_1 mapping from undersampled, calibrationless k-space data.

We provide theoretical support to justify LLR-IRPA, based on results related to cycle spinning in the wavelet-based iterative soft-thresholding algorithm (ISTA)[157]. A proof of convergence of the LLR-IRPA algorithm is given within the ISTA framework, although all reconstructions are implemented with FISTA, an accelerated version of ISTA. Similar to non-cycled wavelet-based ℓ_1-regularization, locally low-rank regularization based on a fixed partition lacks the necessary shift invariance to prevent residual block artifacts. A key advantage of LLR-

IRPA is the simultaneous suppression of block artifacts and reduction of computational load through iterative random shifts.

This chapter is organized as follows: In sections A.3 we describe the theoretical framework for locally low-rank reconstruction with and without iterative random patch adjustments including a proof of shift invariance for the LLR-IRPA algorithm. Section A.4 presents the experimental methods for undersampled parallel imaging and quantitative parameter mapping reconstructions. In section A.5, numerical and imaging results are presented which show equivalent or comparable performance of LLR-IRPA in relation to CLEAR. In Section A.6, we discuss potential implications and extensions of the method, followed by concluding remarks in Section A.7.

A.3 **Theory**

A.3.1 **Locally Low Low-Rank Regularization (LLR) Based on a Fixed Partition of Non-Overlapping Patches**

For simplicity, we consider the case of multi-coil two-dimensional (2D) imaging, although this framework can be adapted to more general 3D or multi-contrast imaging. In the case of 2D multi-coil images, the $M \times N$images from all C coils are vectorized into $\boldsymbol{x} \in \mathbb{C}^{MNC}$. The forward model of the data acquisition is then represented by

$$\boldsymbol{y} = \mathcal{F}\boldsymbol{x} + \boldsymbol{n} \tag{A-1}$$

where $\mathcal{F}: \mathbb{C}^{MNC} \rightarrow \mathbb{C}^{KC}$ is the Fourier undersampling operator, $y \in \mathbb{C}^{KC}$ is the undersampled k-space data, and $n \in \mathbb{C}^{KC}$is a vector of i.i.d Gaussian noise, where $K < MN$. The reduction factor (RF) for the acquisition is defined as MN/K.

To form locally low-rank submatrices, the fixed-partition LLR framework divides the underlying image into a partition Ω of non-overlapping, covering patches. The number of patches within Ω is denoted by $|\Omega|$, and each is labeled as $q \in \Omega$, where $q = 1,2,\ldots,|\Omega|$. For a given set of patch dimensions, the image plane can be divided in a number of different ways by shifting the partition by different pixel amounts along each dimension. Therefore, we denote any particular shift of the partition Ω by Ω_k, where $k \in \{1,2,\ldots,\mathrm{N}_\Omega\}$, and N_Ω is the total number of distinct shifts. Each patch is assumed to have dimensions $m \times n$ where at the image boundaries either (i) periodic boundary conditions are imposed, or (ii) the patch is zero-padded in regions beyond the boundary. This report adopts the latter approach.

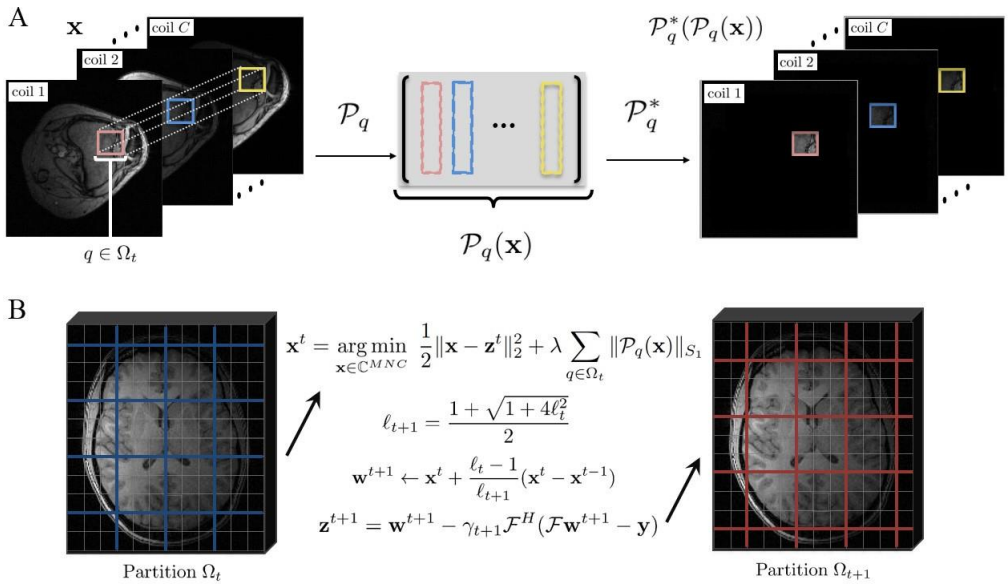

Figure A-1: (A) The patch location $q \in \Omega_t$ from each image $\boldsymbol{x}^{(j)}$ in the multi-coil set $\boldsymbol{x}$ $(j = 1,2,\ldots,C)$ is extracted to form the columns of the locally low rank matrix $P_q(\boldsymbol{x})$. The adjoint operator is applied to reconfigure this matrix onto the original image space. (B) Illustration of the FISTA scheme with a random shift of the partition Ω_t (blue) at iteration t to partition Ω_{t+1} (red) at iteration $t+1$. The patch is zero-padded in locations outside the image boundary.

Let $P_q: \mathbb{C}^{MNC} \rightarrow \mathbb{C}^{mn \times C}$ be the linear operator that extracts from $\boldsymbol{x}$ the image data corresponding to the q^{th} patch of the partition Ωand forms a matrix $P_q(\boldsymbol{x})$ whose k^{th}column is the vectorized patch from the k^{th}coil image, $k = 1, 2, \ldots, C$ (Figure A-1). The underlying image is modeled as locally correlated within a relatively small region across the coil dimension. The key assumption is that the coil sensitivities are locally smooth, so that the cumulative coil sensitivity within a sufficiently small region, i.e. patch, has a low-order representation with respect to some basis. Therefore, in cases where the image patches do not consist entirely of noise, the matrix $P_q(\boldsymbol{x})$ will be low rank[151]. This locally-low rank property is central to the LLR regularization scheme for reconstruction from undersampled data.

Using the inner product $\langle A, \mathrm{B} \rangle_{\mathbb{C}^{mn \times C}} = Re(tr(A^H B))$ over $\mathbb{C}^{mn \times C}$, the adjoint operator P_q^* satisfies

$$\langle P_q(\boldsymbol{x}), Y \rangle_{\mathbb{C}^{mn \times C}} = \langle \boldsymbol{x}, P_q^*(Y) \rangle_2 \tag{A-2}$$

for any $\boldsymbol{x} \in \mathbb{C}^{MNC}$ and $Y \in \mathbb{C}^{mn \times C}$. Specifically, it is defined as the linear operator $P_q^*: \mathbb{C}^{mn \times C} \rightarrow \mathbb{C}^{MNC}$ that maps all vectorized patches in $P_q(\boldsymbol{x})$ back to their respective locations in a vector in $\mathbb{C}^{MNC}$, where all the entries in this vector are zero except those corresponding to the q^{th} patch.

With these operations, we can now define the linear operator $\mathcal{T}_\Omega: \mathbb{C}^{MNC} \rightarrow \chi$, where $\chi \equiv \mathbb{C}^{|\Omega| \times mn \times C}$, and each component of $\mathcal{T}_\Omega \boldsymbol{x}$ is given as

$$[\mathcal{T}_\Omega \boldsymbol{x}]_q = P_q(\boldsymbol{x}) \tag{A-3}$$

for $q = 1,2, \ldots, |\Omega|$. For $\mathbf{X}, \mathbf{Y} \in \chi$, the inner product is

$$\langle \mathbf{X}, \mathbf{Y} \rangle_{\chi} = \sum_{q=1}^{|\Omega|} \mathrm{Re}(\mathrm{tr}(\mathbf{Y}_q^H \mathbf{X}_q)) \tag{A-4}$$

and norm $\|\mathbf{X}\|_{\chi} = \sqrt{\langle \mathbf{X}, \mathbf{X} \rangle_{\chi}}$, where the components $\mathbf{X}_q, \mathbf{Y}_q \in \mathbb{C}^{mn \times C}$. The adjoint $\mathcal{T}_{\Omega}^{*}: \chi \to \mathbb{C}^{MNC}$ is the linear operator that satisfies

$$\langle \mathcal{T}_{\Omega} \boldsymbol{x}, \mathbf{Y} \rangle_{\chi} = \langle \boldsymbol{x}, \mathcal{T}_{\Omega}^{*}(\mathbf{Y}) \rangle_2 \tag{A-5}$$

for any $\mathbf{Y} \in \chi$ and $\boldsymbol{x} \in \mathbb{C}^{MNC}$, and it is defined as

$$\mathcal{T}_{\Omega}^{*} Y = \sum_{q=1}^{|\Omega|} P_q^{*} Y_q \tag{A-6}$$

Because all possible partitions consist only of non-overlapping, contiguous patches that completely cover the entire image[155] we also have that

$$\mathcal{T}_{\Omega}^{*}(\mathcal{T}_{\Omega} \boldsymbol{x}) = \boldsymbol{x} \tag{A-7}$$

$$\mathcal{T}_{\Omega}(\mathcal{T}_{\Omega}^{*} \mathbf{Y}) = \mathbf{Y} \tag{A-8}$$

Since the rank of a matrix is a non-convex function and minimization of rank is an NP hard problem, matrix rank is approximated by the Schatten 1-norm, also known as the nuclear norm. This norm is the closest convex relaxation of matrix rank. We recall the definition of the Schatten p-norm[158] of a matrix $A \in \mathbb{C}^{n_1 \times n_2}$ as

$$\|A\|_{S_p} = \|\sigma(A)\|_p \tag{A-9}$$

where $\sigma(A)$ is the vector of singular values of A, $\sigma_i(A)$is the i^{th} singular value, and $\|\cdot\|_p$ is the ℓ_p-norm. Based on the Schatten 1-norm, the patch-based locally-low rank regularization term can be defined in terms of the mixed $\ell_1 - S_1$ norm[159] which, for an element $\mathbf{X} \in \chi$, is defined as

$$\|\mathbf{X}\|_{1,1} = \sum_{q=1}^{|\Omega|} \|\mathbf{X}_q\|_{S_1} \tag{A-10}$$

Accordingly, the optimization problem is formulated as

$$\hat{\boldsymbol{x}} = \underset{\boldsymbol{x}\in\mathbb{C}^{MNC}}{\operatorname{argmin}} \frac{1}{2}\|\boldsymbol{y} - \mathcal{F}\boldsymbol{x}\|_2^2 + \lambda\|\mathcal{T}_\Omega \boldsymbol{x}\|_{1,1} \tag{A-11}$$

where $\lambda \geq 0$ is a regularization parameter that balances the trade-off between data fidelity and the locally low-rank representation of the image. Equation A-11 represents the general formulation for recovering a locally-low rank image $\boldsymbol{x}$ from its undersampled measurements, assuming a particular partition Ω of non-overlapping, covering patches.

A.3.2 **Optimization Algorithm**

We use the ISTA formalism[160,161] to solve Equation A-11, since the regularization functional is convex but non-smooth[159]. ISTA and its variants are majorization-minimization (MM) algorithms that successively minimize a sequence of surrogate functions that upper bound the original objective function. Using an initial estimate $\boldsymbol{x}_0$, a quadratic upper bound f of the objective function in Equation A-11 can be written as

$$f(\boldsymbol{x}, \boldsymbol{x}_0) = \frac{\alpha}{2}\|\boldsymbol{x} - \boldsymbol{z}\|_2^2 + \lambda\|\mathcal{T}_\Omega \boldsymbol{x}\|_{1,1} \tag{A-12}$$

where $\boldsymbol{z} = \boldsymbol{x}_0 + \frac{1}{\alpha}\mathcal{F}^H(y - \mathcal{F}\boldsymbol{x}_0)$ and $\alpha \geq \lambda_{\max}(\mathcal{F}^H\mathcal{F})$. The algorithm proceeds by iteratively minimizing Equation A-12, setting $\boldsymbol{x}_0$ to the solution of the previous iteration. To minimize the function in Equation A-12, we use the fact that the dual of the mixed $\ell_1 - S_1$ norm is the mixed $\ell_\infty - S_\infty$ norm[159,162]. Thus, for $\mathbf{X} \in \chi$, the $\ell_1 - S_1$ norm can be written equivalently as

$$\|\mathbf{X}\|_{1,1} = \max_{\boldsymbol{\Psi} \in B_{\infty,\infty}} \langle \boldsymbol{\Psi}, \mathbf{X} \rangle_\chi \tag{A-13}$$

where the set $B_{\infty,\infty}$ denotes the $\ell_\infty - S_\infty$ unit norm ball

$$B_{\infty,\infty} = \{\boldsymbol{\Psi} \in \chi : \left\|\boldsymbol{\Psi}_q\right\|_{S_\infty} \leq 1, \forall q = 1, 2, \ldots, |\Omega|\} \tag{A-14}$$

Using these definitions and the adjoint operator $\mathcal{T}_\Omega^*$, the minimization of Equation A-12 can be expressed equivalently as

$$\widehat{\boldsymbol{x}} = \underset{\boldsymbol{x} \in \mathbb{C}^{MNC}}{\operatorname{argmin}} \frac{1}{2}\|\boldsymbol{x} - \boldsymbol{z}\|_2^2 + \frac{\lambda}{\alpha} \cdot \max_{\boldsymbol{\Psi} \in B_{\infty,\infty}} \langle \mathcal{T}_\Omega^* \boldsymbol{\Psi}, \boldsymbol{x} \rangle_2 \tag{A-15}$$

Because the objective function in Equation A-15 is strictly convex in $\boldsymbol{x}$ and concave in $\boldsymbol{\Psi}$, an optimal saddle-point $(\widetilde{\boldsymbol{x}}, \widetilde{\boldsymbol{\Psi}})$ exists[159] at which the objective function attains a common value, and the order of minimization and maximization does not affect the solution. Thus, defining $\mathcal{L}(\boldsymbol{x}, \boldsymbol{\Psi}) = \frac{1}{2}\|\boldsymbol{x} - \boldsymbol{z}\|_2^2 + \frac{\lambda}{\alpha}\langle \mathcal{T}_\Omega^* \boldsymbol{\Psi}, \boldsymbol{x} \rangle_2$,

$$\min_{\boldsymbol{x} \in \mathbb{C}^{MNC}} \max_{\boldsymbol{\Psi} \in B_{\infty,\infty}} \mathcal{L}(\boldsymbol{x}, \boldsymbol{\Psi}) = \boldsymbol{\mathcal{L}}(\widetilde{\boldsymbol{x}}, \widetilde{\boldsymbol{\Psi}}) = \max_{\boldsymbol{\Psi} \in B_{\infty,\infty}} \min_{\boldsymbol{x} \in \mathbb{C}^{MNC}} \mathcal{L}(\boldsymbol{x}, \boldsymbol{\Psi}) \tag{A-16}$$

From Equation A-16, one can identify the primal objective function $\rho(\boldsymbol{x})$ and the dual objective function $s(\boldsymbol{\Psi})$ as

$$\rho(\boldsymbol{x}) = \max_{\boldsymbol{\Psi}\in B_{\infty,\infty}} \mathcal{L}(\boldsymbol{x}, \boldsymbol{\Psi}) = \frac{1}{2}\|\boldsymbol{x}-\boldsymbol{z}\|_2^2 + \frac{\lambda}{\alpha}\|\mathcal{T}_\Omega \boldsymbol{x}\|_{1,1} \tag{A-17}$$

$$s(\boldsymbol{\Psi}) = \min_{x\in\mathbb{C}^{MNC}} \mathcal{L}(\boldsymbol{x}, \boldsymbol{\Psi}) = \frac{1}{2}\left(\|z\|_2^2 - \left\|z - \frac{\lambda}{\alpha}\mathcal{T}_\Omega^*\boldsymbol{\Psi}\right\|_2^2\right) \tag{A-18}$$

Accordingly, one can find the minimizer $\widetilde{\boldsymbol{x}}$ of $\rho(\boldsymbol{x})$ by finding the maximizer $\widetilde{\boldsymbol{\Psi}}$ of $s(\boldsymbol{\Psi})$, using the relation

$$\widetilde{\boldsymbol{x}} = z - \frac{\lambda}{\alpha}\mathcal{T}_\Omega^*\widetilde{\boldsymbol{\Psi}} \tag{A-19}$$

From Equation A-18, one can see that by using Equations A-5, A-7, and A-8,

$$\max_{\boldsymbol{\Psi}\in B_{\infty,\infty}} s(\boldsymbol{\Psi}) = \min_{\boldsymbol{\Psi}\in B_{\infty,\infty}} \frac{1}{2}\left\|\boldsymbol{z} - \frac{\lambda}{\alpha}\mathcal{T}_\Omega^*\boldsymbol{\Psi}\right\|_2^2 = \min_{\boldsymbol{\Psi}\in B_{\infty,\infty}} \frac{1}{2}\left\|\frac{\alpha}{\lambda}\mathcal{T}_\Omega \boldsymbol{z} - \boldsymbol{\Psi}\right\|_\chi^2 \tag{A-20}$$

Therefore, the maximizer of Equation A-18 can be found by projecting $\frac{\alpha}{\lambda}\mathcal{T}_\Omega \boldsymbol{z} \in \chi$ onto the $B_{\infty,\infty}$ unit norm ball. This projection onto $B_{\infty,\infty}$ can be done by projecting each of the components of $\frac{\alpha}{\lambda}\mathcal{T}_\Omega \boldsymbol{z}$ onto the unit norm ball B_{S_∞}[159], the space of matrices with Schatten ∞-norm ≤ 1. If the singular value decomposition of the component matrix $\frac{\alpha}{\lambda}[\mathcal{T}_\Omega \boldsymbol{z}]_q = \mathbf{U}_q \mathrm{diag}\left(\sigma\left(\frac{\alpha}{\lambda}[\mathcal{T}_\Omega \boldsymbol{z}]_q\right)\right)\mathbf{V}_q^H$, then its projection onto B_{S_∞} is

$$P_{B_{S_\infty}}\left(\frac{\alpha}{\lambda}[\mathcal{T}_\Omega \boldsymbol{z}]_q\right) = \frac{\alpha}{\lambda}\mathbf{U}_q \mathrm{diag}\left(\min\left(\sigma([\mathcal{T}_\Omega \boldsymbol{z}]_q), \frac{\lambda}{\alpha}\mathbf{1}\right)\right)\mathbf{V}_q^H = \widetilde{\boldsymbol{\Psi}}_{\boldsymbol{q}} \tag{A-21}$$

Based on Equation A-19 and Equation A-21, we conclude that

$$\widetilde{\boldsymbol{x}} = z - \frac{\lambda}{\alpha}\mathcal{T}_\Omega^*\boldsymbol{\Psi} = \mathcal{T}_\Omega^*\left(\mathcal{T}_\Omega \boldsymbol{z} - \frac{\lambda}{\alpha}\boldsymbol{\Psi}\right) \tag{A-22}$$

$$\Longrightarrow \tilde{\boldsymbol{x}} = \sum_{q=1}^{|\Omega|} P_q^* \left(\mathbf{U}_q diag \left(\mathcal{S}_{\frac{\lambda}{\alpha}} \left[\sigma\left([\mathcal{T}_\Omega \boldsymbol{z}]_q \right) \right] \right) \mathbf{V}_q^H \right)$$

where $\mathcal{S}_\beta[\sigma(\mathbf{X}_q)] = \max(\sigma(\mathbf{X}_q) - \beta, 0)$ is defined as the soft-thresholding operator, applied component-wise on the vector of singular values $\sigma(\mathbf{X}_q)$. Importantly, we note that the minimization of $\rho(\boldsymbol{x})$ is the proximal mapping of the patch-based regularizer $\lambda\|\mathcal{T}_\Omega \boldsymbol{x}\|_{1,1}$:

$$\tilde{\boldsymbol{x}} = \min_{\boldsymbol{x} \in \mathbb{C}^{MNC}} \rho(\boldsymbol{x}) = \text{prox}_{\lambda\|\mathcal{T}_\Omega \cdot\|_{1,1}} \left(\mathbf{z}; \frac{1}{\alpha} \right) \tag{A-23}$$

Summarizing the above, the overall iterative soft-thresholding scheme proceeds as

$$\boldsymbol{z}^t = \mathbf{w}^t - \gamma_t \mathcal{F}^H (\mathcal{F}\mathbf{w}^t - \mathbf{y}) \tag{A-24}$$

$$\boldsymbol{x}^t = \text{prox}_{\lambda\|\mathcal{T}_\Omega \cdot\|_{1,1}} (\boldsymbol{z}^t; \gamma_t) \tag{A-25}$$

$$\ell_{t+1} \leftarrow \frac{1 + \sqrt{1 + 4\ell_t^2}}{2} \tag{A-26}$$

$$\boldsymbol{w}^{t+1} \leftarrow \boldsymbol{x}^t + \frac{\ell_t - 1}{\ell_{t+1}} (\boldsymbol{x}^t - \boldsymbol{x}^{t-1}) \tag{A-27}$$

where $\gamma_t \leq \frac{1}{\alpha}$ is the gradient descent step size and $\boldsymbol{w}^1 = \mathcal{F}^H \boldsymbol{y}$. In short, Equation A-22 represents reconstructing the image after singular-value thresholding of each matrix formed from each patch in the partition. The iterations in Equation A-24 to A-27 represent the ISTA technique for solving Equation A-11, using a fixed partition Ω.

A.3.3 **Locally Low-Rank Regularization (LLR) Based on Overlapping Patches**

LLR regularization based on overlapping patches is well-represented by the state-of-the-art CLEAR algorithm[151]. In this method, the entire image is covered by patches that are overlapped

by a certain factor of the image patch dimensions. Specifically, suppose that patches of dimensions $m \times n$ are used to cover a $M \times N$ image matrix, where $m|M$ and $n|N$. The amount of overlap along the first dimension is designated by a factor $0 < r \leq 1$ of m, i.e., patches overlap each successive patch by rm pixels. Similarly, along the other dimension, patches are overlapped by sn pixels $0 < s \leq 1$). Then the total number of overlapping patches P that cover the image is

$$\mathrm{P} = \left(\frac{\mathrm{N} + \mathrm{n}(1 - \mathrm{s})}{\mathrm{sn}}\right)\left(\frac{\mathrm{M} + \mathrm{m}(1 - \mathrm{r})}{\mathrm{rm}}\right) \tag{A-28}$$

Let Γ be the set of non-overlapping partitions that, when taken together, correspond to the entire collection of P overlapping patches. Then the optimization problem of CLEAR can be expressed within the framework described in the previous section as

$$\hat{\boldsymbol{x}} = \underset{\boldsymbol{x} \in \mathbb{C}^{MNC}}{\operatorname{argmin}} \frac{1}{2} \|\boldsymbol{y} - \mathcal{F}\boldsymbol{x}\|_2^2 + \lambda \cdot rs \sum_{\Omega \in \Gamma} \|\mathcal{T}_\Omega \boldsymbol{x}\|_{1,1} \tag{A-29}$$

Note that this problem entails solving for a significantly higher number of SVDs, as compared to Equation A-11 in which at most only $\left(\frac{M}{m} + 1\right)\left(\frac{N}{n} + 1\right)$ are computed. In addition, the regularization term must be multiplied by a factor rs in order to compensate for taking the SVDs of multiple overlapping patches. Due to overlapping patches, each image patch is actually not independent of the others, since any particular patch in the output image contains contributions from the image patches that surround it. Therefore, including this factor in the regularization term essentially represents a heuristic approach to reconstructing the final image from sets of overlapping patches[163].

A.3.4 **Locally Low-Rank Regularization with Iterative Random Patch Adjustments (LLR-IRPA)**

In the LLR regularization approach described in section B, the partition Ω remains fixed throughout all iterations. As an alternative strategy, the proposed LLR-IRPA method updates the partition at each iteration. This modification leads to a reduced appearance of block artifacts while exhibiting similar behavior to CLEAR in terms of reconstruction error and convergence rate. The partition is shifted by random amounts in each direction. The FISTA iterations are modified such that the partition updates as $\Omega_{k_t+1} \leftarrow \Omega_{k_t}$ where $k_t \in \{1,2,\dots,N_\Omega$ is chosen at random for each iteration t, and Ω_{k_t}runs through the N_Ω possible partitions as the iterative process continues. Note that in this case, each image patch is independent of the others throughout the reconstruction process, in contrast to CLEAR. A major feature is that LLR-IRPA achieves the property of shift-invariance without the need of overlapping patches, leading to a greatly reduced computational load compared to CLEAR.

Although at each iteration we obtain a solution using a different patch arrangement, and thus a different decomposition of the image, we provide a proof which shows that the LLR-IRPA iterations converge to a solution that represents the outcome from averaging the singular value thresholdings from all unique patch-based SVDs of the entire image matrix, i.e., the regularizer is effectively shift-invariant. These results are inspired by the variational justification for cycle spinning using the wavelet transform[157], and a proof of convergence is provided in the next section. For simplicity, this proof is given in the context of ISTA.

A.3.5 **Proof of Shift Invariance**

In order to justify the shift invariance that results from random iterative patch adjustments, we prove the result for the deterministic case, in which the iterations traverse all possible partition shifts. Similar to the case of cycle spinning using the wavelet transform, in the context of patch-based LLR-IRPA regularization, the partition Ω is changed by shifting it by some amount at each iteration. For simplicity, this proof of convergence is given in the context of ISTA[161]. The ISTA iterations are given by

$$\boldsymbol{z}^t = \mathbf{x}^{t-1} - \gamma_t \mathcal{F}^H(\mathcal{F}\mathbf{x}^{t-1} - \mathbf{y}) \tag{A-31}$$

$$\boldsymbol{x}^t = \text{prox}_{\lambda\|\mathcal{T}_\Omega \cdot\|_{1,1}}(\boldsymbol{z}^t; \gamma_t) \tag{A-32}$$

Using the notation introduced in the Theory section, we write the cost function associated with the partition Ω_k as

$$H_k(\boldsymbol{x}) = \frac{1}{2}\|\boldsymbol{y} - \mathcal{F}\boldsymbol{x}\|_2^2 + \lambda\left\|\mathcal{T}_{\Omega_k}\boldsymbol{x}\right\|_{1,1} = D(\boldsymbol{x}) + G_{\Omega_k}(\boldsymbol{x}) \tag{A-33}$$

where the component functions are defined, for notational simplicity, as

$$D(\boldsymbol{x}) \equiv \frac{1}{2}\|\boldsymbol{y} - \mathcal{F}\boldsymbol{x}\|_2^2$$

$$G_{\Omega_k}(\boldsymbol{x}) \equiv \lambda\left\|\mathcal{T}_{\Omega_k}\boldsymbol{x}\right\|_{1,1}$$

We write the cost function whose regularization term represents the average of the nuclear norms of all locally low-rank matrices formed from the N_Ω unique shifts of Ω:

$$h(\boldsymbol{x}) = \frac{1}{N_\Omega}\sum_{k=1}^{N_\Omega} H_k(\boldsymbol{x}) = D(x) + \frac{1}{N_\Omega}\sum_{k=1}^{N_\Omega} G_{\Omega_k}(\boldsymbol{x}) \tag{A-34}$$

The following assumptions are made:

- The feasible set $\mathcal{C} \subseteq \mathbb{C}^{MNC}$ is nonempty, convex, closed and bounded, i.e., $\exists\, d > 0$ such that $\forall\, \boldsymbol{x}, \boldsymbol{y} \in \mathcal{C}, \|\boldsymbol{x} - \boldsymbol{y}\|_2 \leq d$.
- The data fidelity term D is continuously differentiable with Lipschitz continuous gradient, i.e., $\exists\, L > 0$ such that $\forall\, \boldsymbol{x}, \boldsymbol{y} \in \mathcal{C}, \|\nabla D(x) - \nabla D(y)\|_2 \leq L\|\boldsymbol{x} - \boldsymbol{y}\|_2$.
- The gradient of D is bounded and the subgradients of G_{Ω_k} are bounded, i.e., $\exists\, S > 0$ such that $\forall\, \boldsymbol{x} \in \mathcal{C}, \|\nabla D(\boldsymbol{x})\|_2 \leq S$ and $\left\|\partial G_{\Omega_k}(\boldsymbol{x})\right\|_2 \leq S$

Referring to Theorem 1 of the report by Kamilov et al.[157], if $L \geq \lambda_{\max}(\mathcal{F}^H\mathcal{F})$ and the step size $\gamma_t \leq \frac{1}{L\sqrt{t}}$, then we claim that the sequence $\{\boldsymbol{x}^t\}$ generated according to Equations A-31 and A-32 satisfies

$$\lim_{t\to\infty} h(\boldsymbol{x}^t) = h^* \tag{A-35}$$

where $h^* = \min_{\boldsymbol{x}\in\mathcal{C}} h(\boldsymbol{x})$. The claim in Equation A-35 essentially says that shifting the partitions throughout the iteration process leads to the minimization of the cost function that simultaneously minimizes the nuclear norms of the submatrices formed from all partition shifts. Therefore, the underlying regularizer in Equation A-34 is effectively shift-invariant.

For simplicity, we consider the case of an image with square dimensions $N \times N$ and square patch sizes $(m = n)$, such that n divides N (results for arbitrary dimensions can be obtained through similar arguments). In this case $N_\Omega = n^2$ and the number of patches $|\Omega_k|$ within any partition Ω_k falls within $\left[\left(\frac{N}{n}\right)^2, \left(\frac{N}{n}\right)^2 + 2\frac{N}{n} + 1\right]$. We also note that in patch-based LLR regularization, it is generally assumed that each of the $(N-n)^2$ possible (overlapping) patch

locations lead to low-rank submatrices. Therefore, all submatrices $P_q(\boldsymbol{x})$ formed by $\mathrm{q} \in \Omega_k$ for any k, are assumed low-rank.

We first characterize the subdifferential of the function $G_{\Omega_k}(\boldsymbol{x}) \equiv \lambda\left\|\mathcal{T}_{\Omega_k}\boldsymbol{x}\right\|_{1,1}$ to show that the subgradients are indeed bounded[164]. To do so, we find the conjugate function of the mixed $\ell_1 - S_1$ norm. Denote the function $F(\mathbf{X}) = \|\mathbf{X}\|_{1,1}$ for $\mathbf{X} \in \boldsymbol{\chi}$ and denote the function $g(\boldsymbol{x}) = \mathcal{T}_{\Omega_k}\boldsymbol{x}$ for $\boldsymbol{x} \in \mathbb{C}^{MNC}$. Using the duality between the $\ell_1 - S_1$ norm and the $\ell_\infty - S_\infty$ norm, it is straightforward to show the conjugate function F^* of F is

$$F^*(\mathbf{X}) = \begin{cases} 0 & \|X\|_{\infty,\infty} \leq 1 \\ \infty & \text{otherwise} \end{cases} \tag{A-36}$$

i.e., the conjugate is the indicator function of the $\ell_\infty - S_\infty$ unit norm ball. Recalling the well-known fact from convex analysis[164,165] that if $G \in \partial F(\mathbf{X})$ then

$$F^*(\mathbf{G}) + F(\mathbf{X}) = \langle \mathbf{G}, \mathbf{X} \rangle_\chi \tag{A-37}$$

and noting that $G_{\Omega_k}(\boldsymbol{x}) = \lambda\,(F \circ g)(\boldsymbol{x}) = \lambda\, F(g(\boldsymbol{x})$, one can use the chain rule to characterize the subdifferential of G_{Ω_k} at $\boldsymbol{x}$ as the set

$$\partial G_{\Omega_k}(\boldsymbol{x}) = \left\{\lambda\mathcal{T}_{\Omega_k}^*\mathbf{Y} \in \mathbb{C}^{MNC} \middle|\, \|\mathbf{Y}\|_{\infty,\infty} \leq 1,\, \langle \mathcal{T}_{\Omega_k}^*\mathbf{Y}, \boldsymbol{x}\rangle_2 = \left\|\mathcal{T}_{\Omega_k}\boldsymbol{x}\right\|_{1,1}\right\} \tag{A-38}$$

This characterization implies that the subgradients of $G_{\Omega_k}(\boldsymbol{x}) \equiv \lambda\left\|\mathcal{T}_{\Omega_k}\boldsymbol{x}\right\|_{1,1}$ are indeed bounded. We also recall the important fact from convex analysis that if

$$\boldsymbol{x} = \mathrm{prox}_{\lambda\left\|\mathcal{T}_{\Omega_k}\cdot\right\|_{1,1}}(\boldsymbol{z}; \gamma_t) \tag{A-39}$$

then $\boldsymbol{z} - \boldsymbol{x} \in \lambda\,\partial\left(\left\|\mathcal{T}_{\Omega_k}\boldsymbol{x}\right\|_{1,1}\right)$.

Given these observations, we can follow the steps as in the proof of Lemma 1 in the report by Kamilov et al.[157] to conclude that $\forall \boldsymbol{x}^* \in \mathcal{C}$

$$H_{k_t}(\boldsymbol{x}^t) - H_{k_t}(\boldsymbol{x}^*) \leq \frac{1}{2\gamma_t}(\|\boldsymbol{x}^{t-1} - \boldsymbol{x}\|_2 - \|\boldsymbol{x}^t - \boldsymbol{x}\|_2) + 6\gamma_t S^2 \tag{A-40}$$

For convenience, we restate Lemma 2 of the report by Kamilov et al. [157] in this context as

$$\lim_{n \to \infty} \left\{ \frac{1}{nN_\Omega} \sum_{t=1}^{nN_\Omega} H_{k_t}(\boldsymbol{x}^t) \right\} = h(\overline{\boldsymbol{x}}) \tag{A-41}$$

where $\{\boldsymbol{x}^t\}$ is a sequence in $\mathbb{C}$ such that $\boldsymbol{x}^t \to \overline{\boldsymbol{x}}$.

In a similar manner to the proof of Theorem 1 in the report by Kamilov et al.[157], if we let $\boldsymbol{x}^*$ denote a minimizer of the function h and sum the bound in Equation A-40, then

$$\sum_{t=1}^{nN_\Omega} \left(H_{k_t}(\boldsymbol{x}^t) - H_{k_t}(\boldsymbol{x}^*) \right) \leq \frac{d^2}{2\gamma_{nN_\Omega}} + 6S^2 \sum_{t=1}^{nN_\Omega} \gamma_t \tag{A-42}$$

Choosing the step size $\gamma_t \leq \frac{1}{L\sqrt{t}}$ and dividing both sides of Equation A-42 by nN_Ω, the above inequality can be simplified to

$$\frac{1}{nN_\Omega} \sum_{t=1}^{nN_\Omega} H_{k_t}(\boldsymbol{x}^t) - h(\boldsymbol{x}^*) \leq \frac{\mathrm{C}}{\sqrt{n}} \tag{A-43}$$

for a constant C depending on the parameters d, S and L defined above. Therefore, using Equation A-41 and Equation A-43,

$$0 \leq h(\bar{\boldsymbol{x}}) - h(\boldsymbol{x}^*) = \lim_{n \to \infty} \left\{ \frac{1}{nN_\Omega} \sum_{t=1}^{nN_\Omega} H_{k_t}(\boldsymbol{x}^t) \right\} - h^* \leq 0 \qquad \text{(A-44)}$$

where the first inequality is due to the optimality of $\boldsymbol{x}^*$. This result shows that the sequence generated by Equations A-31 and A-32 converges to a minimizer $\boldsymbol{x}^*$ of the function h, which is the cost-function that incorporates the effective shift-invariant regularizer that penalizes the nuclear norms of all submatrices that can be formed from all the N_Ω shifts of the partition Ω. As stated above, this argument considers the deterministic shifting strategy in which all possible N_Ω partitions are traversed throughout the iteration process. However, as is the case for wavelet-based cycle spinning, the most practical method to implement this technique is to shift the partition randomly at each iteration. Although it considers the deterministic case, this proof serves as a justification for the more practical method of iterative random shifting.

A.4 **Methods**

The effectiveness of the proposed algorithm was tested with retrospectively-undersampled data in parallel imaging and quantitative parameter mapping experiments, as well as with prospectively undersampled contrast-enhanced magnetic resonance angiography (CE-MRA) data. Both the CLEAR and LLR-IRPA algorithms, including the reconstruction experiments, were implemented `in-house' using MATLAB (The Mathworks, Natick, MA) and run on a Linux workstation with a 4.4 GHz CPU and 96 GB memory.

Two types of undersampling schemes were tested: (1) reducing the number of samples along a single phase-encoding direction (1D undersampling), and (2) reducing the number of samples along two phase-encoding directions (2D undersampling). For the 2D undersampling case, variable-density, Poisson-disk undersampling masks of various reduction factors (RF) were

applied to the fully-sampled k-space to simulate accelerated acquisitions. The 2D probability density function that characterizes the sampling density was set as a normalized Gaussian with standard deviations σ_x and σ_y equal to one-fourth of the corresponding image dimensions N_x and N_y, in pixels. For the 1D undersampling case, the random sampling density was determined by a one-dimensional normalized Gaussian probability density function with standard deviation equal to one-fourth of the corresponding largest image dimension. For the cases involving quantitative parameter mapping, this standard deviation was set equal to one-fourth the size of the actual phase-encoding dimension. For the CLEAR algorithm, the extent of overlapping was set as one-half the dimensions of the image patch, so that $r = s = \frac{1}{2}$ in Equation A-28. This choice of overlapping ratio provides a balanced trade-off between computational load and the extent of shift-invariance of CLEAR's patch-based regularizer.

We used the first-order, fast iterative soft-thresholding algorithm (FISTA) to solve the associated nuclear-norm regularized optimization problem. We also take ISTA as the algorithmic framework with which to show theoretical results concerning the per-iteration random shifts of the image partitions. All reconstructions were performed with a maximum number of 100 iterations, due to the sublinear rate of convergence $O(\frac{1}{t})$, where t is the iteration counter. Moreover, we set a stopping criterion dependent on the relative error between successive solutions, namely $\|x^{t+1} - x^t\|/\|x^t\| < 10^{-5}$. The regularization parameter λ for both CLEAR and LLR-IRPA was set as the estimated standard deviation of the collection of singular values from all matrices formed from all image patches, computed at each iteration. This estimate was obtained using the median absolute deviation of the collection of singular values.

The quality of the reconstruction was quantified using the normalized root mean square error (nRMSE), defined as

$$\text{nRMSE} = \frac{1}{\max(X_0)} \frac{\|X_0 - X\|_2}{\sqrt{N}} \tag{A-30}$$

where X_0 is the true image and X is the reconstruction image, and N is the number of pixels. The algorithmic performances were compared on the basis of image quality and nRMSE values. Difference images were computed and the rate of convergence was characterized by plotting nRMSE as a function of iteration. The criteria to determine the image quality includes the extent of visible blocky artifacts and preservation of edge-features.

		RF=3			RF=4			RF=5			RF=6			RF=7		
	PS	CLEAR	CLEAR-IRPA	LLR-IRPA	CLEAR	CLEAR-IRPA	LLR-IRPA	CLEAR	CLEAR-IRPA	LLR-IRPA	CLEAR	CLEAR-IRPA	LLR-IRPA	CLEAR	CLEAR-IRPA	LLR-IRPA
Brain	4	2.57E-2	2.54E-2	2.62E-2	3.2E-2	2.95E-2	3.01E-2	3.39E-2	3.31E-2	3.40E-2	3.71E-2	3.59E-2	3.66E-2	4.13E-2	3.93E-2	4.07E-2
	6	2.53E-2	2.52E-2	2.58E-2	2.94E-2	2.90E-2	2.96E-2	3.28E-2	3.22E-2	3.25E-2	3.56E-2	3.46E-2	3.52E-2	3.93E-2	3.82E-2	3.92E-2
	8	2.57E-2	2.54E-2	2.59E-2	2.95E-2	2.91E-2	2.96E-2	3.27E-2	3.21E-2	3.26E-2	3.53E-2	3.45E-2	3.50E-2	3.90E-2	3.80E-2	3.96E-2
	10	2.57E-2	2.58E-2	2.61E-2	2.93E-2	2.90E-2	2.95E-2	3.28E-2	3.21E-2	3.26E-2	3.54E-2	3.46E-2	3.52E-2	3.89E-2	3.79E-2	3.87E-2
	12	2.59E-2	2.57E-2	2.62E-2	2.95E-2	2.92E-2	2.99E-2	3.28E-2	3.20E-2	3.26E-2	3.53E-2	3.48E-2	3.59E-2	3.87E-2	3.79E-2	3.92E-2
	14	2.62E-2	2.60E-2	2.62E-2	2.99E-2	2.92E-2	3.00E-2	3.28E-2	3.21E-2	3.30E-2	3.55E-2	3.47E-2	3.56E-2	3.89E-2	3.81E-2	3.93E-2
Knee	4	2.05E-2	2.05E-2	2.15E-2	2.51E-2	2.51E-2	2.61E-2	3.08E-2	3.06E-2	3.28E-2	3.82E-2	3.78E-2	3.97E-2	4.50E-2	4.32E-2	4.59E-2
	6	2.13E-2	2.13E-2	2.15E-2	2.53E-2	2.53E-2	2.58E-2	2.96E-2	2.95E-2	3.03E-2	3.56E-2	3.51E-2	3.61E-2	4.06E-2	4.06E-2	4.26E-2
	8	2.18E-2	2.18E-2	2.21E-2	2.56E-2	2.56E-2	2.61E-2	2.96E-2	2.96E-2	2.98E-2	3.47E-2	3.49E-2	3.52E-2	3.92E-2	3.91E-2	4.04E-2
	10	2.22E-2	2.22E-2	2.23E-2	2.61E-2	2.59E-2	2.59E-2	2.99E-2	2.97E-2	3.01E-2	3.52E-2	3.46E-2	3.49E-2	3.89E-2	3.89E-2	3.92E-2
	12	2.26E-2	2.24E-2	2.26E-2	2.64E-2	2.63E-2	2.63E-2	3.01E-2	3.01E-2	3.02E-2	3.52E-2	3.48E-2	3.49E-2	3.90E-2	3.89E-2	3.93E-2
	14	2.29E-2	2.28E-2	2.29E-2	2.67E-2	2.69E-2	2.68E-2	3.07E-2	3.07E-2	3.09E-2	3.53E-2	3.54E-2	3.53E-2	3.94E-2	3.98E-2	4.02E-2

Table A1: nRMSE results of retrospective undersampling along two phase-encoding directions, for the brain and knee data sets, at various reduction factors (RF) and patch sizes (PS). Results for CLEAR, LLR-IRPA, and CLEAR using iterative patch adjustments (CLEAR-IRPA) are shown.

A.4.1 Parallel Imaging – Retrospective Undersampling

Two fully-sampled data sets, one of the knee and the brain, were acquired from a healthy volunteer after Institutional Review Board (IRB) approval. The data set of the knee was acquired with a 3T Skyra (Siemens Healthcare, Erlangen, Germany) MRI scanner, using a 3D GRE sequence with the following acquisition parameters: matrix size 160×160, isotropic resolution of 1 mm^2, TE = 3.78 ms, TR = 8.6 ms, flip angle 15°, and bandwidth of 810 Hz/px. The brain data set was acquired with the same scanner and sequence, using the following parameters: matrix size

224×224, isotropic resolution of 1 mm^2, TE = 3.5 ms, TR = 8.5 ms, flip angle 12°, and bandwidth of 400 Hz/px. The knee and brain data sets consisted of 15 and 20 channels, respectively.

These 3D data sets were retrospectively undersampled at reduction factors (RF) of 3, 4, 5, 6, and 7, and were reconstructed using square patch sizes (PS) of side lengths of 4, 6, 8, 10, 12, and 14 pixels. For 2D undersampling, a fully-sampled, square region with a 12-pixel side was retained in each undersampling mask. In the 1D undersampling case, 16 fully sampled central phase-encoding lines were retained for undersampling the k-space of the brain data set, while 12 fully-sampled central lines were kept in the mask for undersampling the k-space of the knee data set. Each data set was reconstructed for each combination of reduction factor and patch size.

To emphasize the advantage of LLR-IRPA in terms of both computational efficiency and reconstruction accuracy, these data sets are also reconstructed with CLEAR using iterative random patch adjustments (CLEAR-IRPA). Reconstruction times and nRMSE values resulting from this additional reconstruction approach are compared with LLR-IRPA.

		RF = 2		RF = 2.5		RF = 3	
PS		CLEAR	LLR-IRPA	CLEAR	LLR-IRPA	CLEAR	LLR-IRPA
Brain	6	2.99E-02	3.03E-02	3.74E-02	3.69E-02	5.32E-02	5.38E-02
	8	3.02E-02	3.03E-02	3.69E-02	3.71E-02	5.36E-02	5.30E-02
	10	3.08E-02	3.07E-02	3.72E-02	3.76E-02	5.39E-02	5.37E-02
	12	3.13E-02	3.11E-02	3.80E-02	3.74E-02	5.40E-02	5.46E-02
Knee	6	2.57E-02	2.60E-02	3.10E-02	3.14E-02	3.55E-02	3.53E-02
	8	2.59E-02	2.61E-02	3.10E-02	3.13E-02	3.56E-02	3.57E-02
	10	2.68E-02	2.61E-02	3.17E-02	3.19E-02	3.63E-02	3.60E-02
	12	2.66E-02	2.66E-02	3.17E-02	3.17E-02	3.59E-02	3.60E-02

Table A-2: CLEAR and LLR-IRPA nRMSE results of retrospective undersampling along a single phase-encoding direction, for the brain and knee data sets, at various reduction factors (RF) and patch sizes (PS).

A.4.2 Parallel Imaging – Prospective Undersampling

Multi-phase, contrast-enhanced cardiac- and ventilator-gated MR angiography data[166] was acquired with prospective variable density Poisson-disk undersampling pattern on a 6-month-old pediatric patient with congenital heart disease. The data was acquired with a 3T Trio (Siemens Healthcare, Erlangen, Germany) scanner. The acquisition matrix size was $480 \times 266 \times 128$, with a total of 12 channels, and a fully-sampled central 24×24 square region. Further image acquisition details are as described in the report by Han et al.[166]. This data was prospectively undersampled with RF = 6.5, and was subsequently reconstructed using CLEAR and LLR-IRPA with PS = 4, 6, 8, 10, 12, and 14.

A.5 Results

A.5.1 Parallel Imaging – Retrospective Undersampling

As shown in Figure A2, reconstructions from the retrospectively undersampled data sets show that LLR-IRPA leads to similar reduction in block artifacts and comparable fidelity to the actual images, in relation to the results from CLEAR. This observation can be seen from the reconstructed and difference images, in which LLR-IRPA exhibits minimal block artifacts and recovers structural features just as well or better than CLEAR. We observe also that, in terms of nRMSE, the larger patch sizes (PS = 10,12,14) lead to better recovery of images undersampled at the higher reduction factors (RF = 5,6,7). For comparison, we also include in the figures images reconstructed with LLR regularization using non-overlapping patches.

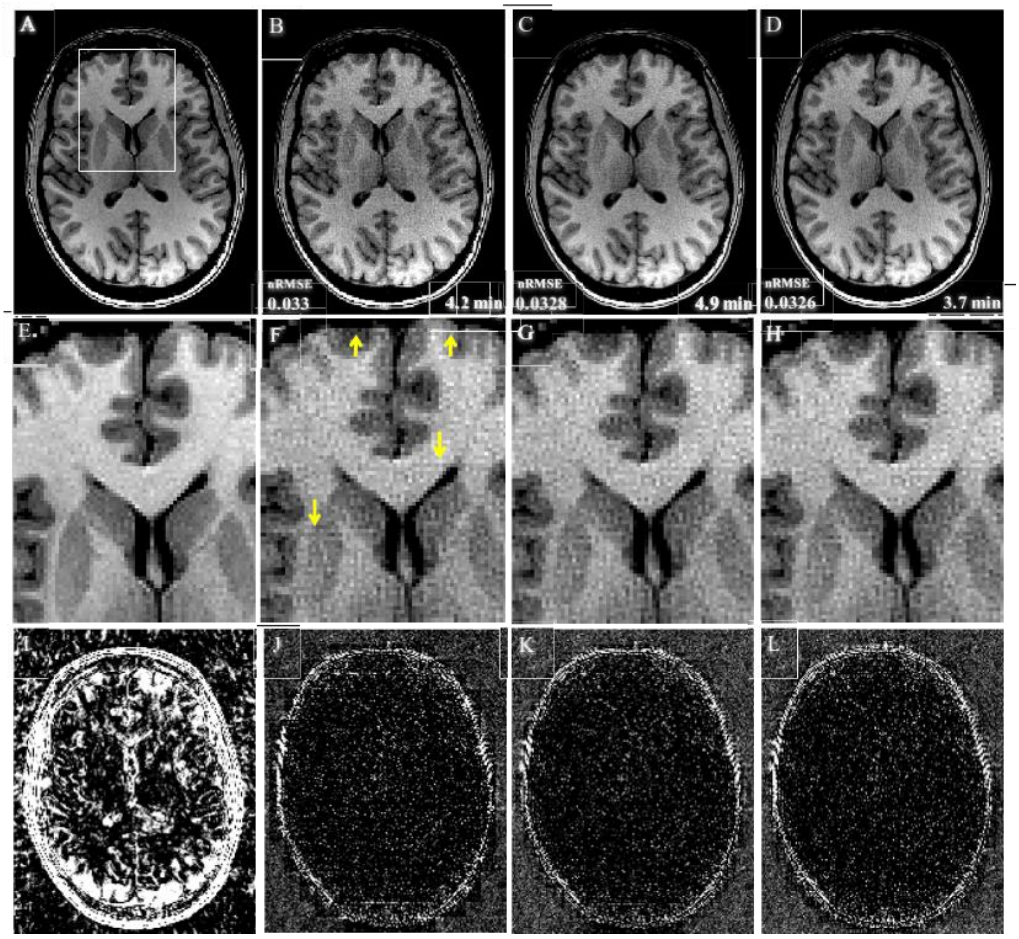

Figure A-2: Brain images reconstructed with RF = 5 and PS = 10×10. Reconstruction times included. (A) Reference image, (B) result using non-overlapping patches (nRMSE = 0.0333), (C) CLEAR (nRMSE = 0.0317). (D) LLR-IRPA (nRMSE = 0.0310). (E)-(H) corresponding zoom-in images. (I) Absolute difference image between the reference and zero-filled reconstructed image. (J), (K), and (L) are absolute difference images for non-overlapping patch-based, CLEAR and LLR-IRPA reconstructions, respectively. Note the reduction in block artifacts (indicated by yellow arrows) using CLEAR and LLR-IRPA in (G) and (H). Window level: 2.4 – 5.6% of the maximum reference signal in (A).

Numerical results listed in Table A1 and Table A2 show that LLR-IRPA is as stable as CLEAR with respect to changes in patch size, in terms of nRMSE. The nRMSE values from LLR-IRPA regularization follow CLEAR's trend as the reduction factor increases, for any given patch size Figure A3. Similarly, at a fixed reduction factor, the nRMSE values obtained from LLR-IRPA are as low or slightly lower than those produced from CLEAR. Finally, it is evident that the LLR-

IRPA strategy leads to convergence of the algorithm to a final value that is very close or equal to that of images reconstructed by CLEAR, although at a much faster rate. These results are consistent with what is expected because, similar to the case of wavelet cycle spinning, the use of various shifted patch arrangements reduces the appearance of block artifacts and avoids the extra computational cost of overlapping patches. In terms of the time per iteration for 2D multi-coil reconstruction experiments, Table A3 demonstrates that LLR-IRPA is computationally more efficient than CLEAR, being approximately 3-4 times faster per iteration.

To show that LLR-IRPA is indeed shift-invariant at no extra computational cost, we also include in Table A2 and Table A3 nRMSE values and computation times from the CLEAR algorithm implemented with per-iterative random shifting. As seen from the tables, the use of per-iterative random shifting in addition to overlapping patches in the CLEAR algorithm results in almost the same performance compared to LLR-IRPA. However, the computational time per iterations is similar to that of conventional CLEAR. Thus, LLR-IRPA achieves a performance that would result from combining the benefits of overlapping patches and random shifting, but with no extra computational cost. Thus, LLR-IRPA retains a definite advantage in both computational efficiency and reconstruction accuracy.

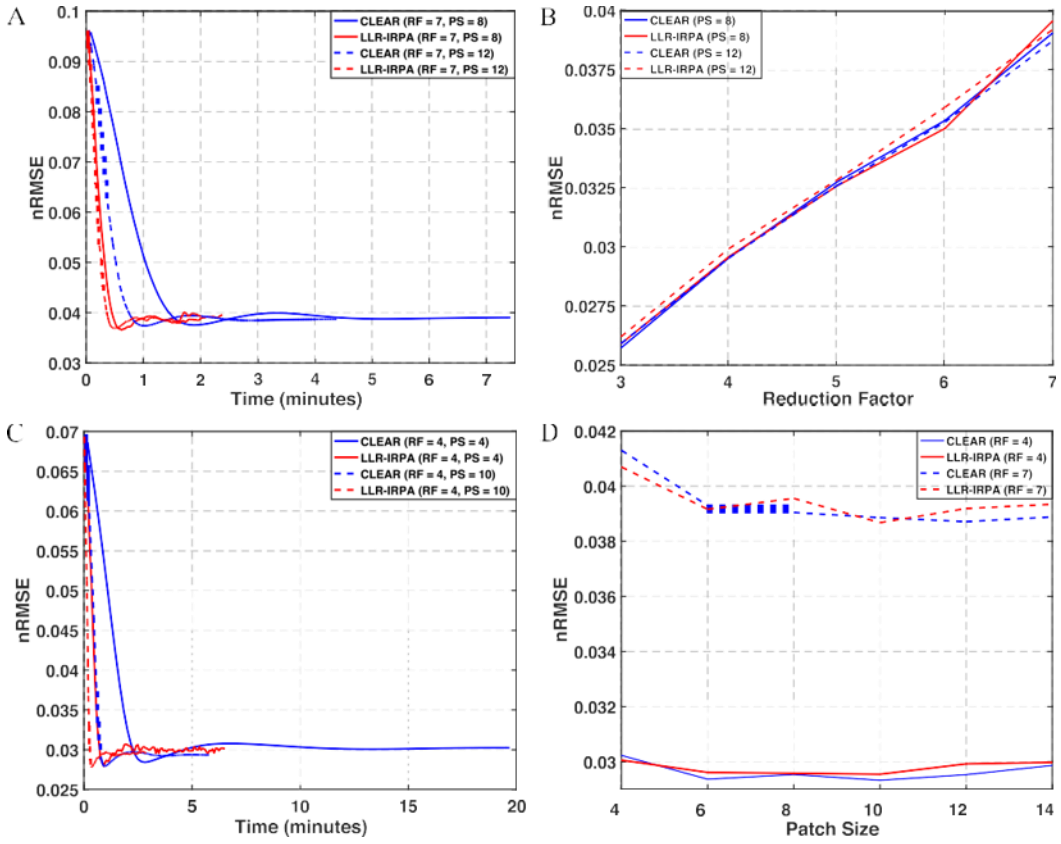

Figure A-3: (A) Algorithmic convergence in terms of nRMSE, at RF = 7 and with PS = 8 and 12. (B) nRMSE values as a function of reduction factor for PS = 8 and 12, using 2D undersampling (C) Algorithmic convergence in terms of nRMSE, at RF = 4 and with PS = 4 and 10. (D) comparing the difference in the effect of patch size on the resulting nRMSE value for RF = 4 and 7. Plots based on reconstruction results from restrospectively undersampled 2D brain image data.

		RF=3			RF=4			RF=5			RF=6			RF=7		
	PS	CLEAR	CLEAR-IRPA	LLR-IRPA	CLEAR	CLEAR-IRPA	LLR-IRPA	CLEAR	CLEAR-IRPA	LLR-IRPA	CLEAR	CLEAR-IRPA	LLR-IRPA	CLEAR	CLEAR-IRPA	LLR-IRPA
Brain	4	12.7	19.1	3.4	11.8	18.8	3.9	10.5	18.7	4.2	9.7	17.7	3.3	9.6	19.7	3.3
	6	7.3	9.6	2.0	5.9	9.5	2.3	5.2	9.3	2.5	5.1	9.3	1.8	5.2	10.3	1.7
	8	8.2	8.2	1.5	6.0	8.7	2.4	4.1	6.6	3.8	4.4	6.3	1.9	4.5	8.7	1.4
	10	7.5	6.3	1.6	3.5	5.4	1.7	3.3	4.9	2.5	3.4	5.9	1.5	3.4	6.6	1.3
	12	4.3	4.5	1.9	2.3	3.9	2.0	2.6	3.8	1.9	2.6	4.9	1.1	2.6	4.8	1.2
	14	2.1	3.6	1.6	2.5	3.8	1.6	2.2	3.1	1.1	2.1	4.5	1.0	2.2	4.0	1.4
Knee	4	5.9	8.8	1.5	6.0	8.6	1.7	5.4	8.9	1.8	4.9	8.5	2.0	4.9	9.3	3.0
	6	4.7	4.9	0.9	5.7	6.0	1.5	3.4	4.8	1.5	3.9	5.1	1.7	3.2	5.2	1.7
	8	2.4	2.8	0.6	3.2	3.5	1.0	2.1	2.9	1.0	2.1	3.5	1.1	1.7	2.8	1.3
	10	1.7	2.0	0.5	2.1	2.4	0.8	1.4	2.0	0.7	1.4	2.5	1.1	1.2	2.0	0.8
	12	1.4	1.5	0.4	2.0	1.9	0.7	1.0	1.6	0.6	1.2	1.9	1.0	1.0	1.5	0.9
	14	1.4	1.5	0.4	1.8	1.6	0.6	0.8	1.4	0.5	1.0	1.6	0.8	0.8	1.4	0.7

Table A3: Average time (seconds) **per iteration** for CLEAR, LLR-IRPA, and CLEAR using iterative random patch adjustments (CLEAR-IRPA) at various reduction factors (RF) and patch sizes (PS), for retrospective undersampling experiments. The matrix sizes for the brain and knee images are $224 \times 224 \times 20$ and $160 \times 160 \times 15$, respectively.

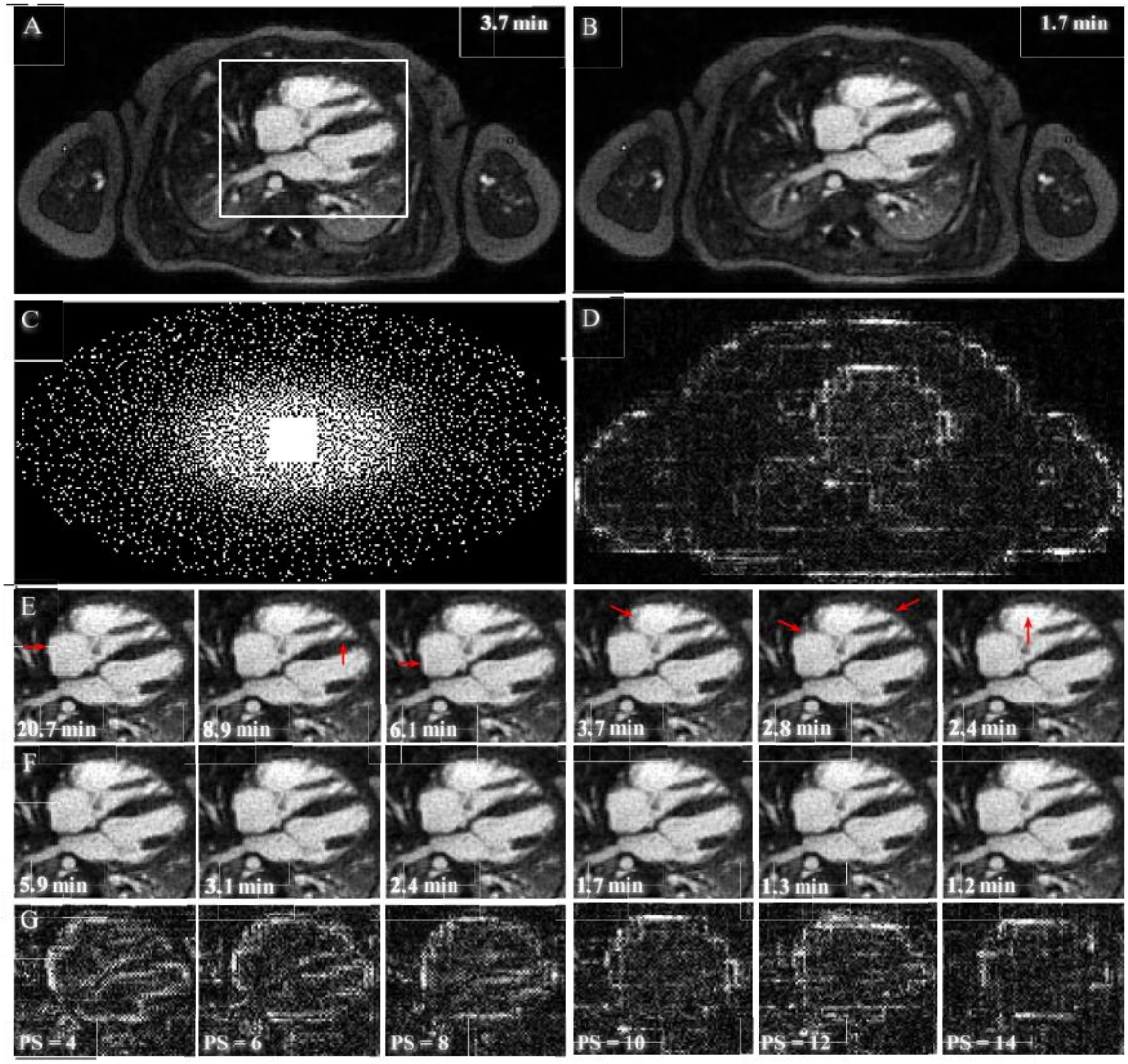

Figure A4: Reconstruction results and times for the prospectively undersampled MRA data set, at a reduction factor of 6.5. (A) CLEAR result and (B) LLR-IRPA result using PS = 10. (C) undersampled variable-density k-space sampling. (D) difference between (A) and (B). Cropped image series (E) shows the progression of CLEAR imaging results as patch size increases from 4 to 14. Red arrows indicate block artifacts in the CLEAR reconstruction. (F) Cropped image series from LLR-IRPA, in which block artifacts are more suppressed in comparison to CLEAR. (G) Difference images between (E) and (F). Window level scaled to 0 – 7.6% of the maximum signal in (A).

A.5.2 Parallel Imaging – Prospective Undersampling

Similar to the results from retrospective undersampling, the prospectively undersampled MRA data set shows comparable results in image quality, except that CLEAR displays more

apparent block artifacts than LLR-IRPA within the myocardium and along its edges, as shown in Figure A4. Due to the shift invariance induced from using different image partitions, the LLR-IRPA reconstructed images remain relatively stable and less prone to block artifacts as a function of patch size. We also see in the difference images between LLR-IRPA and CLEAR that various residual, block artifacts that remain due to the overlapping patches used by CLEAR. One can also observe that LLR-IRPA also avoids artifacts along edges of the anatomy. Importantly, note that the difference images in Figure A4 indicate the contrast in the levels of residual blocks artifacts produced by CLEAR. This result shows that LLR-IRPA can avoid these types of artifacts without compromising image quality. Unlike the retrospectively undersampled experiments, this data retained a much larger central sampling region of size 24×24, and slightly more dense sampling in the central region of k-space. Even in such a case, LLR-IRPA still provides an advantage in terms of robustness to differences in patch size.

A.6 **Discussion**

Although the imaging results show the similarity of the LLR-IRPA and CLEAR reconstruction approaches, it is important to note that these results are affected by the choice of sampling pattern, the sampling density, and the extent of the fully sampled central region, both in the 2D and 1D undersampling experiments. Even though the shift invariance due the random shifting of the patch grid can be reasonably expected to provide consistent improvement in image quality, it may provide more advantageous results in other instances where the sampling density or fully sampled region may not be so favorable. This type of case may arisein a pure calibrationless setting in which no fully sampled region may be acquired, or in cases where the sampling scheme does not produce an incoherent sampling pattern. In these cases, LLR-IRPA may still have an advantage dueto the added redundancy and shift invariance that results from iterative shifting of the image partition. It is important to note that the method reported by Zhang et al.[152], which also shifts partitions at each iteration, depends on an auto-calibration acquisition,

so that it may not be as applicable to general sampling schemes as the calibrationless LLR-IRPA technique, or CLEAR. The LLR-IRPA algorithm is applicable for arbitrary undersampled k-space trajectories without incurring the higher computational cost of CLEAR. Although CLEAR yields equivalent results, its algorithmic framework implicitly assumes that each patch is independent when applying singular-value thresholding and reconstructing each patch, which is not necessarily the case because this method uses overlapping patches. The step of dividing the resulting image by the number of times that each pixel is overlapped, as done in the report by Han et al.[166] is at best a heuristic approach for reconstructing the final image from multiple overlapping patches[163]. This approach only renders the optimization problem of CLEAR more mathematically tractable. In contrast, the LLR-IRPA algorithm treats each patch independently from the others throughout the iterative process, and the framework described in the Theory section provides a mathematically justifiable basis for solving the optimization scheme with shifting, non-overlapping patches.

As mentioned in the Theory section, each partition Ω can be shifted in a number of N_Ω different ways. In contrast to the wavelet cycle spinning strategy, each shift is performed randomly and the number of shifts is dependent on the prescribed patch size. The number of iterations needed to traverse all possible shifts is at least N_Ω, and this number increases as the patch size becomes larger. In the reconstruction performed in this study, the limit of 100 iterations can be approximately sufficient for patch sizes $\leq 10 \times 10$. However, results for patch sizes of 12×12 and 14 ×14 may not reflect those that would be obtained using the corresponding greater number of iterations. Despite the lower number of iterations used, the reconstruction results for these patch sizes still demonstrate considerable improvement, as seen in the MRA images where block artifacts are clearly suppressed in reconstructions with LLR-IRPA. This result shows the

robustness of the LLR-IRPA strategy, which maintains improved computational efficiency compared to CLEAR without introducing block artifacts.

In terms of computational complexity, LLR-IRPA has a significant advantage over CLEAR, without sacrificing algorithmic performance or image quality. In terms of computational cost, to reconstruct a 2D multi-coil $M \times N \times C$ image set using $m \times n$ patches (where $m|M$ and $n|N$), LLR-IRPA would require at most $Q = (\frac{M}{m} + 1)(\frac{N}{n} + 1)$ SVD computations of $mn \times C$ matrices per iteration, whereas CLEAR requires $P = (N + \frac{n(1-s)}{sn})(M + \frac{m(1-r)}{rm})$, where r and s are as given in (28). Suppose, as adopted in the experiments, that $r = s = 12$, and that $\frac{M}{m} = a$ and $\frac{N}{n} = b$. Then $Q = ab + a + b + 1$ while $P = 4ab + 3(a + b) + \frac{9}{4} \approx 4ab + 3(a + b) + 3$. To quote the result given in [16], the number of floating point operations (FLOPS) required for one thin SVD calculation would be

$$\text{FLOPS} = \min(14mnC^2 + 8C^3, 6mnC^2 + 20C^3)$$

Thus, as seen from the comparison of P and Q, this means that CLEAR would require approximately 3 to 4 times more FLOPS than LLR-IRPA. This estimation also agrees with the results in Table A3, which show that the average per-iteration time of LLR-IRPA can be roughly 3 to 4 times shorter than that of CLEAR. Evidently, this makes LLR-IRPA a much more efficient reconstruction scheme that produces comparable if not better imaging results to CLEAR. However, it is important to note that the use of graphical processing units (GPU) would highly accelerated these iteration times, yet the efficiency of LLR-IRPA would still outperform CLEAR.

In the context of local, patch-based methods for accelerated quantitative parameter mapping, we also note that alternative SVD-based techniques such as dictionary learning for blind

compressive sensing also show promise in reducing the computational load of locally low-rank regularized reconstruction[167,168]. In the absence of a learning step, however, LLR-IRPA represents a highly efficient class of algorithms for implementing effectively shift-invariant locally low-rank reconstruction in a calibrationless setting. Globally low rank regularization techniques, such as the k-space domain-based SAKE method for parallel imaging[146], can also operate in a calibrationless setting, yet they may entail significantly more FLOPS per iteration than the locally low rank LLR-IRPA and CLEAR methods, as discussed in the report by Trzasko et al.[151].

Further considerations include examining the performance of LLR-IPRA in more diverse acquisition and reconstruction settings, for example in dynamic reconstructions using more advanced algorithms based on constrained formulations and accelerated convergence schemes. However, while more advance algorithms may improve the convergence rates of LLR-IRPA and CLEAR, the relative computational efficiency between the two methods would not change because CLEAR would still require the computation of many more SVD's per iteration than LLR-IRPA. Therefore, the reconstruction speed of each method may increase, but the relative improvement of LLR-IRPA over CLEAR would remain valid.

A.7 **Conclusion**

In this chapter, we have shown that LLR-IRPA retains the same level of image reconstruction and quantitative parameter mapping results compared to overlapping patch-based LLR regularization, in terms of image quality and nRMSE, but with the distinct advantage of substantially reduced computational load. We describe this patch adjustment strategy for LLR regularization and set a theoretical framework for formulating this novel development in the context of patch-based image reconstruction techniques. This technique is an improvement over

conventional LLR-based algorithms such as CLEAR, since the computational load is substantially reduced without promoting block artifacts. In fact, the amount of acceleration from using random shifting has been shown to reach up to a factor of 3 to 4. The iterative random patch adjustment strategy is experimentally shown to suppress these artifacts while retaining the convergence rate of the more computationally expensive CLEAR algorithm. Experimental results and theoretical analysis of the proposed method support these findings. The implications of LLR-IRPA is to facilitate the application of LLR-based regularization for clinical MRI applications.

REFERENCES

1. Bogner W, Otazo R, Henning A. Accelerated MR spectroscopic imaging—a review of current and emerging techniques. *NMR Biomed*. n/a(n/a):e4314. doi:https://doi.org/10.1002/nbm.4314

2. Valette J, Giraudeau C, Marchadour C, et al. A new sequence for single-shot diffusion-weighted NMR spectroscopy by the trace of the diffusion tensor. *Magn Reson Med*. 2012;68(6):1705-1712. doi:10.1002/mrm.24193

3. Najac C, Lundell H, Kan HE, Webb AG, Ronen I. Single-shot isotropic diffusion-weighted NMR spectroscopy in the human brain at 7T using tetrahedral encoding. In: *Proceedings of the 2020 ISMRM & SMRT Conference & Exhibition*. The International Society for Magnetic Resonance in Medicine; 2020:Abstract 0739.

4. Saucedo A, Macey PM, Thomas MA. Accelerated radial echo-planar spectroscopic imaging using golden angle view-ordering and compressed-sensing reconstruction with total variation regularization. *Magn Reson Med*. 2021;86(1):46-61. doi:10.1002/mrm.28728

5. Nishimura DG. *Principles of Magnetic Resonance Imaging*. Stanford Univ.; 1996. Accessed July 16, 2023. http://books.google.com/books?id=uz9BAQAAIAAJ

6. Bernstein MA, King KF, Zhou XJ. *Handbook of MRI Pulse Sequences*. Elsevier; 2004.

7. Graaf RA de. *In Vivo NMR Spectroscopy: Principles and Techniques*. John Wiley & Sons; 2019.

8. Nelson SJ. Multivoxel Magnetic Resonance Spectroscopy of Brain Tumors. *Mol Cancer Ther*. 2003;2(5):497-507.

9. Barker PB, Bizzi A, Stefano ND, Lin DDM, Gullapalli R. *Clinical MR Spectroscopy: Techniques and Applications*. Cambridge University Press; 2010.

10. Brown TR, Kincaid BM, Ugurbil K. NMR chemical shift imaging in three dimensions. *Proc Natl Acad Sci U S A*. 1982;79(11):3523-3526.

11. Posse S, Tedeschi G, Risinger R, Ogg R, Bihan DL. High Speed1H Spectroscopic Imaging in Human Brain by Echo Planar Spatial-Spectral Encoding. *Magn Reson Med*. 1995;33(1):34-40. doi:10.1002/mrm.1910330106

12. Adalsteinsson E, Irarrazabal P, Topp S, Meyer C, Macovski A, Spielman DM. Volumetric spectroscopic imaging with spiral-basedk-space trajectories. *Magn Reson Med*. 1998;39(6):889-898. doi:10.1002/mrm.1910390606

13. Furuyama JK, Wilson NE, Thomas MA. Spectroscopic imaging using concentrically circular echo-planar trajectories in vivo. *Magn Reson Med*. 2012;67(6):1515-1522. doi:10.1002/mrm.23184

14. Schirda CV, Tanase C, Boada FE. Rosette spectroscopic imaging: Optimal parameters for alias-free, high sensitivity spectroscopic imaging. *J Magn Reson Imaging*. 2009;29(6):1375-1385. doi:10.1002/jmri.21760

15. Hingerl L, Bogner W, Moser P, et al. Density-weighted concentric circle trajectories for high resolution brain magnetic resonance spectroscopic imaging at 7T: DW-CONCEPT for High Resolution Brain MRSI at 7T. *Magn Reson Med*. 2018;79(6):2874-2885. doi:10.1002/mrm.26987

16. Emir UE, Burns B, Chiew M, Jezzard P, Thomas MA. Non-water-suppressed short-echo-time magnetic resonance spectroscopic imaging using a concentric ring *k* -space trajectory. *NMR Biomed*. 2017;30(7):e3714. doi:10.1002/nbm.3714

17. Feng L, Grimm R, Block KT, et al. Golden-angle radial sparse parallel MRI: Combination of compressed sensing, parallel imaging, and golden-angle radial sampling for fast and flexible dynamic volumetric MRI. *Magn Reson Med*. 2014;72(3):707-717. doi:10.1002/mrm.24980

18. Glover GH, Pauly JM. Projection Reconstruction Techniques for Reduction of Motion Effects in MRI. *Magn Reson Med*. 1992;28(2):275-289. doi:10.1002/mrm.1910280209

19. Ramirez MS, Lee J, Walker CM, et al. Radial spectroscopic MRI of hyperpolarized [1- ^{13}C] pyruvate at 7 tesla: Radial MRI of Hyperpolarized Pyruvate at 7T. *Magn Reson Med*. 2014;72(4):986-995. doi:10.1002/mrm.25004

20. Ludwig D, Korzowski A, Ruhm L, Ladd ME, Bachert P. Three-dimensional 31P Radial Echo-Planar Spectrocopic Imaging in vivo at 7T. *Proc Intl Soc Mag Reson Med*. 2017;25:Abstract 1247.

21. Boer VO, Ronen I, Pedersen JO, Petersen ET, Lundell H. Metabolite diffusion weighted imaging with golden angle radial echo planar spectroscopic imaging. *Proceeding 27th Annu Meet ISMRM Montr Can*. Published online 2019:3616.

22. Chan RW, Ramsay EA, Cheung EY, Plewes DB. The influence of radial undersampling schemes on compressed sensing reconstruction in breast MRI. *Magn Reson Med*. 2012;67(2):363-377. doi:10.1002/mrm.23008

23. Winkelmann S, Schaeffter T, Koehler T, Eggers H, Doessel O. An Optimal Radial Profile Order Based on the Golden Ratio for Time-Resolved MRI. *IEEE Trans Med Imaging*. 2007;26(1):68-76. doi:10.1109/TMI.2006.885337

24. Feng L, Axel L, Chandarana H, Block KT, Sodickson DK, Otazo R. XD-GRASP: Golden-angle radial MRI with reconstruction of extra motion-state dimensions using compressed sensing. *Magn Reson Med*. 2016;75(2):775-788. doi:10.1002/mrm.25665

25. Chandarana H, Feng L, Block TK, et al. Free-Breathing Contrast-Enhanced Multiphase MRI of the Liver Using a Combination of Compressed Sensing, Parallel Imaging, and Golden-Angle Radial Sampling. *Invest Radiol*. 2013;48(1). doi:10.1097/RLI.0b013e318271869c

26. Chambolle A. An Algorithm for Total Variation Minimization and Applications. *J Math Imaging Vis*. 2004;20(1/2):89-97. doi:10.1023/B:JMIV.0000011321.19549.88

27. Block KT, Uecker M, Frahm J. Undersampled radial MRI with multiple coils. Iterative image reconstruction using a total variation constraint. *Magn Reson Med*. 2007;57(6):1086-1098. doi:10.1002/mrm.21236

28. Furuyama JK, Wilson NE, Burns BL, Nagarajan R, Margolis DJ, Thomas MA. Application of compressed sensing to multidimensional spectroscopic imaging in human prostate. *Magn Reson Med*. 2012;67(6):1499-1505. doi:10.1002/mrm.24265

29. Nassirpour S, Chang P, Avdievitch N, Henning A. Compressed sensing for high-resolution nonlipid suppressed ^{1}H FID MRSI of the human brain at 9.4T. *Magn Reson Med*. 2018;80(6):2311-2325. doi:10.1002/mrm.27225

30. Chatnuntawech I, Gagoski B, Bilgic B, Cauley SF, Setsompop K, Adalsteinsson E. Accelerated 1H MRSI using randomly undersampled spiral-based k-space trajectories. *Magn Reson Med*. 2015;74(1):13-24. doi:10.1002/mrm.25394

31. Kasten J, Lazeyras F, Ville DVD. Data-Driven MRSI Spectral Localization Via Low-Rank Component Analysis. *IEEE Trans Med Imaging*. 2013;32(10):1853-1863. doi:10.1109/TMI.2013.2266259

32. Klauser A, Courvoisier S, Kasten J, et al. Fast high-resolution brain metabolite mapping on a clinical 3T MRI by accelerated H-FID-MRSI and low-rank constrained reconstruction. *Magn Reson Med*. 2019;81(5):2841-2857. doi:https://doi.org/10.1002/mrm.27623

33. Lam F, Ma C, Clifford B, Johnson CL, Liang ZP. High-resolution 1H-MRSI of the brain using SPICE: Data acquisition and image reconstruction. *Magn Reson Med*. 2016;76(4):1059-1070. doi:10.1002/mrm.26019

34. Bhattacharya I, Jacob M. Compartmentalized low-rank recovery for high-resolution lipid unsuppressed MRSI: High-Resolution Lipid Unsuppressed MRSI. *Magn Reson Med*. 2017;78(4):1267-1280. doi:10.1002/mrm.26537

35. Andronesi OC, Gagoski BA, Sorensen AG. Neurologic 3D MR Spectroscopic Imaging with Low-Power Adiabatic Pulses and Fast Spiral Acquisition. *Radiology*. 2012;262(2):647-661. doi:10.1148/radiol.11110277

36. Chiew M, Jiang W, Burns B, et al. Density-weighted concentric rings k-space trajectory for 1H magnetic resonance spectroscopic imaging at 7 T. *NMR Biomed*. 2018;31(1):e3838. doi:https://doi.org/10.1002/nbm.3838

37. Bottomley PA. Spatial localization in NMR spectroscopy in vivo. *Ann N Y Acad Sci*. 1987;508:333-348. doi:10.1111/j.1749-6632.1987.tb32915.x

38. Scheenen TWJ, Klomp DWJ, Wijnen JP, Heerschap A. Short echo time 1H-MRSI of the human brain at 3T with minimal chemical shift displacement errors using adiabatic refocusing pulses. *Magn Reson Med*. 2008;59(1):1-6. doi:10.1002/mrm.21302

39. Ogg RJ, Kingsley PB, Taylor JS. WET, a T1- and B1-insensitive water-suppression method for in vivo localized 1H NMR spectroscopy. *J Magn Reson B*. 1994;104(1):1-10. doi:10.1006/jmrb.1994.1048

40. Fessler JA, Sutton BP. Nonuniform fast Fourier transforms using min-max interpolation. *IEEE Trans Signal Process*. 2003;51(2):560-574. doi:10.1109/TSP.2002.807005

41. Beck A, Teboulle M. Fast Gradient-Based Algorithms for Constrained Total Variation Image Denoising and Deblurring Problems. *IEEE Trans Image Process*. 2009;18(11):2419-2434. doi:10.1109/TIP.2009.2028250

42. Fessler JA. Michigan Image Reconstruction Toolbox. https://web.eecs.umich.edu/~fessler/code/index.html

43. Hanson LG, Schaumburg K, Paulson OB. Reconstruction strategy for echo planar spectroscopy and its application to partially undersampled imaging. *Magn Reson Med*. 2000;44(3):412-417. doi:10.1002/1522-2594(200009)44:3<412::AID-MRM11>3.0.CO;2-P

44. Klose U. In vivo proton spectroscopy in presence of eddy currents. *Magn Reson Med*. 1990;14(1):26-30. doi:10.1002/mrm.1910140104

45. Bydder M, Hamilton G, Yokoo T, Sirlin CB. Optimal phased-array combination for spectroscopy. *Magn Reson Imaging*. 2008;26(6):847-850. doi:10.1016/j.mri.2008.01.050

46. Near J, Edden R, Evans CJ, Paquin R, Harris A, Jezzard P. Frequency and phase drift correction of magnetic resonance spectroscopy data by spectral registration in the time domain: MRS Drift Correction Using Spectral Registration. *Magn Reson Med*. 2015;73(1):44-50. doi:10.1002/mrm.25094

47. Simpson R, Devenyi GA, Jezzard P, Hennessy TJ, Near J. Advanced processing and simulation of MRS data using the FID appliance (FID-A)—An open source, MATLAB - based toolkit. *Magn Reson Med*. 2017;77(1):23-33. doi:10.1002/mrm.26091

48. Cabanes E, Confort-Gouny S, Le Fur Y, Simond G, Cozzone PJ. Optimization of Residual Water Signal Removal by HLSVD on Simulated Short Echo Time Proton MR Spectra of the Human Brain. *J Magn Reson*. 2001;150(2):116-125. doi:10.1006/jmre.2001.2318

49. Provencher SW. Estimation of metabolite concentrations from localized in vivo proton NMR spectra. *Magn Reson Med*. 1993;30(6):672-679. doi:10.1002/mrm.1910300604

50. Soher BJ, Semanchuk P, Todd S, Steinberg J, Young K. VeSPA: integrated applications for RF pulse design, spectral simulation and MRS data analysis. *Proc Intl Soc Mag Reson Med*. 2011;19:1410.

51. Scheffler K, Hennig J. Reduced circular field-of-view imaging. *Magn Reson Med*. 1998;40(3):474-480. doi:10.1002/mrm.1910400319

52. Smith TB, Nayak KS. MRI artifacts and correction strategies. *Imaging Med*. 2010;2(4):445-457. doi:10.2217/iim.10.33

53. Wang J, Chen Z, Wang Y, Yuan L, Xia L. A Feasibility Study of Geometric-Decomposition Coil Compression in MRI Radial Acquisitions. *Comput Math Methods Med*. 2017;2017:1-9. doi:10.1155/2017/7685208

54. Cunningham CH, Vigneron DB, Chen AP, et al. Design of flyback echo-planar readout gradients for magnetic resonance spectroscopic imaging. *Magn Reson Med*. 2005;54(5):1286-1289. doi:10.1002/mrm.20663

55. Saucedo A, Sarma M, Thomas MA. Radial Flyback Echo-Planar Spectroscopic Imaging with Golden Angle Sampling and Total Variation-based Compressed Sensing Reconstruction. *Proc Intl Soc Mag Reson Med*. 2020;28:2865.

56. Ong F, Uecker M, Lustig M. Accelerating Non-Cartesian MRI Reconstruction Convergence Using k-Space Preconditioning. *IEEE Trans Med Imaging*. 2020;39(5):1646-1654. doi:10.1109/TMI.2019.2954121

57. Uecker M, Lai P, Murphy MJ, et al. ESPIRiT—an eigenvalue approach to autocalibrating parallel MRI: Where SENSE meets GRAPPA. *Magn Reson Med*. 2014;71(3):990-1001. doi:10.1002/mrm.24751

58. Sutton BP, Noll DC, Fessler JA. Fast, iterative image reconstruction for MRI in the presence of field inhomogeneities. *IEEE Trans Med Imaging*. 2003;22(2):178-188. doi:10.1109/TMI.2002.808360

59. Fessler JA, Lee S, Olafsson VT, Shi HR, Noll DC. Toeplitz-based iterative image reconstruction for MRI with correction for magnetic field inhomogeneity. *IEEE Trans SIGNAL Process*. 2005;53(9):10.

60. Weller DS, Ramani S, Fessler JA. Augmented Lagrangian with Variable Splitting for Faster Non-Cartesian $\rm L_1$-SPIRiT MR Image Reconstruction. *IEEE Trans Med Imaging*. 2014;33(2):351-361. doi:10.1109/TMI.2013.2285046

61. Bhave S, Eslami R, Jacob M. Sparse spectral deconvolution algorithm for noncartesian MR spectroscopic imaging. *Magn Reson Med*. 2014;71(2):469-476. doi:https://doi.org/10.1002/mrm.24693

62. Rowland BC, Liao H, Adan F, Mariano L, Irvine J, Lin AP. Correcting for Frequency Drift in Clinical Brain MR Spectroscopy. *J Neuroimaging*. 2017;27(1):23-28. doi:https://doi.org/10.1111/jon.12388

63. Johnson G, Jung KJ, Wu EX, Hilal SK. Self-correction of proton spectroscopic images for gradient eddy current distortions and static field inhomogeneities. *Magn Reson Med*. 1993;30(2):255-261. doi:10.1002/mrm.1910300217

64. Maudsley AA, Hilal SK. Field inhomogeneity correction and data processing for spectroscopic imaging. *Magn Reson Med*. 1985;2(3):218-233. doi:10.1002/mrm.1910020305

65. Bilgic B, Chatnuntawech I, Fan AP, et al. Fast image reconstruction with L2-regularization. *J Magn Reson Imaging*. 2014;40(1):181-191. doi:10.1002/jmri.24365

66. Basharat M, Payne GS, Morgan VA, Parker C, Dearnaley D, deSouza NM. TE = 32 ms vs TE = 100 ms echo-time 1H-magnetic resonance spectroscopy in prostate cancer: Tumor metabolite depiction and absolute concentrations in tumors and adjacent tissues. *J Magn Reson Imaging*. 2015;42(4):1086-1093. doi:10.1002/jmri.24875

67. Basharat M, Jafar M, deSouza NM, Payne GS. Evaluation of short-TE 1H MRSI for quantification of metabolites in the prostate. *NMR Biomed*. 2014;27(4):459-467. doi:10.1002/nbm.3082

68. Tayari N, Heerschap A, Scheenen TWJ, Kobus T. In vivo MR spectroscopic imaging of the prostate, from application to interpretation. *Anal Biochem*. 2017;529:158-170. doi:10.1016/j.ab.2017.02.001

69. Chen AP, Cunningham CH, Ozturk-Isik E, et al. High-speed 3T MR spectroscopic imaging of prostate with flyback echo-planar encoding. *J Magn Reson Imaging*. 2007;25(6):1288-1292. doi:10.1002/jmri.20916

70. Palombo M, Shemesh N, Ronen I, Valette J. Insights into brain microstructure from in vivo DW-MRS. *NeuroImage*. 2018;182:97-116. doi:10.1016/j.neuroimage.2017.11.028

71. Ligneul C, Palombo M, Hernández-Garzón E, et al. Diffusion-weighted magnetic resonance spectroscopy enables cell-specific monitoring of astrocyte reactivity in vivo. *NeuroImage*. 2019;191:457-469. doi:10.1016/j.neuroimage.2019.02.046

72. Harada M, Uno M, Hong F, Hisaoka S, Nishitani H, Matsuda T. Diffusion-weighted in vivo localized proton MR spectroscopy of human cerebral ischemia and tumor. *NMR Biomed*. 2002;15(1):69-74. doi:10.1002/nbm.759

73. Zheng DD, Liu ZH, Fang J, Wang XY, Zhang J. The Effect of Age and Cerebral Ischemia on Diffusion-Weighted Proton MR Spectroscopy of the Human Brain. *Am J Neuroradiol*. 2012;33(3):563-568. doi:10.3174/ajnr.A2793

74. Genovese G, Diaz-Fernandez B, Lejeune FX, et al. Longitudinal Monitoring of Microstructural Alterations in Cerebral Ischemia with in Vivo Diffusion-weighted MR Spectroscopy. *Radiology*. Published online 2022:220430.

75. van der Toorn A, Dijkhuizen RM, Tulleken CAF, Nicolay K. Diffusion of metabolites in normal and ischemic rat brain measured by localized 1H MRS. *Magn Reson Med*. 1996;36(6):914-922. doi:10.1002/mrm.1910360614

76. Wood ET, Ronen I, Techawiboonwong A, et al. Investigating Axonal Damage in Multiple Sclerosis by Diffusion Tensor Spectroscopy. *J Neurosci*. 2012;32(19):6665-6669. doi:10.1523/JNEUROSCI.0044-12.2012

77. Bodini, B., Branzoli, F., Poirion, E., et al. Energy dysregulation and neuro-axonal dysfunction in MS measured in-vivo with diffusion-weighed spectroscopy. *Mult Scler J*. 2015;21:491-492.

78. Steel RM, Bastin ME, McConnell S, et al. Diffusion tensor imaging (DTI) and proton magnetic resonance spectroscopy (1H MRS) in schizophrenic subjects and normal controls. *Psychiatry Res Neuroimaging*. 2001;106(3):161-170. doi:10.1016/S0925-4927(01)00080-4

79. Ellegood J, Hanstock CC, Beaulieu C. Trace apparent diffusion coefficients of metabolites in human brain using diffusion weighted magnetic resonance spectroscopy. *Magn Reson Med*. 2005;53(5):1025-1032. doi:10.1002/mrm.20427

80. Deelchand DK, Auerbach EJ, Marjańska M. Apparent diffusion coefficients of the five major metabolites measured in the human brain in vivo at 3T: ADC of Human Brain Metabolites at 3T. *Magn Reson Med*. 2018;79(6):2896-2901. doi:10.1002/mrm.26969

81. Genovese G, Marjańska M, Auerbach EJ, et al. In vivo diffusion-weighted MRS using semi-LASER in the human brain at 3 T: Methodological aspects and clinical feasibility. *NMR Biomed*. 2021;34(5). doi:10.1002/nbm.4206

82. Najac C, Branzoli F, Ronen I, Valette J. Brain intracellular metabolites are freely diffusing along cell fibers in grey and white matter, as measured by diffusion-weighted MR spectroscopy in the human brain at 7 T. *Brain Struct Funct*. 2016;221(3):1245-1254. doi:10.1007/s00429-014-0968-5

83. Jara H, Wehrli FW. Determination of Background Gradients with Diffusion MR Imaging. *J Magn Reson Imaging*. 1994;4(6):787-797. doi:10.1002/jmri.1880040608

84. Neeman M, Freyer JP, Sillerud LO. A simple method for obtaining cross-term-free images for diffusion anisotropy studies in NMR microimaging. *Magn Reson Med*. 1991;21(1):138-143. doi:10.1002/mrm.1910210117

85. Reese TG, Heid O, Weisskoff RM, Wedeen VJ. Reduction of eddy-current-induced distortion in diffusion MRI using a twice-refocused spin echo. *Magn Reson Med*. 2003;49(1):177-182. doi:10.1002/mrm.10308

86. Alexander AL, Tsuruda JS, Parker DL. Elimination of eddy current artifacts in diffusion-weighted echo-planar images: The use of bipolar gradients. *Magn Reson Med*. 1997;38(6):1016-1021. doi:10.1002/mrm.1910380623

87. Finsterbusch J. Eddy-current compensated diffusion weighting with a single refocusing RF pulse. *Magn Reson Med*. 2009;61(3):748-754. doi:10.1002/mrm.21899

88. Frahm J, Merboldt KD, Hänicke W. Localized proton spectroscopy using stimulated echoes. *J Magn Reson 1969*. 1987;72(3):502-508. doi:10.1016/0022-2364(87)90154-5

89. Mori S, Van Zijl PCM. Diffusion Weighting by the Trace of the Diffusion Tensor within a Single Scan. *Magn Reson Med*. 1995;33(1):41-52. doi:10.1002/mrm.1910330107

90. de Graaf RA, Braun KPJ, Nicolay K. Single-shot diffusion trace1H NMR spectroscopy. *Magn Reson Med*. 2001;45(5):741-748. doi:10.1002/mrm.1101

91. Chun T, Uluğ AM, van Zijl PCM. Single-shot diffusion-weighted trace imaging on a clinical scanner. *Magn Reson Med*. 1998;40(4):622-628. doi:10.1002/mrm.1910400415

92. Valette J, Ligneul C, Marchadour C, Najac C, Palombo M. Brain Metabolite Diffusion from Ultra-Short to Ultra-Long Time Scales: What Do We Learn, Where Should We Go? *Front Neurosci*. 2018;12:2. doi:10.3389/fnins.2018.00002

93. Marchadour C, Brouillet E, Hantraye P, Lebon V, Valette J. Anomalous Diffusion of Brain Metabolites Evidenced by Diffusion-Weighted Magnetic Resonance Spectroscopy *in Vivo*. *J Cereb Blood Flow Metab*. 2012;32(12):2153-2160. doi:10.1038/jcbfm.2012.119

94. Ligneul C, Valette J. Probing metabolite diffusion at ultra-short time scales in the mouse brain using optimized oscillating gradients and "short"-echo-time diffusion-weighted MRS. *NMR Biomed*. 2017;30(1):e3671. doi:10.1002/nbm.3671

95. Döring A, Kreis R. Magnetic resonance spectroscopy extended by oscillating diffusion gradients: Cell-specific anomalous diffusion as a probe for tissue microstructure in human brain. *NeuroImage*. 2019;202:116075. doi:10.1016/j.neuroimage.2019.116075

96. Güllmar D, Haueisen J, Reichenbach JR. Analysis of *b* -value calculations in diffusion weighted and diffusion tensor imaging: *b* -Value Calculations. *Concepts Magn Reson Part A*. 2005;25A(1):53-66. doi:10.1002/cmr.a.20031

97. Szczepankiewicz F, Sjölund J. Cross-term-compensated gradient waveform design for tensor-valued diffusion MRI. *J Magn Reson*. 2021;328:106991. doi:10.1016/j.jmr.2021.106991

98. Zheng G, Price WS. Suppression of background gradients in (B0 gradient-based) NMR diffusion experiments. *Concepts Magn Reson Part A*. 2007;30A(5):261-277. doi:10.1002/cmr.a.20092

99. Cohen Y, Avram L, Frish L. Diffusion NMR Spectroscopy in Supramolecular and Combinatorial Chemistry: An Old Parameter—New Insights. *Angew Chem Int Ed*. 2005;44(4):520-554. doi:10.1002/anie.200300637

100. Kuchel PW, Pagès G, Nagashima K, et al. Stejskal–tanner equation derived in full. *Concepts Magn Reson Part A*. 2012;40A(5):205-214. doi:10.1002/cmr.a.21241

101. Landheer K, Schulte R, Geraghty B, et al. Diffusion-weighted J-resolved spectroscopy: Diffusion-Weighted J-Resolved Spectroscopy. *Magn Reson Med*. 2017;78(4):1235-1245. doi:10.1002/mrm.26514

102. Hanstock C, Beaulieu C. Rapid acquisition diffusion MR spectroscopy of metabolites in human brain. *NMR Biomed*. 2021;34(5). doi:10.1002/nbm.4270

103. Kan HE, Techawiboonwong A, van Osch MJP, et al. Differences in apparent diffusion coefficients of brain metabolites between grey and white matter in the human brain measured at 7 T: Trace ADCs of Multiple Brain Metabolites at 7 T. *Magn Reson Med*. 2012;67(5):1203-1209. doi:10.1002/mrm.23129

104. Posse S, Cuenod CA, Le Bihan D. Motion Artifact Compensation in^ 1H Spectroscopic Imaging by Signal Tracking. *J Magn Reson B*. 1993;102:222-222.

105. Posse S, Cuenod CA, Le Bihan D. Human brain: proton diffusion MR spectroscopy. *Radiology*. 1993;188(3):719-725. doi:10.1148/radiology.188.3.8351339

106. Gabr RE, Sathyanarayana S, Schär M, Weiss RG, Bottomley PA. On restoring motion-induced signal loss in single-voxel magnetic resonance spectra. *Magn Reson Med*. 2006;56(4):754-760. doi:10.1002/mrm.21015

107. Helms G, Piringer A. Restoration of motion-related signal loss and line-shape deterioration of proton MR spectra using the residual water as intrinsic reference. *Magn Reson Med*. 2001;46(2):395-400. doi:10.1002/mrm.1203

108. Roebuck JR, Hearshen DO, O'Donnell M, Raidy T. Correction of phase effects produced by eddy currents in solvent suppressed1H-CSI. *Magn Reson Med*. 1993;30(3):277-282. doi:10.1002/mrm.1910300302

109. Zhu G, Gheorghiu D, Allen PS. Motional degradation of metabolite signal strengths when using STEAM: A correction method. *NMR Biomed*. 1992;5(4):209-211. doi:10.1002/nbm.1940050408

110. An L, Willem van der Veen J, Li S, Thomasson DM, Shen J. Combination of multichannel single-voxel MRS signals using generalized least squares. *J Magn Reson Imaging*. 2013;37(6):1445-1450. doi:10.1002/jmri.23941

111. Provencher SW. Automatic quantitation of localized in vivo 1H spectra with LCModel. *NMR Biomed*. 2001;14(4):260-264. doi:10.1002/nbm.698

112. Van AT, Holdsworth SJ, Bammer R. In vivo investigation of restricted diffusion in the human brain with optimized oscillating diffusion gradient encoding: In Vivo Oscillating Gradient Diffusion in the Human Brain. *Magn Reson Med*. 2014;71(1):83-94. doi:10.1002/mrm.24632

113. Wood ET, Ercan AE, Branzoli F, et al. Reproducibility and optimization of in vivo human diffusion-weighted MRS of the corpus callosum at 3T and 7T. *NMR Biomed*. 2015;28(8):976-987. doi:10.1002/nbm.3340

114. Ercan AE, Techawiboonwong A, Versluis MJ, Webb AG, Ronen I. Diffusion-weighted chemical shift imaging of human brain metabolites at 7T: DW-CSI of the Human Brain at 7T. *Magn Reson Med*. 2015;73(6):2053-2061. doi:10.1002/mrm.25346

115. Fotso K, Dager SR, Landow A, et al. Diffusion tensor spectroscopic imaging of the human brain in children and adults: Diffusion Tensor Spectroscopic Imaging in Human Brain. *Magn Reson Med*. 2017;78(4):1246-1256. doi:10.1002/mrm.26518

116. Bito Y, Hirata S, Nabeshima T, Yamamoto E. Echo-Planar Diffusion Spectroscopic Imaging. *Magn Reson Med*. 1995;33(1):69-73. doi:10.1002/mrm.1910330110

117. Bito Y, Hirata K, Ebisu T, et al. Diffusion-weighted Line-scan Echo-planar Spectroscopic Imaging Technique to Reduce Motion Artifacts in Metabolite Diffusion Imaging. *Magn Reson Med Sci*. 2015;14(1):43-50. doi:10.2463/mrms.2014-0024

118. Kim DH, Adalsteinsson E, Spielman DM. Spiral readout gradients for the reduction of motion artifacts in chemical shift imaging. *Magn Reson Med*. 2004;51(3):458-463. doi:10.1002/mrm.20004

119. Stehning C, Börnert P, Nehrke K, Eggers H, Stuber M. Free-breathing whole-heart coronary MRA with 3D radial SSFP and self-navigated image reconstruction. *Magn Reson Med*. 2005;54(2):476-480. doi:10.1002/mrm.20557

120. Welch EB, Rossman PJ, Felmlee JP, Manduca A. Self-navigated motion correction using moments of spatial projections in radial MRI. *Magn Reson Med*. 2004;52(2):337-345. doi:10.1002/mrm.20151

121. Wong EC, Cox RW, Song AW. Optimized isotropic diffusion weighting. *Magn Reson Med*. 1995;34(2):139-143. doi:10.1002/mrm.1910340202

122. Saucedo A, Thomas MA. Single Shot Diffusion Trace Spectroscopic Imaging using Radial Echo Planar Trajectories. *Proceeding 32nd Annu Meet ISMRM Tor Can*. Published online 2023:5024.

123. Hargreaves BA, Pauly JM, Nishimura DG. Comparison of Even and Odd Projection-Reconstruction Sampling Strategies. *Proceeding 7th Annu Meet ISMRM Phila USA*. Published online 1999:658.

124. Block KT, Uecker M. Simple Method for Adaptive Gradient-Delay Compensation in Radial MRI. *Proceeding 19th Annu Meet ISMRM Quebec Can*. Published online 2011:2816.

125. Armstrong T, Dregely I, Stemmer A, et al. Free-breathing liver fat quantification using a multiecho 3D stack-of-radial technique: Free-Breathing Radial Liver Fat Quantification. *Magn Reson Med*. 2018;79(1):370-382. doi:10.1002/mrm.26693

126. Eldirdiri A, Posse S, Hanson LG, et al. Development of a Symmetric Echo-Planar Spectroscopy Imaging Framework for Hyperpolarized 13C Imaging in a Clinical PET/MR Scanner. *Tomography*. 2018;4(3):110-122. doi:10.18383/j.tom.2018.00006

127. Gordon JW, Vigneron DB, Larson PEZ. Development of a symmetric echo planar imaging framework for clinical translation of rapid dynamic hyperpolarized ^{13}C imaging: Rapid Imaging of Hyperpolarized ^{13}C with Symmetric EPI. *Magn Reson Med*. 2017;77(2):826-832. doi:10.1002/mrm.26123

128. Schuff N, Ezekiel F, Gamst AC, et al. Region and tissue differences of metabolites in normally aged brain using multislice 1H magnetic resonance spectroscopic imaging. *Magn Reson Med*. 2001;45(5):899-907. doi:10.1002/mrm.1119

129. Hetherington HP, Pan JW, Mason GF, et al. Quantitative 1H spectroscopic imaging of human brain at 4.1 T using image segmentation. *Magn Reson Med*. 1996;36(1):21-29. doi:10.1002/mrm.1910360106

130. Helenius J, Soinne L, Perkiö J, et al. Diffusion-Weighted MR Imaging in Normal Human Brains in Various Age Groups. *Am J Neuroradiol*. 2002;23(2):194-199.

131. Alhamud A, Tisdall MD, Hess AT, Hasan KM, Meintjes EM, van der Kouwe AJW. Volumetric navigators for real-time motion correction in diffusion tensor imaging. *Magn Reson Med*. 2012;68(4):1097-1108. doi:10.1002/mrm.23314

132. Hess AT, Andronesi OC, Dylan Tisdall M, Gregory Sorensen A, van der Kouwe AJW, Meintjes EM. Real-time motion and B0 correction for localized adiabatic selective refocusing (LASER) MRSI using echo planar imaging volumetric navigators. *NMR Biomed*. 2012;25(2):347-358. doi:10.1002/nbm.1756

133. Deshmane A, Blaimer M, Breuer F, et al. Self-calibrated trajectory estimation and signal correction method for robust radial imaging using GRAPPA operator gridding. *Magn Reson Med*. 2016;75(2):883-896. doi:10.1002/mrm.25648

134. Duyn JH, Yang Y, Frank JA, van der Veen JW. Simple Correction Method fork-Space Trajectory Deviations in MRI. *J Magn Reson*. 1998;132(1):150-153. doi:10.1006/jmre.1998.1396

135. BART Toolbox. Accessed July 19, 2023. https://mrirecon.github.io/bart/

136. Murphy M, Alley M, Demmel J, Keutzer K, Vasanawala S, Lustig M. Fast \ell_1 -SPIRiT Compressed Sensing Parallel Imaging MRI: Scalable Parallel Implementation and Clinically Feasible Runtime. *IEEE Trans Med Imaging*. 2012;31(6):1250-1262. doi:10.1109/TMI.2012.2188039

137. Vasanawala S, Murphy M, Alley M, et al. Practical parallel imaging compressed sensing MRI: Summary of two years of experience in accelerating body MRI of pediatric patients. In: *2011 IEEE International Symposium on Biomedical Imaging: From Nano to Macro*. ; 2011:1039-1043. doi:10.1109/ISBI.2011.5872579

138. Vasanawala SS, Alley MT, Hargreaves BA, Barth RA, Pauly JM, Lustig M. Improved Pediatric MR Imaging with Compressed Sensing. *Radiology*. 2010;256(2):607-616. doi:10.1148/radiol.10091218

139. Majumdar A, Ward RK. Exploiting rank deficiency and transform domain sparsity for MR image reconstruction. *Magn Reson Imaging*. 2012;30(1):9-18. doi:10.1016/j.mri.2011.07.021

140. Haldar JP, Liang ZP. Spatiotemporal imaging with partially separable functions: A matrix recovery approach. In: *2010 IEEE International Symposium on Biomedical Imaging: From Nano to Macro*. ; 2010:716-719. doi:10.1109/ISBI.2010.5490076

141. Haldar JP, Liang ZP. Low-rank approximations for dynamic imaging. In: *2011 IEEE International Symposium on Biomedical Imaging: From Nano to Macro*. ; 2011:1052-1055. doi:10.1109/ISBI.2011.5872582

142. Trzasko JD. Exploiting local low-rank structure in higher-dimensional MRI applications. In: *Wavelets and Sparsity XV*. Vol 8858. SPIE; 2013:551-558. doi:10.1117/12.2027059

143. Majumdar A. Improved dynamic MRI reconstruction by exploiting sparsity and rank-deficiency. *Magn Reson Imaging*. 2013;31(5):789-795. doi:10.1016/j.mri.2012.10.026

144. Lingala SG, Hu Y, DiBella E, Jacob M. Accelerated Dynamic MRI Exploiting Sparsity and Low-Rank Structure: k-t SLR. *IEEE Trans Med Imaging*. 2011;30(5):1042-1054. doi:10.1109/TMI.2010.2100850

145. Otazo R, Candès E, Sodickson DK. Low-rank plus sparse matrix decomposition for accelerated dynamic MRI with separation of background and dynamic components. *Magn Reson Med*. 2015;73(3):1125-1136. doi:10.1002/mrm.25240

146. Shin PJ, Larson PEZ, Ohliger MA, et al. Calibrationless parallel imaging reconstruction based on structured low-rank matrix completion. *Magn Reson Med*. 2014;72(4):959-970. doi:10.1002/mrm.24997

147. Chiew M, Smith SM, Koopmans PJ, Graedel NN, Blumensath T, Miller KL. k-t FASTER: Acceleration of functional MRI data acquisition using low rank constraints. *Magn Reson Med*. 2015;74(2):353-364. doi:10.1002/mrm.25395

148. Zhao B, Haldar JP, Brinegar C, Liang ZP. Low rank matrix recovery for real-time cardiac MRI. In: *2010 IEEE International Symposium on Biomedical Imaging: From Nano to Macro*. ; 2010:996-999. doi:10.1109/ISBI.2010.5490156

149. Zhao B, Lu W, Hitchens TK, Lam F, Ho C, Liang ZP. Accelerated MR parameter mapping with low-rank and sparsity constraints. *Magn Reson Med*. 2015;74(2):489-498. doi:10.1002/mrm.25421

150. Trzasko J, Manduca A. Local versus Global Low-Rank Promotion in Dynamic MRI Series Reconstruction. In: *Proceedings of the 2011 ISMRM Conference*. The International Society for Magnetic Resonance in Medicine; 2011:Abstract 4371.

151. Trzasko JD, Manduca A. Calibrationless parallel MRI using CLEAR. In: *2011 Conference Record of the Forty Fifth Asilomar Conference on Signals, Systems and Computers (ASILOMAR)*. ; 2011:75-79. doi:10.1109/ACSSC.2011.6189958

152. Zhang T, Pauly JM, Levesque IR. Accelerating parameter mapping with a locally low rank constraint. *Magn Reson Med*. 2015;73(2):655-661. doi:10.1002/mrm.25161

153. Zhang T, Cheng JY, Potnick AG, et al. Fast pediatric 3D free-breathing abdominal dynamic contrast enhanced MRI with high spatiotemporal resolution. *J Magn Reson Imaging*. 2015;41(2):460-473. doi:10.1002/jmri.24551

154. Rao EKR, Yip PC. Karhunen-Loeve transform. In: *The Transform and Data Compression Handbook*. 1st ed. CRC PRESS; 2001:1-34.

155. Xu Y, Yin W. A fast patch-dictionary method for whole image recovery. Published online August 16, 2014. doi:10.48550/arXiv.1408.3740

156. Cai JF, Candès EJ, Shen Z. A Singular Value Thresholding Algorithm for Matrix Completion. *SIAM J Optim*. 2010;20(4):1956-1982. doi:10.1137/080738970

157. Kamilov US, Bostan E, Unser M. Variational Justification of Cycle Spinning for Wavelet-Based Solutions of Inverse Problems. *IEEE Signal Process Lett*. 2014;21(11):1326-1330. doi:10.1109/LSP.2014.2334306

158. Bhatia R. *Matrix Analysis*. Springer-Verlag; 1997.

159. Lefkimmiatis S, Ward JP, Unser M. Hessian Schatten-Norm Regularization for Linear Inverse Problems. *IEEE Trans Image Process*. 2013;22(5):1873-1888. doi:10.1109/TIP.2013.2237919

160. Guerquin-Kern M, Haberlin M, Pruessmann KP, Unser M. A Fast Wavelet-Based Reconstruction Method for Magnetic Resonance Imaging. *IEEE Trans Med Imaging*. 2011;30(9):1649-1660. doi:10.1109/TMI.2011.2140121

161. Beck A, Teboulle M. A Fast Iterative Shrinkage-Thresholding Algorithm for Linear Inverse Problems. *SIAM J Imaging Sci*. 2009;2(1):183-202. doi:10.1137/080716542

162. Liu J, Ye J. Efficient L1/Lq Norm Regularization. Published online September 24, 2010. doi:10.48550/arXiv.1009.4766

163. Mairal J, Bach F, Ponce J, Sapiro G, Zisserman A. Non-local sparse models for image restoration. In: *2009 IEEE 12th International Conference on Computer Vision*. ; 2009:2272-2279. doi:10.1109/ICCV.2009.5459452

164. Lewis A. The Convex Analysis of Unitarily Invariant Matrix Functions. *J Convex Anal*. 1970;2.

165. Boyd SP, Vandenberghe L. *Convex Optimization*. Cambridge University Press; 2004.

166. Han F, Rapacchi S, Khan S, et al. Four-dimensional, multiphase, steady-state imaging with contrast enhancement (MUSIC) in the heart: A feasibility study in children. *Magn Reson Med*. 2015;74(4):1042-1049. doi:10.1002/mrm.25491

167. Bhave S, Lingala SG, Johnson CP, Magnotta VA, Jacob M. Accelerated whole-brain multi-parameter mapping using blind compressed sensing. *Magn Reson Med*. 2016;75(3):1175-1186. doi:10.1002/mrm.25722

168. Zhu Y, Zhang Q, Liu Q, et al. PANDA- T1ρ: Integrating principal component analysis and dictionary learning for fast T1ρ mapping. *Magn Reson Med*. 2015;73(1):263-272. doi:10.1002/mrm.25130